Karl-Johan Reite

Modeling and control of trawl systems

Doctoral thesis
for the degree of doktor ingeniør

Trondheim, August 2006

Norwegian University of
Science and Technology
Department of Marine Technology
Faculty of Engineering Science and Technology

NTNU
Innovation and Creativity

NTNU
Norwegian University of Science and Technology

Doctoral thesis
for the degree of doktor ingeniør

Department of Marine Technology
Faculty of Engineering Science and Technology

ISBN 82-471-8024-3 (printed ver.)
ISBN 82-471-8023-5 (electronic ver.)
ISSN 1503-8181

Doctoral Theses at NTNU, 2006:131

Printed by Tapir Uttrykk

Abstract

This thesis is motivated by the possible benefits of a more precise trawl control system with respect to both environmental impact and fishing efficiency. It considers how the control performance of a pelagic trawl system can be improved, partly by introducing a control architecture tailor-made for the trawl system subject to industrial requirements, and partly by developing a trawl door control concept.

A mathematical model of the trawl system is developed, including an accurate model of the hydrodynamic forces on the trawl doors. This model estimates both the steady state and the transient forces on trawl doors moving in six degrees of freedom. The steady state hydrodynamic forces are based on wind tunnel experiments. To estimate the transient forces, a software code based on potential theory is developed. This software estimates the time-dependency of the forces from circulation about the foil, the angular damping forces, and the forces from relative accelerations between the fluid and the trawl door.

Various concepts for trawl door control are evaluated. This is done both analytically, by simulations and by towing tank experiments. Based on the results, a new trawl door control concept is proposed. The trawl door control concept is developed to fulfill the demands on both energy consumption, robustness and control performance. Because of the contradictory demands on performance, stability and energy efficiency, the control concept is improved using numerical optimization. The optimization is based on time-domain simulations of the trawl system.

The design of an overall trawl control architecture taking advantage of the trawl door control system is presented. This takes industrial constraints into account, such as the energy supply on the trawl doors. The control system is based on model predictive control and facilitates complex objectives, constraints and process models. The use of model predictive control is made possible by letting PID plant controllers act as a layer between the model predictive controller and the trawl system. The model predictive controller is thus able to operate on a stable and predictable system with no fast dynamics. To reduce the energy consumption of the trawl door, conventional feedback control is avoided on this part of the control system, and step wise feedforward control is instead employed.

The main contributions in this work are the mathematical modeling of the hydrodynamic forces on a trawl door, the design of a control architecture tailor-made for trawl system control and the method for optimization of the trawl door control concept.

Acknowledgements

This work has been carried out under the supervision of Professor Asgeir J. Sørensen at the Department of Marine Technology, Faculty of Engineering Science and Technology, Norwegian University of Science and Technology. I would like to express my sincere gratitude to him for his guidance and invaluable encouragement, and I would like to thank my advisor, Professor Harald Ellingsen at the Department of Marine Technology.

I would also like to thank my colleague at SINTEF Fisheries and Aquaculture, Vegar Johansen, for a fruitful cooperation and my former colleague Svein Ersdal for valuable help.

This work has financed by the Norwegian Research Council, the Bioproduction and Processing Division, directed through SINTEF Fisheries and Aquaculture.

Declaration

Chapter 2 and parts of Chapter 1 is written in cooperation with Vegar Johansen.

Nomenclature and conventions

General

The following notation is adopted throughout this thesis, unless otherwise is explicitly stated.

- Vectors are expressed either in coordinate free form, denoted by small, not bold letters with an arrow accent, or as one-dimensional arrays giving its coordinates in a specific frame, denoted by bold, small letters. Matrices and multidimensional arrays are denoted by bold, capital letters.

$$\begin{array}{ll} \vec{d} & \text{A coordinate free vector.} \\ \mathbf{d}^a & \text{The coordinates of } \vec{d} \text{ decomposed in the frame } a. \\ \mathbf{M} & \text{A matrix or multidimensional array.} \end{array} \tag{1}$$

- The diagonal of a matrix $\mathbf{M}$ is denoted by

$$\mathsf{diag}\left(\mathbf{M}\right), \tag{2}$$

  and a diagonal matrix may be described as

$$\mathsf{diag}\left(\mathbf{d}\right), \tag{3}$$

  where $\mathbf{d}$ is a vector of the elements on the diagonal.

- The general rule for subscripts for geometric vectors are: $\mathbf{v}_{to,from}^{frame}$. "frame" is the frame in which the coordinates of the vector is decomposed. "from" and "to" are the start and end point of the vector, respectively. These may be either points, frame origins or both.

- $\vec{d}_{ba}$ is the coordinate free vector from the origin of the frame a to the origin of the frame b. $\mathbf{d}_{ba}^c$ is the coordinates of this vector, decomposed in the frame c.

- If the elements of a vector or matrix are not explicitly stated, they may be referenced by their index, as for example:

$$\mathbf{d}_{ba}^c = \begin{bmatrix} d_{ba,1}^c & d_{ba,2}^c & d_{ba,3}^c \end{bmatrix}^T. \tag{4}$$

$$\mathbf{R}_n^b = \begin{bmatrix} R_{n,11}^b & R_{n,12}^b & R_{n,13}^b \\ R_{n,21}^b & R_{n,22}^b & R_{n,23}^b \\ R_{n,31}^b & R_{n,32}^b & R_{n,33}^b \end{bmatrix}. \tag{5}$$

- The length of a vector is referenced as

$$d_{ba} = \left\| \vec{d}_{ba} \right\| = \|\mathbf{d}_{ba}^{c}\| = \sqrt{\sum_{i} \left(d_{ba,i}^{c} \right)^{2}}. \tag{6}$$

- Frames are designated small letters, like a.
- Points are designated capital letters, like A.
- The use of left-hand frames and belonging variables are distinguished from the corresponding right-hand frames and variables by the use of an additional superscript l to the frame notation.
- The symbols may be composed of four different parts: Base letters, superscripts, subscripts and accents. Each part may also be a compound statement, but this is avoided if possible.

Base letters

The following letters are given specific meanings throughout the text. Their meanings are further specified through the use of subscripts, superscripts and accents. Symbols of a small scope are not included in this list. The compound symbols are explained as they are introduced in the text.

Greek letters

α	Angle of attack.
β	Angle of slip.
γ	Angle of roll.
γ	Vortex.
Γ	Circulation.
δ	Rudder angle.
Δ	Difference between two comparable items.
$\mathbf{\Delta}$	Matrix of differences.
$\varepsilon, \boldsymbol{\varepsilon}$	Deviation, error, difference between actual and desired values.
ζ	Relative damping.
$\boldsymbol{\eta}$, $\vec{\eta}$	Generalized position vector, $\boldsymbol{\eta} = \begin{bmatrix} \mathbf{p}^T & \mathbf{\Theta}^T \end{bmatrix}^T$.
θ	Angle about an y-axis.
$\mathbf{\Theta}$, $\vec{\Theta}$	Euler angles between two frames, $\mathbf{\Theta} = \begin{bmatrix} \phi & \theta & \psi \end{bmatrix}^T$.
λ	Scale (length ratio between two similar shaped objects).
μ	Dynamic viscosity.
$\boldsymbol{\nu}$, $\vec{\nu}$	Generalized velocity vector, $\boldsymbol{\nu} = \begin{bmatrix} \mathbf{v}^T & \boldsymbol{\omega}^T \end{bmatrix}^T$
ρ	Density.
σ	Reduced time.
σ	Standard deviation.

$\boldsymbol{\tau}$, $\vec{\tau}$	Generalized force vector. $\boldsymbol{\tau} = \begin{bmatrix} \mathbf{f}^T & \mathbf{m}^T \end{bmatrix}^T$
ϕ	Angle about a x-axis.
Φ	Velocity potential.
ψ	Heading.
ψ	Angle about a z-axis.
$\boldsymbol{\omega}$, $\vec{\omega}$	Angular velocity vector. $\boldsymbol{\omega} = \begin{bmatrix} p & q & r \end{bmatrix}^T$.

Roman letters

a	Center of area.
$a, \mathbf{a}$	Element(s) of $\mathbf{q}$.
A	Area.
$\mathit{A}\mathrm{R}$	Aspect ratio.
c	Chord length.
c	Coefficient.
c	Control signal element.
$\mathbf{C}$	Coefficient vector.
d	Diameter.
d	Small change.
d	Damping.
D	Drag force.
$\vec{e}$	Unity vector, direction vector.
E	Young's modulus.
E	Energy.
$\mathbf{E}$	Mirroring transformation matrix.
$\mathbf{f}$, $\vec{f}$	Force vector.
$f, \mathbf{f}$	Function.
F	Force.
$g, \mathbf{g}, \vec{g}$	The gravity acceleration.
G	Center of gravity.
h	Height or span.
i	Index.
$\mathbf{I}$	The identity matrix.
j	Index.
$\mathbf{J}$	The influence matrix of the corrector.
k	Constant.
k	Stiffness.
$k\,()$	The Wagner function or a representation of it.
$\mathbf{K}$	The gain matrix of the corrector.
l	Length.
L	Length.
L	Lift force.
m	Mass.

$\mathbf{m}$, $\vec{m}$	Moment vector.
M	Moment (2D).
$\mathbf{M}$	Mass matrix.
n	Index.
N	Number of items.
$\mathbf{n}$,$\vec{n}$	Normal vector.
o	Origin of a frame.
O	Objective value.
$O\left(\right)$	Objective function.
p	Rotational velocity about a x-axis.
p	Pressure.
$\mathbf{p}$	Position vector, $\mathbf{p} = \begin{bmatrix} x & y & z \end{bmatrix}^T$
$p, \mathbf{p}$	Parameters of a model.
$\mathbf{P}$	Transformation matrix.
q	Rotational velocity about a y-axis.
$\bar{q}$	The average of the velocities on each side of a trailing vortex sheet.
$\mathbf{q}$	Condensed control signal, used in the model predictive control optimization.
r	Rotational velocity about a z-axis.
r	Roll angle.
$r\left(\right)$	Reducing function.
$\mathbf{r}$	Reference.
R	Resistance.
R_e	Reynolds number.
$\mathbf{R}$	Rotation matrix.
s	Distance.
S	Surface area.
S	Shear force.
$\mathbf{S}$	Cross product matrix ($\mathbf{a} \times \mathbf{b} = \mathbf{S}\left(\mathbf{a}\right)\mathbf{b}$).
t	Time.
T	Time constant.
T	Tension.
T	Thrust.
$\mathbf{T}$	Angular transformation matrix.
$\mathbf{T}$	Vector or matrix of time constants.
u	Velocity along a x-axis.
$u_H\left(\right)$	The Heaviside function.
$\mathbf{u}$	Model (control) input vector.
U	Velocity amplitude.
v	Velocity along an y-axis.
$\mathbf{v}$, $\vec{v}$	Linear velocity vector.
w	Velocity along a z-axis.
W	Mechanical work or energy.
x	Position along a x-axis.

x	Model state.
$\mathbf{x}$	Model state vector.
y	Position along an y-axis.
$\mathbf{y}$	Model output vector.
z	Position along a z-axis.

Super- and subscripts

Super and subscripts are included in the symbols to specify e.g. frames, objects, points and causes.

Symbols

$^{\infty}$	Steady state.

Greek

Υ	Hydrodynamic.
ϱ	Combined buoyancy and gravity.

Roman

^{0}	Initial.
^{2D}	Two dimensional.
a	Acceleration.
A	Added mass.
A	The accurate control plant model.
b	Boundary.
b	Bridle
c	Circulation.
CR	Crowfoot.
d	Trawl door.
d	The trawl door frame.
d	Desired values.
d	Damping
D	Drag.
h	The hydrodynamic frame.
F	The fast control plant model.
F	Friction.
$\mathbf{g}$, $\vec{g}$	The gravity acceleration vector.
l	Lower.
L	Lift.
m	The trawl door model.
m	The trawl door model frame.

$_{\max}$	Maximum value.
$_{\min}$	Minimum value.
n	The global frame
n	Normal.
opt	Optimum, optimized.
N	Center of the trawl net opening.
p	Port side.
P	Prediction.
Q	The port trawl door.
R	The starboard trawl door.
s	The scale frame.
s	The ship frame.
s	Starboard side.
S	The ship.
t	The wind tunnel frame.
t	The trawl system frame.
t	Tangential.
u	Upper.
v	Velocity.
w	Trawl net wing (after specifiers for upper/lower and port/starboard).
w	Warp.
w	The water frame.

Accents

Accents are included in the symbols to specify e.g. mathematical operations and origin of the effects that are described by the symbol.

$\hat{}$	Designates the parameterization of the steady state hydrodynamic forces for the reference trawl door.
$\hat{}$	Designates relative positions in the trawl system.
$\hat{}$	Designates relative points in time for the model predictive control signal.
$\bar{}$	Designates mean values.
$\bar{}$	Designates the parameterization of the steady state hydrodynamic forces for a general trawl door.
$\tilde{}$	Designates results from the VLM.
$\vec{}$	Designates a vector in coordinate free form.
$\dot{}$	Time derivative; $\dot{x} = \frac{\partial}{\partial t}x$.

Notation examples

The following shows some examples of the notation used in this thesis:

$\mathbf{f}^b_{O\Upsilon}$	$\in \mathbb{R}^3$	$[N]$	The hydrodynamic force attacking the point O decomposed in the frame b.
$\mathbf{m}^b_{O\Upsilon}$	$\in \mathbb{R}^3$	$[Nm]$	The hydrodynamic moment about the point O decomposed in the frame b.
$\boldsymbol{\tau}^b_{O\Upsilon}$	$= \begin{bmatrix} \mathbf{f}^b_{O\Upsilon} \\ \mathbf{m}^b_{O\Upsilon} \end{bmatrix}$	$[N,\ Nm]$	The hydrodynamic generalized force in the point O decomposed in the frame b.
$\mathbf{v}^b_{Oa}$	$= \begin{bmatrix} u^b_{Oa} \\ v^b_{Oa} \\ w^b_{Oa} \end{bmatrix}$	$[m/s]$	The linear velocity of a point O relative to the frame a decomposed in the frame b.
$\boldsymbol{\omega}^b_{Oa}$	$= \begin{bmatrix} p^b_{Oa} \\ q^b_{Oa} \\ r^b_{Oa} \end{bmatrix}$	$\left[s^{-1}\right]$	The angular velocity of the point O relative to the frame a decomposed in the frame b.
$\boldsymbol{\nu}^b_{Oa}$	$= \begin{bmatrix} \mathbf{v}^b_{Oa} \\ \boldsymbol{\omega}^b_{Oa} \end{bmatrix}$	$\left[m/s,\ s^{-1}\right]$	The total velocity vector of a point O relative to the frame a decomposed in the frame b.
$\mathbf{p}^b_{Oa}$	$= \begin{bmatrix} x^b_{Oa} \\ y^b_{Oa} \\ z^b_{Oa} \end{bmatrix}$	$[m]$	The position of the point O relative to the origin in frame a decomposed in the frame b.
$\boldsymbol{\Theta}_{ba}$	$= \begin{bmatrix} \phi_{ba} \\ \theta_{ba} \\ \psi_{ba} \end{bmatrix}$	$[-]$	The Euler angles from the frame a to the frame b.
$\boldsymbol{\eta}^b_{Oa}$	$= \begin{bmatrix} \mathbf{p}^b_{Oa} \\ \boldsymbol{\Theta}_{ba} \end{bmatrix}$	$[m,\ -]$	The position and orientation vector of frame b with respect to frame a.
$\mathbf{R}_{\boldsymbol{\Theta}}(\boldsymbol{\Theta}_{ba})$	$\in \mathbb{R}^{3\times3}$	$[-]$	The rotation function from the frame a to the frame b.
$\mathbf{T}_{\boldsymbol{\Theta}}(\boldsymbol{\Theta}_{ba})$	$\in \mathbb{R}^{3\times3}$	$[-]$	The angular rotation function from the frame a to the frame b.

Abbreviations

CIM	The control influence model.
ACPM	The accurate control plant model.
FCPM	The fast control plant model.
MPC	Model predictive control.
PPM	The process plant plant model.
VLM	The vortex lattice method and the software based upon it.

Frame conversions

Conversions between different frames are done according to:

$$\begin{aligned} \mathbf{p}_{Oa}^{b} &= \mathbf{R}\left(\mathbf{\Theta}_{ba}\right)\mathbf{p}_{Oa}^{a} && (7)\\ \mathbf{p}_{Oa}^{a} &= \mathbf{R}\left(\mathbf{\Theta}_{ab}\right)\mathbf{p}_{Oa}^{b} && (8)\\ \mathbf{R}\left(\mathbf{\Theta}_{ab}\right) &= \left(\mathbf{R}\left(\mathbf{\Theta}_{ba}\right)\right)^{T}. && (9) \end{aligned}$$

To avoid using the rotation function in long expressions, it is for simplicity sometimes replaced by rotation matrices. These are defined as

$$\mathbf{R}_{a}^{b} = \mathbf{R}\left(\mathbf{\Theta}_{ba}\right). \tag{10}$$

Trigonometric functions

The trigonometric functions are abbreviated as:

$$\begin{aligned} \mathbf{c}_{*} &= \cos\left(*\right) && (11)\\ \mathbf{s}_{*} &= \sin\left(*\right) && (12)\\ \mathbf{t}_{*} &= \tan\left(*\right), && (13) \end{aligned}$$

where $*$ is the name of the arbitrary argument of the functions.

Contents

Chapter 1

Introduction

1.1 Background and motivation

Fish trawling is today of great importance for both economics and food supply, and is responsible for 40% of the world catch (Watson et al., 2004). According to FAO (2002), the total capture fisheries production in 2000 reached 94.8 million tons, the highest level ever. The estimated first sale value of this production amounted to some US$81 billion. Among the world's exporters of fish, Norway was third after China and Thailand in 2002 with an exported value of $3.6 billions.

The *eco-efficiency* of trawling may be defined as the ratio between the value of the catch and the environmental impact. The environmental impact from the fishing vessel is mainly due to fuel consumption and waste from the operation, while the trawl gear may cause removal and damage to target and by-catch species and organisms like corals and sponges.

Improved controllability of the trawl gear could render aimed fishing for fish schools possible, as well as improved maneuvering close to obstacles and control of the net shape for optimal fishing efficiency. Systems for more precise control of trawl gear should therefore lead to:

- Improved catch capability in relation to the fuel consumption.
- Reduced seabed impact and improved obstacle avoidance.
- Improved selectivity.

Environmental effects of food production are increasingly focused, also when it comes to fish. Not only the content and the quality of the fish as food are important to the consumers. The environmental effects of how the fish is caught or produced, processed and brought to the market are becoming important issues as well. There are even examples of convenience chains refusing to sell fish caught by trawl. Another consequence of the increased environmental awareness is the ban against bottom trawling outside the coast of Alaska.

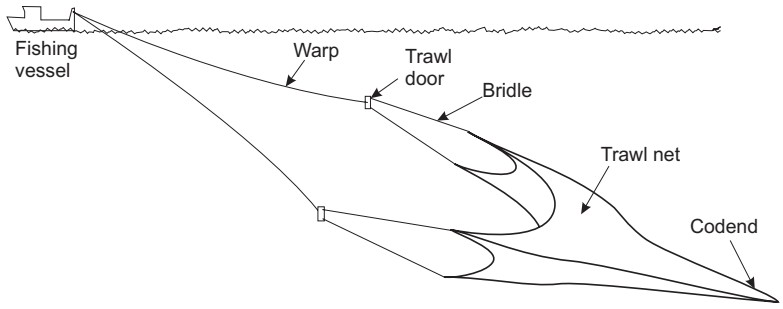

Figure 1.1: The main characteristics of trawl systems.

1.2 Previous work

A brief overview of previous work is given here. Further details related to specific topics are introduced in the appropriate chapters.

1.2.1 Present industrial practice

The trawl system is today manually controlled through changes in vessel speed, vessel heading and warp lengths. Since the distance between the vessel and the net can be long (up to $1-2\,\mathrm{km}$), the use of vessel control is both slow and difficult to get accurate on the trawl itself. The control is often aided by various control systems:

- The autopilot keeps the desired heading of the vessel under the influence of waves, wind, current and the forces from the trawl system.
- The winch control system keeps the desired average length of the trawl warps, and may also keep them in equal tension. It may also maintain the symmetry of the trawl system, based on a flow sensor on the headline of the trawl (Scanmar, 2000).

The main common characteristics of trawl systems are shown in Figure 1.1. More details are given in Section 2.2.2.

1.2.2 Conceptual proposals

Various concepts for controlling trawl systems have been proposed in the past. Some have been patented, but, as far as we know, none are used in commercial fishing. For generating the forces needed to control a trawl system, the trawl doors have gained the most attention (Shenker, 2005; Scanmar, 2000). Control has also been obtained by rotating the warps (NPO Promrybolovstva).

Since marine seismic survey systems resemble trawl systems, control concepts used for seismic surveys may be applicable for trawling. Such concepts are described in Petroleum Geo-Services (2001), Henriksen (2000), Geco (1993), Schlumberger (2002).

1.2.3 Mathematical modeling

Bridles, warps and parts of pelagic trawl nets may be treated as cables under the influence of gravity, hydrostatic, hydrodynamic and control forces. There are many surveys of cable mechanics (Triantafyllou, 1987, 1991; Irvine, 1981; Gatti, 2002) and the hydrodynamic forces on cables (Ersdal, 2004; Ferro and Hou, 1984; Casarella and Parsons, 1970; Chakrabarti, 1987). There are, however, less literature available on cable models suitable for real-time control applications. Such a model is presented in Johansen et al. (2006).

The trawl doors are usually three-dimensional multifoils with no thickness, large curvature and small aspect ratio. The hydrodynamic forces on such foils are usually only considered for steady state conditions in three degrees of freedom (3dof). Both the steady state forces and the transient forces may be estimated using either experiments or computational fluid dynamics analysis (Mulvany et al., 2004; Margason et al., 1971; Takinaci, 2003; Ren et al., 2000). A two-dimensional model for the prediction of the behavior of towed underwater vehicles is described in Paschen (1997).

Several different approaches have been developed to construct mathematical models of general net structures, and some of these are focusing on trawl nets. The approaches may be classified into:

- Formal finite element approaches based on "super meshes" (Priour, 1997, 1999, 2001, 2003, 2005; Tronstad, 2000).
- Direct methods and pragmatic models based on mass points interconnected by springs (Lader et al., 2003; Lee et al., 2001a; Suzuki et al., 2003) .
- Interconnected rigid bar models, both with and without inertial forces (Bessonneau and Marichal, 1998; Niedzwiedz, 1999; Theret, 1994; Vincent, 1999; Tsukrov et al., 2003).

Several studies have revealed that hydrodynamic loads on net structures are complex due to hydroelasticity (Fredheim, 2005; Fredheim and Faltinsen, 2003; Paschen, 2003; Paschen et al., 2004). The loads may be calculated for separate twines (low solidity) or for net panels (high solidity) (Stewart and Ferro, 1987; Årsnes et al., 1990).

Ship motions are traditionally divided into maneuvering and seakeeping applications. Surveys of these topics are found in Journée and Massie (2001); Fossen (2002) and references therein. Fossen (2005) demonstrates how maneuvering and seakeeping based on strip theory may be unified in one model. This approach is relevant for maneuvering and control of trawl systems because it is easy to include gear response forces in the model.

1.2.4 Automatic control

There is not much available literature on control strategies and methods for automatic control of trawl systems, and none have been found to control the movements in both the horizontal and the vertical plane. There is also a lack of documentation of full-scale field experiments to confirm the performance of the theories. The following proposals are found:

- Control of a midwater trawl system in the vertical plane by adjusting the vessel thrust based on optimal control (Umeda, 1991).
- Control of a midwater trawl system in the vertical plane by adjusting the warp lengths using a controller based on fuzzy logic (Lee, 1995, 1999; Lee et al., 2001b).
- Control of a midwater trawl system in the horizontal plane by adjusting the trawl doors angle of attack (Johansen et al., 2002).

In Pedersen (1996), the couplings between the movements of a towed seismic array and the heading of the ship is analyzed, and appropriate measures are suggested. Petroleum Geo-Services (2004) proposes to decouple the movements of the towed seismic array from the horizontal movements of the ship, using the ship winches. This work may also be relevant for the purpose of trawl control.

1.3 Present work

1.3.1 Scope of work

Main goal

The main goal of this work is:

"To develop a trawl control system with improved precision and bandwidth, based on practical considerations"

The practical considerations imply that the control system must be inexpensive, give low maintenance costs and maintain fishing efficiency.

Assumptions

To avoid spending too much effort in investigating all possibilities with regard to how to achieve the main goals of this thesis, some limitations are done. The following assumptions and requirements are therefore made:

- If the precision and bandwidth of the trawl control system is increased, then bottom contact can be lighter. It can also increase the fishing efficiency and reduce the probability of accidents.
- Even if it is possible to control the trawl system using only vessel speed, vessel heading and warp length, the extra performance gained by using the trawl doors as actuators will be worth the extra cost and complexity.
- The scarcity of local energy supply at the trawl doors will make it necessary to develop a trawl door control system which is as energy efficient as possible. This is assumed best achieved by a feedforward controller with a low update rate.
- The control system needs the ability to take complex properties and objectives into account, such as loss of fishing efficiency during maneuvers, energy consumption and catch rate.

- The strong nonlinearities of the trawl system need to be considered in the control system design, including steady and transient hydrodynamic forces on the trawl doors in all six degrees of freedom.
- Most trawl system measurements are inaccurate and with a low update rate.

Research methodology

The research methodology of this work is based on the main goal and assumptions as stated above. The main goal will be fulfilled by completing the following tasks:

1. Define a trawl system case to model and control.
2. Develop a sufficiently accurate 6 dof mathematical model of the trawl doors, including the steady and unsteady hydrodynamic forces. This should be based on both experimental and numerical methods.
3. Develop a sufficiently accurate mathematical model of the trawl system to act as the process plant model. This model should include the trawl doors, the warps, the bridles, the ship and the net.
4. Develop a trawl door control concept which as far as possible meets the demands on energy efficiency, hydrodynamic efficiency, robustness, initial cost and maintenance. Develop a mathematical model of this concept, and optimize it with regard to chosen criteria.
5. Develop the necessary observers, based on independent models of the trawl system.
6. Develop a model corrector to minimize the negative effects of model inaccuracies. The models should be updated based on available measurements and the state estimates from the observers.
7. Develop the overall trawl control system using model predictive control, and state explicit goals of the control system. The interface between the top level controller and the local controllers should also be defined.
8. Demonstrate the performance of the control system through simulations.

1.3.2 The work process

As many aspects of the control system affect each other, developing a system for trawl control had to be an iterative process. Because of this, the thesis is written thematically, rather than chronologically. The following is a chronological description of the work process.

It was considered that using the trawl doors as actuators would be the best way to improve the trawl system control performance. An analytical evaluation of proposed and possible control concepts were therefore done. To make the final choice of the trawl door control concept, towing tank experiments were performed. As a result of the experiments, the basic trawl door control concept was chosen.

An accurate mathematical model of all parts of the trawl system was developed to be able to develop and assess the control concept. The modelling of the hydrodynamic forces on the trawl doors gained the most attention, because of their possible destabilizing effect. A mathematical model of the hydrodynamic forces on a trawl door was made. Wind tunnel experiments were performed to calculate the steady state forces, and a software tool was developed to estimate the transient forces.

The design of the trawl door control concept was improved using numerical optimization, based on simulations of the complete trawl system.

Finally, the overall trawl control architecture was designed to take advantage of the trawl door control concept, and case studies were performed to verify the results.

1.3.3 Contributions

Parts of the contributions within **mathematical modeling** are presented in Reite and Sørensen (2004) and Reite and Sørensen (2006). The main contributions are:

- A mathematical model of the hydrodynamic forces on the trawl door (Section 3.3).
- A mathematical model of the geometrical flexibility of the cable elements of the trawl system (Section 3.4.2).
- Modeling and assembly of all parts of the trawl system into a complete and computational efficient model (Section 3.4).

The main contribution within **trawl system control** is the design of a control architecture tailor-made for trawl system control, as well as a description of some of the implementation considerations applicable for such a control system (Chapters 4 and 5). These contributions are partly presented in Reite et al. (2006).

The main contributions within **trawl door control** are:

- An analytical evaluation of possible control concepts (Section 6.2).
- An evaluation of control concepts of special interest, using towing tank experiments (Section 6.5).
- A method for optimization of the control concept (Section 6.7).

1.3.4 Organization of the thesis

The organization of this thesis is thematic, rather than chronological, and may be summarized as follows:

Chapter 2	Background information about fish trawling, both in terms of trawling technology and its impact on economy, environment and politics.
Chapter 3	Mathematical modeling of the trawl system, in particular the hydrodynamic forces on the trawl doors.
Chapter 4	Development of the trawl control system architecture.
Chapter 5	Verification of the performance of the proposed control system through case studies.
Chapter 6	Development of the trawl door control concept.
Chapter 7	Final conclusions.
The appendices	Additional information and data not necessary for the general understanding of the work.

Each of the main chapters are preceded by a short introduction, giving an overview over former and present work in that specific area.

Chapter 2

Fish trawling

2.1 The world's fisheries

Industrial fisheries and aquaculture production have been developed as a result of an increasing market for marine protein around the world.

2.1.1 Production

The sea covers two thirds of the world's surface and contains by far its largest natural food resource. According to The Food and Agriculture Organization (FAO) of the United Nations, the diets of 2.6 billion people depend on fish as a source of animal protein. FAO also reports that the world's production of fish has increased steadily from 19 million tons in 1950 to 133 million tons in 2002, excluding the production of aquatic plants.

Norway, with only 4.6 million citizens, produced 3% of the world's captured fish in 1985, and this number had not changed in 2002.

2.1.2 Stock management

The discovery of the Grand Banks outside the east coast of Newfoundland, represents the beginning of distant water fisheries. During the 1950s, foreign fishermen experienced the cod fisheries on this very productive area as a gold rush. The international nature of this fishery complicated the management of the stock, resulting in a total collapse in the early 1990s. This is the classical case of how even modern stock management may fail to preserve fish resources.

There are many similar examples. According to the International Council for Exploration of the Sea (ICES), the Northeast Atlantic stock of blue whiting is threatened. The reason for this is probably that the participating countries have not agreed in how to divide the resource among themselves. The result is that there has been no total allowable catch (TAC) for blue whiting, and the classical "tragedy of the commons" have taken place (Heino, 2004). Northern prawn in the Svalbard zone had no restrictions on fishing until 1997. Then Norway, Russia, Iceland and the European Union agreed on dividing the fishery by licences and total number of days-at-sea, distributed over the different

nationalities. In practice, this implied unlimited fishery for the nations involved, because the total number of days-at-sea is high. A consequence of this management regime has been that the fleet of Norwegian fishing vessels capturing this specie has increased its capacity (Standal, 2003). This stands in sharp contrast to the governments' expressed goals.

2.1.3 Markets

The consumption of fish for human food has increased the latest 50 years. The world excluding China increased the annual consumption from almost 8 kg per capita in 1950 to about 13 kg per capita in 2002. The consumption in China was stable on about 5 kg per capita until the mid 80's, and increased to remarkable 27 kg per capita in 2002.

Japan and the United States of America are the two countries importing most fish commodities. In 2002 they imported products for $13.6 billions and $10 billions, respectively (Vannuccini, 2004). Among the world's exporters of fish, Norway were third after China and Thailand in 2002 with an exported value of $3.6 billions.

World fisheries have changed dramatically the last fifty years. In the 1950s Atlantic cod and herring dominated the capture production, but today low-grade species, Anchoveta, Alaska pollock and Skipjack tuna have become more important. In 2002 75% of the production was used for direct food purposes.

In its role as healthy protein, fish is changing its position in world cultures. From being a cheap source of essential protein in many industrialized societies and a basic subsistence for coastal dwellers, fish has obtained superior status in developed countries. With this comes the requests for higher quality and environmental-friendly production. Unilever, one of the largest international traders in fish products, announced in 1996 that they by 2005 would not purchase fish from unsustainable fisheries. The wholesaler company Coop Sweden has claimed that they will only buy cod that is caught by long lining vessels, and not from trawlers, as raw material for their own brands. This is probably done to support the environmental image of the company, as trawling is in general considered less environmental friendly than for instance longlining.

2.2 Trawling technology

2.2.1 History of trawl technology development

The first written sources describing fishing with trawling gear are from the early 1300's (Karlsen, 1997). Important technology milestones have been the introduction of engine power, mechanical hauling devices, acoustic equipment for fish finding and surveillance, radio navigation systems, synthetic materials and the stern trawler.

The first stern trawler was introduced in 1953 (Warner, 1998). The stern ramp made it possible to haul the trawl net from aft rather than over the side, making the hauling process both quicker and safer. Increased size and capacity gave it the capability to fish the deep seas in an extent never seen before. This technology was soon adapted by other leading fishing nations like Russia, Germany, Britain, Spain, Japan and Norway.

In 1969, the Germans introduced midwater trawling with increased maneuverability, making it possible to move the gear up and down in the water column (Wigan, 1998).

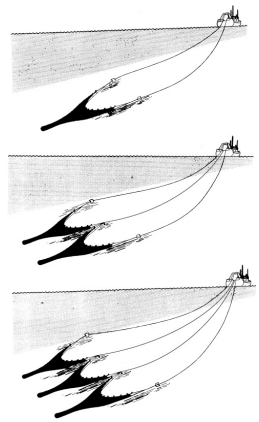

Figure 2.1: Single, double and triple trawl. Adopted from Engås et al. (1996)

This reduced the by-catch considerably for herring and other pelagic species. The trend for midwater trawling the last decades has been to increase the size of the meshes in the foremost part of the net. This has decreased the drag force on the net substantially, making it possible to increase the overall net size.

In recent years, much of the development within bottom trawling has been focussed on the development of larger, heavier and stronger vessels and gear (Sendlak, 1999). Modern ground gears for bottom trawling, such as the rock hopper gear, also makes it possible to fish in areas with more rugged bottom profiles.

More recent advances in trawl fishery are the introduction of double and triple trawls, mounting two or three smaller nets between the two trawl doors, see Figure 2.1. Such systems have lower towing resistance than single trawls compared to their width.

Instrumentation technology, like acoustic equipment for fish finding and surveillance (echo sounders and sonars), satellite-based positioning systems (i.e. GPS), satellite communication (i.e. Inmarsat) and radars, have been of great importance for safer and more efficient trawling. Trawl gear surveillance systems provide information on parameters like distance between the trawl doors, net opening height, amount of catch, depth of the trawl doors and depth of the net.

2.2.2 Trawl systems overview

Figure 2.2 illustrates the different parts of a typical midwater trawl system. The top drawing shows the system as viewed from the port side, and the lower drawing shows it as seen from above. The major components are the *fishing vessel*, the *trawl doors* and the *trawl net*. The *warp lines* connect the vessel to each trawl door, and the *bridle lines* connect each trawl door to the upper and lower *wing* of the corresponding side of the net. The *headline* connects the two upper wings, and the *footrope/ground rope* connects the two lower wings. The *codend* is the aft end of the net, forming a bag where the catch is collected.

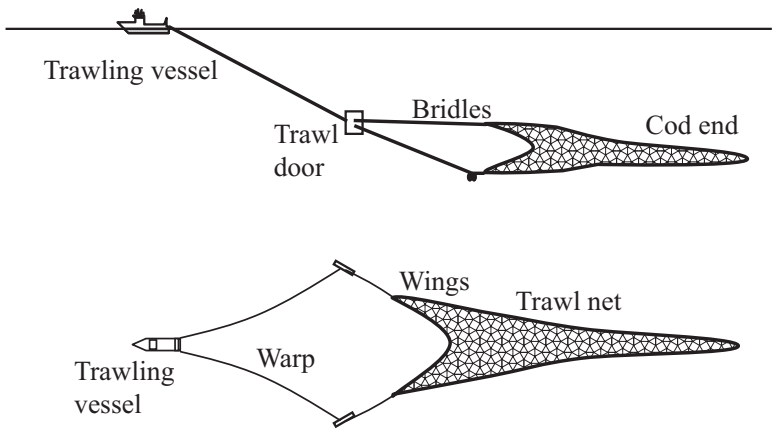

Figure 2.2: A trawl system seen from the side (top) and from above (bottom).

The vessel typically tows the trawl system at a forward speed of approximately $2-5$ knots, depending on the target species. The trawl doors are vertical hydrofoils, and the hydrodynamic forces on them maintain the horizontal opening of the trawl net. In addition, their weight helps keeping the trawl system at the wanted depth.

As the trawl net passes through the water, the purpose of the foremost end of the net is mainly to herd the targeted species towards the center trajectory of the net. Further aft the net is in principle filtering the targeted species from the water and collecting the catch in the codend. Depending on the area and targeted species, devices for expelling unwanted catch are mandatory and may be mounted further downstream in the net. Restrictions on the smallest net mesh size are also common for this purpose.

2.2.3 The various trawling concepts

Trawl systems are often divided into three groups, according to how they are both built and used: *Bottom trawls*, *semipelagic trawls* and *midwater (pelagic) trawls*. The characteristics of these groups are illustrated in Figure 2.3 and further described in the following.

Bottom trawls

Bottom trawls are made to catch fish and crustaceans living either at or very near the bottom. The height of the trawl can therefore be significantly less than what it would have to be for midwater trawling. When used for catching bottom fish, the height of the trawl is usually 8 m or less, even if the width of the trawl opening may be more than 50 m. In addition, noise and dust clouds from the trawl doors and the bridles herds the targeted species towards the trawl opening, increasing the effective trawl opening substantially.

The bottom trawl doors are built with a low aspect ratio to make them stable even while being dragged over rough bottom. The penetration of the bottom sediments may

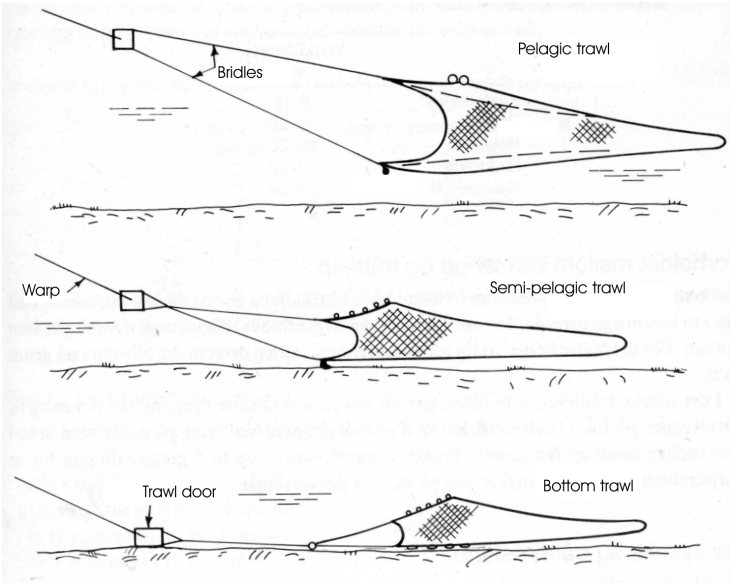

Figure 2.3: Midwater, semipelagic and bottom trawl. From Karlsen (1989).

provide up to 30 % of the total spreading forces. Their hydrodynamic efficiency is decreased because of the reduced aspect ratio, while the bottom contact decreases the lift-to-drag ratio even more.

A *ground gear* is mounted under the lower part of the net opening. This keeps the net from being damaged from obstacles at the bottom, while preventing catch from escaping under the net. The ground gear can be up to 5000 kg, and it creates a significant amount of resistance. Also the trawl net itself must be built to withstand some bottom contact. Because of this and the low efficiency of the trawl doors, the drag of a bottom trawl is high in relation to its size. This is the main reason why the eco-efficiency of bottom trawling is low compared to most other fisheries (Huse (ed) et al., 2002). The need for bottom contact also explains why bottom trawling is accused of inflicting damage to the seabed and coral reefs.

Semipelagic trawls

Semipelagic trawls are hydrodynamically balanced, but still made to have light bottom contact with either the trawl doors or the trawl net. Their main advantage is that they are more efficient than bottom trawls for species that are not living very close to the bottom. What distinguishes semipelagic trawls from bottom trawls and midwater trawls are not so much how they are built as how they are rigged and used (Karlsen, 1989).

Midwater trawls

Midwater trawls are in principle made for no bottom contact and must therefore meet less strict demands on strength and abrasive resistance. When the trawl is sufficiently large, the targeted fish will only sense and avoid the closest net panels in the foremost part of the trawl. These meshes can be therefore be made very big, adding little to the total towing resistance. In addition, the trawl doors do not have to be able to operate with bottom contact, and can therefore be made more hydrodynamic efficient than bottom trawl doors.

Altogether, this means that midwater trawls can have a small towing resistance in relation to their size. They can as a consequence be much larger than other trawl types for a vessel with a given maximum towing force.

2.2.4 State of the art control of trawl systems

It is today possible to manually change some properties of the trawl system while this is onboard the vessel. Such adjustments are used for adapting the trawl system to the general fishing conditions, but they can not be used for controlling the trawl while fishing. These properties include:

- The fastening positions of the warp and the bridles on the trawl door.
- The amount of weight attached to the lower wings.
- The length of the lower bridles (the set-back of the lower wings).
- The amount of weight attached to the trawl doors.

While fishing, the trawl system is today manually controlled through changes in setpoints of:

- Propeller pitch controller (thrust).
- Propeller/engine speed controller (thrust).
- Autopilot (heading).
- Winch controller (warp lengths and tension, and trawl net symmetry).

The distance between the vessel and the net can be up to $1 - 2\,\text{km}$. The trawl gear response of these controller actions are therefore slow and difficult to predict. This response is also limited by the available thrust and winch capabilities. In addition, control actions often lead to deformation of the trawl net, leading to fish escaping or being caught in the trawl net meshes. The fishing ability may therefore be seriously decreased during such maneuvers.

2.3 Challenges in trawl fishery

2.3.1 Stock management

The management of fish stocks are problematic for several reasons. The optimum long term regulatory measures will usually lead to unacceptable short term socioeconomic consequences. In addition, stock management is complicated by growing technical capabilities and inaccurate resource estimates and understanding. History has shown that scarcity of political vigilance and courage to make unpopular decisions may be the main hindrance for sustainable stock management, and this is the case even today.

FAO's pessimistic and optimistic estimates for the production of captured fish in 2010 are 80 million and 105 million tons, respectively. In other words, there is no expectation of a big increase in the capture production. Instead, major challenges are identified for maintenance of the 2002 level. According to FAO, technical measures (e.g. gear, time and area restrictions) dominate fisheries management efforts as methods for achieving the conservation of fish stocks. In 1999, measured with respect to maximum sustainable yield for the high-value species, FAO estimated that the world's fishing fleet was capable of fishing at least 30% more (Gréboval, 1999). The current trend is also towards bigger trawlers with higher capacities (Standal, 2005). FAO's opinion is that overcapacity in the fishing fleet poses a fundamental challenge in the fisheries, because it leads to an increased pressure on fish stocks and a decrease in economic profit. The main effort in developing new fishing gear should thus not be to increase the capacity of the fleet, but to increase the profitability margins for the fishing vessels. Important contributions may be increased quality and reduced maintenance, oil consumption and investments.

2.3.2 Bottom impact

As early as in 1376, British fishermen from the Thames port complained about the seabed damage from use of a beam trawl like device (Robinson, 1996). In the recent years, the negative impacts of trawling have gained increasing attention, mainly focusing on its impact on the seafloor, such as destruction of coral reefs and other bottom habitats. The environmental impacts from trawling may be divided in environmental impact from the fishing vessel and impact from the fishing gear. The impacts from the vessel is mainly related to fuel consumption and waste from the operation, while the impact from the trawling gear itself will be related to the removal of target and by-catch species, as well as the impact on the seabed itself. The physical impact of fishing on the ocean bottom (Paschen et al., 2000) is particular important on rare or fragile coral, sponge and other organisms attached to the seabed (Gianni, 2004).

Trawling is annually covering an area equivalent to approximately half of the world's continental shelves (Watling and Norse, 1998). The severity of the seabed impact is however disputed, and may vary from mixing up of a sandy sea bottom to destruction of coral reefs. It is estimated that bottom trawling and dredging have damaged up to half of all the coral reefs in the North-East Atlantic (Fossså, 2000). In the New Zealand zone, the Graveyard seamount complex, photographic studies showed that there were close to 100% coral cover on unfished seamounts and only $2\% - 3\%$ cover on fished seamounts (Clark and O'Driscoll, 2003). In Norway, The Institute for Marine Research (IMR) estimates that $30\% - 50\%$ of the cold-water coral reefs within the Norwegian Exclusive Economic

Figure 2.4: Pictures of lophelia pertusa on the seafloor off Steinavær in Andfjord, Norway. Photos by IMR (Fosså, 2003).

Zone (EEZ) have been damaged by bottom trawl fishing (Fosså et al., 2002). Figure 2.4 shows undamaged coral reefs off the mainland of Norway.

Effects on the biodiversity seem to be more severe in hard bottom habitats than on soft sea floors (Huse (ed) et al., 2002), and less severe for areas exposed to natural stress, such as wave actions, current, eutrophication and salinity fluctuations. Experiments performed inside the Marine Protected Area around Bear Island in the Barents Sea in 2000 and 2001 found only small changes in the biodiversity attributed to fishing gear disturbance.

As the bottom properties vary between trawling grounds, it is not an easy task to predict the bottom effects of this activity. Referring to the principle of precautionary, a sound strategy would however be to take actions to avoid this bottom disturbance as far as possible.

2.3.3 Energy efficiency

Since the trawl must be towed at a significant speed behind the trawler, it creates a large drag force. This translates into a high energy consumption while trawling. A LCA (life cycle assessment) study in Ellingsen and Aanondsen (2006) finds that of the environmental impacts studied, cod trawling are dominated by the contributions from the burning of fossil fuel during fishing.

Some innovations have been done, such as double and triple trawls for bottom trawling, and the use of very large meshes in the mouth of midwater trawls. This has increased the hydrodynamic efficiency of the trawl nets, but no improvements in the eco-efficiency of the trawl systems are found (Ellingsen and Aanondsen, 2005). The reason for this is probably regulations and the reductions in important fish stocks. It is not known how the technological development towards bigger vessels with more engine power and larger gear has affected the eco-efficiency.

2.3.4 Selection properties

The selection properties of the trawl is frequently discussed and criticized. The trawl net selection properties are determined by the size and opening of the meshes, letting the smallest individuals escape. The sorting in the codend is however hindered by the meshes being forced together by the tension in the net, and by the fish already in the codend. Experiments have indicated that by turning the net panels, the meshes are kept more open, and the selection process is enhanced (Digre and Hansen, 2005).

Another problem is that also nontargeted species will be caught. In the later years these aspects have been addressed by using different arrangements of sorting grids. These can sort out small fish and fry from fish trawls, as well as fish from shrimp trawls. Much effort has been put into the development of such devices, and their performance have been steadily improved. Sorting grids are now mandatory in some fisheries.

2.3.5 Health and security

Being deck-hands onboard a trawler is in its origin a demanding and exposed occupation. For the period 1990 to 1999 the average number of fatalities per 10 000 man-labour year was 9.2 in the Norwegian fishing fleet, whereas this figure was down on 1.6 for Norwegian farming and forestry in the same period (ICES, 2000), which is also rather high compared to other industries. To illustrate this further, it can be noted that in 1999 the average accident level for the six most exposed land based occupations in Norway was 1.5.

Trawl systems are often operated on rough sea floor and close to obstacles like wrecks and sub-sea oil installations. This sometimes leads to situations where the trawl net or other parts of the trawl system gets caught, which again may lead to loss of gear and catch. In bad weather, such situations constitute great dangers for the crew and vessel, sometimes with fatal consequences. The risk level is illustrated by the tragic loss of the Norwegian trawlers Langtind in 1982, Børge Aleksander in 1990, Njord in 1992 and Roaldsnes in 1995.

2.3.6 Quality of catch

The quality of fish captured by trawling is subject for frequent discussion. Studies have shown that the quality of the catch is reduced for hauls of long duration and/or with high percentage of codend filling (Hattula et al., 1995; Neilson et al., 1989). Factors like how the fish is taken onboard the ship, weather conditions and on board handling (e.g. bleeding, icing) are also important for the quality (Botta and Bonnell, 1988), but there seems to be an overall concordance that trawl captures generally have lower quality than certain other fishing gears. It should be noted that some gears used also returns catch of significantly lower quality than trawling.

2.4 Motivation for improved trawl control

The present control of trawl systems is slow, difficult to get accurate and very dependent on the captain's skills. Increased bandwidth and accuracy with respect to the geometry and trajectory of the trawl gear, would improve the eco-efficiency of the trawl system.

Bottom impact could be reduced by decreasing the contact force between the seabed and the trawl gear. Accurate control of trawl net trajectory could reduce the contact force, making it possible to avoid vulnerable seabed areas and to catch demersal species with midwater trawls.

The energy efficiency is highly dependent on the gear's catching ability and towing resistance. Fish congregated in small shoals could be caught using smaller trawls with better control, reducing towing resistance while maintaining catching ability. The energy efficiency could be further improved by controlling the net shape and reducing the spread of the trawl while passing areas without fish.

The selection properties of the trawl system are affected by both the selection in the net and by the trajectory of the net. More precise control of the trawl gear may improve the selectivity by avoiding schools of unwanted fish or by keeping the net in a distance to the seabed where unwanted species are less likely to be caught.

Health and security issues in the trawl fisheries are partly due to accidents where the trawl have got caught in obstacles on the seabed. Some of these accidents may have been prevented by an improved ability to control and position the trawl gear.

Catch quality is affected by the duration of the hauls, the amount of catch and how it is taken onboard the ship. Smaller, more maneuverable trawl gear would probably lead to shorter hauls and improved quality.

These considerations indicate some benefits of systems for improved trawl control. This could contribute to turn the current trend from building larger and heavier equipment towards lighter gear and improved control, making it possible to obtain the same capture capacity with less investments. The consequences of fluctuating quotas would then become less severe for the industry, reducing the socioeconomic consequences. This would make it easier for the government to adapt the quotas to resource variations and obtain the optimal long-term management, increasing the maximum sustainable yield.

Chapter 3

Mathematical modeling

3.1 Introduction

An accurate mathematical model of the trawl system is needed to facilitate evaluation and development of the control system and the control concept. The development of this model is elaborated in this chapter.

3.1.1 Previous work

The ship

Ship motions are traditionally divided into maneuvering and seakeeping applications. Surveys of these topics are found in Journée and Massie (2001); Fossen (2002) and references therein. The hydrodynamic coefficients of the hull can be obtained either by measurements or by calculations. One possibility is to use commercially available computer programs such as ShipX (VERES) by MARINTEK (Fahti, 2004) and SEAWAY by Amarcon (Journée and Adegeest, 2003), which are based on potential theory and strip theory. Tønnessen (1999) treats how the forces from unsteady viscous flow around sharp corners can be estimated using a finite element method. A computer efficient nonlinear time-domain strip theory formulation for dynamic positioning and low-speed maneuvering is presented in Fossen and Smogeli (2004).

The warps and the bridles

Bridles, warps and parts of pelagic trawl nets may be treated as cables under the influence of gravity, hydrostatic and hydrodynamic forces. There are many surveys of cable mechanics (Triantafyllou, 1987, 1991; Irvine, 1981; Gatti, 2002) and the hydrodynamic forces on cables (Ersdal, 2004; Ferro and Hou, 1984; Casarella and Parsons, 1970; Chakrabarti, 1987). There are, however, less literature available on cable models suitable for real-time control applications.

Modeling of cables using a finite element method (FEM) or a finite difference method makes it necessary to calculate the in-line dynamics of the cable elements, slowing down

the time integration. A method avoiding calculation of this dynamics is presented in Johansen et al. (2006), being more efficient during time domain analysis.

The hydrodynamic forces on the trawl doors

2D linearized theory Linearized two dimensional theory gives analytical solutions for the steady and unsteady hydrodynamic forces on 2D foils (Newman, 1977), based on the following assumptions:

- The foil is thin.
- The foil operates at small angles of attack.
- The unsteady motion is small.

These assumptions are not valid for a conventional trawl door. The main discrepancies will probably arise from:

- 3D effects.
- Large angles of attack.
- Significant camber.
- Perturbations consisting of movements in all 6 degrees of freedom.

The 2D linearized theory is therefore of limited relevance. Some aspects of the theory is presented in the following, to provide a basis for exploring the unsteady hydrodynamic forces on trawl doors.

Kelvin's theorem states that for each change in vorticity $\Delta\Gamma$ around a foil, a vortex equal to $-\Delta\Gamma$ must be shed into the wake (Newman, 1977). This vortex influences the foil through the velocity it induces on the foil. Since each shed vortex stays relatively stationary in relation to the fluid, the distance between the vortex and the foil will usually increase with time, causing the effect of each transient to rapidly decay.

The influence of such transients may be accounted for by the use of appropriate functions of time. In these functions the reduced time σ_t is used. σ_t is the relative distance the foil has traveled, in terms of chord lengths, and it is defined as

$$\sigma_t \equiv \frac{1}{c}\int_0^t \bar{q}dt \ , \tag{3.1}$$

where c is the foil cord length, t is time and $\bar{q} = \frac{q^+ + q^-}{2}$ is the average of the velocities on each side of the trailing vortex sheet. This is illustrated in Figure 3.1.

According to 2D linearized theory, the lift force develop according to the Wagner function if sudden, small speed changes are imposed (Newman, 1977). Although the Wagner function is known exactly, it is not in a convenient analytic form. It is therefore usually replaced by a simple exponential or algebraic approximation, which makes it

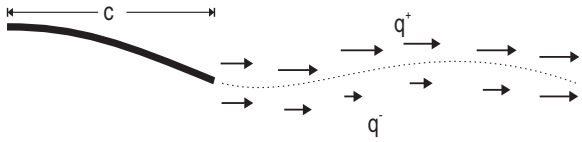

Figure 3.1: The trailing vortex sheet of a 2D foil.

possible to compute the unsteady hydrodynamics with a series of practical numerical tools. Küssner (1940) approximates the Wagner function as

$$2k_1(\sigma_t) \approx 1 + \frac{\sigma_t}{2\sigma_t + 2} + \frac{\sigma_t^2}{(2\sigma_t + 2)^2} + O\left(\sigma_t^3\right) \quad , \quad s > 0 \tag{3.2}$$

where $k_1(\sigma_t)$ is an expansion of the expression

$$k_2(\sigma_t) \approx \frac{\sigma_t + 1}{\sigma_t + 2}, \tag{3.3}$$

where $k_2(\sigma_t)$ is a candidate of approximating the Wagner function. An exponential approximation to the Wagner function is written as (Jones, 1940):

$$k_3(\sigma_t) \approx 1.0 - 0.165e^{-0.0455\sigma_t} - 0.335e^{-0.3\sigma_t}, \quad \sigma_t > 0. \tag{3.4}$$

The approximation $k_3(\sigma_t)$ is found to agree with the exact solution to an accuracy of within 1%, which is sufficiently for most practical purposes (Leishman, 2002). These three approximations of the Wagner function are shown in Figure 3.2. The correct values are from Woods (1961).

Other methods The hydrodynamic steady state forces on a foil can for some shapes be found in the literature. Collections of experimental data for the so-called NACA series of foils can for example be found in Abbott and Doenhoff (1959). Such experimental series are however most often describing foils with significant thickness, while the thickness of trawl doors are usually negligible.

The hydrodynamic forces on a trawl door are usually found from experiments in either a wind tunnel or a flume tank. The forces are traditionally represented by lift and drag coefficients for some steady states, and sometimes also by the longitudinal center where the hydrodynamic forces attack. Such coefficients tell users and the manufacturers about how efficient the trawl door is, and they are also helpful when the trawl door size and rigging should be chosen.

Both the steady state forces and the unsteady forces may also be estimated using computational fluid dynamics analysis, like solving the Navier-Stokes equations with a finite element method (Mulvany et al., 2004), or by using methods based on potential theory, for example vortex lattice, source panels or surface potential distributions (Margason et al., 1971), possibly including boundary layer effects (Takinaci, 2003). Such methods have been proposed implemented in a numerical wind tunnel, see for example Ren et al. (2000), but they are computational demanding.

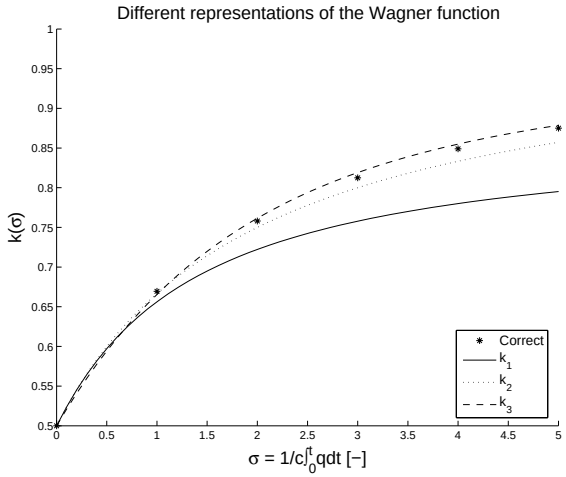

Figure 3.2: Different representations of the Wagner function.

The trawl net

Several different approaches have been developed to construct mathematical models of general net structures. Several studies have revealed that hydrodynamic loads on net structures are complex due to hydroelasticity (Fredheim, 2005; Fredheim and Faltinsen, 2003; Paschen, 2003; Paschen et al., 2004). The loads may be calculated for separate twines (low solidity) or for net panels (high solidity) (Stewart and Ferro, 1987; Årsnes et al., 1990). The approaches may be classified into:

- Formal finite element approaches based on "super meshes" (Priour, 1997, 1999, 2001, 2003, 2005; Tronstad, 2000).
- Direct methods and pragmatic models based on mass points interconnected by springs (Lader et al., 2003; Lee et al., 2001a; Suzuki et al., 2003).
- Interconnected rigid bar models with and without inertial forces (Bessonneau and Marichal, 1998; Niedzwiedz, 1999; Theret, 1994; Vincent, 1999; Tsukrov et al., 2003).

3.1.2 Present work

The ship

The ship movements are described in 3dof according to Fossen (2002), and the hydrodynamic forces on the ship are found from Blanke and Christensen (1993). In addition, the external forces and moments on the ship caused by the warps are included.

The warps and the bridles

The warps and the bridles are modelled as a series of nodes connected by nonlinear damped springs, with the mass and hydrodynamic forces of the line distributed amongst the nodes. The model of these nonlinearities are based on numerical simulations, and it is adapted to simulations of trawl systems. This model keeps the computational effort low, while still obtaining an adequate degree of accuracy.

The trawl doors

The steady state hydrodynamic forces on a specific trawl door are found in all 6dof from wind tunnel experiments as a function of the angle of attack and the angle of slip. A method for extending these forces to other kinds of trawl doors and to outside the normal operating range of the trawl doors is further proposed. In addition, transient effects, such as the acceleration dependent and the velocity dependent forces, are estimated using a numerical method based on potential theory.

The dynamics of the trawl doors are calculated in 6dof, based on estimations of its mass matrix and the forces acting on it, such as the forces from the bridles and the warp, the gravity and buoyancy forces and the hydrodynamic forces.

The trawl net

The trawl net is treated as interconnected cable elements. The forces on each cable element are found from nonlinear equations of the length, length change, velocities relative to the water, dimensions and material. These forces are then distributed amongst the connecting nodes.

3.2 The kinematics of the trawl system

3.2.1 Trawling reference frames

The global frame

The global frame is fixed to the tangent plane of the Earth at a point in the vicinity of the trawl system. The axes point true North, East and down. This frame is assumed to be inertial, neglecting the Coriolis forces. The global frame is denoted by the index n.

The water frame

The water frame follows the sea water. Since it is only used in calculating relative velocities, the placement of its origin is not important. The rotational velocity of the water is assumed to be negligible, so this frame is assumed to maintain a constant orientation in relation to the global frame. The origin is in the vicinity of the trawl system, and the orientation is set equal to that of the global frame. The water frame is denoted by the index w.

The trawl door frames

The trawl door frames are fixed to the trawl doors. A left-hand frame is used for the port trawl door and a right-hand frame for the starboard trawl door. These frames are denoted by the indices d and d^l, respectively. The left-hand frame is related to a similar right-hand frame by $y^{d^l} = -y^d$. This definition ensures that the geometric information about the trawl doors, such as shape and fastening points, is identical on both sides, and that the hydrodynamic orientation angles are defined the same way. The only difference between the two sides is the sign of the moment coefficients, which are changed for the port door.

The trawl door frames and orientation angles are shown in Figure 3.3. The left part shows a trawl door as seen from the port side, the upper part to the right shows the starboard trawl door as seen from above, and the lower part to the right shows the port trawl door as seen from above. The trawl door hydrodynamic orientation angles are defined by the relative speed of the door frame origin in relation to the surrounding fluid. This relative speed is given in the door frame as

$$\mathbf{v}_{dw}^d = \mathbf{v}_{dn}^d - \mathbf{v}_{wn}^d = \begin{bmatrix} v_{dw,1}^d & v_{dw,2}^d & v_{dw,3}^d \end{bmatrix}^T. \tag{3.5}$$

The total velocity vectors relative to the global frame and the water are respectively given as

$$\boldsymbol{\nu}_{dn}^d = \begin{bmatrix} \mathbf{v}_{dn}^d \\ \boldsymbol{\omega}_{dn}^d \end{bmatrix}, \quad \boldsymbol{\nu}_{dw}^d = \begin{bmatrix} \mathbf{v}_{dw}^d \\ \boldsymbol{\omega}_{dw}^d \end{bmatrix}, \tag{3.6}$$

where $\boldsymbol{\omega}_{dn}^d = \begin{bmatrix} p_{dn}^d & q_{dn}^d & r_{dn}^d \end{bmatrix}^T$ and $\boldsymbol{\omega}_{dw}^d = \begin{bmatrix} p_{dw}^d & q_{dw}^d & r_{dw}^d \end{bmatrix}^T$ are the angular velocity of the trawl door in relation to the global frame and the water frame, respectively, decomposed in the trawl door frame. The total hydrodynamic velocity, U_d, the trawl door angle of attack, α^d, and the angle of slip, β^d, are defined as

$$U_d = \|\vec{v}_{dw}\| = \left\|\mathbf{v}_{dw}^d\right\|, \tag{3.7}$$

$$\alpha^d = -\arcsin \frac{v_{dw,2}^d}{\left\| \begin{bmatrix} v_{dw,1}^d & v_{dw,2}^d \end{bmatrix} \right\|}, \tag{3.8}$$

$$\beta^d = \arcsin \frac{v_{dw,3}^d}{\left\| \begin{bmatrix} v_{dw,1}^d & v_{dw,3}^d \end{bmatrix} \right\|}. \tag{3.9}$$

The trawl door hydrodynamic force frame

The frame of the hydrodynamic forces on the trawl door, $(L,\ D,\ S)$, is shown in Figure 3.4. It constitutes a left-hand frame for the port trawl door and a right-hand frame for the starboard trawl door. The hydrodynamic forces are denoted Υ and taken to attack in the trawl door frame origin, d. They are collected in the vector $\mathbf{f}_{d\Upsilon}^h = \begin{bmatrix} L & D & S \end{bmatrix}^T$ in the hydrodynamic force frame, or $\mathbf{f}_{d\Upsilon}^d = \begin{bmatrix} f_{d\Upsilon,1}^d & f_{d\Upsilon,2}^d & f_{d\Upsilon,3}^d \end{bmatrix}^T$ in the trawl door frame. The following definitions are used:

- Lift force, L, is the hydrodynamic force perpendicular to both the z^d-axis and the relative fluid velocity. It is positive for $f_{d\Upsilon,2}^d > 0$.

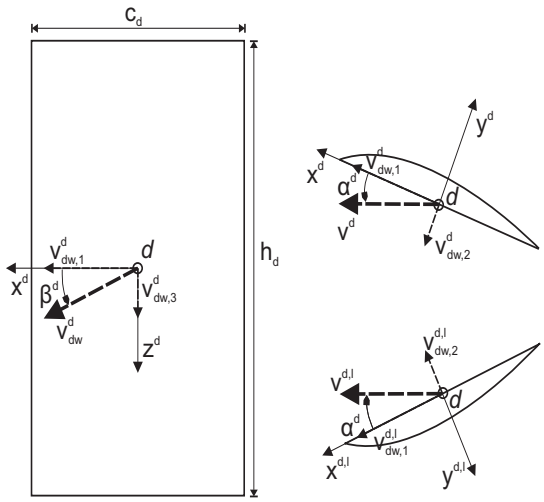

Figure 3.3: Trawl door coordinate system and orientation angles.

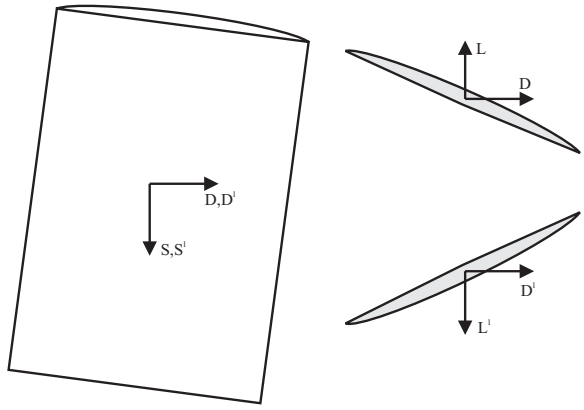

Figure 3.4: The hydrodynamic force frame of the trawl doors.

- Drag force, D, is the hydrodynamic force in the direction of the relative fluid velocity.
- Shear force, S, is as the hydrodynamic force perpendicular to both the relative water velocity and the y^d-axis. It is positive for $f^d_{d\Upsilon,3} > 0$.

The ship frame

The origin of the ship frame is fixed to the ship's center of gravity. The ship frame is denoted by the index s, and its principal axes point forward, starboard and down:

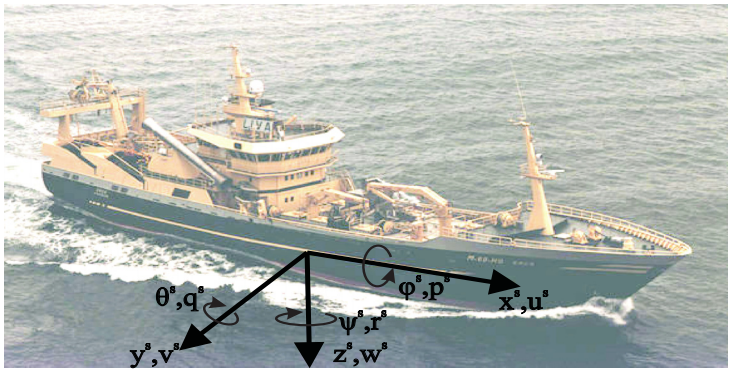

Figure 3.5: The body fixed ship frame.

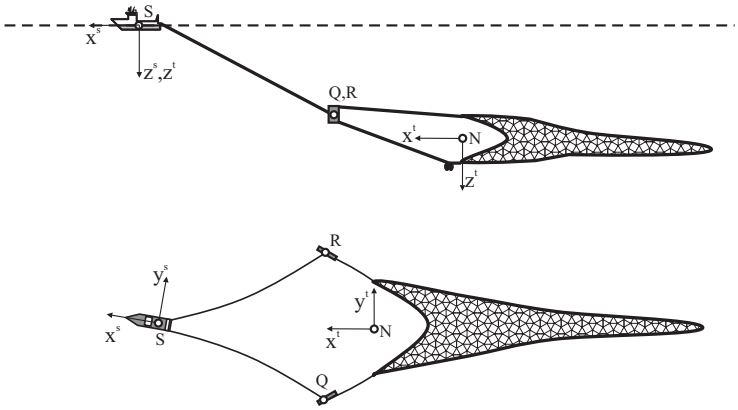

Figure 3.6: The ship and trawl system frames.

- The x^s-axis is the normal forward direction of the ship.
- The y^s-axis is the starboard direction.
- The z^s-axis points downwards when the ship is in its normal state.

The ship frame is shown in Figure 3.5. The ship velocity in relation to the n-frame, decomposed in the ship frame, is defined as

$$\boldsymbol{\nu}^s_{sn} = \begin{bmatrix} u^s_{sn} & v^s_{sn} & w^s_{sn} & p^s_{sn} & q^s_{sn} & r^s_{sn} \end{bmatrix}^T. \tag{3.10}$$

The trawl system frame

The trawl system frame is defined by the direction between the ship and the center of the trawl net opening. The center of the trawl net opening is defined as the average position of the four trawl net wings. The trawl system frame is denoted by the index t. The axes of this frame are defined as:

- The x^t-axis is a projection of the vector from the trawl net opening to the ship onto the horizontal plane.
- The y^t-axis is in the horizontal plane, normal to the x^t-axis and pointing to the starboard.
- The z^t-axis points towards the center of the earth.

The trawl system frame is shown in Figure 3.6.

3.2.2 General coordinate transformations

Coordinate transformations are thoroughly described in Egeland and Gravdahl (2002). Rotation matrices are used in one of two ways:

1. To find the coordinates of a vector in another frame:

$$\mathbf{v}^b = \mathbf{R}_a^b \mathbf{v}^a. \tag{3.11}$$

   The rotation matrix acts as a rotation matrix.

2. To find the new coordinates of a vector that is rotated in a way such that $\mathbf{q}^b = \mathbf{v}^a$:

$$\mathbf{q}^a = \left(\mathbf{R}_a^b\right)^T \mathbf{v}^a. \tag{3.12}$$

   The rotation matrix acts as a transformation matrix.

There are various methods available to obtain these matrices, using descriptions such as Euler angles and quaternions. Using Euler angles causes a singularity when the cosine of one of the Euler angles is zero ($\cos(\theta) = 0$). In a research and development phase this is not significant, since θ can be chosen to represent the angle to give the least probability for failure. The consequences of a failure is also rather limited. Euler angles have physical meaning and are easier to interpret than other representations, which is important during the initial stages. This is why Euler angles are chosen in this work, even if it would also be possible to find the Euler angles from a quaternion representation.

Rotation between two right-hand frames

Rotation of a vector between two right-handed coordinate systems, using Euler angles, is given by Fossen (2002). In the present work, additional indices are employed to the Euler angles to increase generality, and $\mathbf{\Theta}_{ba} = \begin{bmatrix} \phi_{ba} & \theta_{ba} & \psi_{ba} \end{bmatrix}^T$ designate the Euler angles from the a-frame to the b-frame. These are the rotations about the x-, y- and

z-axes, respectively, that must be made in a specific order to the a-frame to align it with the b-frame. If nothing else is explicitly stated, it will throughout this thesis be used a rotation order zyx when defining the Euler angles. For notational simplicity the indices of the individual elements of $\mathbf{\Theta}_{ba}$ are omitted in the following.

The principal rotation matrices about the x-, y-, and z-axes are found to be

$$\mathbf{R}_x\left(\mathbf{\Theta}_{ba}\right) = \begin{bmatrix} 1 & 0 & 0 \\ 0 & c_\varphi & s_\varphi \\ 0 & -s_\varphi & c_\varphi \end{bmatrix}, \tag{3.13}$$

$$\mathbf{R}_y\left(\mathbf{\Theta}_{ba}\right) = \begin{bmatrix} c_\theta & 0 & -s_\theta \\ 0 & 1 & 0 \\ s_\theta & 0 & c_\theta \end{bmatrix}, \tag{3.14}$$

$$\mathbf{R}_z\left(\mathbf{\Theta}_{ba}\right) = \begin{bmatrix} c_\psi & s_\psi & 0 \\ -s_\psi & c_\psi & 0 \\ 0 & 0 & 1 \end{bmatrix}. \tag{3.15}$$

These matrices can be used for calculating the coordinates of a vector in one frame from the coordinates in another frame, when the second frame is found by rotating the first frame about one of its principal axes. By successive rotations about the three principal axes, it is thus possible to obtain any frame. It is also evident that the order of the rotations are important.

Letting $\mathbf{R}_{\mathbf{\Theta}}\left(\mathbf{\Theta}_{ba}\right)$ designate the function giving the rotation matrix from the right-hand frame a to the right-hand frame b, the definitions of the principal rotations yield

$$\begin{aligned} \mathbf{R}_{\mathbf{\Theta}}\left(\mathbf{\Theta}_{ba}\right) &= \mathbf{R}_x\left(\mathbf{\Theta}_{ba}\right)\mathbf{R}_y\left(\mathbf{\Theta}_{ba}\right)\mathbf{R}_z\left(\mathbf{\Theta}_{ba}\right) \\ &= \begin{bmatrix} c_\theta c_\psi & c_\theta s_\psi & -s_\theta \\ -c_\varphi s_\psi + c_\psi s_\theta s_\varphi & c_\psi c_\varphi + s_\theta s_\psi s_\varphi & c_\theta s_\varphi \\ s_\psi s_\varphi + c_\psi c_\varphi s_\theta & -c_\psi s_\varphi + c_\varphi s_\theta s_\psi & c_\theta c_\varphi \end{bmatrix}. \end{aligned} \tag{3.16}$$

The resulting matrix $\mathbf{R}_a^b \in SO\left(3\right)$, where $SO\left(3\right)$ is the special orthogonal group of order 3 (Egeland and Gravdahl, 2002), will satisfy

$$\mathbf{R}_a^b\left(\mathbf{R}_a^b\right)^T = \left(\mathbf{R}_a^b\right)^T\mathbf{R}_a^b = \mathbf{I}, \quad \det\mathbf{R}_a^b = 1, \tag{3.17}$$

which implies that the inverse rotation matrix is given by $\left(\mathbf{R}_a^b\right)^{-1} = \left(\mathbf{R}_a^b\right)^T$. It can therefore be stated that

$$\mathbf{R}_{\mathbf{\Theta}}\left(\mathbf{\Theta}_{ba}\right) = \left(\mathbf{R}_{\mathbf{\Theta}}\left(\mathbf{\Theta}_{ab}\right)\right)^T. \tag{3.18}$$

Rotation between right-hand and left-hand frames

For rotation between the defined right-hand and left-hand frames of the trawl doors, the right-hand Euler angles and coordinates may be found from the left-hand Euler angles and coordinates. For the present case, this is done according to

$$\mathbf{\Theta}_{ba} = \mathbf{E}_l\mathbf{\Theta}^l_{b^l a}\ , \quad \mathbf{p}^b = \mathbf{E}_l\mathbf{p}^{b^l}, \tag{3.19}$$

where $\mathbf{E}$ is the mirroring transformation matrix. The mirroring transformation matrix is in this case found to be

$$\mathbf{E} = \mathbf{E}^T = \begin{bmatrix} 1 & 0 & 0 \\ 0 & -1 & 0 \\ 0 & 0 & 1 \end{bmatrix}, \tag{3.20}$$

and the function giving the transformation matrix from the right-hand frame a into the left-hand frame b^l is found as

$$\begin{aligned} \mathbf{R}_{\boldsymbol{\Theta}^l}\left(\boldsymbol{\Theta}_{b^l a}\right) &= \mathbf{E}\mathbf{R}_x\left(\mathbf{E}\boldsymbol{\Theta}_{b^l a}\right)\mathbf{R}_y\left(\mathbf{E}\boldsymbol{\Theta}_{b^l a}\right)\mathbf{R}_z\left(\mathbf{E}\boldsymbol{\Theta}_{b^l a}\right) \\ &= \begin{bmatrix} c_{\theta^l}c_{\psi^l} & c_{\theta^l}s_{\psi^l} & s_{\theta^l} \\ c_{\varphi^l}s_{\psi^l} + c_{\psi^l}s_{\theta^l}s_{\varphi^l} & -c_{\psi^l}c_{\varphi^l} + s_{\theta^l}s_{\psi^l}s_{\varphi^l} & -c_{\theta^l}s_{\varphi^l} \\ s_{\psi^l}s_{\varphi^l} - c_{\psi^l}c_{\varphi^l}s_{\theta^l} & -c_{\psi^l}s_{\varphi^l} - c_{\varphi^l}s_{\theta^l}s_{\psi^l} & c_{\theta^l}c_{\varphi^l} \end{bmatrix}. \end{aligned} \tag{3.21}$$

Euler angle update from angular velocity in right-hand frames

The time derivatives of the Euler angles may be found from the angular rate vector and the angular transformation matrix $\mathbf{T}_{\boldsymbol{\Theta}}\left(\boldsymbol{\Theta}\right) \in \mathbb{R}^{3\times 3}$ (Fossen, 2002) as

$$\dot{\boldsymbol{\Theta}}_{ba} = \mathbf{T}_{\boldsymbol{\Theta}}\left(\boldsymbol{\Theta}_{ba}\right)\boldsymbol{\omega}_{ba}^{b}. \tag{3.22}$$

For notational simplicity, the indices of the elements of $\boldsymbol{\Theta}_{ba}$ are omitted in the following. The transformation matrix is derived by

$$\begin{aligned} \boldsymbol{\omega}_{ba}^{b} &= \begin{bmatrix} \dot{\varphi} \\ 0 \\ 0 \end{bmatrix} + \mathbf{R}_x\left(\boldsymbol{\Theta}_{ba}\right)\begin{bmatrix} 0 \\ \dot{\theta} \\ 0 \end{bmatrix} + \mathbf{R}_x\left(\boldsymbol{\Theta}_{ba}\right)\mathbf{R}_y\left(\boldsymbol{\Theta}_{ba}\right)\begin{bmatrix} 0 \\ 0 \\ \dot{\psi} \end{bmatrix} \\ &= \begin{bmatrix} 1 & 0 & -s_\theta \\ 0 & c_\varphi & s_\varphi c_\theta \\ 0 & -s_\varphi & c_\varphi c_\theta \end{bmatrix}\begin{bmatrix} \dot{\varphi} \\ \dot{\theta} \\ \dot{\psi} \end{bmatrix} \end{aligned} \tag{3.23}$$

This gives the angular transformation matrix and its inverse for right-hand frames as

$$\mathbf{T}_{\boldsymbol{\Theta}}^{-1}\left(\boldsymbol{\Theta}_{ba}\right) = \begin{bmatrix} 1 & 0 & -s_\theta \\ 0 & c_\varphi & s_\varphi c_\theta \\ 0 & -s_\varphi & c_\varphi c_\theta \end{bmatrix}, \tag{3.24}$$

$$\mathbf{T}_{\boldsymbol{\Theta}}\left(\boldsymbol{\Theta}_{ba}\right) = \begin{bmatrix} 1 & t_\theta s_\varphi & c_\varphi t_\theta \\ 0 & c_\varphi & -s_\varphi \\ 0 & \frac{s_\varphi}{c_\theta} & \frac{c_\varphi}{c_\theta} \end{bmatrix}, \quad c_\theta \neq 0. \tag{3.25}$$

Euler angle update from angular velocity in left-hand frames

For left-hand frames, the angular transformation matrix may be derived by

$$\dot{\mathbf{\Theta}}_{ba} = \mathbf{T}_{\mathbf{\Theta}}\left(\mathbf{\Theta}_{ba}\right)\boldsymbol{\omega}_{ba}^{b}, \tag{3.26}$$

$$\mathbf{E}\dot{\mathbf{\Theta}}_{b^la} = \mathbf{T}_{\mathbf{\Theta}}\left(\mathbf{E}\mathbf{\Theta}_{b^la}\right)\mathbf{E}\boldsymbol{\omega}_{b^la}^{b^l}, \tag{3.27}$$

$$\dot{\mathbf{\Theta}}_{b^la} = \mathbf{E}\mathbf{T}_{\mathbf{\Theta}}\left(\mathbf{E}\mathbf{\Theta}_{b^la}\right)\mathbf{E}\boldsymbol{\omega}_{b^la}^{b^l}, \tag{3.28}$$

$$\dot{\mathbf{\Theta}}_{b^la} = \mathbf{T}_{\mathbf{\Theta}^l}\left(\mathbf{\Theta}_{b^la}\right)\boldsymbol{\omega}_{b^la}^{b^l}, \tag{3.29}$$

$$\mathbf{T}_{\mathbf{\Theta}^l}\left(\mathbf{\Theta}_{b^la}\right) = \mathbf{E}\mathbf{T}_{\mathbf{\Theta}}\left(\mathbf{E}\mathbf{\Theta}_{b^la}\right)\mathbf{E}, \tag{3.30}$$

$$\mathbf{T}_{\mathbf{\Theta}^l}\left(\mathbf{\Theta}_{b^la}\right) = \begin{bmatrix}1 & 0 & 0\\ 0 & -1 & 0\\ 0 & 0 & 1\end{bmatrix}\begin{bmatrix}1 & -t_{\theta_l}s_{\varphi_l} & -c_{\varphi_l}t_{\theta_l}\\ 0 & c_{\varphi_l} & -s_{\varphi_l}\\ 0 & \frac{s_{\varphi_l}}{c_{\theta_l}} & \frac{c_{\varphi_l}}{c_{\theta_l}}\end{bmatrix}\begin{bmatrix}1 & 0 & 0\\ 0 & -1 & 0\\ 0 & 0 & 1\end{bmatrix}. \tag{3.31}$$

This gives the angular transformation matrix for left-hand frames and its inverse as

$$\mathbf{T}_{\mathbf{\Theta}^l}^{-1}\left(\mathbf{\Theta}_{b^la^l}\right) = \begin{bmatrix}1 & 0 & s_{\theta_l}\\ 0 & c_{\varphi_l} & -s_{\varphi_l}c_{\theta_l}\\ 0 & s_{\varphi_l} & c_{\varphi_l}c_{\theta_l}\end{bmatrix}, \tag{3.32}$$

$$\mathbf{T}_{\mathbf{\Theta}^l}\left(\mathbf{\Theta}_{b^la^l}\right) = \begin{bmatrix}1 & t_{\theta_l}s_{\varphi_l} & -c_{\varphi_l}t_{\theta_l}\\ 0 & c_{\varphi_l} & s_{\varphi_l}\\ 0 & -\frac{s_{\varphi_l}}{c_{\theta_l}} & \frac{c_{\varphi_l}}{c_{\theta_l}}\end{bmatrix}, \quad c_{\theta_l} \neq 0. \tag{3.33}$$

3.3 The hydrodynamic forces on a trawl door

The hydrodynamic forces on the trawl doors affect the trawl system and its efficiency to a great extent. It is therefore crucial to calculate these forces as accurate as possible during simulation of the trawl system. The hydrodynamic forces on a trawl door are governed by the velocities and accelerations of the trawl door in all six dof in relation to the surrounding water, as well as memory effects. Its motion is determined by these forces, in addition to gravity and buoyancy forces and the forces from the warp and bridle lines. Because of the strong interdependencies between the hydrodynamic forces on the trawl door, the position, orientation, velocities and accelerations of the trawl door, only small errors in the force calculation may give large discrepancies in its dynamic behavior. All forces affecting the trawl door, in all six dof, must therefore be thoroughly investigated and calculated.

Until now, the properties of main interest have been the hydrodynamic lift and drag forces on the trawl doors during steady state conditions. The other hydrodynamic forces and moments have been taken into account by tuning the rigging of the trawl door, in a process involving both industrial experience and trial and error. To simulate the control system, however, the trawl door process plant model needs to include hydrodynamic forces and moments in all six degrees of freedom. Even if the trawl doors mainly operate in nearly steady state conditions, the model should also include unsteady forces, since these may be important during control of the trawl system.

A model including both steady state and transient hydrodynamic forces in all six dof is developed in this section. The purpose of the model is to analyze the effect and performance of the control actions during simulations. It must therefore be sufficiently

accurate to verify controller solutions, and it should be as computational efficient as possible. The unsteady forces are divided into forces during circulation build-up, acceleration dependent and velocity dependent forces.

3.3.1 Representation of the hydrodynamic moments

Various formulations for representing the hydrodynamic moments of lifting surfaces may be used. This section motivates the choice made for this thesis.

2D lifting surfaces

There are in 2D foil theory two different formulations commonly used to express the hydrodynamic steady-state forces and moment on the foil. The most intuitive formulation is maybe stating the hydrodynamic force vector $\mathbf{f}_{d\Upsilon}^{d,2D} = \begin{bmatrix} f_{d\Upsilon,1}^{d,2D} & f_{d\Upsilon,2}^{d,2D} & 0 \end{bmatrix}^T$ and the center of pressure, R^{2D}, with the coordinates $\mathbf{p}_{R^{2D}d}^{d} = \begin{bmatrix} p_{R^{2D}d,1}^{d} & p_{R^{2D}d,2}^{d} & 0 \end{bmatrix}^T$. When both $\mathbf{f}_{d\Upsilon}^{d,2D}$ and $\mathbf{p}_{R^{2D}d}^{d}$ are known, this yields the forces and moment acting on the foil. Another formulation is stating the hydrodynamic forces and moment directly. The forces are then assumed to attack in a fixed point, and the moment is given about this point.

To show the relation between the two formulations, or more specifically between $\mathbf{p}_{R^{2D}d}^{d}$ and $\mathbf{m}_{d\Upsilon}^{d,2D} = \begin{bmatrix} 0 & 0 & m_{d\Upsilon,3}^{d,2D} \end{bmatrix}^T$, let the point R^{2D} be confined to a straight line approximating the foil mean camber line. The relation between the two formulations is then given by

$$\mathbf{m}_{d\Upsilon}^{d,2D} = \mathbf{f}_{d\Upsilon}^{d,2D} \times \mathbf{p}_{R^{2D}d}^{d}. \tag{3.34}$$

It is of interest to find if it is always possible to use a formulation where the center of pressure represents the hydrodynamic moment. The straight line approximating the foil is given by its normal vector $\mathbf{n}^{d,2D} = \begin{bmatrix} n_1^{d,2D} & n_2^{d,2D} & 0 \end{bmatrix}^T$ and the point P^{2D} on the line, $\mathbf{p}_{P^{2D}d}^{d} = \begin{bmatrix} p_{P^{2D}d,1}^{d} & p_{P^{2D}d,2}^{d} & 0 \end{bmatrix}^T$. This gives

$$\begin{aligned} \left(\mathbf{n}^{d,2D}\right)^T \cdot \left(\mathbf{p}_{R^{2D}d}^{d} - \mathbf{p}_{P^{2D}d}^{d}\right) &= 0, \\ &\Updownarrow \qquad (3.35) \\ \left(\mathbf{n}^{d,2D}\right)^T \cdot \mathbf{p}_{R^{2D}d}^{d} &= \left(\mathbf{n}^{d,2D}\right)^T \cdot \mathbf{p}_{P^{2D}d}^{d}. \qquad (3.36) \end{aligned}$$

Combining (3.34) and (3.36) gives

$$\begin{bmatrix} \left(\mathbf{f}_{d\Upsilon}^{d,2D}\right)^T \\ \left(\mathbf{n}^{d,2D}\right)^T \end{bmatrix} \mathbf{p}_{R^{2D}}^{d} = \begin{bmatrix} m_{d\Upsilon,3}^{d,2D} \\ \left(\mathbf{n}^{d,2D}\right)^T \cdot \mathbf{p}_{P^{2D}d}^{d,} \end{bmatrix}. \tag{3.37}$$

There is a unique solution of (3.37) if $\vec{f}^{2D}$ and $\vec{n}^{2D}$ are not normal to each other. This means that as long as the hydrodynamic force vector has a component normal to the plane of the foil, one can always find a point of attack giving the correct moment vector. The two different representations in the 2D case are shown in Figure 3.7.

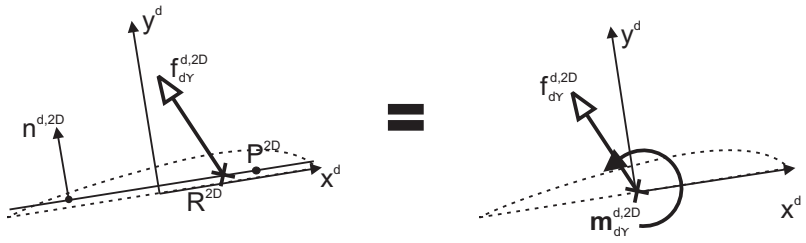

Figure 3.7: Two different formulations of force and moment for a 2D foil. Left: The moment is given by the assumed attack point of the force. Right: The force is assumed attacking in a fixed point, and a moment is added.

3D lifting surfaces

In the 3D case all six force and moment components are present, in contrast to the 2D case. Extending the procedure used in the 2D case to three dimensions would give

$$\begin{bmatrix} 0 & f^d_{d\Upsilon,3} & -f^d_{d\Upsilon,2} \\ -f^d_{d\Upsilon,3} & 0 & f^d_{d\Upsilon,1} \\ f^d_{d\Upsilon,2} & -f^d_{d\Upsilon,1} & 0 \\ n^d_1 & n^d_2 & n^d_3 \end{bmatrix} \begin{bmatrix} p^d_{Rd,1} \\ p^d_{Rd,2} \\ p^d_{Rd,3} \end{bmatrix} = \begin{bmatrix} m^d_{d\Upsilon,1} \\ m^d_{d\Upsilon,2} \\ m^d_{d\Upsilon,3} \\ \left(\mathbf{n}^d\right)^T \cdot \mathbf{p}^d_{Pd} \end{bmatrix}, \tag{3.38}$$

$$\Updownarrow$$

$$\mathbf{A}\mathbf{p}^d_{Rd} = \mathbf{b}. \tag{3.39}$$

This system is consistent if and only if the vector $\mathbf{b}$ is in the column space of $\mathbf{A}$. The column space of $\mathbf{A}$ is found to be

$$\left\{ \begin{bmatrix} 0 \\ 1 \\ -\frac{f^d_{d\Upsilon,2}}{f^d_{d\Upsilon,3}} \\ 0 \end{bmatrix}, \begin{bmatrix} 0 \\ 0 \\ 0 \\ 1 \end{bmatrix}, \begin{bmatrix} 1 \\ 0 \\ -\frac{f^d_{d\Upsilon,1}}{f^d_{d\Upsilon,3}} \\ 0 \end{bmatrix} \right\}. \tag{3.40}$$

If $\mathbf{b}$ is in this space, then $\mathbf{b}$ can be written as a linear combination of (3.40) according to

$$\begin{bmatrix} 0 & 0 & 1 \\ 1 & 0 & 0 \\ -\frac{f^d_{d\Upsilon,2}}{f^d_{d\Upsilon,3}} & 0 & -\frac{f^d_{d\Upsilon,1}}{f^d_{d\Upsilon,3}} \\ 0 & 1 & 0 \end{bmatrix} \begin{bmatrix} k_1 \\ k_2 \\ k_3 \end{bmatrix} = \begin{bmatrix} m^d_{d\Upsilon,1} \\ m^d_{d\Upsilon,2} \\ m^d_{d\Upsilon,3} \\ \left(\mathbf{n}^d\right)^T \cdot \mathbf{p}^d_{Rd} \end{bmatrix}, \tag{3.41}$$

$$\Updownarrow \tag{3.42}$$

$$\begin{aligned} k_1 &= m^d_{d\Upsilon,2}, \\ k_2 &= \left(\mathbf{n}^d\right)^T \cdot \mathbf{p}^d_{rd}, \\ k_3 &= m^d_{d\Upsilon,1}, \\ m^d_{d\Upsilon,3} &= -m^d_{d\Upsilon,2}\frac{f^d_{d\Upsilon,2}}{f^d_{d\Upsilon,3}} - m^d_{d\Upsilon,1}\frac{f^d_{d\Upsilon,1}}{f^d_{d\Upsilon,3}}. \end{aligned} \tag{3.43}$$

This is the case if, and only if

$$m^d_{d\Upsilon,1} f^d_{d\Upsilon,1} + m^d_{d\Upsilon,2} f^d_{d\Upsilon,2} + m^d_{d\Upsilon,3} f^d_{d\Upsilon,3} = 0. \tag{3.44}$$

In the general case, (3.44) is not fulfilled and (3.41) can not be solved. Hence, it is not straightforward to represent the moments by the force vector and its point of attack. A better approach is to take the hydrodynamic forces to attack in a fixed point on the trawl door and calculate the moments accordingly. The hydrodynamic forces are in the remainder of this thesis taken to attack in the origin of the trawl door frame, and the moments are taken to act about the same point. The hydrodynamic forces and moments acting on the trawl door are in the following designated $\mathbf{f}^d_{d\Upsilon}$ and $\mathbf{m}^d_{d\Upsilon}$, and the generalized hydrodynamic force is designated

$$\boldsymbol{\tau}^d_{d\Upsilon} = \begin{bmatrix} \left(\mathbf{f}^d_{d\Upsilon}\right)^T & \left(\mathbf{m}^d_{d\Upsilon}\right)^T \end{bmatrix}^T. \tag{3.45}$$

3.3.2 Wind tunnel experiments

Since the steady state coefficients are important properties of the trawl doors, they should be found as accurate as possible. Wind tunnel experiments on a representative model-scale trawl door were therefore performed. This made it possible to find the hydrodynamic forces and moments in all six degrees of freedom for various combinations of orientation angles.

The hydrodynamic forces are for a given orientation (in relation to the relative water velocity) assumed proportional to the square of the relative velocity. Measurements for only one velocity should therefore suffice. The hydrodynamic forces and moments acting on the model are designated $\mathbf{f}^{m^l}_{m^l\Upsilon}$ and $\mathbf{m}^{m^l}_{m^l\Upsilon}$, and the generalized hydrodynamic force vector is designated

$$\boldsymbol{\tau}^{m^l}_{m^l\Upsilon} = \begin{bmatrix} \left(\mathbf{f}^{m^l}_{m^l\Upsilon}\right)^T & \left(\mathbf{m}^{m^l}_{m^l\Upsilon}\right)^T \end{bmatrix}^T. \tag{3.46}$$

Experimental setup

The basis for the experiments was a port trawl door with area 15m^2, of the type Thyborøn 8. The suction side of this trawl door is shown in the left part of Figure 3.9, and the pressure side of a starboard trawl door is shown in the right part of the same figure. This trawl door is a multifoil consisting of three foils; two small front foils followed by a larger aft foil. Its cross-section is shown in Figure 3.8. The aspect ratio of this trawl door is found as

$$\mathcal{AR} = \frac{h_d^2}{A_d} = 1.45, \tag{3.47}$$

where h_d is the span (height), and A_d is the planform area of the trawl door. This aspect ratio is less than what is common for pelagic and larger than what is common for bottom trawling. The experimental results should therefore represent a compromise for both types of trawling.

The model used for the experiments was in scale $1:5$ of the full scale trawl door, with an area of $A_m = 0.6\,\text{m}^2$. The experiments were performed in a horizontal wind tunnel,

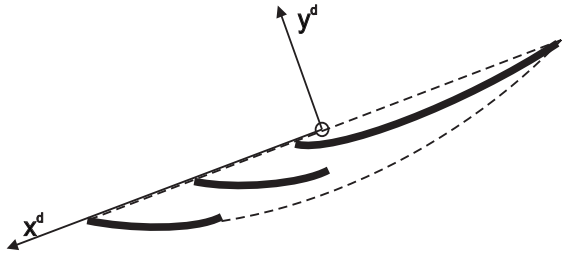

Figure 3.8: Principal cross section of the trawl door used in the experiments.

with experimental setup as shown in Figure 3.10. The air speed was approximately 16 m/s during the experiments, giving a Reynolds number

$$R_n = \frac{\rho_a U_m c_m}{\mu_a} = 7.1 \times 10^5, \tag{3.48}$$

where ρ_a and μ_a are the density and the dynamic viscosity of the air. For the full scale trawl door the Reynolds number would be

$$R_n = \frac{\rho_w U_d c_d}{\mu_w} = 4.8 \times 10^6, \tag{3.49}$$

where ρ_w and μ_w are the density and the dynamic viscosity of the sea water. The influence of this difference is assumed negligible, since the separation is dominated by the sharp edges of the trawl door.

The trawl door model was placed with the suction side upwards in the wind tunnel. Left-hand frames are used for the model and the hydrodynamic forces, since the tests were performed with a port trawl door. The model could be rotated about the wind

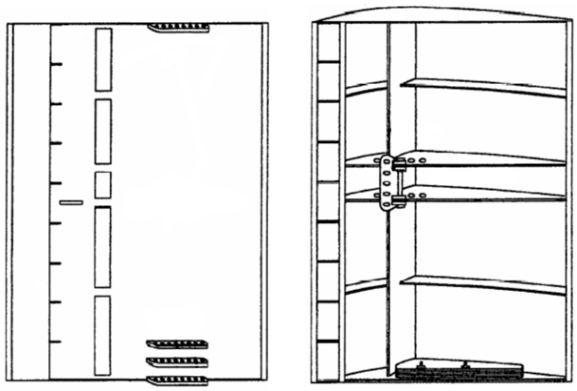

Figure 3.9: Suction side of a port trawl door and pressure side of a starboard trawl door.

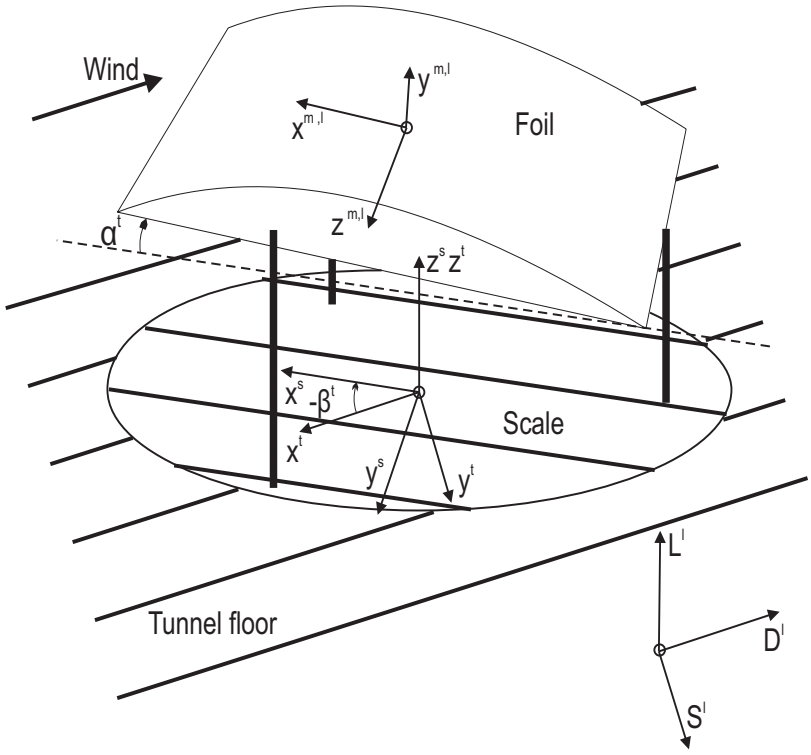

Figure 3.10: Experimental setup and coordinate systems.

tunnel z^t-axis to give variations in the angle of slip, β^t, and about the model z^{m^l}-axis to give variations in the angle of attack, α^t. Steady state forces and moments were measured in the scale frame by force transducers under the floor of the wind tunnel.

Figure 3.11 shows the various combinations of orientation angles for the recorded measurements, for both the hydrodynamic and the wind tunnel definitions. The sign of β^t is changed to allow for easier comparison. The dotted line connects the same combination of angles in the two different representations. Since the purpose of the experiments were to support simulations of trawl systems, the measurements were primarily chosen to give high precision in the normal working range of the trawl doors. Additional measurements were recorded to give increased precision where the coefficients were expected to vary the most. To provide the possibility of interpolation outside the normal working range of the trawl door, measurements for extreme orientations were also recorded.

Reference frames used for the experiments

The model frame The model frame m^l is similar to the trawl door frame d^l, defined in Section 3.2.1.

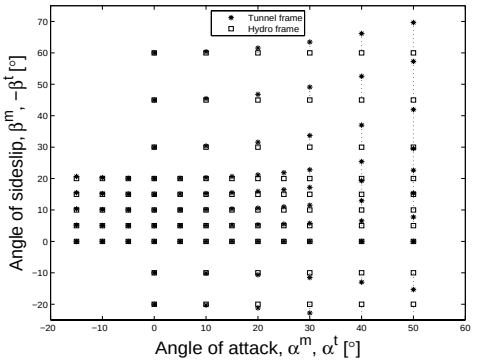

Figure 3.11: Orientations for recorded measurements.

The wind tunnel frame The wind tunnel frame is shown in Figure 3.10. The z^t-axis points strictly upwards, perpendicular to the wind. The origin is located in the centre of the scale. The x^t-axis is horizontal, pointing straight into the wind. The y^t-axis is given from the fact that this is a right-hand frame.

The scale frame The scale frame is shown in Figure 3.10. The scale frame and the wind tunnel frame coincides for $\beta^t = 0$, but the scale frame follows the model as this is rotated about the z^t-axis.

Experiment orientation angles The wind tunnel angle of attack, α^t, is measured as the angle between the x^s- and the x^{m^l}-axis. α^t is defined to be positive in the intended range of operation. The wind tunnel slip angle, β^t, is measured as the angle between the x^s- and the x^t-axis. It is defined to be positive for counter-clockwise rotation about the z^t-axis.

Experiment transformations

Rotations between scale and model frame For rotations between the scale and model frames, the order of the primary rotations is xyz to make use of the measured orientation angles. This means that equation (3.21) is not valid, but the principal rotations may be used. The Euler angles are found to be

$$\boldsymbol{\Theta}_{m^l s} = \begin{bmatrix} -\frac{\pi}{2} & 0 & -\alpha^t \end{bmatrix}^T, \tag{3.50}$$

and the principal rotations yield

$$\begin{aligned} \mathbf{R}_s^{m^l} &= \mathbf{R}_l \mathbf{R}_z \left(\mathbf{T}_l \boldsymbol{\Theta}_{m^l s}\right) \mathbf{R}_y \left(\mathbf{T}_l \boldsymbol{\Theta}_{m^l s}\right) \mathbf{R}_x \left(\mathbf{T}_l \boldsymbol{\Theta}_{m^l s}\right) \\ &= \begin{bmatrix} c_{\alpha^t} & 0 & s_{\alpha^t} \\ -s_{\alpha^t} & 0 & c_{\alpha^t} \\ 0 & 1 & 0 \end{bmatrix}. \end{aligned} \tag{3.51}$$

Rotations between scale and tunnel frame The rotation from tunnel to scale frames is given by

$$\mathbf{\Theta}_{st} = \begin{bmatrix} 0 & 0 & \beta^t \end{bmatrix}^T, \tag{3.52}$$

and (3.16) yields

$$\mathbf{R}_t^s = \begin{bmatrix} c_{\beta^t} & s_{\beta^t} & 0 \\ -s_{\beta^t} & c_{\beta^t} & 0 \\ 0 & 0 & 1 \end{bmatrix}. \tag{3.53}$$

Rotations between tunnel and model frame The rotations from tunnel to model frame can be found from

$$\begin{aligned} \mathbf{R}_t^{m^l} &= \left(\mathbf{R}_{m^l}^s\right)^T \mathbf{R}_t^s \\ &= \begin{bmatrix} c_{\alpha^t} c_{\beta^t} & c_{\alpha^t} s_{\beta^t} & s_{\alpha^t} \\ -c_{\beta^t} s_{\alpha^t} & -s_{\alpha^t} s_{\beta^t} & c_{\alpha^t} \\ -s_{\beta^t} & c_{\beta^t} & 0 \end{bmatrix}. \end{aligned} \tag{3.54}$$

Forces in the trawl door frame The forces in the model frame can be found from the forces in the scale frame according to

$$\mathbf{f}^{m^l} = \mathbf{R}_s^{m^l} \mathbf{f}^s. \tag{3.55}$$

Forces in the hydrodynamic force frame The forces in the hydrodynamic force frame can be found from the forces in the scale frame by

$$\mathbf{f}^{h^l} = \mathbf{R}_s^{h^l} \mathbf{f}^s \ . \tag{3.56}$$

$\mathbf{R}_s^{h^l}$ is found from (3.21), using

$$\mathbf{\Theta}_{h^l s} = \begin{bmatrix} -\frac{\pi}{2} & \beta^t & -\frac{\pi}{2} \end{bmatrix}^T. \tag{3.57}$$

and this yields

$$\mathbf{R}_s^{h^l} = \begin{bmatrix} 0 & 0 & 1 \\ -c_{\beta^t} & -s_{\beta^t} & 0 \\ -s_{\beta^t} & c_{\beta^t} & 0 \end{bmatrix}. \tag{3.58}$$

Positions in scale and tunnel frame The position vector of an arbitrary point B given in the model frame is in the scale frame found to be

$$\mathbf{p}_B^s = \mathbf{R}_{m^l}^s \left(\mathbf{p}_{Bm^l}^{m^l} - \mathbf{p}_{Pm^l}^{m^l} \right) + \mathbf{p}_P^s, \tag{3.59}$$

where P is a pivot point which remains fixed in both scale and model frame. $\mathbf{R}_{m^l}^s$ is found from (3.21).

Hydrodynamic moments in the model frame The hydrodynamic moments are transferred to the model axes. The measured forces are taken to attack in the origin of the model frame. The hydrodynamic moment about the origin of the model frame decomposed in the model frame is

$$\mathbf{m}^{m^l}_{m^l\Upsilon} = \mathbf{R}^{m^l}_{s}(\mathbf{m}^{s}_{s\Upsilon} - \mathbf{p}^{s}_{m^l s} \times \mathbf{f}^{s}_{m^l\Upsilon}), \tag{3.60}$$

where $\mathbf{m}^s_{s\Upsilon}$ is the measured moment about the scale frame origin given in the scale frame. $\mathbf{p}^s_{m^l s}$is found from (3.59).

The steady-state forces

The hydrodynamic steady-state coefficients are in the model frame found as

$$C^{\infty}_{m\Upsilon,i}(\alpha^m,\beta^m) = \frac{f^{m^l}_{m^l\Upsilon,i}(\alpha^m,\beta^m)}{\frac{1}{2}\rho_a A_m U_m^2}\ ,\ i=1,\ 2,\ 3 \tag{3.61}$$

$$C^{\infty}_{m\Upsilon,4}(\alpha^m,\beta^m) = s_m\frac{m^{m^l}_{m^l\Upsilon,1}(\alpha^m,\beta^m)}{\frac{1}{2}\rho_a A_m h_m U_m^2}, \tag{3.62}$$

$$C^{\infty}_{m\Upsilon,5}(\alpha^m,\beta^m) = s_m\frac{m^{m^l}_{m^l\Upsilon,2}(\alpha^m,\beta^m)}{\frac{1}{2}\rho_a A_m \sqrt{h_m^2+(c_m)^2}U_m^2}, \tag{3.63}$$

$$C^{\infty}_{m\Upsilon,6}(\alpha^m,\beta^m) = s_m\frac{m^{m^l}_{m^l\Upsilon,3}(\alpha^m,\beta^m)}{\frac{1}{2}\rho_a A_m c_m U_m^2}, \tag{3.64}$$

where A_m, h_m and l_m are the planform area, span and cord length of the model, respectively. ρ_a is the density of the air in the wind tunnel, and s_m designates if this is the model of a port ($s_m = -1$) or starboard ($s_m = 1$) trawl door. The superscript ∞ indicates that these are the steady-state coefficients. These definitions of the frames, hydrodynamic orientation angles and coefficients give the same coefficients for both port and starboard trawl doors.

The measured steady-state hydrodynamic force and moment coefficients in the model frame are shown in Figures 3.12 to 3.17, using the definitions in (3.61) to (3.64).

The hydrodynamic steady-state force coefficients are in the hydrodynamic force frame found as

$$C^{\infty}_{L}(\alpha^m,\beta^m) = \frac{f^{h^l}_{m^l\Upsilon,1}(\alpha^m,\beta^m)}{\frac{1}{2}\rho_a A_m U_m^2}, \tag{3.65}$$

$$C^{\infty}_{D}(\alpha^m,\beta^m) = \frac{f^{h^l}_{m^l\Upsilon,2}(\alpha^m,\beta^m)}{\frac{1}{2}\rho_a A_m U_m^2}\ , \tag{3.66}$$

$$C^{\infty}_{S}(\alpha^m,\beta^m) = \frac{f^{h^l}_{m^l\Upsilon,3}(\alpha^m,\beta^m)}{\frac{1}{2}\rho_a A_m U_m^2}\ . \tag{3.67}$$

The measured steady-state hydrodynamic force coefficients in the hydrodynamic force frame are shown in Figures 3.18 to 3.20, using the definitions in (3.65) to (3.67).

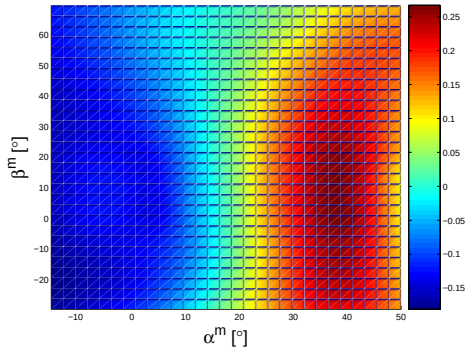

Figure 3.12: Measured coefficient of hydrodynamic forces along trawl door x^m-axis, $C^{\infty}_{m\Upsilon,1}$, for varying angles of slip and attack.

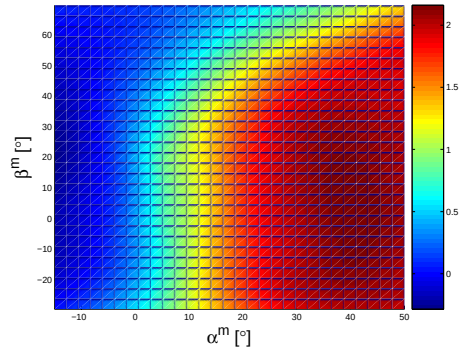

Figure 3.13: Measured coefficient of hydrodynamic forces along trawl door y^m-axis, $C^{\infty}_{m\Upsilon,2}$, for varying angles of slip and attack.

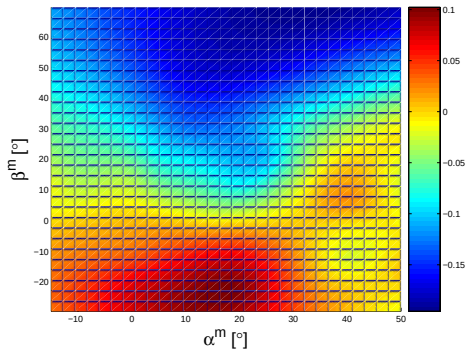

Figure 3.14: Measured coefficient of hydrodynamic forces along trawl door z^m-axis, $C^{\infty}_{m\Upsilon,3}$, for varying angles of slip and attack.

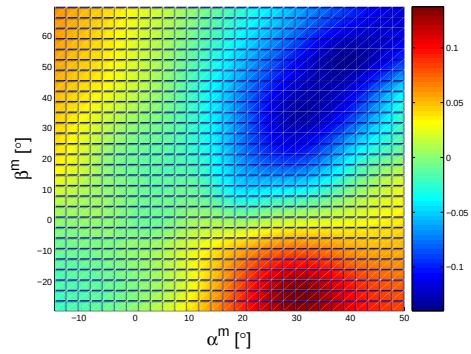

Figure 3.15: Moment coefficient about trawl door x^m-axis, $C^{\infty}_{m\Upsilon,4}$, for varying angles of slip and attack.

Comments to the steady-state coefficients

Figure 3.12 shows how the hydrodynamic force along the trawl door x^m-axis is almost independent of the angle of slip, but it is positive and increases steadily with the angle of attack in the normal operating range of the trawl door. This is probably a result of some of the individual foils operating at a lower angle of attack than the trawl door as a whole, causing one component of their lift force to act in the x^m-direction.

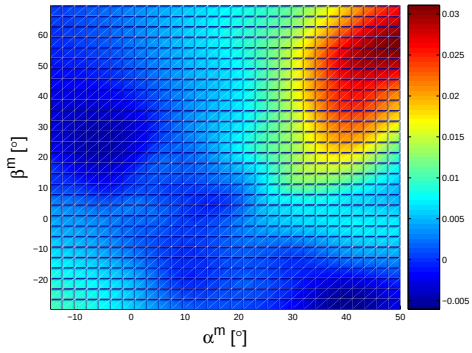

Figure 3.16: Moment coefficient about trawl door y^m-axis, $C^{\infty}_{m\Upsilon,5}$, for varying angles of slip and attack.

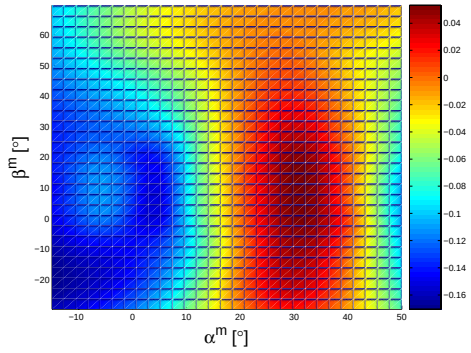

Figure 3.17: Moment coefficient about trawl door z^m-axis, $C^{\infty}_{m\Upsilon,6}$, for varying angles of slip and attack.

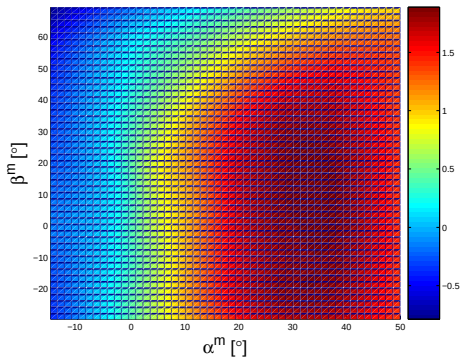

Figure 3.18: Coefficient of hydrodynamic lift, C^{∞}_{L}, for varying angles of slip and attack.

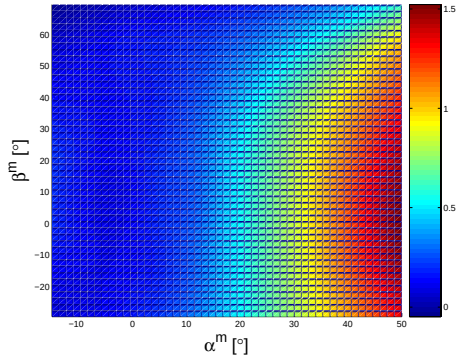

Figure 3.19: Coefficient of hydrodynamic drag, C^{∞}_{D}, for varying angles of slip and attack.

Figure 3.13 shows how the force along the trawl door y^m-axis for small angles of slip is almost independent of this. In spite of the lower angles of attack for the two frontmost foils, this force is positive also for negative angles of attack, because of the curvature of the trawl door. It increases steadily with the angle of attack, until it reaches its maximum value at approximately 40 °. At this point, it is likely that the decrease in force is due to the occurrence of stalling.

Figure 3.14 shows how the force along the trawl door z^m-axis for small angles of attack is roughly proportional to the angle of slip, but this relationship is less evident for higher angles of attack.

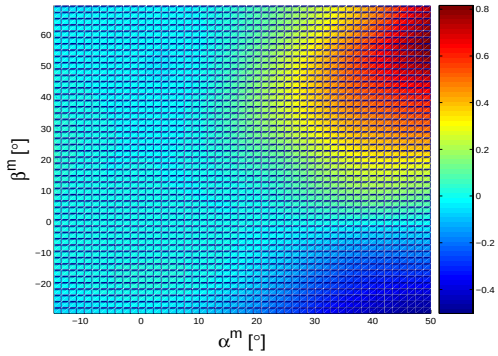

Figure 3.20: Coefficient of hydrodynamic shear force, C_S^∞, for varying angles of slip and attack.

Figure 3.15 shows the coefficient of hydrodynamic moment about the x^m-axis for various hydrodynamic orientation angles of the model. The moment is approximately zero for $\beta^m = 0$, positive for $\beta^m < 0$ and negative for $\beta^m > 0$. This explains an effect experienced when moving the bridle fastening points on the door: When moving such a point upwards, the trawl door rolls inwards. If only the effect of the forces in the bridle and warp lines are regarded, the opposite roll direction would be expected. The reason for rolling inwards is that the upwards moving of the bridles fastening points makes the trawl door tilt backwards. This tilting creates a roll moment of larger magnitude than the moment from the bridles, and in the opposite direction (inwards).

Figure 3.16 shows the coefficient of hydrodynamic moment about the y^m-axis for various hydrodynamic orientation angles of the model. For a given angle of attack in the normal operating range, there seems to be a simple relation between the angle of slip and the moment coefficient. This coefficient is roughly -0.006 for $\beta^m = 0$, and it varies approximately inversely proportional to β^m.

Figure 3.17 shows the coefficient of hydrodynamic moment about the z^m-axis for various hydrodynamic orientation angles of the model. The coefficient is largest for $\alpha^m \approx 30\,^\circ$ and $\beta^m \approx 0\,^\circ$. For angles of attack, α^m, between $20\,^\circ$ and $40\,^\circ$ and angles of slip $|\beta^m| < 30\,^\circ$, the coefficient seems to decrease roughly proportional to the angular distance from this minimum, $\sqrt{(\alpha^m - 30\,^\circ)^2 + \beta^m}$.

Figure 3.18 shows the coefficient of hydrodynamic lift for the model for various hydrodynamic orientation angles. For moderate angles of slip, the lift coefficient is fairly independent of the angle of slip, and it increases approximately linearly with the angle of attack up to $\alpha^m \approx 18\,^\circ$. For $\alpha^m > 18\,^\circ$ the increase in lift is declining, and maximum lift is approximately $C^\infty_{L,\max} \approx 1.9$ for $\alpha^m_{\max} \approx 30\,^\circ$ and $\beta^m_{\max} \approx 10\,^\circ$. The lift coefficient for zero slip (as marked by the line **BB** in Figure 3.18) and its derivative with respect to the angle of attack (angle of attack in radians) is shown in Figure 3.22.

Figure 3.19 shows the coefficient of hydrodynamic drag of the model for various hydrodynamic orientation angles. The drag coefficient is fairly independent of the angle of slip, and it is linearly increasing with the angle of attack for $\alpha^m > 10\,^\circ$. For reasonable angles of slip, the minimum drag is seen to be approximately $C^\infty_{D,\min} \approx 0.11$ for $\alpha^m \approx -5\,^\circ$. For the hydrodynamic orientation angles giving maximum lift ($\alpha^m_{\max} \approx 30\,^\circ$ and $\beta^m_{\max} \approx 10\,^\circ$), the drag coefficient is approximately $C^\infty_{D,\max} \approx 0.84$. This gives the ratio between lift and drag for maximum lift: $\frac{C^\infty_{L,\max}}{C^\infty_{D,\max}} \approx 2.3$. It is seen that both the lift and the drag coefficients are quite indifferent to changes in the angle of slip in the normal working area. This is important during normal operation, since it means that the trawl doors can be rigged to give the desired angle of attack, without paying too much attention to the angle of slip. This is also beneficial when developing a control system, since the effort can be focused towards the angles of attack and roll.

Figure 3.20 shows the coefficient of hydrodynamic shear force for the model for various hydrodynamic orientation angles. The shear force is seen to be zero for zero β^m, positive for negative β^m and negative for positive β^m. The shear force is not perfectly symmetric about $\beta^m = 0$, due to the fact that the model itself is not perfectly symmetric about the plane $z^m = 0$.

Figure 3.21 shows how $C^\infty_{m\Upsilon,6}$ and its derivative with respect to α^m varies with α^m for zero slip (as marked by the line **AA** in Figure 3.17) . The derivative $\frac{dC^\infty_{m\Upsilon,6}}{d\alpha^m}|_{\beta^m=0}$ is negative in the intervals $-5\,^\circ < \alpha^m < 4\,^\circ$ and $\alpha^m > 30\,^\circ$. In these intervals an increase in α^m gives an decrease in $C^\infty_{m\Upsilon,6}$. This added moment is counteracting the increase (or decrease) in α^m, and in these regions the hydrodynamic moment therefore stabilizes the trawl door angle of attack. For the regions where $\frac{dC^\infty_{m\Upsilon,6}}{d\alpha^m}|_{\beta^m=0} > 0$, the hydrodynamic moment $m^{d,\infty}_{d\Upsilon,3}$ adds instability to the system. If the trawl door is operated at such angles of attack, the angle of attack is therefore more likely to oscillate. This may lead to oscillations in the trawl system and should be avoided. On the other hand, the ratio between hydrodynamic lift and drag is higher for angles of attack smaller than $30\,^\circ$. So stabilizing the trawl door at such angles could be beneficial from both economic and environmental points of view. Stabilization may be achieved by means of a feedback control system, but such control would be energy demanding. A better way would be to use the rigging of the trawl door, or even change its hydrodynamic properties. This rises a conflict of interest, since the more stable the trawl door is, the more energy the control actions consume. The rigging should therefore be carefully chosen, so that one gains stability over the whole working range of the trawl door, while avoiding unnecessary stability in some areas leading to very energy demanding control actions.

Figure 3.22 shows the lift coefficient for zero slip (as marked by the line **BB** in Figure 3.18) and its derivative with respect to the angle of attack (angle of attack in radians). According to 2D foil theory, a two-dimensional flat plate at small angles of attack would have a lift coefficient given by $C^{2D}_L = 2\pi \sin\alpha$ (Newman, 1977), which yields $\frac{dC^{2D}_L}{d\alpha} = 2\pi\cos\alpha$. This linearized 2D theory result is also shown in

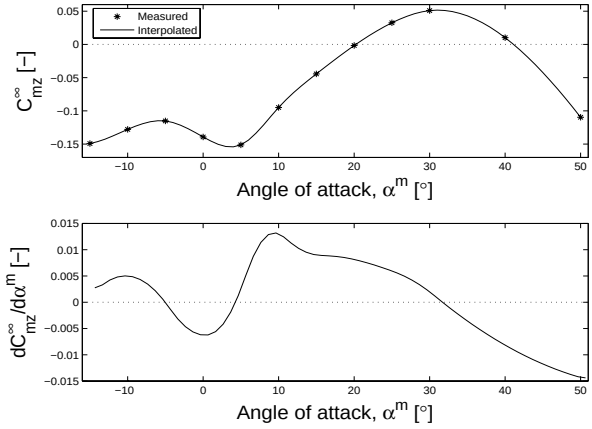

Figure 3.21: Dependence of $C^{\infty}_{m\Upsilon,6}$ and $\frac{dC^{\infty}_{m\Upsilon,6}}{d\alpha^d}$ on α^d for $\beta^d = 0$.

Figure 3.22. The slope of the lifting curve of the trawl door is far less than what the 2D linearized theory would predict. This is caused by the three dimensional effects which reduces the lift of the door. It can also be seen that the lift at zero angle of attack is different than zero. This is caused by the curvature of the trawl door.

3.3.3 Modeling the steady-state coefficients

Measurements for 90 different combinations of orientation angles were obtained during the wind tunnel experiments. The main purpose of these experiments was to facilitate a mathematical model for numerical simulations of the trawl system. The hydrodynamic forces on the trawl door are therefore needed for orientation angles both between and outside the range of these measurements. It is also of interest to estimate the hydrodynamic properties of other types of trawl doors. Direct use of look up tables would probably add to the computational effort during simulation, because of the non-smooth data. It was therefore chosen to perform a parameterization of the steady-state coefficients from the experiments.

Parameterization of the measured coefficients

Parameterization facilitates smoothing of the experimental results, as well as easy extrapolation for orientation angles outside the normal operating range. To limit the computational effort during simulation, the parameterization is carried out with as few parameters as possible. The accuracy in the normal operating range of the trawl door is emphasized.

The parameter functions, $\hat{\mathbf{C}}^{\infty}_{m\Upsilon}\left(\alpha^m, \beta^m, \hat{\mathbf{K}}_{m\Upsilon}\right)$, are found partly by trial and error and partly by the use of physical insight. They return the six steady state coefficients

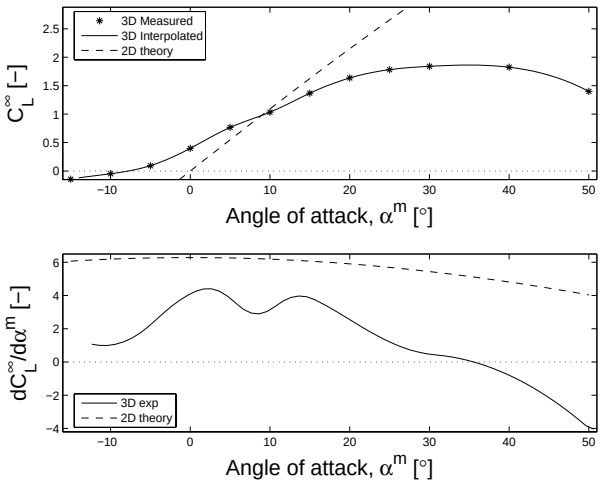

Figure 3.22: The steady state lift coefficient for zero slip angle.

as a function of the angle of attack, the angle of slip and a constant parameter matrix, $\hat{\mathbf{K}}_{m\Upsilon}$. This is selected to reflect the experimental data as well as possible, using numerical optimization.

For each dof a candidate objective function is proposed to be

$$O_i = \sum_{n=1}^{N} w_n \left(C^{\infty}_{m\Upsilon,in} - \hat{C}^{\infty}_{m\Upsilon,in} \left(\alpha_n^m, \beta_n^m, \hat{\mathbf{K}}_{m\Upsilon,i} \right) \right)^2, \tag{3.68}$$

where $C^{\infty}_{m\Upsilon,in}$ is the measurement n of the coefficient i, $\hat{C}^{\infty}_{m\Upsilon,in}$ is the calculated coefficient i for this measurement, and $\hat{\mathbf{K}}_{m\Upsilon,i}$ is the row i of the parameter matrix for calculating the hydrodynamic coefficients. w_n is the value of the weight function for the measurement n. The weight function emphasizes the measurements in the expected operating range of the trawl door used in a control system, and it is defined as

$$w_n = \frac{1}{k_1^2 + (k_2 \alpha^m_{\max} - \alpha_n^m)^2 + (\beta_n^m)^2}, \tag{3.69}$$

where k_1 and k_2 are factors chosen as 1 and $\frac{2}{3}$ to avoid too much weight in the central working area and for high angles of attack. $\alpha^m_{\max}$ is the angle of attack that gives maximum hydrodynamic lift for zero angle of slip. α_n^m and β_n^m are the hydrodynamic angles of attack and slip during the measurement n, respectively.

The simplex search method of Lagarias et al. (1998), incorporated in the `fminsearch` function of the Matlab™ software, are used in finding each row vector of the parameter matrix giving the lowest value of the objective functions:

$$\mathbf{K}^{opt}_{m\Upsilon,i} = \arg \min_{\hat{\mathbf{K}}_{m\Upsilon,i}} \left(O_i \right). \tag{3.70}$$

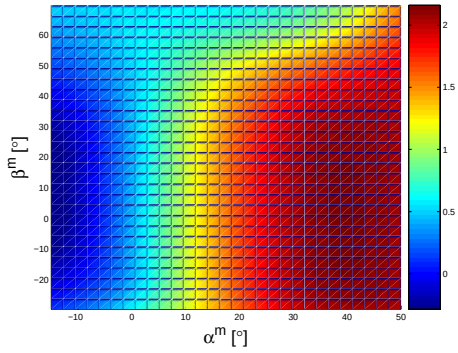

Figure 3.23: Calculated coefficient of hydrodynamic force along trawl door y^d-axis.

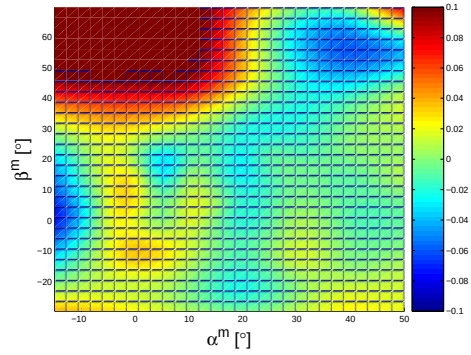

Figure 3.24: Error in calculated coefficient of hydrodynamic force along trawl door y^d-axis.

When this optimum parameter matrix is inserted into the parameter functions, the steady-state coefficients in all degrees of freedom can be calculated by

$$\bar{\mathbf{C}}^{\infty}_{m\Upsilon}\left(\alpha^m, \beta^m\right) = \hat{\mathbf{C}}^{\infty}_{m\Upsilon}\left(\alpha^m, \beta^m, \mathbf{K}^{opt}_{m\Upsilon}\right). \tag{3.71}$$

The result of the parameterization is a function of 42 parameters giving the six steady-state hydrodynamic force and moment coefficients of trawl doors of this specific type. The resulting parameterization functions of the steady-state coefficients, $\hat{\mathbf{C}}^{\infty}_{m\Upsilon}\left(\alpha^m, \beta^m, \mathbf{K}^{opt}_{m\Upsilon}\right)$, are given in Appendix C, along with the resulting optimal parameter matrix, $\mathbf{K}^{opt}_{m\Upsilon}$.

Figure 3.23 shows the parameterized coefficient of steady state hydrodynamic force in the y^m-direction, and Figure 3.24 shows the ratio between the error and the range of the measured values. It is seen that in the area of main interest, the errors are less than 2% of the measured range. For most purposes this would be negligible. Further details of the parameterization results are given in Appendix C.

Extending the model to other kinds of trawl doors

Different kinds of trawl doors has different hydrodynamic characteristics. These characteristics need to be approximated for each trawl door. This can be done by:

- Using the same procedure as before for each kind of trawl door.
- Using numerical methods (computational fluid dynamics).
- Extend the known properties of this model to other kinds of trawl doors.

The first procedure would give accurate results, but would also require much resources for each new kind of trawl door to be analyzed. The second approach would probably require less resources, but also give less reliable results. To use the third approach, the

steady state hydrodynamic coefficients must be assumed to be very similar in shape. This is not necessarily the case, since a multifoil can be designed for different hydrodynamic properties. So without taking into account the curvature, size, placement and internal angle of attack of each foil, it is in general impossible to describe the hydrodynamic properties of a given multifoil.

If the requirements to the mathematical model is not too strict, and the hydrodynamic performance of the trawl door in question is not too different from the model used in the wind tunnel experiments, extending the known properties of the presented model may be the best solution. Since most mid-water trawl doors have to meet approximately the same design criteria, it may be assumed that the hydrodynamic performance of such trawl doors are comparable.

To find the hydrodynamic properties for another trawl door using this approach, it is assumed that the following hydrodynamic properties of the trawl door is known for zero angle of slip:

- The angle of attack for which maximum lift is obtained, $\alpha^d_{\max}$.
- The angle of attack for which no lift is obtained, α^d_0.
- The maximum lift coefficient, $C^{d,\infty}_{L,\max}$.
- The drag coefficient at $\alpha^d_{\max}$, $C^{d,\infty}_{D,\max}$.
- The coefficient of moment about trawl door z^d-axis at $\alpha^d_{\max}$, $C^{d,\infty}_{6,\max}$.

The steady state hydrodynamic coefficients may then be approximated as

$$\bar{\mathbf{C}}^{\infty}_{d\Upsilon}\left(\alpha^d, \beta^d\right) = \mathbf{C}_{dm} \cdot \bar{\mathbf{C}}^{\infty}_{m\Upsilon}\left(\alpha^m, \beta^m\right), \tag{3.72}$$

using the hydrodynamic orientation angles

$$\alpha^m = \alpha^m_0 + \left(\alpha^d - \alpha^d_0\right) \frac{\alpha^m_{\max} - \alpha^m_0}{\alpha^d_{\max} - \alpha^d_0}, \tag{3.73}$$

$$\beta^m = \beta^d, \tag{3.74}$$

and the correction coefficient matrix

$$\mathbf{C}_{dm} = diag\left\{\frac{C^d_{D,\max}}{C^m_{D,\max}}, \frac{C^d_{L,\max}}{C^m_{L,\max}}, 1, \frac{C^d_{L,\max}}{C^m_{L,\max}}, \frac{C^d_{D,\max}}{C^m_{D,\max}}, \frac{C^d_{6,\max}}{C^m_{6,\max}}\right\}, \tag{3.75}$$

where the values found for the model is $C^m_{L,\max} \approx 1.9$, $C^m_{D,\max} \approx 0.84$, $C^m_{6,\max} \approx 0.05$, $\alpha^m_0 \approx -8\,^\circ$ and $\alpha^m_{\max} \approx 30\,^\circ$.

Extending the model to outside the normal operating range

If using the parameterization (3.72) for simulation purposes, problems could arise if the trawl door orientation angles leave the normal operating range. It is therefore necessary to extend the parameterization to cover all possible combinations of the orientation angles.

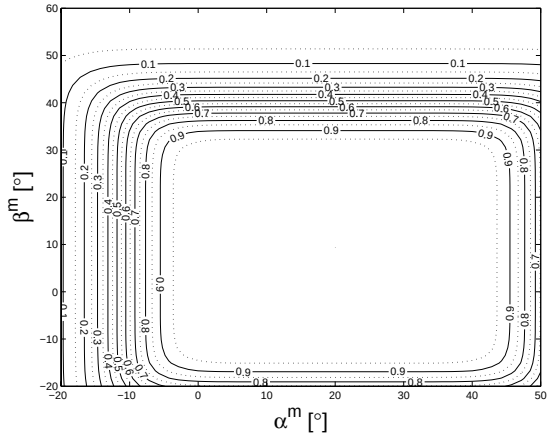

Figure 3.25: The reducing function used for avoiding problems outside the normal operating range.

It is proposed to do this by replacing the hydrodynamic coefficients by some asymptotic damping coefficients as the trawl door leaves its normal operating range. The structural forces and the asymptotic damping forces will then in such cases presumably force the trawl door back to its normal operating range. Since the asymptotic damping only influence the calculations when the trawl door is outside the intended range of operation, the actual coefficients are not significant, as long as they are positive. This ensures that energy is dissipated from the system. The vector of asymptotic damping coefficients is for simplicity set to

$$\boldsymbol{\xi}_\infty = \begin{bmatrix} 1 & 1 & 1 & 1 & 1 & 1 \end{bmatrix}^T. \tag{3.76}$$

The hydrodynamic forces and moments are found by interpolating between the values found from the parameterization and the asymptotic values, $\boldsymbol{\xi}_\infty$. This interpolation is done by a reducing function which is close to 1 in the normal operating range, but rapidly reduced towards 0 outside this range. It is important that this reducing function is decreasing fast enough to suppress the higher order terms in the parameter functions. To fulfill these requirements, a proposed reducing function is

$$r\left(\alpha^d, \beta^d\right) = \frac{1}{1 + a^b \left((k_2 \alpha^d_{\max} - \alpha^d)^b + \left(\beta^d - k_3\right)^b \right)}, \tag{3.77}$$

where $k_2 = \frac{2}{3}$ as in (3.69), $k_3 = 0.15$, $a = 1.8$ and $b = 10$. This reducing function is shown in Figure 3.25 for the trawl door model used in the wind tunnel experiments.

Extending the model to all angles of attack and slip, the steady state hydrodynamic

forces in the trawl door frame are calculated as

$$\bar{\tau}^{d,\infty}_{d\Upsilon,i} = \frac{1}{2}\rho_w A_d U_d^2 \bar{C}^{\infty}_{d\Upsilon,i} r - \rho_w A_d U_d \xi_{\infty,i} (1-r)\, \nu^d_{dw,i} \ , i = 1,2,3 \tag{3.78}$$

$$\bar{\tau}^{d,\infty}_{d\Upsilon,4} = \frac{1}{2} s_d \rho_w A_d h_d U_d^2 \bar{C}^{\infty}_{d\Upsilon,4} r - \rho_w A_d h_d U_d \xi_{\infty,4} (1-r)\, \nu^d_{dw,4} \ , \tag{3.79}$$

$$\bar{\tau}^{d,\infty}_{d\Upsilon,5} = \begin{array}{l} \frac{1}{2} s_d \rho_w A_d \sqrt{h_d^2 + (c_d)^2}\, U_d^2 \bar{C}^{\infty}_{d\Upsilon,5} r \\ -\rho_w A_d \sqrt{h_d^2 + (c_d)^2}\, U_d \xi_{\infty,5} (1-r)\, \nu^d_{dw,5} \end{array} \ , \tag{3.80}$$

$$\bar{\tau}^{d,\infty}_{d\Upsilon,6} = \frac{1}{2} s_d \rho_w A_d c_d U_d^2 \bar{C}^{\infty}_{d\Upsilon,6} r - \rho_w A_d c_d U_d \xi_{\infty,6} (1-r)\, \nu^d_{dw,6}, \tag{3.81}$$

where s_d designates if this is a port ($s_d = -1$) or starboard ($s_d = 1$) trawl door, $r = r\left(\alpha^d, \beta^d\right)$ and $\bar{C}^{\infty}_{d\Upsilon,i} = \bar{C}^{\infty}_{d\Upsilon,i}\left(\alpha^d, \beta^d\right)$. A similar procedure is used for calculating the hydrodynamic forces in the hydrodynamic force frame.

3.3.4 Transient effects

When a foil is subject to changes in velocities relative to the ambient fluid, the hydrodynamic forces and moments are different from those expected from steady-state theory and measurements. These effects may be of interest for trawl door controller design, since both stability and performance are affected, and they should therefore be implemented into the process plant model. Due to their limited significance, it is chosen to estimate the transient forces using numerical methods.

Numerical solution of transient effects for trawl doors

There are several numerical methods possible for estimating the hydrodynamic forces on a 3D foil. In Margason et al. (1971) aerodynamic coefficients are compared, using one vortex lattice method (VLM), one source panel method, two low-order surface potential distributions and two high-order surface potential distributions. The computed lift coefficients are shown in Figures 3.26 and 3.27 for a 45 ° swept-back and a 45 ° swept-forward wing, respectively. It is noted that the VLM predicts the experimental data quite well, probably due to the fact that it neglects the effects of both thickness and viscosity. Since these effects seem to cancel each other, the result is better than several more complex methods. For a trawl door the effect of thickness is probably far less than the effect of viscosity, and the results are probably less accurate than these figures suggest. The VLM is not be able to accurately recreate the forces along the x^d-axis, the z^d-axis or around the y^d-axis ($\tau^d_{d\Upsilon,i},\ i = 1,3,5$), since these are greatly influenced by viscosity. These forces are, however, regarded as the least important ones, and the VLM is chosen because of its simplicity and computational efficiency. By scaling its results against the steady state values found from the wind tunnel experiments, it is believed that the development of the hydrodynamic forces and moments with time are adequately predicted.

The vortex lattice method

A 3D vortex has constant strength and can not terminate in the fluid. It can, however, terminate on the boundaries. Figure 3.28 shows a 3D vortex with strength Γ that form

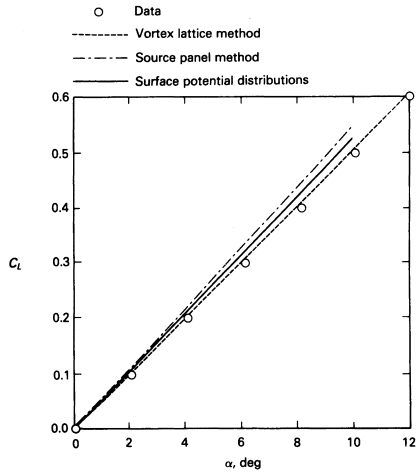

Figure 3.26: Comparison of numerical methods for 45° swept-back wing, NACA 64A010 section, aspect ratio 3.0. From Margason et al. (1971).

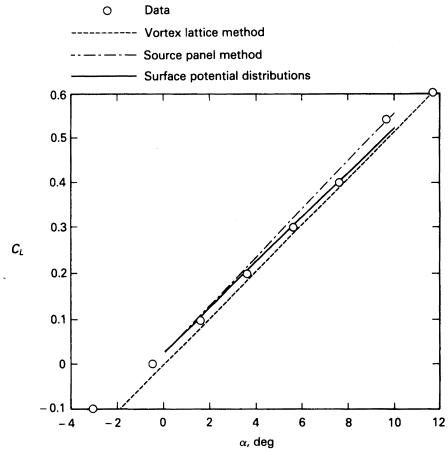

Figure 3.27: Comparison of numerical methods for 45° swept-forward wing, NACA 64A112 section, aspect ratio 3.55. From Margason et al. (1971).

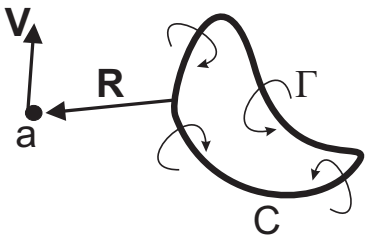

Figure 3.28: A 3D vortex along the contour C with strength Γ inducing a velocity in the point a.

a line along the contour C, in the vicinity of the point a. The velocities $\mathbf{V}$ induced in a can be found from

$$\mathbf{V} = -\frac{\Gamma}{4\pi}\int_C \frac{\mathbf{R}\times d\mathbf{l}}{R^3}, \tag{3.82}$$

where $\mathbf{R}$ is the vector from each point along C to the point a, and R is the length of $\mathbf{R}$ (Newman, 1977).

The vortex lattice method is essentially a method where the part of the flow caused by the foil is modeled as a lattice of 3D vortices. The strength of the vortices are found by requiring the relative fluid velocity normal to the foil to be zero. This relative fluid velocity is the sum of the relative velocity between the surrounding water and the foil and the velocities induced by each vortex on the foil and in the wake. These calculations are done by dividing the foil into several panels, placing vortices and a control point in each panel. It is here chosen to describe the vortex system on the foil by square ring vortices surrounding each control point. The ring vortices are placed so that the leading vortex elements coincide with the quarter-chord line of the panel, while the control points are placed in the centre of each ring. When using this configuration, the strength of each vortex ring can be estimated by demanding that there should be no flow through the control points (Katz and Plotkin, 1991). The velocity through a control point $\mathbf{c}_n$ from a line vortex element between the points $\mathbf{r}_1$and $\mathbf{r}_2$ can be found from this expression, and the solution is

$$\mathbf{V} = \frac{\Gamma}{4\pi}\int_C \frac{\mathbf{r}_1\times\mathbf{r}_2}{|\mathbf{r}_1\times\mathbf{r}_2|^2}(\mathbf{r}_2-\mathbf{r}_1)\cdot\left(\frac{\mathbf{r}_1}{r_1}-\frac{\mathbf{r}_2}{r_2}\right). \tag{3.83}$$

To include transient effects, the changes in vorticity on the foil must be transferred to the wake. The induced velocities from all shed vortices must be calculated and subtracted from the free stream relative velocity between the foil and the surrounding fluid. For each time step the strength of the leading vortex rings in the wake are set equal to the strength of the corresponding trailing vortex rings of the foil in the previous time step. The position of the leading corner points of the vortex rings in the wake are set to match the position of the trailing corner points of the trailing vortex rings of the foil at a time $k\Delta t$ after last time step. $k = 0.3$ is used in this work, as proposed by Katz and Plotkin (1991). Figure 3.29 shows the grid used for describing the vortex system on the foil and in the wake.

The velocities induced by the wake affect not only the foil, but also the wake itself. This effect is called wake roll-up, and it makes the wake narrower with time. This is

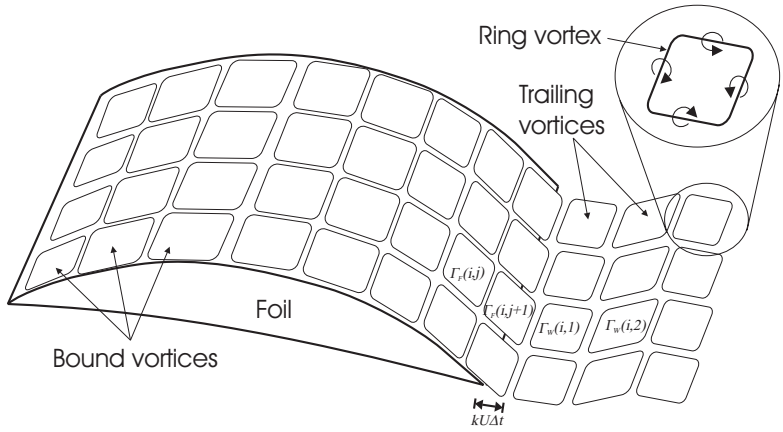

Figure 3.29: Overview of the vortex lattice method.

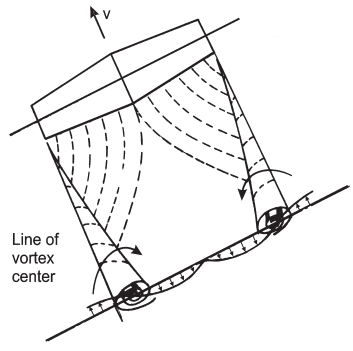

Figure 3.30: Wake roll up behind a 3D foil. From Hoerner (1975).

illustrated in Figure 3.30 from Hoerner (1975). In order to reduce computation time, this effect is not implemented. The effect of the wake on the foil is in other words assumed to be as if the wake remains stationary where it is shed. This will probably influence the solutions only in a minor degree, since the induced velocities on the foil from the wake decrease with approximately the square of the time since each vortex was shed.

The implementation aspects of the vortex lattice method is described in more detail in Appendix D.

Calculation of the unsteady forces

The hydrodynamic forces are found from the fluid accelerations and from the circulation about the foil. The distribution of these forces are then used for finding the hydrodynamic moments. The forces caused by the **fluid accelerations** are found from Bernoulli's equation. The pressure difference between the suction and the pressure side of the foil from these accelerations is

$$\Delta p^a = \rho_w \frac{\partial \left(\Phi^+ - \Phi^-\right)}{\partial t}, \tag{3.84}$$

where the velocity potential on the upper (Φ^+) and lower (Φ^-) side can be found by integrating the local vorticity from the leading edge to the local longitudinal position

$$\Phi^{\pm} = \pm \int_{-\frac{1}{2}c_f}^{x^f} \frac{\gamma}{2} dl, \tag{3.85}$$

where c_f is the foil chord length, γ is the local vorticity and x^f is the local longitudinal coordinate, which is equal to $\pm\frac{c_f}{2}$ at the leading and trailing ends, respectively (Katz and Plotkin, 1991).

The forces from **circulation** are found from the law of Kutta-Joukowski (Newman, 1977). The forces on each part of each ring vortex are found from

$$\mathbf{f}_d^c(i,j,n) = \rho_w l(i,j,n)\, \mathbf{U}(i,j) \times \mathbf{\Gamma}(i,j,n), \tag{3.86}$$

where $l(i,j,n)$ is the length of the vortex element number n of the panel (i,j), $\mathbf{\Gamma}(i,j,n)$ is the strength of this vortex element and $\mathbf{U}(i,j)$ is its relative velocity.

The dynamics of the various hydrodynamic forces and moments are of quite different importance for the behavior of the trawl doors. The most important ones are those either of a large magnitude in relation to the other forces affecting the same dof or affecting other parts of the trawl system. This applies in particular to the forces $\tau^d_{d\Upsilon,i},\ i \in \{2,4,6\}$, where the subscript i denotes dof number i of the trawl door, and these are therefore given extra attention.

To estimate the unsteady forces, the unsteady effects are divided into:

- Forces from circulation build-up, $\boldsymbol{\tau}^c_d$.
- Forces from angular velocities, $\boldsymbol{\tau}^\nu_d$.
- Forces from accelerations relative to the ambient water, $\boldsymbol{\tau}^a_d$.

dof	Steady state	Circulation build-up	Angular velocities	Accele-rations
1	$C^{\infty}_{d\Upsilon,1}$	$T_{dc,1}$	-	-
2	$C^{\infty}_{d\Upsilon,2}$	$T_{dc,2}$	-	$C^{a}_{d,22}$
3	$C^{\infty}_{d\Upsilon,3}$	$T_{dc,3}$	-	-
4	$C^{\infty}_{d\Upsilon,4}$	$T_{dc,4}$	$C^{\nu}_{d,44}$	$C^{a}_{d,44}$
5	$C^{\infty}_{d\Upsilon,5}$	$T_{dc,5}$	$C^{\nu}_{d,55}$	-
6	$C^{\infty}_{d\Upsilon,6}$	$T_{dc,6}$	$C^{\nu}_{d,66}$	$C^{a}_{d,66}$

Table 3.1: The different components of the hydrodynamic forces for each dof in the model.

In sum these forces add up to the total hydrodynamic force vector

$$\boldsymbol{\tau}^{d}_{d\Upsilon} = \boldsymbol{\tau}^{c}_{d} + \boldsymbol{\tau}^{\nu}_{d} + \boldsymbol{\tau}^{a}_{d}. \tag{3.87}$$

Table 3.1 shows an overview of the various coefficients included to calculate the hydrodynamic forces and moments in the model. The coefficients are explained as they are introduced.

The steady state values of $\boldsymbol{\tau}^{d}_{d\Upsilon}$ are estimated from the parameterization of equation (3.72). The VLM is used to investigate how the hydrodynamic forces on the trawl door develops with time, when the trawl door experiences

- Changes in linear velocity components.
- Steady angular velocity components about the x^d- and z^d-axis.
- Relative accelerations between the trawl door and the surrounding water.

Since viscous effects are important for the damping moment about the y^d-axis, this moment can not be found by the VLM. Instead, it is approximated using an analytical method.

Forces from circulation build-up

It is assumed that when the trawl door experiences a change in its states, the hydrodynamic forces from circulation build-up develop as the step response of a linear system, as shown in Figure 3.31. In this figure, *F_final* is the steady state force for the new condition, *F_initial* is the steady state force for the initial condition and *T_step* is the time when a step in the conditions occur. The time constant T is found as the time from the change happens until the response reaches *F_t*, which is found as 63% (more accurately: $1 - e^{-1}$) of the final step response. The reason for choosing this representation, is that its response characteristics seem appropriate (its derivative decays as the steady state value is approached). In addition, time integration of this representation is computational efficient.

When the initial value, the final value and the time constant is known, the response of such a system can be calculated. The dynamics of the hydrodynamic forces from

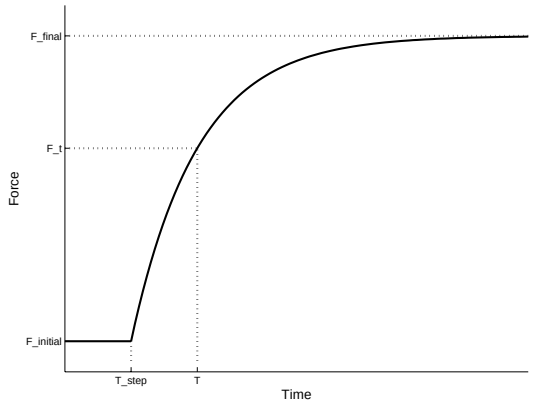

Figure 3.31: The step response of a linear system.

circulation build-up are formulated as

$$\frac{d\tau_{d,i}^{c}}{dt} = \frac{1}{T_{dc,i}} \left(\tau_{d\Upsilon,i}^{d,\infty} - \tau_{d,i}^{c} \right), \; i = 1 \ldots 6, \tag{3.88}$$

where $\tau_{d\Upsilon,i}^{d,\infty}$ is the steady state generalized force in the dof i found from the wind tunnel experiments, $\tau_{d,i}^{c}$ is the generalized force in the dof i from circulation about the foil, and $T_{dc,i}$ is the time constant in the dof i.

Since the initial and final steady state forces can be found from the parameterization in the previous section, only the time constants, $T_{dc,i}$, needs to be estimated. These are approximated from the VLM solutions. The variables calculated by the VLM are in the following indicated by the tilde ($\tilde{}$) accent.

It is assumed that the individual foil of the trawl door are close enough for the circulation build up to be similar to a monofoil of the same aspect ratio. The aspect ratio of the foil in the simulations is increased from 1.45 to 1.54 to include the effects from the end plates. Eight different step responses of a monofoil without end plates are simulated, using the VLM software. The steps are defined in Table 3.2.

The step responses are shown in Figures 3.32 - 3.35. Each figure shows the step responses from both the negative and positive step, marked by a + and a − in the legend, respectively. The legend indicates which response corresponding to which force component. The solid-drawn lines show the approximations resulting from the calculated time constants.

It is worth noting that even if the change in angle of attack is the same in Figures 3.33 and 3.35, the development of the hydrodynamic forces are quite different. It is further seen that even if the response in some dof and for some steps are adequately described by the proposed approximations, others are not. This indicates that an accurate model would have to calculate the hydrodynamic forces not only from the angles of attack and slip, but also from the relative velocities. In addition, the step responses would have to be approximated not only by that of a linear system. In spite of these imperfections, these approximations are proposed due to their simplicity and low importance.

j	Step		
1	ΔU_d	$=$	$-0.2\,\mathrm{m/s}$
2	$\Delta\alpha^d$	$=$	$-5\,^\circ$
3	Δp^d_{dw}	$=$	$-0.2\,\mathrm{rad/s}$
4	$\Delta\psi^d_{dw}$	$=$	$-5\,^\circ$
5	ΔU_d	$=$	$0.2\,\mathrm{m/s}$
6	$\Delta\alpha^d$	$=$	$5\,^\circ$
7	Δp^d_{dw}	$=$	$0.2\,\mathrm{rad/s}$
8	$\Delta\psi^d_{dw}$	$=$	$5\,^\circ$

Table 3.2: The various steps for which the responses were analyzed.

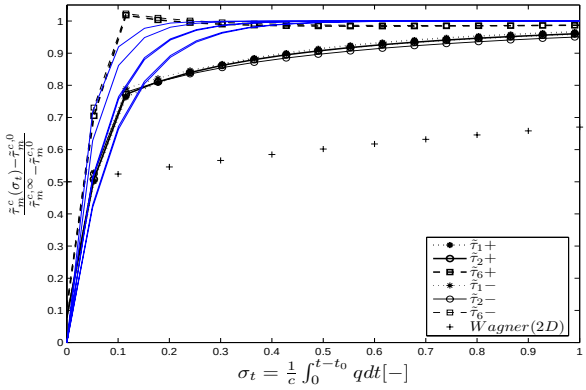

Figure 3.32: Normalized response of the hydrodynamic circulation forces for steps in the forward velocity, steps 1 and 5.

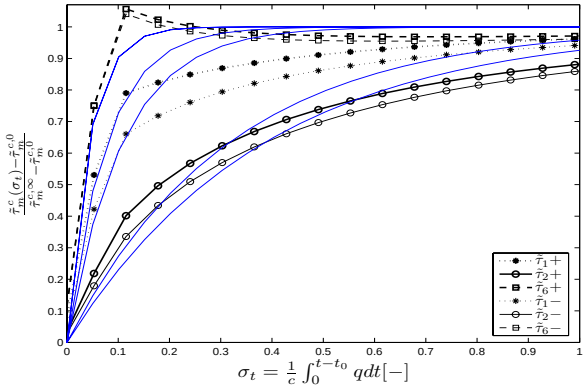

Figure 3.33: Normalized response of the hydrodynamic circulation forces for steps in the angle of attack, from changes in velocities, steps 2 and 6.

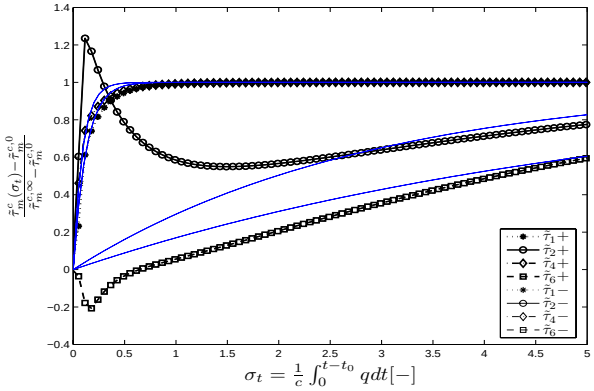

Figure 3.34: Normalized response of the hydrodynamic circulation forces for steps in rotational speed about the x^d-axis, steps 3 and 7.

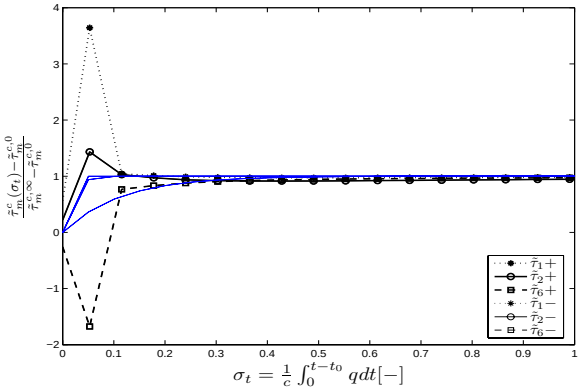

Figure 3.35: Normalized response of the hydrodynamic circulation forces for steps in the angle of attack, from changes in the orientation, steps 4 and 8.

The time constants are dependent on the actual transient causing the change in circulation, and for each dof and each step the time constant in terms of reduced time $\sigma_{dc,ij}$ are approximated as the value fulfilling the equation

$$\tilde{\tau}^c_{d,ij}\left(\tilde{\sigma}^0_{t,j}+\sigma_{dc,ij}\right)=\left(1-e^{-1}\right)\left(\tilde{\tau}^{c,\infty}_{d,ij}-\tilde{\tau}^{c,0}_{d,ij}\right)+\tilde{\tau}^{c,0}_{d,ij}, \tag{3.89}$$

where $\tilde{\sigma}^0_{t,j}$ is the reduced time for step number j and $\tilde{\tau}^c_{ij}(t)$ is the generalized force from circulation about the foil in dof number i at time t after step number j. $\tilde{\tau}^{c,0}_{d,ij}$ and $\tilde{\tau}^{c,\infty}_{d,ij}$ are the generalized force in dof number i from circulation about the foil at the time of the step j and infinitely long time thereafter, respectively.

This formulation is equal to finding the time after the step when the change in force or moment in the actual dof has reached approximately 63% of the final change. The time constants in terms of reduced time found for the simulated steps are collected in the matrix $\tilde{\boldsymbol{\sigma}}_{dc}$, with the values

$$\tilde{\boldsymbol{\sigma}}_{dc}=\begin{bmatrix} 0.070 & 0.108 & 0.125 & 0.001 & 0.093 & 0.077 & 0.125 & 0.001\\ 0.071 & 0.384 & 2.851 & 0.018 & 0.091 & 0.315 & 2.851 & 0.018\\ 0.000 & 0.000 & 0.000 & 0.000 & 0.000 & 0.000 & 0.000 & 0.000\\ 0.000 & 0.000 & 0.091 & 0.000 & 0.000 & 0.000 & 0.091 & 0.000\\ 0.000 & 0.000 & 0.000 & 0.000 & 0.000 & 0.000 & 0.000 & 0.000\\ 0.040 & 0.043 & 5.374 & 0.112 & 0.051 & 0.043 & 5.374 & 0.112 \end{bmatrix}. \tag{3.90}$$

The corresponding average steps in the hydrodynamic forces and moments are collected in the matrix $\tilde{\boldsymbol{\Delta}}^c_d=\left[\tilde{\tau}^{c,\infty}_{d,ij}-\tilde{\tau}^{c,0}_{d,ij}\right]$. This is scaled according to the ratio between the maximum value of the hydrodynamic force coefficient in the y^d-direction found from the wind tunnel experiments and the VLM, respectively. The approximate changes in hydrodynamic forces for an arbitrary trawl door from these steps are then found as

$$\boldsymbol{\Delta}^c_d = \tilde{\boldsymbol{\Delta}}^c_d\frac{C_{2,\max}}{\tilde{C}_{2,\max}} \tag{3.91}$$

$$\boldsymbol{\Delta}^c_d = \begin{bmatrix} 97.05 & 379.90 & 0.0 & 0.0 & 0.0 & 65.14\\ 273.4 & 415.97 & 0.0 & 0.0 & 0.0 & 80.08\\ 1.47 & 0.296 & 5.19 & 21.10 & 1.95 & 0.028\\ 273.49 & 415.97 & 0.0 & 0.0 & 0.0 & 80.08\\ 103.12 & 406.06 & 0.0 & 0.0 & 0.0 & 72.66\\ 221.45 & 445.11 & 0.0 & 0.0 & 0.0 & 88.91\\ 1.473 & 0.296 & 5.19 & 21.10 & 1.95 & 0.028\\ 273.49 & 415.97 & 0.0 & 0.0 & 0.0 & 80.08 \end{bmatrix}^T,$$

where the row i corresponds to the dof i and the column j corresponds to the step j. The values in rows $1-3$ are given in N, and the values in rows $4-6$ are given in Nm.

To calculate the time dependency of the hydrodynamic forces and moments as a linear system, as shown in (3.88), it is necessary to reduce the matrix $\boldsymbol{\sigma}_{dc}$ to a vector. This means that a common time constant for each dof must be found from the time constants

for all eight steps in this dof. It is assumed that the size of the steps are representative for the transients the trawl door experiences during normal operation, and the changes in forces and moments from these steps are therefore used as weights for finding the time constants. The time constants are thus approximated by

$$T^0_{dc,i} = \frac{\sum_{j=1}^{8} \mathbf{\Delta}^c_{d,ij} \boldsymbol{\sigma}_{dc,ij}}{\sum_{j=1}^{8} \mathbf{\Delta}^c_{d,ij}} \frac{c_d}{U_d}, \; i = 1 \ldots 6. \tag{3.92}$$

This gives $T^0_{dc,3} = 0$ and $T^0_{dc,5} = 0$, since the chosen numerical representation can not calculate the dynamic of the forces in these dof. This dynamic is probably not important for the behavior of the trawl doors. To make it possible to treat the dynamics of the hydrodynamic forces in a consistent way, it is however chosen to approximate these coefficients as the smallest time constant of the other dof. This gives the resulting time constants

$$\mathbf{T}_{dc} = \begin{bmatrix} 0.051 & 0.154 & 0.051 & 0.091 & 0.051 & 0.068 \end{bmatrix}^T \frac{c_d}{U_d}. \tag{3.93}$$

These time constants are only valid for trawl doors of similar shapes and aspect ratios, but since these parameters is not varying very much for mid-water trawl doors, no corrections are done in this work.

Forces from angular velocities

Since the forces from angular velocities were not measured during the experiments, these must be estimated by other means. It is assumed that pressure forces are dominant for rotations about the x^d-axis and the z^d-axis, while viscous forces are dominant for rotations about the y^d-axis. The damping moments about the x^d-axis and the z^d-axis are therefore estimated using VLM simulations, while the damping moment about the y^d-axis are estimated using knowledge about the drag of the trawl door at zero angles of attack.

The moments about the x^d-axis and the z^d-axis Based on an integration of Morrisons equation (Faltinsen, 1990) over the trawl door area, the moments about the x^d-axis and the z^d-axis are chosen to be approximated by

$$\tau^v_{d,4} = \frac{1}{2} \rho_w A_d h_d^3 C^\nu_{d,44} \left| p^d_{dw} \right| p^d_{dw}, \tag{3.94}$$

$$\tau^v_{d,6} = \frac{1}{2} \rho_w A_d c_d^3 C^\nu_{d,66} \left| r^d_{dw} \right| r^d_{dw}, \tag{3.95}$$

where the coefficients $C^\nu_{d,44}$ and $C^\nu_{d,66}$ are estimated using VLM simulations. This is only done for angles of attack equal to $20\,^\circ$. This is assumed to be the most representative angle of attack when used in a control system, since the lift force can be both increased and decreased by controlling the angle of attack. $C^\nu_{d,44}$ is estimated by simulating the moment about the x^d-axis as the foil moves through the water with constant angle of attack and various constant angular velocities about the direction of the forward velocity.

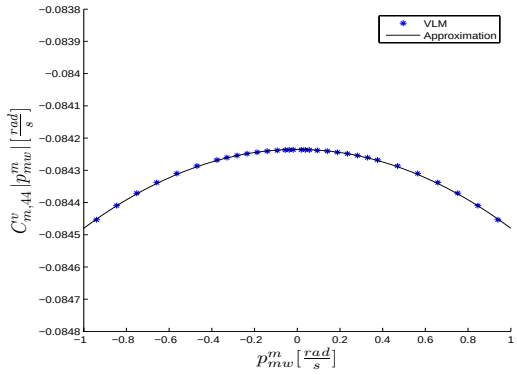

Figure 3.36: Angular damping from angular velocity about the x^d-axis.

The coefficient is found from the solution after the transients have disappeared. The angular velocity about the x^d-axis is found as

$$p^d_{dw} = \cos\left(\psi^{VLM}\right) p^{VLM}_{dw}, \tag{3.96}$$

where ψ^{VLM} and p^{VLM}_{dw} are the angle of attack and angular velocity about the x-axis in the VLM frame. This frame is an inertial right hand coordinate system which coincides with the trawl door frame for zero angles of attack and slip.

$C^\nu_{d,66}$ is estimated by giving r^d_{dw} a fixed value, so that the angle of attack of the foil passes $20\,^\circ$. The coefficient is then estimated from the VLM solution at the instant the angle of attack is $20\,^\circ$. This damping is affected by what happens before the angle of attack reaches $20\,^\circ$, but this is not accounted for in this work.

The VLM solutions are corrected for the higher forces in the experimental data, and the coefficients giving the hydrodynamic forces from angular velocities are approximated as

$$\begin{aligned} C^\nu_{d,44}\left|p^d_{dw}\right| &\approx \tilde{C}^\nu_{d,44}\left|p^d_{dw}\right| \frac{C_{2,\max}}{\tilde{C}_{2,\max}} \\ &\approx -0.084235 - \left(0.0157 p^d_{dw}\right)^2, \end{aligned} \tag{3.97}$$

$$\begin{aligned} C^\nu_{d,66}\left|r^d_{dw}\right| &\approx \tilde{C}^\nu_{d,66}\left|r^d_{dw}\right| \frac{C_{2,\max}}{\tilde{C}_{2,\max}} \\ &\approx -1.04 - 30(r^d_{dw} - 0.18)^8 + 0.08 r^d_{dw}. \end{aligned} \tag{3.98}$$

These approximations are shown in Figures 3.36 and 3.37, along with the corresponding VLM simulations used for investigating the relation between angular velocities and moments about the x^d-and the z^d-axes.

The moment about the y^d-axis As viscous effects are dominant in the damping moment about the y^d-axis, and the VLM is based on potential theory, the VLM can

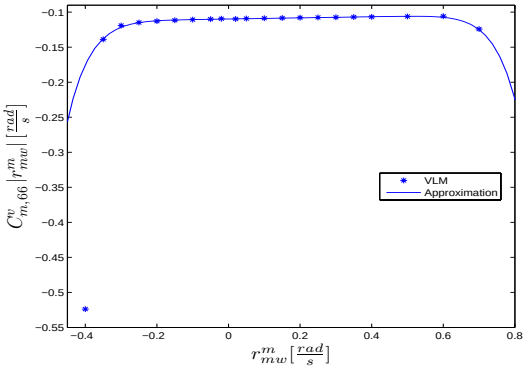

Figure 3.37: Angular damping from angular velocity about the z^d-axis.

not be used for estimating the damping moment about the y^d-axis. To approximate this damping, the drag and shear forces on an area element of the trawl door are assumed to depend only upon the relative velocity in the corresponding direction, and common force coefficients. The forces acting on an area element in local trawl door x^d- and z^d-direction are thus described by

$$df_x = -\frac{1}{2}\rho_w C_x \left(v^d_{dw,1} + q^d_{dw} z^d\right) \left|v^d_{dw,1} + q^d_{dw} z^d\right| dA, \tag{3.99}$$

$$df_z = -\frac{1}{2}\rho_w C_z \left(v^d_{dw,3} - q^d_{dw} x^d\right) \left|v^d_{dw,3} - q^d_{dw} x^d\right| dA, \tag{3.100}$$

where $C_x = C^{\infty}_{d\Upsilon,1}\big|_{\alpha^d=0,\beta^d=0}$ and $C_z = C^{\infty}_{d\Upsilon,3}\Big|_{\alpha^d=0,\beta^d=\frac{\pi}{2}}$. The moment about the y^d-axis of the trawl door may then be approximated as the sum of the moment from the shear forces and the drag forces:

$$m_y = \int_{A_d} \left(df_x z^d - df_z x^d\right). \tag{3.101}$$

Large linear velocities The case of large linear velocities compared to the angular velocities is first considered. If the relative velocities in the x^d-direction are positive for all area elements:

$$\begin{aligned} &v^d_{dw,1} + q^d_{dw} z^d > 0 \text{ for } -\frac{h_d}{2} < z^d < \frac{h_d}{2}, \\ &\implies v^d_{dw,1} > \left|q^d_{dw}\right| \frac{h_d}{2}. \end{aligned} \tag{3.102}$$

If the relative velocities in the x^d direction are negative for all area elements:

$$\begin{aligned} &v^d_{dw,1} + q^d_{dw} z^d < 0 \text{ for } -\frac{h_d}{2} < z^d < \frac{h_d}{2}, \\ &\implies v^d_{dw,1} < -\left|q^d_{dw}\right| \frac{h_d}{2}. \end{aligned} \tag{3.103}$$

If (3.102) or (3.103) is fulfilled and the trawl door is rectangular, the moment on the trawl door from the hydrodynamic forces along the x^d-axis can be approximated as

$$m_{yx}^H = \pm\frac{1}{12}\rho_w A_d h_d^2 C_x v_{dw,1}^d q_{dw}^d. \tag{3.104}$$

In the equation (3.104) the upper sign is to be used if (3.102) is fulfilled, and the lower sign is to be used if (3.103) is fulfilled.

The moment on the trawl door from the hydrodynamic forces along the z^d-axis can be estimated in the same manner. If the relative velocities in the z^d-direction are positive for all area elements:

$$\begin{aligned} &v_{dw,3}^d + q_{dw}^d x^d > 0 \text{ for } -\frac{c_d}{2} < x^d < \frac{c_d}{2}, \\ &\implies v_{dw,3}^d > \left|q_{dw}^d\right| \frac{c_d}{2}, \end{aligned} \tag{3.105}$$

where c_d is the chord length of the trawl door. If the relative velocities in the z^d-direction are negative for all area elements:

$$\begin{aligned} &v_{dw,3}^d + q_{dw}^d x^d < 0 \text{ for } -\frac{c_d}{2} < x^d < \frac{c_d}{2}, \\ &\implies v_{dw,3}^d < -\left|q_{dw}^d\right| \frac{c_d}{2}. \end{aligned} \tag{3.106}$$

If (3.105) or (3.106) is fulfilled, the moment on the trawl door from the hydrodynamic forces along the z^d-axis can be approximated as

$$m_{yz}^H = \pm\frac{1}{12}\rho_w A_d c_d^2 C_z v_{dw,3}^d q_{dw}^d. \tag{3.107}$$

In the equation (3.107) the upper sign is to be used if 3.105 is fulfilled, and the lower sign is to be used if (3.106) is fulfilled. The resulting damping moment about the y^d-axis for high speeds of the trawl door in relation to the angular velocity about the y^d-axis can then be found by

$$m_y^H = -\frac{1}{12}\rho_w A_d \left(h_d^2 C_x \left|v_{dw,1}^d\right| + c_d^2 C_z \left|v_{dw,3}^d\right|\right) q_{dw}^d. \tag{3.108}$$

Low linear velocities For low linear velocities or large angular velocity about the y^d-axis, this does not give satisfying results. If

$$\left|v_{dw,1}^d\right| \ll \left|q_{dw}^d\right| \frac{h_d}{2} \quad \wedge \quad \left|v_{dw,3}^d\right| \ll \left|q_{dw}^d\right| \frac{c_d}{2}, \tag{3.109}$$

the damping moments about y^d-axis may be estimated as

$$dm_y^L = -\frac{1}{2}\rho_w C_x q_{dw}^d \left|q_{dw}^d\right| \left(z^d\right)^2 \left|z^d\right| dA + \frac{1}{2}\rho_w C_z q_{dw}^d \left|q_{dw}^d\right| \left(x^d\right)^2 \left|x^d\right| dA, \tag{3.110}$$

$$\begin{aligned} m_y^L &= -\rho_w q_{dw}^d \left|q_{dw}^d\right| \left(C_x c_d \int_0^{\frac{h_d}{2}} \left(z^d\right)^3 dz^d + C_z h_d \int_0^{\frac{c_d}{2}} \left(x^d\right)^3 dx^d\right) \\ &= -\frac{1}{64}\rho_w A_d q_{dw}^d \left|q_{dw}^d\right| \left(h_d^3 C_x + c_d^3 C_z\right). \end{aligned} \tag{3.111}$$

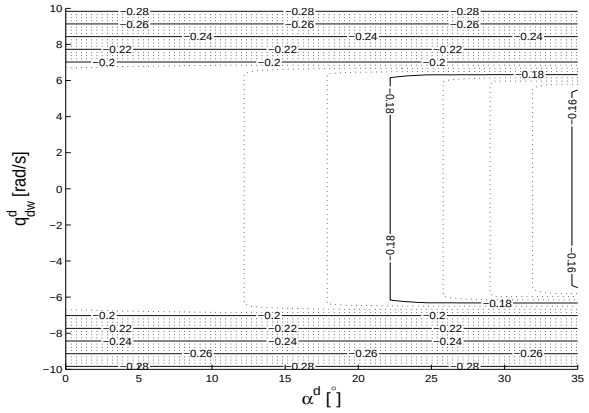

Figure 3.38: Coefficient of damping moment about the y^d-axis for various angles of attack, for $\beta^d = 0°$.

Resulting damping moment about the y^d-axis The damping moment about the y^d-axis is proposed calculated according to the speed region giving the most damping:

$$\tau^{\nu}_{d,5} = \frac{1}{12}\rho_w A_d C^{\nu}_{d,55} q^d_{dw} \ , \tag{3.112}$$

where

$$C^{\nu}_{d,55} = \min\left(C^{\nu L}_{d,55}, C^{\nu H}_{d,55}\right), \tag{3.113}$$

$$C^{\nu L}_{d,55} = -\frac{3}{16}\left|q^d_{dw}\right|\left(h_d^3 C_x + c_d^3 C_z\right), \tag{3.114}$$

$$C^{\nu H}_{d,55} = -h_d^2 C_x \left|v^d_{dw,1}\right| - c_d^2 C_z \left|v^d_{dw,3}\right|. \tag{3.115}$$

For this trawl door, C_z is not measured, but due to how the trawl doors are designed to reduce C_x, it is assumed that $C_z = 2C_x$. The values $C_x = 0.11$ and $C_z = 0.22$ are therefore proposed. The resulting coefficient $C^{\nu}_{d,55}$ is shown in Figure 3.38 and 3.39 for various orientations. In Figure 3.38 the angle of slip is held constant $\beta^d = 0\,°$, and in Figure 3.39 the angle of attack is held constant $\alpha^d = 30\,°$.

Forces from acceleration of the foil in relation to the fluid

The forces and moments from acceleration of the foil in relation to the fluid are in each dof assumed to be dependent on only the acceleration in the same dof, and are for the dof $i = 2, 4, 6$ expressed as

$$\tau^a_{22} = \frac{1}{2}\rho_w A_d^{\frac{3}{2}} C^a_{d,22} \dot{v}^d_{dw,2}, \tag{3.116}$$

$$\tau^a_{44} = \frac{1}{2}\rho_w A_d^{\frac{3}{2}} h_d^2 C^a_{d,44} \dot{p}^d_{dw}, \tag{3.117}$$

$$\tau^a_{66} = \frac{1}{2}\rho_w A_d^{\frac{3}{2}} c_d^2 C^a_{d,66} \dot{r}^d_{dw}. \tag{3.118}$$

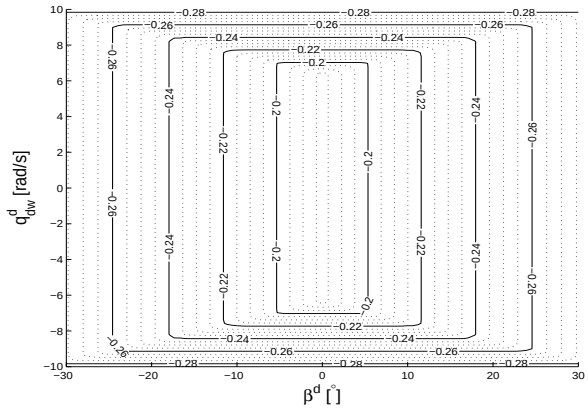

Figure 3.39: Coefficient of damping moment about the y^d-axis for various angles of slip, for $\alpha^d = 20°$.

These forces are estimated using VLM simulations. After a steady state is established, the foil is given a constant acceleration. The acceleration dependent forces are then interpreted as the forces from the time derivative of the velocity potential in the beginning of the acceleration. This is done for various steady states (in terms of angle of attack and forward speed) and for various accelerations. It is found that the dependence on forward speed is negligible, while there is a very small dependence on the size of the acceleration and more dependence on the angle of attack.

As an example, the VLM time series for accelerations along the y^d-axis is shown in Figure 3.40. Each line represents a different combination of forward speed, acceleration and angle of attack. The asterisks (*) marks the values used for further calculations. These are plotted in Figure 3.41 as a function of angle of attack.

The coefficients in equations (3.116) - (3.118) are estimated from the VLM solutions. The coefficients are approximated as

$$C^a_{d,22} = -1.1 + 0.5\left(\alpha^d\right)^2, \tag{3.119}$$

$$C^a_{d,44} = -0.0581 - 0.0013\alpha^d, \tag{3.120}$$

$$C^a_{d,66} = -0.039 - 0.005\alpha^d. \tag{3.121}$$

The calculations and approximations of these coefficients are shown in Figures 3.41 - 3.43.

Verification of the model of the acceleration dependent forces To verify the model of the acceleration dependent forces, it is compared to the results from strip theory. It should be noted that using strip theory for these aspect ratios is highly questionable, as 3D effects are bound to be important. This is especially true for the rotations, since these inertia terms are much affected by the forces around the edges of the trawl door. Disregarding the effects of forward velocity, curvature and angles of attack and slip, strip theory can for the present case only provide coarse approximations of the acceleration dependent forces.

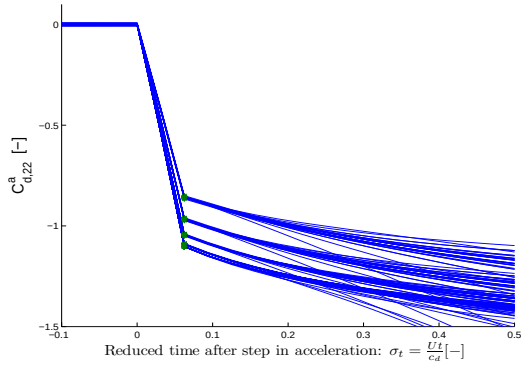

Figure 3.40: Force from accelerations along the trawl door y^d-axis, time series from the VLM.

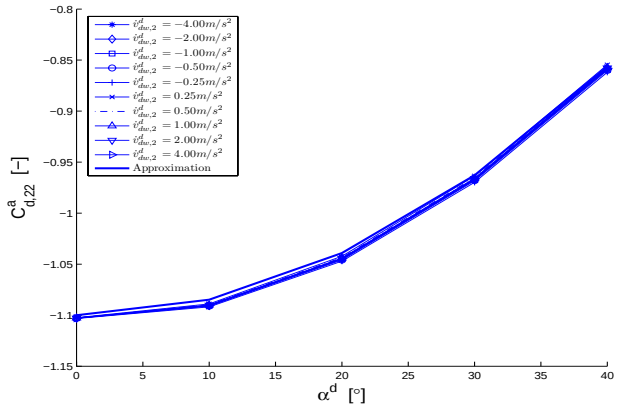

Figure 3.41: Force from accelerations along the trawl door y^d-axis.

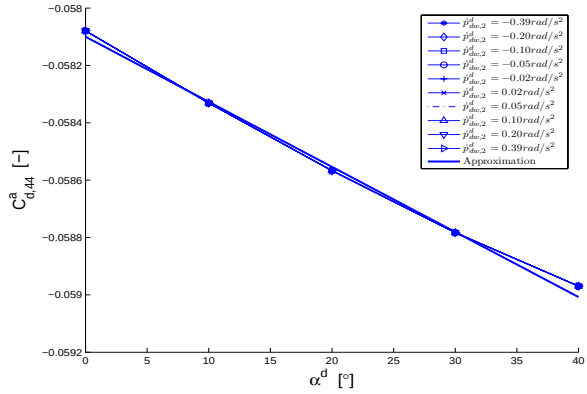

Figure 3.42: Moment from angular accelerations about the trawl door x^d-axis.

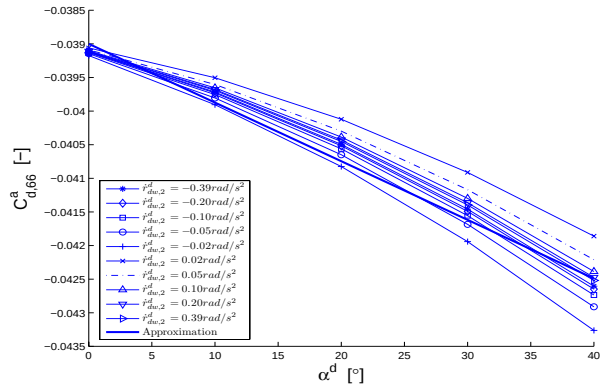

Figure 3.43: Moment from angular accelerations about the trawl door z^d-axis.

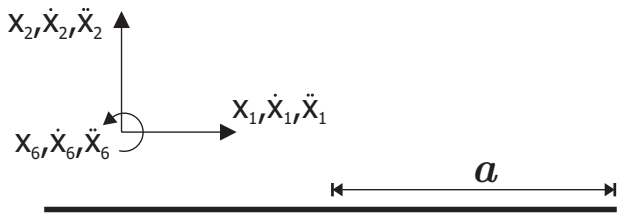

Figure 3.44: The coordinate system of the 2D body for added mass calculations by Newman.

If the effect of viscosity is neglected, the acceleration dependent forces on a two dimensional flat plate segment can be calculated from

$$df_1 = 0, \tag{3.122}$$
$$df_2 = \pi\rho_w a^2 \ddot{x}_2, \tag{3.123}$$
$$df_6 = \frac{1}{8}\pi\rho_w a^4 \ddot{x}_6, \tag{3.124}$$

where a is half the segment length, and the coordinate system is illustrated in Figure 3.44 (Newman, 1977).

The hydrodynamic forces on the trawl door from accelerations in the y^d-direction are approximated as those on a flat plate at rest. The ratio between the correct and the strip theory solution for the acceleration dependent forces on a flat plate, normal to the plate, is 0.579 and 0.7568 in the case of an aspect ratio of 1.0 and 2.0, respectively (Sarpkaya and Isaacson, 1981). The aspect ratio of the flat plate is for the present case set to 1.45, which is that of the trawl door. Using linear interpolation with regard to aspect ratio, the forces are estimated as

$$\begin{aligned}\hat{\tau}^a_{22} &= -\left(0.579 + \frac{0.7568 - 0.579}{2.0 - 1.0}\left(1.45 - 1.0\right)\right)\frac{\pi}{4}\rho_w h_d c_d^2 \dot{v}^d_{dw,2} \\ &= -0.659\,01\frac{\pi}{4}\rho_w h_d c_d^2 \dot{v}^d_{dw,2}.\end{aligned} \tag{3.125}$$

For the other two degrees of freedom, strip theory yields

$$\begin{aligned}\hat{\tau}^a_{44} &= -\int_{-\frac{h_d}{2}}^{\frac{h_d}{2}} \pi\rho_w \left(\frac{c_d}{2}\right)^2 \dot{p}^d_{dw} z^2 dz \\ &= -\frac{\pi}{4}\rho_w c_d^2 \dot{p}^d_{dw} \int_{-\frac{h_d}{2}}^{\frac{h_d}{2}} z^2 dz \\ &= -\frac{\pi}{48}\rho_w c_d^2 h_d^3 \dot{p}^d_{dw}.\end{aligned} \tag{3.126}$$

$$\begin{aligned}\hat{\tau}^a_{66} &= -\int_{-\frac{h_d}{2}}^{\frac{h_d}{2}} \frac{1}{8}\pi\rho_w \left(\frac{c_d}{2}\right)^4 \dot{r}^d_{dw} dz \\ &= -\frac{1}{8}\pi\rho_w \left(\frac{c_d}{2}\right)^4 \dot{r}^d_{dw} \int_{-\frac{h_d}{2}}^{\frac{h_d}{2}} dz \\ &= -\frac{1}{128}\pi\rho_w c_d^4 h_d \dot{r}^d_{dw}. \end{aligned} \tag{3.127}$$

The ratios between the strip theory solutions for a flat plate at zero speed and the VLM solutions for a trawl door at an angle of attack and a forward speed are:

$$\begin{aligned}\frac{\tau^a_{22}}{\hat{\tau}^a_{22}} &= \frac{\frac{1}{2}\rho_w A_d^{\frac{3}{2}} C^a_{d,22} \dot{v}^d_{dw,2}}{-0.66\frac{\pi}{4}\rho_w h_d c_d^2 \dot{v}^d_{dw,2}}, \\ &= -\frac{2}{0.66\pi}\sqrt{\mathbb{AR}} C^a_{d,22}. \end{aligned} \tag{3.128}$$

$$\begin{aligned}\frac{\tau^a_{44}}{\hat{\tau}^a_{44}} &= \frac{\frac{1}{2}\rho_w A_d^{\frac{3}{2}} h_d^2 C^a_{d,44} \dot{p}^d_{dw}}{-\frac{\pi}{48}\rho_w c_d^2 h_d^3 \dot{p}^d_{dw}} \\ &= -\frac{24}{\pi}\sqrt{\mathbb{AR}} C^a_{d,44} \end{aligned} \tag{3.129}$$

$$\begin{aligned}\frac{\tau^a_{66}}{\hat{\tau}^a_{66}} &= \frac{\frac{1}{2}\rho_w A_d^{\frac{3}{2}} (c_d)^2 C^a_{d,66} \dot{r}^d_{dw}}{-\frac{1}{128}\pi\rho_w c_d^4 h_d \dot{r}^d_{dw}} \\ &= -\frac{64}{\pi}\sqrt{\mathbb{AR}} C^a_{d,66} \end{aligned} \tag{3.130}$$

In these formulas, the aspect ratio $\mathbb{AR} = 1.45$ is inserted for the ratio between trawl door span, h_d, and chord, c_d. The hydrodynamic coefficients for zero angle of attack, $C^a_{d,22} = -1.1$, $C^a_{d,44} = -0.0581$ and $C^a_{d,66} = -0.039$, are used. The ratios between the two solutions are found to be $\frac{\tau^a_{22}}{\hat{\tau}^a_{22}} = 1.3$, $\frac{\tau^a_{44}}{\hat{\tau}^a_{44}} = 0.53$ and $\frac{\tau^a_{66}}{\hat{\tau}^a_{66}} = 0.96$. It seems plausible that the acceleration dependent hydrodynamic forces on the trawl door, as calculated from the VLM method are close to the correct values. The difference between the VLM and the strip theory values may arise from the effects of forward speed and curvature of the trawl door, as well as the corrections on the 3D effects.

3.3.5 The resulting model

As long as the trawl door is not too far from its intended range of operation, and the hydrodynamic properties are not too different from the model used in the wind tunnel experiments, the hydrodynamic forces and moments acting on it may be approximated as stated in the present work. This may be implemented into a state space model, so

that the instantaneous hydrodynamic forces developed by an arbitrary mid-water trawl door is approximated as

$$\boldsymbol{\tau}_{d\Upsilon}^{d} = \boldsymbol{\tau}_{d}^{c} + \boldsymbol{\tau}_{d}^{\nu} + \boldsymbol{\tau}_{d}^{a}, \tag{3.131}$$

$$\dot{\boldsymbol{\tau}}_{d}^{c} = diag(\mathbf{T}_{dc})^{-1} \left(\boldsymbol{\tau}_{d}^{c} - \bar{\boldsymbol{\tau}}_{d\Upsilon}^{d,\infty} \right). \tag{3.132}$$

In order to summarize, the following calculation procedure is proposed.

1. Calculate α^d and β^d from (3.8) and (3.9).
2. Calculate $\bar{\mathbf{C}}_{d\Upsilon}^{\infty}\left(\alpha^d, \beta^d\right)$ from (3.72), using $\bar{\mathbf{C}}_{m\Upsilon}^{\infty}\left(\alpha^m, \beta^m\right)$ found from (3.71).
3. Calculate $r\left(\alpha^d, \beta^d\right)$ from (3.77).
4. Find $\bar{\boldsymbol{\tau}}_{d\Upsilon}^{d,\infty}$ from (3.78) - (3.81), using the values of $\boldsymbol{\xi}_{\infty}$ found from (3.76).
5. Find $\dot{\boldsymbol{\tau}}_{d}^{c}$ and $\boldsymbol{\tau}_{d}^{c}$ from (3.132).
6. Find $\tau_{d,4}^{v}$ from (3.97) inserted into (3.94).
   Find $\tau_{d,6}^{v}$ from (3.98) inserted into (3.95).
   Find $\tau_{d,5}^{v}$ from (3.112) - (3.115).
7. Find $\boldsymbol{\tau}_{d}^{a}$ from (3.119) - (3.121) inserted into (3.116) - (3.118).

3.4 The trawl system process plant model

A sufficient accurate process plant model of the trawl system is needed to be able to configure and analyze possible control system strategies and to optimize the trawl door control concept. While only small changes in the hydrodynamic forces and moments on the trawl door could be greatly magnified by its impact on the trawl door orientation angles and movements, the hydrodynamic forces acting on the net, the warps and the bridles vary more slowly with the shape of the trawl system. The needed level of detail and accuracy for these parts are therefore less than for the trawl doors.

As long as the warps are relatively long, they act as a damped spring with low stiffness and high damping. The wave frequency movements of the trawl vessel do probably in such cases influence the trawl system only to a minor extent, and the accuracy of the vessel model is of little consequence.

Modeling of the hydrodynamic forces on net panels are treated in for example Løland (1991), for aquaculture applications. For trawl applications, especially pelagic trawls, the solidity of the net is generally far smaller than for what is usually treated in the literature. For this reason, as well as for computational efficiency and simplicity, the net is in this work modeled as interconnected cable elements.

3.4.1 The trawl door process plant model

The trawl door equation of motion

The dynamics of the trawl door may be described as

$$\dot{\mathbf{x}}_1 = \mathbf{R}_d^n \mathbf{x}_3, \tag{3.133}$$

$$\dot{\mathbf{x}}_2 = \mathbf{T}_{\boldsymbol{\Theta}}(\mathbf{x}_2)\,\mathbf{x}_4, \tag{3.134}$$

$$\begin{bmatrix} \dot{\mathbf{x}}_3 \\ \dot{\mathbf{x}}_4 \end{bmatrix} = \left(\mathbf{M}_d^{RB}\right)^{-1}\left(\boldsymbol{\tau}_{dw}^d + \boldsymbol{\tau}_{db_u}^d + \boldsymbol{\tau}_{db_l}^d + \boldsymbol{\tau}_{d\Upsilon}^d + \boldsymbol{\tau}_{d\varrho}^d\right), \tag{3.135}$$

where the states are designated

$$\begin{aligned} \mathbf{x} &= \begin{bmatrix} \mathbf{x}_1^T & \mathbf{x}_2^T & \mathbf{x}_3^T & \mathbf{x}_4^T \end{bmatrix}^T, \\ \mathbf{x}_1 &= \begin{bmatrix} x_{dn}^n & y_{dn}^n & z_{dn}^n \end{bmatrix}^T, \\ \mathbf{x}_2 &= \begin{bmatrix} \varphi & \theta & \psi \end{bmatrix}^T, \\ \mathbf{x}_3 &= \begin{bmatrix} u_{dn}^d & v_{dn}^d & w_{dn}^d \end{bmatrix}^T, \\ \mathbf{x}_4 &= \begin{bmatrix} p_{dn}^d & q_{dn}^d & r_{dn}^d \end{bmatrix}^T, \end{aligned}$$

and $\mathbf{M}_d^{RB} \in \mathbb{R}^{6\times 6}$ is the rigid body mass matrix of the trawl door. $\boldsymbol{\tau}_{dw}^d$, $\boldsymbol{\tau}_{db_u}^d$ and $\boldsymbol{\tau}_{db_l}^d$ are the generalized forces from the warp and the bridles, and $\boldsymbol{\tau}_{d\varrho}^d$ is the sum of the generalized gravity and buoyancy forces. $\boldsymbol{\tau}_{d\Upsilon}^d$is the generalized hydrodynamic force vector, approximated by (3.131). The Coriolis force terms are neglected due to the low speeds and the small masses of the system.

The trawl door rigid body mass matrix

According to Fossen (2002) the rigid body mass matrix can be found from

$$\mathbf{M}_d^{RB} = \begin{bmatrix} m_d\mathbf{I}_{3\times 3} & -m_d\mathbf{S}\left(\mathbf{p}_{G_d d}^d\right) \\ m_d\mathbf{S}\left(\mathbf{p}_{Gd}^d\right) & \mathbf{I}_d \end{bmatrix}, \tag{3.136}$$

where $\mathbf{I}_{3\times 3}$ is the identity matrix, m_d is the mass of the trawl door, $\mathbf{p}_{G_d d}^d$ is the center of gravity, decomposed in the trawl door frame, and $\mathbf{I}_d \in \mathbb{R}^{3x3}$ is the inertia matrix about the origin of the trawl door frame. The cross product matrix is defined as

$$\mathbf{S}(\boldsymbol{\lambda}) = \begin{bmatrix} 0 & -\lambda_3 & \lambda_2 \\ \lambda_3 & 0 & -\lambda_1 \\ -\lambda_2 & \lambda_1 & 0 \end{bmatrix}, \tag{3.137}$$

$$\boldsymbol{\lambda} = \begin{bmatrix} \lambda_1 \\ \lambda_2 \\ \lambda_3 \end{bmatrix}. \tag{3.138}$$

The elements of the inertia matrix are designated

$$\mathbf{I}_d = \begin{bmatrix} I_x & -I_{xy} & -I_{xz} \\ -I_{yx} & I_y & -I_{yz} \\ -I_{zx} & -I_{zy} & I_z \end{bmatrix}, \tag{3.139}$$

and the matrix can be found from

$$\begin{aligned}\mathbf{I}_d &= \mathbf{I}_{G_d} - m_d \mathbf{S}^2\left(\mathbf{p}^d_{G_d d}\right) \\ &= \mathbf{I}_{G_d} - m_d\left(\mathbf{p}^d_{G_d d}\left(\mathbf{p}^d_{G_d d}\right)^T - \left(\mathbf{p}^d_{G_d d}\right)^T \mathbf{p}^d_{G_d d}\mathbf{I}_{3\times 3}\right),\end{aligned} \tag{3.140}$$

where $\mathbf{I}_{G_d}$ is the inertia matrix about the center of gravity. Neglecting cross coupling terms, this can be found from

$$\mathbf{I}_{G_d} \approx \begin{bmatrix} I_{G_d,11} & 0 & 0 \\ 0 & I_{G_d,22} & 0 \\ 0 & 0 & I_{G_d,33} \end{bmatrix}, \tag{3.141}$$

where

$$\begin{aligned} I_{G_d,11} &= \frac{1}{12}\frac{m_d}{2}\left(\left(h_d - 2z^d_{G_d d}\right)^2 + \left(h_d + 2z^d_{G_d d}\right)^2\right) \\ &= \frac{1}{12}h_d^2 m_d + \frac{1}{3}m_d\left(z^d_{G_d d}\right)^2, \end{aligned} \tag{3.142}$$

$$\begin{aligned} I_{G_d,22} &= \frac{1}{12}h_d^2 m_d + \frac{1}{3}m_d\left(z^d_{G_d d}\right)^2 + \frac{1}{12}c_d^2 m_d + \frac{1}{3}m_d\left(x^d_{G_d d}\right)^2 \\ &= \frac{m_d}{12}\left(c_d^2 + h_d^2 + 4\left(x^d_{G_d d}\right)^2 + 4\left(z^d_{G_d d}\right)^2\right), \end{aligned} \tag{3.143}$$

$$\begin{aligned} I_{G_d,33} &= \frac{1}{12}\frac{m_d}{2}\left(\left(c_d - 2x^d_{G_d d}\right)^2 + \left(c_d + 2x^d_{G_d d}\right)^2\right) \\ &= \frac{1}{12}c_d^2 m_d + \frac{1}{3}m_d\left(x^d_{G_d d}\right)^2. \end{aligned} \tag{3.144}$$

The following properties are derived from measurements on the model

$$m_d = 28kg\left(\frac{A_d}{A_m}\right)^{\frac{3}{2}}, \tag{3.145}$$

$$\mathbf{p}^d_{G_d d} = \begin{bmatrix} 0.003 & -0.053 & 0.11 \end{bmatrix}^T \left(\frac{A_d}{A_m}\right)^{\frac{1}{2}}, \tag{3.146}$$

where A_m is the area of the trawl door model.

Forces and moments from external lines (the warp and the bridles)

The forces in the endpoints of the warp and the bridles are calculated by a dynamic cable model. The forces and properties of the cable are distributed amongst some representative nodes, and the forces acting on the endpoints are taken to act on the fastening points. The generalized force from each line is calculated as (exemplified by the warp force)

$$\tau^d_{dw} = \begin{bmatrix} \mathbf{R}^d_n \mathbf{f}^n_{dw} \\ \mathbf{p}^d_{W^d d} \times \left(\mathbf{R}^d_n \mathbf{f}^n_{dw}\right) \end{bmatrix} \tag{3.147}$$

where $\mathbf{f}_{dw}^n$ is the force from the warp on the trawl door, decomposed in the global frame. The forces from the other external lines are found in a similar manner. From measurements on the trawl door model, the following original fastening points are established:

$$\mathbf{p}_{wd}^d = \begin{bmatrix} 0.155 & -0.05 & -0.07 \end{bmatrix}^T \sqrt{\frac{A_d}{A_m}}, \tag{3.148}$$

$$\mathbf{p}_{b_l d}^d = \begin{bmatrix} -0.111 & -0.094 & 0.367 \end{bmatrix}^T \sqrt{\frac{A_d}{A_m}}, \tag{3.149}$$

$$\mathbf{p}_{b_u d}^d = \begin{bmatrix} -0.074 & 0.097 & -0.463 \end{bmatrix}^T \sqrt{\frac{A_d}{A_m}}, \tag{3.150}$$

where w, b_l and b_u designates warp, lower bridle and upper bridle, respectively.

Forces and moments from buoyancy and gravity

If the trawl door is made of materials of homogeneous density with no cavities capable of trapping air during submergence, the buoyancy and gravity force attack in the same point. The sum of these forces are calculated as

$$\begin{aligned} \vec{f}_{d\varrho} &= \vec{f}_{dg}^d + \vec{f}_{db}^d \\ &= m_d \vec{g} - \rho_w V_d \vec{g} \\ &= m_d \frac{\rho_d - \rho_w}{\rho_d} \vec{g}, \end{aligned} \tag{3.151}$$

where $\vec{g}$ is the gravity vector, V_d and ρ_d is the volume and density of the materials in the trawl door, respectively. This gives

$$\boldsymbol{\tau}_{d\varrho}^d = m_d \frac{\rho_d - \rho_w}{\rho_d} \begin{bmatrix} \mathbf{g}^d \\ \mathbf{p}_{G_d d}^d \times \mathbf{g}^d \end{bmatrix}, \tag{3.152}$$

where $\boldsymbol{\tau}_{d\varrho}^d$ is the generalized forces on the trawl door from buoyancy and gravity.

3.4.2 The warps, the bridles and the trawl net

The warps, the bridles and the meshes of the trawl net are treated as interconnected cables. The behavior of these cables are governed by the internal and external forces acting on them. In relation to their bending stiffness, these cables are relatively long and tensioned. Therefore, their bending stiffness is not significant for their behavior, and this is ignored. For numerical simulations, these cables are modeled as a series of nodes connected by nonlinear damped springs. The mass and hydrodynamic forces acting on the cable are distributed amongst the nodes.

A regular trawl consists of a large number of meshes. Trying to model each of these meshes would yield unrealistic computational effort. The trawl net is therefore modeled using far fewer meshes. The front parts of a mid-water trawl net are of such a low solidity that the net with respect to hydrodynamic forces can be regarded as individual cables with little or no influence from the rest of the trawl net. This gradually changes for the

parts further aft, and at the cod end the influence from the rest of the net is substantial. To approximate these effects, single cables are used to mimic the effect of several meshes in the front parts, while the drag and mass of a sphere are added aftmost to simulate the effect of the cod end. The overall dimensions of the trawl are kept close to those of a real trawl, and the thickness of the lines are adjusted to give the amount of drag predicted from experiments.

The procedure for calculating the forces acting on each cable element is described in the following.

Hydrodynamic forces on cables

Ersdal (2004) shows that the cross flow principle is inaccurate for cables in near axial flow and proposes a more accurate method. This method forms the basis for calculating the normal hydrodynamic forces on the cable members of the trawl net, while the normal hydrodynamic forces on the warps and the bridles are calculated according to the cross flow principle. A unifying model may provide improved accuracy, but in order to save computational effort, this is not implemented. In the following, only the calculation of the hydrodynamic forces on the trawl net is described, as the cross flow principle is decribed in several textbooks.

Hydrodynamic tangential forces The cross section area of a cable, A_c, is approximated by

$$A_c = \frac{\pi}{4} d_c^2, \tag{3.153}$$

where d_c is the cable diameter. The *hydrodynamic length* of each element is introduced, calculated as

$$l_h = k l_e + (1 - k)\, l_0, \tag{3.154}$$

where l_e is the actual distance between the end nodes of the element, l_0 is the unstretched length of the element and k is an interpolation factor between 0 and 1. The hydrodynamic velocity of each element, $\vec{v}_{ew}$, is set aequal to the average of the velocities of the two end nodes in relation to the ambient water. The tangential velocity of each element is found as

$$\vec{v}_t = \frac{\vec{l}_e \cdot \vec{v}_{ew}}{l_e^2} \vec{l}_e, \tag{3.155}$$

where $\vec{l}_e$ is the vector between the two end nodes of the element. The hydrodynamic tangential force on an element is calculated as

$$\vec{f}_{v_t} = -\frac{1}{2} \rho_w C_t d_c l_h v_{ew}^2 \frac{\vec{v}_t}{v_t}, \tag{3.156}$$

where the tangential friction coefficient C_t is found as

$$C_t = \pi C_F, \tag{3.157}$$

where C_F is the averaged friction force coefficient. C_F is calculated in Ackroyd (1982) as a function of the Reynolds numbers based on length and radius of the cable. These

Part	**Length**	**Diameter**	$R_{n,L}$	$R_{n,a}$	ε	$\frac{L}{\varepsilon}$
Warp	1600 m	0.03 m	2.3×10^6	21	0.003	5.3×10^5
Warp	300 m	0.03 m	4.3×10^5	21	0.003	1.0×10^5
Bridle	300 m	0.02 m	4.3×10^5	15	0.002	1.5×10^5

Table 3.3: The Reynolds numbers of some typical trawl system components.

are found as

$$R_{n,L} = \frac{Ul_c}{\nu}, \tag{3.158}$$

$$R_{n,a} = \frac{Ua}{\nu}, \tag{3.159}$$

where l_c is the length of the cable and a is the radius of the cable. $R_{n,L}$ will for the warps depend upon how the trawl is operated. It is also not obvious which lengths to use in the calculation of the Reynolds number for other parts of the trawl system, as it consists of many interconnected cables. This problem is for the trawl net alleviated by scaling the drag of the trawl net with respect to model experiments. The value of C_F will therefore affect the modeling of the trawl net only to a minor degree.

In Table 3.3 the Reynolds numbers for some typical trawl system components are calculated for a speed of $U = 2\,\text{m/s}$ and a dynamic viscosity of water at 10°, $\nu = 1.4 \times 10^{-3}\,\text{Ns/m}^2$. From a plot in Ackroyd (1982), it is seen that the variation of the resulting friction coefficients are small, and a common value of $C_F = 0.03$ seems to be representative for the elements in this table. This does not include the effects of roughness, which will probably increase the friction. White (1994) describes the relation between $R_{n,L}$, roughness and drag coefficient for a flat plate. Assuming the roughness of stranded wires to be approximately 10 % of the diameter, the values found for $\frac{l_c}{\varepsilon}$ is shown in Table 3.3. According to White (1994), these values would give no significant increase in the drag of a flat plate. Therefore, the effect of roughness is assumed negligible also for the warps and the bridles, and the value $C_F = 0.03$ will be used for the model.

Hydrodynamic normal forces The normal velocity of each cable element is found as

$$\vec{v}_n = \vec{v}_{ew} - \vec{v}_t. \tag{3.160}$$

The hydrodynamic normal force on each element is assumed to be of the form

$$\vec{f}_{v_n} = -\frac{1}{2}\rho_w C_n d_c l_h v_{ew}^2 \frac{\vec{v}_n}{v_n}, \tag{3.161}$$

where the normal pressure coefficient is found as

$$C_n = C_{n1} \sin(\alpha) + C_{n2} \sin^2(\alpha). \tag{3.162}$$

The term $\sin(\alpha)$ may be calculated as

$$\sin(\alpha) = \frac{v_n}{v_{ew}}, \tag{3.163}$$

and Ersdal (2004) has in experiments estimated these coefficients to $C_{n1} = 0.07$ and $C_{n2} = 1.3$.

Hydrodynamic forces from acceleration in relation to the water These forces are implemented as a constant additional mass term. This added mass is for each cable element found as

$$m^a = C_m A_c l_e \rho_w, \tag{3.164}$$

where C_m is the added mass coefficient. It is assumed that the water frame is not accelerated in relation to the global frame. The hydrodynamic forces from acceleration of the element in relation to the global frame can then be approximated as

$$\vec{f}^a = -C_m A_c l_e \rho_w \dot{\vec{v}}_{en}, \tag{3.165}$$

where $\dot{\vec{v}}_{en}$ is the average acceleration of the element ends in relation to the n-frame, and the added mass coefficient is set to $C_m = 0.8$, as proposed by Ersdal (2004).

Structural forces in cable elements

Element stiffness and damping forces The flexibility of a straight cable is mainly due to stretching of its filaments and radial compression. The flexibility of a curved cable, on the other hand, mainly originates in the interaction between the normal forces acting on the cable and the curvature of the cable. The relative importance of these effects varies with the amount of tension in the cable, the amount of normal forces and the length of the cable. For the present application, the normal forces consist mostly of hydrodynamic forces and gravity forces. When the tension increases, the flexibility due to radial compression and stretching of the filaments becomes more significant. Therefore, the relation between tension and elongation of such a cable varies with tension, specific weight, diameter and relative velocity of the cable. Assuming that some normal forces are acting on the element and that the element bending stiffness is low compared to its length, the contracting force are larger than zero even when the distance between the ends of the element is significant shorter than the unstretched length of the element.

The warps are usually characterized by their long length, their angle towards the relative water velocity and their weight. This makes them dominated by the geometrical flexibility. For a correctly designed trawl net, most elements are approximately straight, adding little geometrical flexibility. The relation between the tension and the elongation may then be assumed to be linear (Milgram et al., 1988). For simulation purposes, however, the relation for less tension is needed, especially during transient behavior.

For accurate modeling of curved cables under influence of dynamic tangential and normal forces, the cables are traditionally divided into very small elements. Because of computational efficiency, however, it is desirable to make these elements as large as possible. In this work, increased accuracy of the mathematical modeling of large elements is achieved by developing a quasi-static model which includes the effects of geometrical flexibility within each element. The development of this model is treated in the following.

Figure 3.45 and the contents of Table 3.4 is found in Lovatt et al. (2005) and show the stiffness and strength properties of some common materials. According to UK Centre for Materials Education (2004), the twisting of the cords reduces the effective Young's

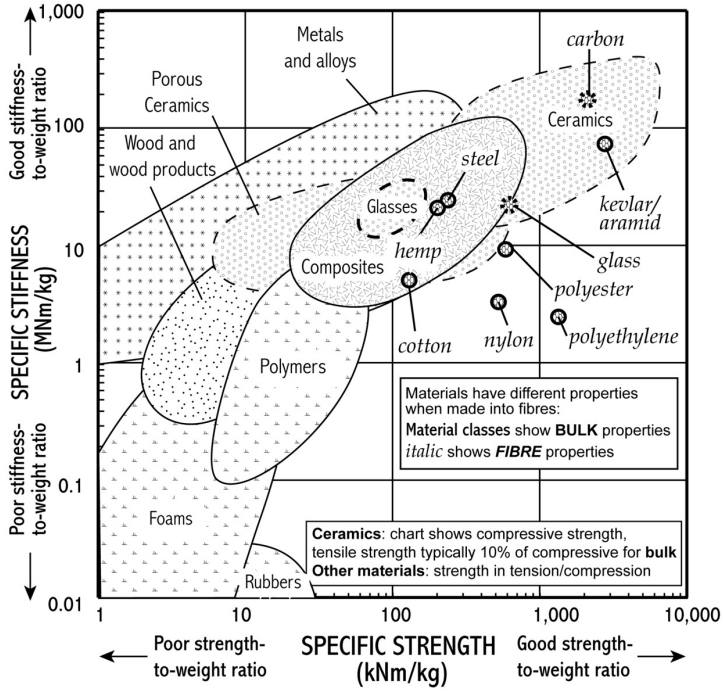

Figure 3.45: Strength and stiffness of some common materials. From Lovatt et al. (2005).

modulus by a factor of about 2. The Young's modulus of steel wires and nylon ropes may then be estimated to

$$E_s = \frac{210\,\text{GPa}}{2} = 105\,\text{GPa}, \tag{3.166}$$

$$E_n = \frac{3.9\,\text{GPa}}{2} = 1.95\,\text{GPa}, \tag{3.167}$$

where $E_s$and E_n are the Young's modulus for steel wires and nylon ropes, respectively. The values varies with both the material and the way the rope or wire is braided or twined, but these approximations are used for the model.

The parameterized cable element includes a parameterization of the relation between the position of the end nodes and the tension between these nodes. To find this relation, numerical simulations of a discretized cable element are utilized. This makes it possible to implement the effects of both gravity, buoyancy and hydrodynamic forces on the geometric flexibility. Figure 3.46 shows the three different detail levels of the cable elements considered:

Material	Young's modulus	Density	Strength
Carbon Fibre	300 GPa	1,770 kg/m^3	3,430 MPa
Aramid Fibre	124 GPa	1,450 kg/m^3	3,930 MPa
Polyester Fibre	13.2 GPa	1,390 kg/m^3	784 MPa
Nylon Fibre	3.9 GPa	1,140 kg/m^3	616 MPa
Alloy Steel	210 GPa	7,800 kg/m^3	1,330 MPa

Table 3.4: Some properties of various materials. From Lovatt et al. (2005).

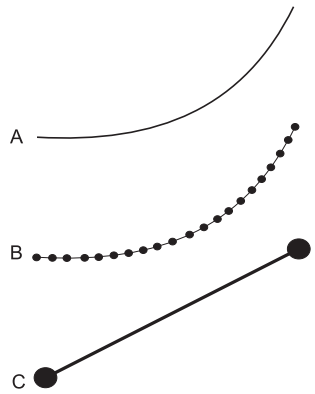

Figure 3.46: The different detail levels of a cable element.

A - The continuous cable element.
B - The discretized cable element.
C - The parameterized cable element.

The parameterization is performed for some specific cases only, chosen to reflect normal conditions for the trawl simulations. These cases are shown in terms of the element characteristics of the elements in Table 3.5, where d is the diameter of the cable, l_0 is the unstretched length of the element, α_h is the horizontal angle between the element and the relative water velocity, α_v is the angle between the element and the horizontal plane, E is the Young's modulus of the element, ρ is the specific weight of the element and n is the number of sub-elements in the discretization.

Calculation procedure In the resulting parameterization, the contracting forces between the two nodes of the element is found by replacing the strain in the element by an effective strain, ε_{eff}. The tension in the element is found as

$$T = A_c E_c \varepsilon_{eff}, \tag{3.168}$$

where the effective strain includes effects from both stiffness and damping. The forces on each end point of each element is calculated from the tension by

Case	**Function**	**Material**	d $[mm]$	l_0 $[m]$	α_h $[^\circ]$	α_v $[^\circ]$	E [GPa]	ρ [kg/m^3]	n [-]
1	Warp	Steel	30	50	14	18	105	7800	20
2				100					
3				200					
4				300					
5	Upper bridle	Steel	20	10	12	12	105	7800	20
6				20					
7				30					
8				50					
9	Lower bridle	Steel	20	10	12	5	105	7800	20
10				20					
11				30					
12				50					
13	Trawl net	Polyamid	20	5	10	0	1.95	1140	20
14				20					
15				50					
16				100					

Table 3.5: The properties of the simulated elements.

$$\vec{f}_{t,ij} = T\,\frac{\vec{l}_{ij}}{l_{ij}}, \tag{3.169}$$

where i and j are the numbers of the nodes at the ends of the cable element.

The internal damping of each cable element is estimated from the relative velocities between its end nodes. This damping includes dissipation of energy from both longitudinal and transversal hydrodynamic forces and internal friction. It is approximated as a linear function of the compression speed of the cable element, l_e, even if it probably includes both lower and higher order terms. This damping force is especially important for numerical simulations of stretched cable elements, because of the stiffness in such a system.

To find a suitable formulation for such damping, the dynamics of the length of a cable element is compared to a system of a fixed point, a mass point, a linear spring and a linear damper

$$m\ddot{l} + d\dot{l} + kl = 0,$$

where m is the mass, k is the spring stiffness and d is the damping coefficient. The damping coefficient in terms of relative damping is for such a system found as

$$d = 2\zeta\sqrt{km}, \tag{3.170}$$

where ζ is the relative damping ratio of the system. The mass and stiffness of this system

may be related to a cable element as

$$m \propto \rho_c A_c l_0, \tag{3.171}$$

$$k \propto \frac{A_c E_c}{l_0}. \tag{3.172}$$

Using this, the damping force on a cable element, in terms of relative damping, is assumed to be proportional to

$$2\zeta A_c \sqrt{E_c \rho_c} \dot{l}_e. \tag{3.173}$$

To keep a constant relative damping for different cable elements, the change in tension in the cable element caused by the damping is calculated as

$$\Delta T_{damp} = k_{damp} A_c \sqrt{E_c \rho_c} \dot{l}_e.$$

The damping force is implemented as a shift in the strain of the cable:

$$\Delta T_{damp} = A_c E_c \Delta \varepsilon_{eff} = k_{damp} A_c \sqrt{E_c \rho_c} \dot{l}_e, \tag{3.174}$$

$$\Delta \varepsilon_{damp} = k_{damp} \sqrt{\frac{\rho_c}{E_c}} \dot{l}_e. \tag{3.175}$$

The effective strain in the element is proposed found from

$$\varepsilon_{eff} = \max\left(\varepsilon_{nodes} + \Delta\varepsilon, \varepsilon_{\min}\right), \tag{3.176}$$

$$\varepsilon_{nodes} = \frac{l_e - l_0}{l_0}, \tag{3.177}$$

$$\Delta\varepsilon = \Delta\varepsilon_1 + \frac{\Delta\varepsilon_{2,\max}}{1 + k_{rise}\Delta\varepsilon_1} + \Delta\varepsilon_{damp}, \tag{3.178}$$

$$\Delta\varepsilon_1 = \left|\varepsilon_{nodes}\right|, \tag{3.179}$$

$$\Delta\varepsilon_{2,\max} = \frac{\left(k_{weight}\Delta\rho d_c + k_{speed}\right) l_e d_c}{A_c E_c} \left(\varepsilon_{nodes} + 1\right), \tag{3.180}$$

$$\Delta\rho = \rho_c - \rho_w, \tag{3.181}$$

where $\varepsilon_{\min}$ is the minimum effective strain.

Estimating the parameters of the cable model By curve fitting the model to the results from the numerical simulations, the stiffness parameters are estimated to

$$k_{speed} = 990, \tag{3.182}$$

$$k_{weight} = 90, \tag{3.183}$$

$$k_{rise} = 30. \tag{3.184}$$

The value of the damping coefficient is chosen to give good computational efficiency, and it is set to

$$k_{damp} = 1.5. \tag{3.185}$$

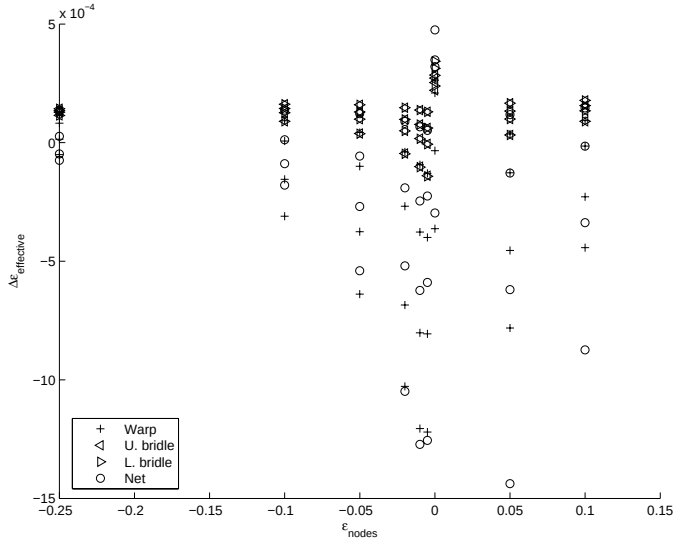

Figure 3.47: Difference between element parameterization and numerical simulation,

Model verification The difference between the numerical simulations of the discretized cable element (B) and the resulting parameterization (C) is shown in Figure 3.47. The difference is shown for the cases in Table 3.5, in terms of effective strain.

Gravity and buoyancy forces

The gravity and buoyancy forces act in opposite directions along the z^n-axis. These forces are therefore combined and calculated by

$$\vec{f}_{\varrho} = A_c l_e \left(\rho_c - \rho_w\right) \vec{g}. \tag{3.186}$$

The resulting model

The forces acting on each node is found as the sum of half the forces acting on each element connected to this node. The mass of each node is found as the sum of half the mass of each element connected to this node. The acceleration dependent hydrodynamic forces are treated as an added mass, and the equation of motion for each node is

$$\frac{1}{2}\sum_{j=1}^{N} A_c^j l_e^j \left(\rho_c^j + \rho_w\right) \vec{v}_{cn} = \frac{1}{2}\sum_{j=1}^{N} \left(\vec{f}_{v_t}^{\,j} + \vec{f}_{v_n}^{\,j} + \vec{f}_t^{\,j} + \vec{f}_d^{\,j} + \vec{f}_{\varrho}^{\,j}\right), \tag{3.187}$$

where N is the number of elements connected to the node. For notational simplicity, reference to the node numbers are omitted. The superscript j on a force vector denotes the connected element number j of this node. $\vec{v}_{cn}$ is the acceleration of the node in relation to the n-frame. $\vec{f}_d$ is an additional damping force, which allows for increased

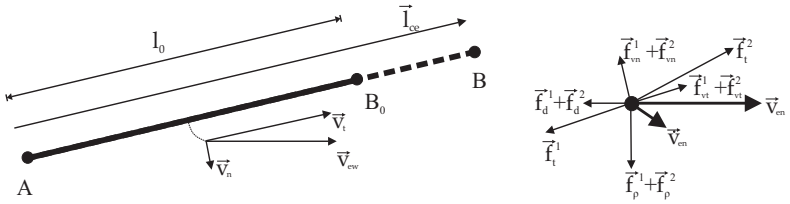

Figure 3.48: Cable element and cable node notation.

damping of the system. This is not implemented in the simulations, because it is not physically justified and not necessary. It may, however be advantageous for other systems, and is therefore included in the model formulation. The method is illustrated in Figure 3.48.

3.4.3 The trawl winches

The trawl winches control the length of the warps. Hydraulic winches are the most common, but electric winches are also used. Their characteristics are:

- Maximum warp tension depends on the length of the warp and the speed of the winch.
- Maximum speed of the winch depends on the warp tension and the length of the warp.
- There is a time delay between control command and execution depending upon the control command.
- The maximum speed may depend upon operational issues, such as which hydraulic pumps are connected and the power generation (the frequency of the power supply).
- There are dynamics in the rotational speed.
- The relation between drum speed and warp tension can be changed at any time during operation, by choosing which and how many hydraulic pumps are connected, as well as how the hydraulic motors are connected.

To increase computational performance, the dynamics of the winches are disregarded. The maximum achievable speed of the winch is regarded as a function of tension alone. It is assumed governed by the maximum hauling power, the maximum speed, the maximum torque and the current radius of the drum. The mathematical model is formulated as

$$\dot{l}_0 = -\omega r, \tag{3.188}$$

$$\omega = \begin{cases} \min\left(\frac{P_{\max}}{Tr}, \omega_{\max}\right) & \text{for} \quad \varepsilon > \varepsilon_{\max} \quad \wedge \quad T \leq \frac{Q_{\max}}{r} \\ 0 & \text{for} \quad \varepsilon > \varepsilon_{\max} \quad \wedge \quad T > \frac{Q_{\max}}{r} \\ 0 & \text{for} \quad \varepsilon \leq \varepsilon_{\max} \\ -\omega_{\max} & \text{for} \quad \varepsilon < -\varepsilon_{\max} \end{cases}, \tag{3.189}$$

$$\varepsilon = l_0 - l_{0d}, \tag{3.190}$$

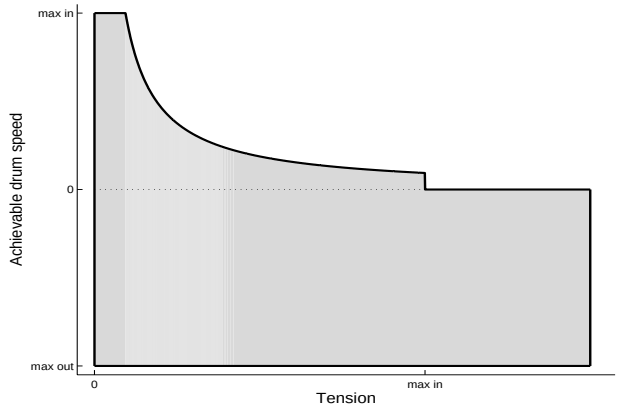

Figure 3.49: The achievable angular velocity of the winch drum.

where l_0 is the stretched warp length, r is the current radius of the drum (including the wire layers) and ω is the angular velocity of the drum. $P_{\max}$ is the maximum available mechanical power on the drum, T is the tension in the warp, ε and $\varepsilon_{\max}$ is the actual and maximum allowed deviation between desired and actual warp length, $Q_{\max}$ is the maximum torque available for turning the winch and $\omega_{\max}$ is the maximum turning rate of the drum.

The attainable speed range of the drum is shown in Figure 3.49. In the model, only maximum, minimum and zero velocities are used.

3.4.4 The ship

The ship equations of motion

The ship equations of motion are formulated as

$$\mathbf{M}_s \dot{\boldsymbol{\nu}}^s_{sn} = \boldsymbol{\tau}^s_{s\Upsilon} + \boldsymbol{\tau}^s_{sw_p} + \boldsymbol{\tau}^s_{sw_s} + \boldsymbol{\tau}^s_{sT} + \boldsymbol{\tau}^s_{s\varrho}, \tag{3.191}$$

$$\dot{\boldsymbol{\eta}}^n_{sn} = \begin{bmatrix} \mathbf{R}(\boldsymbol{\Theta}_{ns}) & \mathbf{0}_{3\times3} \\ \mathbf{0}_{3\times3} & \mathbf{T}_{\boldsymbol{\Theta}}(\boldsymbol{\Theta}_{ns}) \end{bmatrix} \boldsymbol{\nu}^s_{sn}, \tag{3.192}$$

$$\mathbf{M}_s = \mathbf{M}^{RB}_s + \mathbf{M}^A_s \tag{3.193}$$

where $\mathbf{M}^{RB}_s \in \mathbb{R}^{6\times6}$ is the rigid body mass matrix of the ship, $\mathbf{M}^A_s$ is the added mass matrix of the ship (Fossen, 2002), $\dot{\boldsymbol{\nu}}^s_{sn}$ is the acceleration of the ship in relation to the n-frame, decomposed in the ship frame, $\boldsymbol{\tau}^s_{s\Upsilon}$ is the generalized hydrodynamic forces, excluding the acceleration dependent hydrodynamic forces, $\boldsymbol{\tau}^s_{sw_p}$ and $\boldsymbol{\tau}^s_{sw_s}$ are the generalized forces from the port and starboard warp, $\boldsymbol{\tau}^s_{sT}$ is the generalized forces from the propeller and the rudder and $\boldsymbol{\tau}^s_{s\varrho}$ is the sum of the forces from the buoyancy and the weight of the ship. $\boldsymbol{\eta}^n_{sn} = \begin{bmatrix} (\mathbf{p}^n_{sn})^T & \boldsymbol{\Theta}^T_{ns} \end{bmatrix}^T$ is the generalized position vector of the ship in the ned frame, decomposed in the ned frame, and $\mathbf{0}_{3\times3}$ is a 3×3 matrix of zeros.

It is assumed that the wave generated motions of the vessel are attenuated by the warps, so that no wave frequency forces affect the trawl doors. The correctness of this assumption depends on the length, density and mass of the warps, as well as the vessel motions. A 500 m steel wire warp with a diameter of 30 mm has a mass of approximately 2800 kg and an added mass of approximately 350 kg. Considering this and the geometrical flexibility and hydrodynamic damping, it seems probable that the ship motions in heave, roll and pitch do not affect the trawl system for low seastates. If it is further assumed that the *mean value* of heave, roll and pitch do not change because of external forces, such as warp tensions and hydrodynamic forces, these dof may be excluded from the ship model. This leaves a 3dof ship model, formulated as

$$\dot{\boldsymbol{\nu}}^s_{sn} = \mathbf{P}_s^T \left(\mathbf{M}_s^3\right)^{-1} \left(\boldsymbol{\tau}^{s,3}_{s\Upsilon} + \boldsymbol{\tau}^{s,3}_{sw_p} + \boldsymbol{\tau}^{s,3}_{sw_s} + \boldsymbol{\tau}^{s,3}_{sT}\right), \tag{3.194}$$

where $\mathbf{M}_s^3 \in \mathbb{R}^{3\times 3}$ is the reduced total mass matrix, $\mathbf{P}_s \in \mathbb{R}^{3\times 6}$ is a reduction matrix and the superscript 3 specifies that only the dof 1, 2 and 6 are present. The relation between the 6 dof and the 3 dof forces and mass matrices are

$$\boldsymbol{\tau}^{s,3} = \mathbf{P}_s \boldsymbol{\tau}^s, \tag{3.195}$$

$$\mathbf{M}_s^3 = \mathbf{P}_s \mathbf{M}_s. \tag{3.196}$$

The reduction matrix $\mathbf{P}_s$ is found as

$$\mathbf{P}_s = \begin{bmatrix} 1 & 0 & 0 & 0 & 0 & 0 \\ 0 & 1 & 0 & 0 & 0 & 0 \\ 0 & 0 & 0 & 0 & 0 & 1 \end{bmatrix}. \tag{3.197}$$

The hydrodynamic forces on the ship hull

The hydrodynamic forces on the hull of the ship are be a nonlinear function of velocity relative to the ambient water, including memory effects. In addition, there are forces from wave and wind. These forces may play a significant role during rough conditions, especially for vessels with a shortage of thrust and control forces. For this thesis it is, however, assumed a surplus of available thrust and control forces, making it possible to compensate for any influence from waves and wind. This eases the demands of accuracy on the mathematical modeling of the hydrodynamic and aerodynamic forces, and only the hydrodynamic forces for a vessel in calm water are considered.

The model should not necessarily calculate the hydrodynamic forces on a specific trawling vessel, but rather provide a coarse estimate for a typical vessel. This places less strict demands on accuracy, and this is further emphasized by the fact that most of the hydrodynamic forces can be cancelled by the use of thrust and rudder.

The hydrodynamic forces on a ship hull may be found from a variety of sources, such as model tests, empirical formulas or numerical methods. In Digernes and Yi (1983), empirical formulas for the resistance of fishing vessels are proposed, based on model tests of 54 different vessels. For this thesis, the simplest of these formulas is used to find the resistance of the trawl vessel. This formula estimates the resistance as

$$P = a \left(\frac{L}{B}\right)^b \left(\frac{B}{T}\right)^c \nabla^\delta e^{\beta F_n}, \tag{3.198}$$

where L is ship waterline length, B is ship breadth, T is ship draught and ∇ is ship deplacement in metric tons. F_n is the Froude number, defined as $F_n = \frac{U_s}{\sqrt{gL}}$. P is the power of the resistance force in horse power. The coefficients are given as $a = 5.3943 \times 10^{-4}$, $b = 0.618$, $c = 0.634$, $\delta = 1.110$ and $\beta = 15.831$. This formula is, however, only valid in a narrow range of Froude numbers.

The hydrodynamic forces attacking a specific naval vessel in surge, sway and yaw is described by 23 non-zero coefficients in Blanke and Christensen (1993). This vessel is different from a normal trawler in both size and shape, but the coefficients are scaled to achieve sufficient accuracy. This scaling is not described. The part of the resistance dependent on the forward velocity is found as

$$R_s = k_R u_s \left| u_s \right|, \tag{3.199}$$

where u_s is the ship speed along local x^s-axis and k_R is the resistance coefficient. The resistance coefficient of the model is substituted by a value found from (3.198) for a Froude number of 0.3, which is the Froude number for which most experimental data was available. k_R is hence found as

$$k_R = \frac{0.735a \left(\frac{L}{B}\right)^b \left(\frac{B}{T}\right)^c \nabla^\delta e^{0.3\beta}}{\left(0.3\sqrt{gL}\right)^3}. \tag{3.200}$$

The propeller and the rudder

The propeller and rudder performance are influenced by properties such as

- Engine dynamics and time delays.
- Propeller pitch and rpm control.
- Maximum engine torque, which is a function of engine speed and ambient conditions.
- Varying power outtake from shaft generators and pumps.
- Varying power intake from electrical motors.
- Cavitation and ventilation of propeller and rudder.
- Influence from vessel velocities in all six dof and the wake of the ship.
- The rudder angle.
- The vessel draught, trim and roll.
- Waves

All these properties influence the direction and amplitude of the thrust in a nonlinear way.

The thrust In Blanke and Christensen (1993) the transversal rudder force is found as

$$Y = k\delta u^2, \tag{3.201}$$

where δ is rudder angle and u is the forward velocity of the ship. It is obvious that this model is not satisfactory for trawling simulations, since it does not take into account the velocity induced by the propeller over the rudder. The rudder force of the model is therefore replaced. For the simulations, the thrust from the propeller is taken to attack in the rudder stock. The direction of the thrust is approximated to the direction of the rudder, and the total thrust vector is found as

$$\boldsymbol{\tau}_{sT}^{s} = \begin{bmatrix} \mathbf{f}_{sT}^{s} \\ \mathbf{m}_{sT}^{s} \end{bmatrix}, \tag{3.202}$$

where $\boldsymbol{\tau}_{sT}^{s}$ is the generalized thrust force. The thrust force $\mathbf{f}_{sT}^{s}$ and the thrust moment $\mathbf{m}_{sT}^{s}$ is calculated as

$$\mathbf{f}_{sT}^{s} = \max\left(T_d, T_{\max}\left(U_s, \alpha^r\right)\right) \begin{bmatrix} \cos\delta \\ \sin\delta \\ 0 \end{bmatrix}, \tag{3.203}$$

$$\mathbf{m}_{sT}^{s} = \mathbf{p}_{rs}^{s} \times \mathbf{f}_{sT}^{s}, \tag{3.204}$$

where T_d is the desired thrust, $T_{\max}$ is the maximum thrust as a function of the forward velocity U_s and the rudder angle δ and $\mathbf{p}_{rs}^{s}$ is the position of the rudder stock decomposed in the ship frame. $T_{\max}$ is found as

$$T_{\max}\left(U_s\right) = \left(T_{BP} - k_T U_s\right)\cos\delta, \tag{3.205}$$

and k_T is found from

$$T_{\max}\left(U_{s,\max}\right) = R_s\left(U_{s,\max}\right) \tag{3.206}$$

$$T_{BP} - k_T U_{s,\max} = R_s\left(U_{s,\max}\right) \tag{3.207}$$

$$k_T = \frac{T_{BP} - R_s\left(U_{s,\max}\right)}{U_{s,\max}}, \tag{3.208}$$

where $U_{s,\max}$ is the maximum velocity of the ship for the current condition when not towing anything, $R_s\left(U_{s,\max}\right)$ is the resistance of the ship at this speed and T_{BP} is the bollard pull of the ship.

The autopilot The autopilot is approximated as

$$\delta_d = K_{p,\delta}\varepsilon_\psi + K_{d,\delta}\dot{\psi} + K_{i,\delta}\int_0^t \varepsilon_\psi\left(\tau\right) d\tau, \tag{3.209}$$

where δ_d is the desired rudder angle, $K_{p,\delta}$, $K_{d,\delta}$ and $K_{i,\delta}$ is the proportional, derivative and integral gain constant. The heading deviation is found as

$$\varepsilon_\psi = f_{cyclic}\left(\Delta\varepsilon\right), \tag{3.210}$$

$$\Delta\varepsilon = \psi - \psi_d, \tag{3.211}$$

where ψ_d is the desired heading and f_{cyclic} is a function returning its argument $\pm\, 2n\pi$, where $n \in N$, so that the returned value lies between $-\pi$ and π. The dynamics of the rudder is sacrificed for increased computational performance, and it is assumed that the desired rudder angle is acquired instantaneously while limited to a maximum angle. This is formulated as

$$\delta = \text{sign}\,(\delta_d)\ \ \min\,(\ |\delta_d|\ \ ,\ \ \delta_{\max}\ )\,, \tag{3.212}$$

where δ is actual rudder angle and $\delta_{\max}$ is maximum rudder angle.

Chapter 4

The trawl control system

4.1 Introduction

The emphasis of this chapter is the development of the supervisory trawl control system. The goal of this system is to guide the trawl system in such a way that the given objectives are optimized subject to the given constraints. These objectives could be related to for example collision avoidance, bottom impact, fuel consumption and the amount of caught fish. The control actions must be based on input from the operator as well as sensors both on the ship and on the trawl. The position of the various parts of the trawl system are not known, and must be estimated from a few inaccurate measurements with a low update rate.

The main goal of this thesis is stated in the introduction as:

"To develop a trawl control system with increased precision and bandwidth, based on practical considerations"

Bandwidth is in this respect interpreted as the inverse of the response time of the trawl net after a control signal is given. The control performance indicators measuring the fulfillment of the main goal is:

- The path following accuracy of the trawl net.
- The dynamic response of the trawl net.
- The compliance to industrial constraints.

The industrial requirements are that the control system must be inexpensive, be easy to use, have low maintenance costs and at least maintain the fishing efficiency. Extra benefits may be gained in terms of rules and regulations, if the eco-efficiency of trawling is improved in relation to conventional trawl systems.

The trawl control system must be able to change properties or generate forces that affect the path of the trawl system. This is today achieved through manual control of the setpoints of the following plant and low level controllers:

- The autopilot, which operates the rudder machinery.
- The engine speed controller, which controls the amount of fuel injected into the engine cylinders per cycle.
- The winch controllers, which operates the actuators controlling the winches.
- The propeller pitch controller, which controls the propeller pitch according to operator input and engine constraints.

It would be possible to improve the responsiveness of the trawl system by adding actuators controlling the forces acting either on the trawl doors or on the trawl net. Such concepts have, however, not yet been implemented in commercial trawl fisheries. This thesis does not consider actuators on the trawl net, even though such a system would probably yield the best results with regard to control bandwidth. The reason for this is mostly that a control system based on applying control forces directly on the trawl net would be complex with respect to energy supply, protection and force generation. The technical and commercial risk levels are therefore assumed to be high in developing such solutions. The development of controllable trawl doors is, on the other hand, assumed to represent a lower risk level. It is therefore chosen to concentrate on developing a trawl control system based on control of the trawl doors, in addition to controlling the ship speed, the ship heading and the warp lengths.

4.1.1 Previous work

Control algorithms

There is not much available literature on control algorithms for automatic control of trawl systems, and none have been found to control the movements in both the horizontal and the vertical plane. There is also a lack of published full-scale field experiments to confirm the performance of the theories.

Control of a mid-water trawl system in the *vertical plane* is described in Lee (1995, 1999); Lee et al. (2001b), where a controller based on fuzzy logic controls the depth of the trawl by adjusting the warp length. Instead of being dependent on a mathematical model of the trawl system, the control system is taught how to respond by an experienced captain. Extensive modeling of the trawl system is thus avoided. This method has shown good results in the vertical plane during sea trials of a small-scale mid-water trawl system (Lee, 1999), even when using a very simple system model. The robustness in all six dof, subject to the effects of varying control trajectories, nonlinearities and constraints is, however, not shown.

Modeling, simulation and control of a trawl system in the *horizontal plane* have been described by Johansen et al. (2002). The total trawl system, including the vessel, the warps, the trawl doors, the bridles and the trawl net are described. Local PID controllers are used for controlling the sway motion of the trawl doors according to a predefined trajectory. The chosen concept changes the position of the sweep lines fastening point on the trawl doors in the transversal direction. This controls the trawl doors angle of attack and thereby their lift force and transversal position. The control system is verified through simulations and seems to perform well.

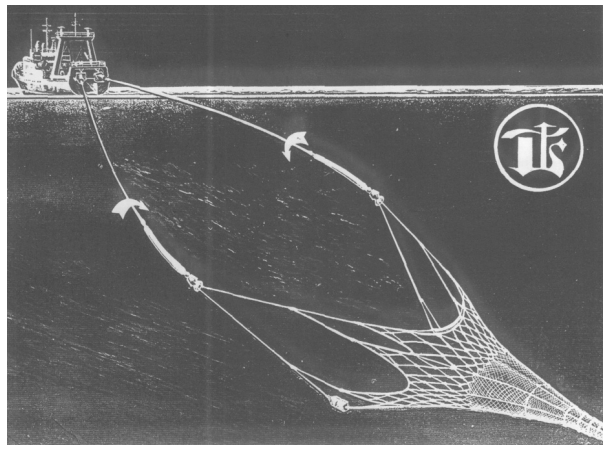

Figure 4.1: The principle of using warp rotation to replace the trawl doors.

Control concepts

Many control concepts have been proposed, whereof most focus on how to control the hydrodynamic forces on the trawl doors. Since trawl door control concepts are treated in Section 6, it is omitted in the following. Other relevant work on control concepts includes:

- By rotating the warps, Russian scientists were able to remove the trawl doors (NPO Promrybolovstva). By altering the rotational speed of the warps, the spreading and vertical forces on the trawl net could be controlled. Full scale sea trials have been performed, and the total resistance of the trawl system was reported to decrease by 20%. The concept is shown in Figure 4.1.
- It is in a patent (Petroleum Geo-Services, 2004) suggested to use the ship winches to decouple the movements of the towed seismic array from the movements of the ship, as shown in Figure 4.2.
- The Norwegian company Scantrol has developed a control system for maintaining the symmetry of the trawl system in relation to its velocity relative to the surrounding water, regardless of currents and ship movements (Scantrol, 2000). The basic parts of this system is shown in Figure 4.3, but this system is in particular well suited for controlling the symmetry of multiple trawl nets. Scantrol reports that the system is used by more than 20 fishing vessels.

4.1.2 Present work

The proposed control system is based on model predictive control (MPC), and is able to take strong nonlinearities, constraints and nonlinear objectives into account. The system uses step-wise feedforward control of the trawl doors to reduce their energy consumption.

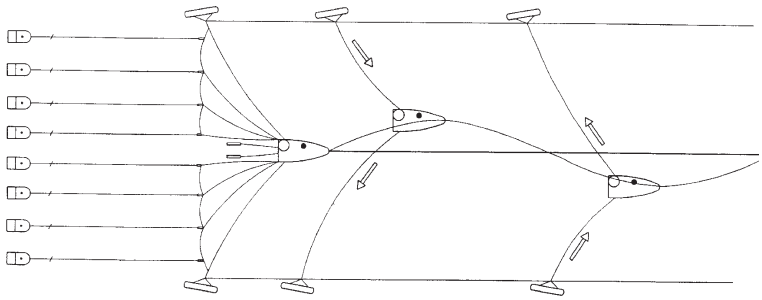

Figure 4.2: Decoupling of the movements of the ship and the towed array by using the ship winches.

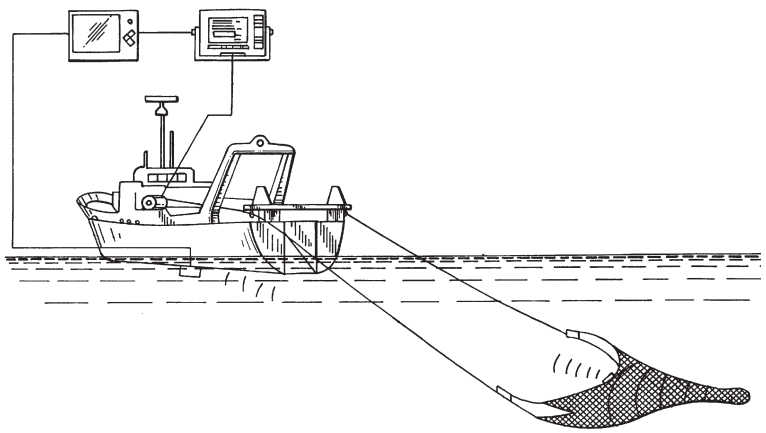

Figure 4.3: Controlling the symmetry of the trawl net by using the winches and a symmetry sensor.

A trajectory controller with subcontrollers are used to ensure stability and predictable behavior between MPC updates, thus reducing the necessary control update rate. A simplified control plant model reduces the prediction time, and the internal control signal in the MPC is condensed, reducing the number of unknowns of the optimization problem. The state estimation is performed by independent models.

Section 4.2.4 presents the propsed trawl control system architecture. The various parts of this system is elaborated in the remainder of this chapter. Case studies verifying the various parts of the control architecture are presented in Chapter 5, and the basics of numerical optimization and MPC are presented in Appendix A.

4.2 Control architecture overview

4.2.1 Control architecture requirements

The trawl system possesses some characteristics that put special requirements on the control system. Some specific requirements posed on the trawl control architecture in this work are:

- It should be able to handle state measurements that are inaccurate, rare and available at uneven intervals.
- It should be able to include nonlinear properties and objectives.
- It should be able to use the trawl doors as actuators, while limiting their energy consumption.
- It should allow long term objectives to be taken into account by the captain.
- It should maximize the short term profit, while taking safety and legal restrictions into account.
- Upgrading existing trawlers should be feasible by utilizing already installed equipment and control systems.

4.2.2 Control philosophy

Since the experience and skills of the captain are essential in utilizing all available information, (past experience, sensor systems, maps and communication with both other vessels and shore), the proposed trawl control system aims to aid the captain in using the plant and low level controllers. In addition, the dynamic response of the trawl system is improved by introducing trawl door control. The trawl control system acts as a layer between the captain and the plant and low level controllers, leaving him to concentrate on the higher level decisions.

To conform to the stated objectives and constraints, the proposed control system is based on model predictive control (MPC) for finding optimal trajectories of both the trawl system and the setpoints of plant and low level controllers. The trajectory controller uses plant and low level controllers to ensure performance between the updates

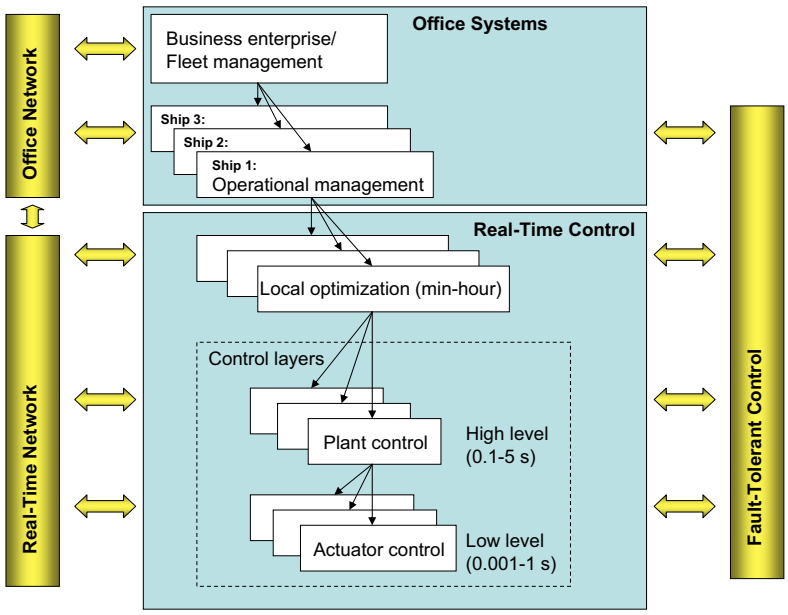

Figure 4.4: The control hierarchy. From Sørensen (2005).

from the MPC. Since many of the system characteristics are highly nonlinear, iterative optimization methods are employed for accurate results.

Iterative optimization methods also facilitate nonlinear objective functions, making it possible to include any kind of objectives and constraints. The objective function must be able to predict the fulfillment of future objectives for an arbitrary trajectory of the trawl system, estimating:

- Future catch.
- Future cost.
- Future energy consumption on the trawl doors.
- Future compliance to safety and legal constraints.

Sørensen (2005) proposes to divide the control hierarchy as illustrated in Figure 4.4. The trawl control system relates to this formalized hierarchy as follows:

- The business enterprise and fleet management functions provides the strategic decisions, such as the species to catch, the general area to go to and scheduling of major maintenance. This is part of the operational input in Figure 4.5.
- The operational management provides the tactical decisions, such as the more specific area to go to, when to start and stop towing and when and where to make deliveries. This is also part of the operational input in Figure 4.5.

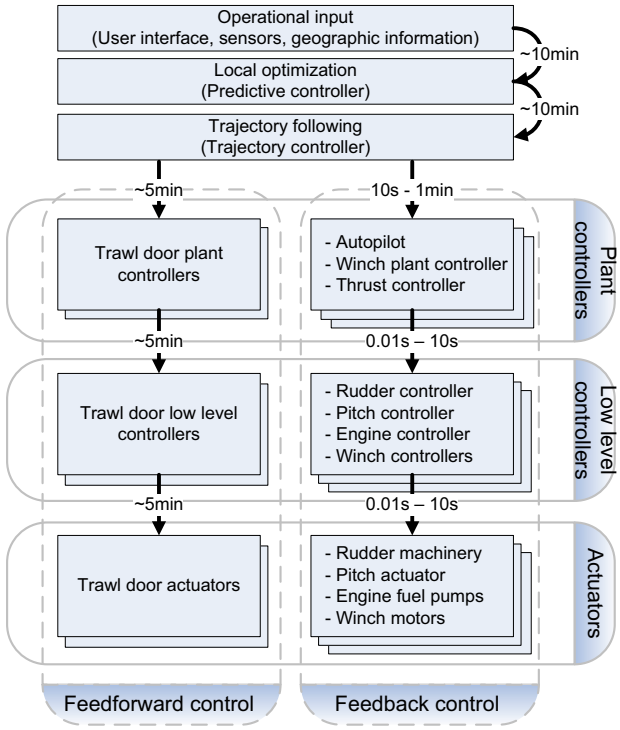

Figure 4.5: The different control layers and the use of feedforward control.

- The local optimization consists of the decisions taken to optimize the short term results, such as the desired three dimensional trajectory to follow while towing. This function is implemented in the local optimization block in Figure 4.5.
- The plant control consists of the actions taken to follow the path found by the local optimization, such as setpoints of the autopilot and the thrust controllers. This function is divided between the trajectory following block and the plant controllers in Figure 4.5.
- The actuator control consists of the low level controllers in Figure 4.5.

The work in this thesis is focused towards real-time control and monitoring, regarding the operational and business enterprise management as premise providers. The objective of the control system is in other words to assist the captain in the local optimization and to execute the plant control.

The control system is divided into different layers, as illustrated in Figure 4.5. A rough estimate of the intervals for communication between the blocks are given next to the arrows. These layers are abstractions that increase the modularity and reduce the complexity of the system, also facilitating future improvements of the various modules and layers. Each layer controls some instabilities and/or fast dynamics of the system,

presenting slower dynamics for its superior layer. To conserve energy on the trawl doors, the trawl door controllers use only step-wise feedforward control action at a limited update rate. This implies that the trawl door control concept must render the trawl doors open loop stable.

Some parts of the total trawl system are dominated by slow dynamics, while other are dominated by faster and unstable dynamics. By using plant and low level controllers to provide stability and command following properties of the fastest dynamics of the trawl system, the MPC may relate to a stable plant with only slow dynamics. This allows for less frequent control signal updates, facilitating iterative optimization methods.

4.2.3 Preliminaries

Mathematical models of different complexity levels are needed for different purposes. It is in this work distinguished between *control plant models* and *process plant models*. These are defined in Sørensen (2005) as:

- **A control plant model** is a simplified mathematical description containing only the main physical properties of the process or plant. This model may constitute a part of the controller. The control plant model is also used in analytical stability analysis based on e.g. Lyapunov stability and passivity.

- **A process plant model** is a comprehensive description of the actual process and should be as detailed as needed. The main purpose of this model is to simulate the real plant dynamics. The process plant model is used in numerical performance and robustness analysis and testing of the control systems.

Process plant models do in other words act as the real process when testing and verifying control systems, while control plant models are regarded as models that are simplified to make them better fit the needs of the control system. For the present work, control plant models of three different complexity levels are introduced:

***The accurate control plant model* (ACPM)** is used in estimating the states of the real system. It uses the mathematical model developed in Chapter 3, which is the most accurate model available.

***The fast control plant model* (FCPM)** is used for optimizing the control output, and it is part of the objective function of the optimization. Since this model must be able to run many times faster than real-time, it is designed to be faster than the ACPM.

***The control influence model* (CIM)** is a static model containing the mapping between the control actions and the effect on the trawl system. It is used in calculating the control signals to various controllers from the deviation between the state estimations and the state predictions.

In addition to the control plant models, the following terms are frequently used in this work, and therefore briefly explained:

The process plant model (PPM) is based on the same formulation as the ACPM, but some of its parameters are changed to make it differ as much from the ACPM as the real process is expected to. This is done to ensure that the robustness of the control system, with regard to modeling errors, is tested through the verification procedures.

Observers are mechanisms for reconstructing the states of a dynamic system, and can do this based on poor, infrequent and few measurements. Observers frequently contain two main parts; the corrector and the predictor. The predictor predicts the states of the system, while the corrector corrects the states based on the available measurements.

Independent models are also used for estimating the states of dynamic systems. These act as regular observers, except they do not correct the states of the system according to the measurements. Instead, they estimate the states based only on the known input and the mathematical model of the system. Independent models are therefore dependent on accurate mathematical models of the system in question, as well as accurate information about the system input.

4.2.4 Outline of the control architecture

An overview of the proposed trawl system control architecture is shown in Figure 4.6. The variable names are interpreted as follows:

- The vectors $\mathbf{x}$, $\mathbf{u}$, $\mathbf{p}$, $\mathbf{r}$ and $\mathbf{y}$ represent states, control signals, parameters, references and outputs of a model, respectively.
- The subscripts A, F and S designate the ACPM, the FCPM and the trawl system, respectively. The subscript P designates a prediction.
- Variables without time reference reflect the current time. A variable $\mathbf{x}$ at time t_2 is referred to as $\mathbf{x}(t_2)$. The trajectory of the same variable between the times t_1 and t_2 is referred to as $\mathbf{x}(t_{1:2})$.

The various components of the control system are explained in more detail in the following sections, but their function is briefly explained here:

The predictive controller provides the trajectory controller with regular updates of the trawl system reference trajectory and the control signal predicted to achieve this trajectory. It is based on numerical optimization and FCPM simulations.

The trajectory controller makes the trawl system follow the reference from the predictive controller, adding an additional control term to the estimated control signal. This control term is calculated by a multiple input multiple output PID feedback controller.

The trawl system is the real trawl system. It is for the case studies replaced by the PPM.

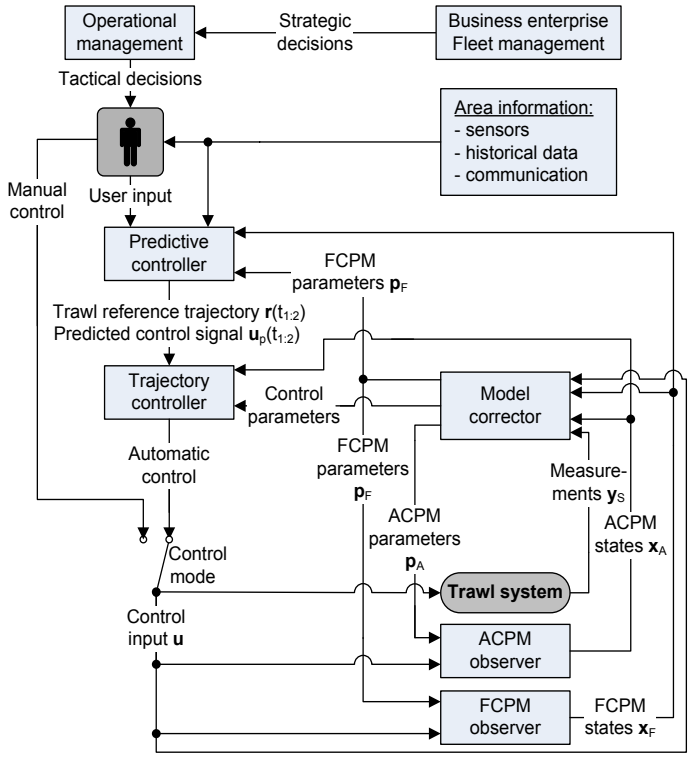

Figure 4.6: A schematic overview of the trawl control system architecture.

The ACPM observer is an independent model based on the ACPM, estimating the current ACPM states. It takes some model parameters as its input, making model adaptation possible.

The FCPM observer is an independent model based on the FCPM, estimating the current FCPM states. It takes some model parameters as its input, making model adaptation possible.

The model corrector calculates the model parameters of the ACPM, the FCPM and the CIM from the measurements on the trawl system and the known states from the models.

4.3 The predictive controller

The predictive controller uses numerical optimization to find the optimum trajectory of the trawl system. An overview is given in Figure 4.7. The vector $\mathbf{q}$ is the condensed control signal, O_1 and O_2 are the objective values of a specific solution, where O_1 only

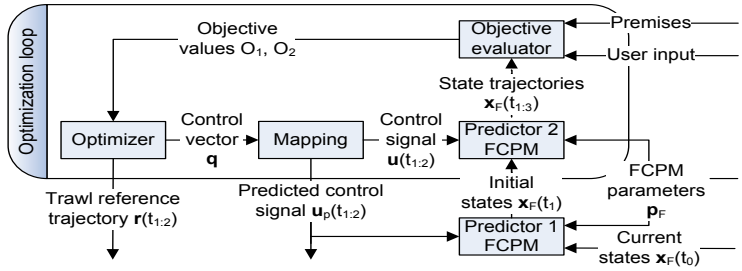

Figure 4.7: The predictive controller.

takes safety and legal constraints into account and O_2 takes all objectives into account. The defined points in time are:

- t_0 - A new optimization starts.
- t_1 - The next output should be ready.
- t_2 - The current control horizon ends.
- t_3 - The current prediction horizon ends.

The FCPM is run as part of the objective function, and any kind of objectives may in principle be evaluated. There is, however, a practical limitation on computational effort. Assuming that the final solution is within the legal and safety restrictions, the predictive controller outputs:

- The trawl system optimum trajectories.
- The predicted control signal trajectories.

4.3.1 Algorithm

The algorithm of the outer loop may be summarized as:

1. Predictor 1 receives $\mathbf{u}_P(t_{1:2})$ from the last optimization, $\mathbf{x}_F(t_0)$ from the FCPM observer and $\mathbf{p}_F$ from the model corrector, and calculates $\mathbf{x}_F(t_1)$.
2. Predictor 2 receives $\mathbf{x}_F(t_1)$ as its initial states and $\mathbf{p}_F$ from the model corrector.
3. The objective evaluator receives user input and premises.
4. The optimization is performed.
5. The optimizer returns $\mathbf{r}_F(t_{1:2})$, and the mapping returns $\mathbf{u}_P(t_{1:2})$.

The algorithm of one iteration of the optimization loop may be summarized as follows:

1. The optimizer outputs $\mathbf{q}$.
2. The mapping function maps $\mathbf{q}$ to $\mathbf{u}(t_{1:2})$.
3. Predictor 2 takes $\mathbf{u}(t_{1:2})$, $\mathbf{x}_F(t_1)$ and $\mathbf{p}_F$ as its input, and returns $\mathbf{x}_F(t_{1:3})$ to the objective evaluation.
4. The objective evaluation returns the objective values $O_1$and O_2.
5. Based on the optimization method and the objective values of previous iterations, the optimizer outputs a different $\mathbf{q}$.

4.3.2 Objectives

The optimum trajectory of the trawl system depends upon the known objectives, premises and constraints. The ultimate objectives and constraints typically consist of short term and long term measures of economy and safety, such as to minimize risk of injury and death and to maximize profit over the lifetime of the ship. The fulfillment of these depends upon a variety of premises, which can be divided according to which part of the control system they affect:

Business enterprise and fleet management premises include current and expected oil prices, expected needs for maintenance, repairs and upgrades, current and expected price and delivery situation for different species, and current and expected fish quotas.

Operational management premises include all business enterprise and fleet management premises in addition to: Weather forecasts, experiences with different fishing grounds for different species at different times at different weather conditions, and geographical knowledge (depths, obstacles and forbidden areas).

Local optimization premises include all operational management premises in addition to: Trawl system knowledge (catch efficiency, vulnerability and amount of catch) and surroundings sensors (sonars, echo sounders, radar and weather measurements).

For the remainder of this work, all business enterprise and fleet or operational management premises are assumed taken into account by the captain. The structure of the control system, however, facilitates the inclusion of such premises and objectives without any fundamental changes. The goal of the control system is to find the trajectory that maximizes short term profit while taking the requirements and constraints into account. This calls for prediction of both future catch and future costs for any given trajectory of the trawl system within the governing constraints.

There will typically exist constraints on the trawl system trajectory, including such as:

- The minimum horizontal and vertical distance to known seabed obstacles.

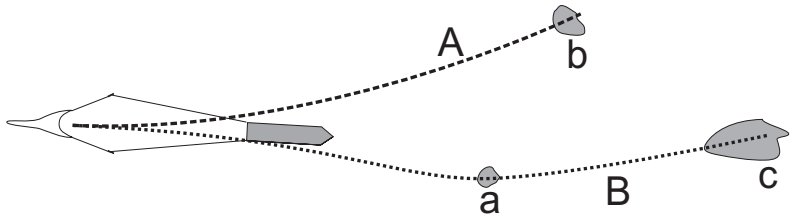

Figure 4.8: The importance of the length of the prediction horizon.

- The minimum distance to other trawls.
- The minimum distance to other ships.
- Desired footrope bottom pressure or distance to bottom.

In addition to evaluating an arbitrary trawl system trajectory with regard to such constraints, the objective function includes the ability to estimate the profitability of a given trajectory. This is elaborated in the following.

Catch prediction

If knowledge from previous hauls and information from other vessels are disregarded, there are no catch predictions available outside sonar range. In addition, the certainty of the predictions of future catch depend upon how far away it is in distance and time. This may lead to problems as new information becomes available and older information gets updated.

The influence of the prediction horizon is illustrated in Figure 4.8. The capital letters **A** and **B** refer to the optimum trajectory found for a shorter and longer prediction horizon, respectively. It is easily seen how a too short prediction horizon (case **A**) may lead to a sub-optimal choice of trajectory. This happens as only the fish schools **a** and **b** are seen initially, causing the system to target **b**, since this is the largest. When the considerably larger fish school **c** is detected, it is not possible to reach this.

It is also understood that trying to utilize a too long prediction horizon may lead to problems as the uncertainty of the information may lead to chasing imaginary schools of fish. As a compromise it is here suggested to weight the information with its estimated certainty. A system must therefore exist to identify and quantify possible catch ahead. This system should supply the following information to the control system:

- Positions and depths of possible catch ahead.
- The expected amount of catch if towing through each position.

This information must be updated as new information becomes available.

Cost prediction

Since the system is not responsible for taking strategic decisions, like when to stop fishing, it is concerned mainly with the changes it is able to make in the short term profit. The differences in costs for various trawl system trajectories are therefore more interesting than the absolute values, and the modeling of fixed costs are as a consequence less important. Important variable costs to model are for example fuel consumption and expected wear and tear (winches, warps, machinery). In addition, the use of actuators on the trawl door should be penalized, since such use is limited. This penalty should be calculated in relation to the expected haul length and the amount of energy left.

Safety and regulations constraints

To ensure the safety and the law-abidingness of the trawl system, the control system should be able to predict if a given trawl system trajectory is safe and legal or not. For these predictions, the control system needs information about:

- Other vessels and floating constructions (from radar).
- Sea bed obstacles and danger zones (from maps and user supplied information).
- Forbidden areas (from maps and regulations).

The primary task of the control system is to find a safe and legal trajectory for the trawl system. The search for maximum profit should therefore only start after such a trajectory is found.

4.3.3 Industrialization aspects

The border between the responsibilities of the captain and the control system may naturally evolve as the capabilities of and the confidence in the system and its hardware grows. The development may happen in stages:

1. Waypoint following: The captain inputs 3D waypoints and the system makes the center of the trawl opening pass these as closely as possible.
2. Catch control: The system monitors the fish finding equipment, estimates the amount of potential catch and controls the trawl to give as much catch as possible. The loss of catch and catching efficiency due to control actions should be modeled and taken into account.
3. Earnings control: In addition to the elements of catch control, also other financial terms are incorporated, such as wear and tear on the equipment, oil consumption and changes in maintenance needs.

Independent of these stages, it is also possible to implement safety control as a part of the objective function. The system would monitor other ships, the estimated positions of other trawls, obstacles like oil rigs and bottom topography, and try to avoid any conflicts. This kind of control would have to include either predictions on the behavior of other

vessels or a system for exchange of intents, and this is not explored any further in this thesis.

With stages 2 or 3 and safety control implemented, the system would in theory be able to take full short term control of the vessel. This would however also require robust methods to handle possible failures in both the control system (software, hardware) and the trawl system (power, actuators, machinery).

4.3.4 The objective evaluation function

The objective evaluation function should return a value reflecting how well a proposed control trajectory performs with regard to the stated objectives, constraints and premises for the given timespan. The timespan of the predictions depends upon the kind of objectives and premises to take into account. If strategic decisions should be made, the operation of the ship would have to be simulated for long timespans. This would add both to the complexity of the model, introducing discrete events, and to the necessary time to find a near-optimal solution. Strategic decisions are also often based on previous experiences and communication with people on other ships and onshore, and is therefore far more complicated to implement. The importance of strategic decisions increases with increased prediction horizon and varies with the kind of fishery in question. Since this work is restricted to tactical decisions, the prediction horizon may be shortened considerably.

For waypoint following, the optimization problem is simplified. If the order of the waypoints are determined by the captain, the goal is to find the control signals to reach the waypoints in the predetermined order. This makes it possible to find initial control setpoints close to the solution without numerical optimization. One way to achieve this is to simulate the performance of a simple feedback controller, and use its control commands as initial values for the optimization.

The optimization

It is in general not possible to guarantee fast and predictable convergence when optimizing nonlinear systems. Since the control system operates under real-time conditions, the optimization must be aborted when output is needed, and the best result that is found so far should be returned. To ensure that this result is acceptable, the optimization will first search for a suboptimal, fail safe solution and then for the optimum solution. The initial conditions of the first optimization are found by augmenting the previous control signal, taking only constraints into account. The second optimization will use the solution from the first as its initial conditions and implement all objectives.

There are many optimization routines available. These can be divided by the kind of problems they are developed to handle, and further by how they search for the optimum. The ideal optimization routine should always find the global optimum within the available time. The problem to solve will for the present case be nonlinear and likely to contain multiple local optima. This makes the optimization more challenging and time consuming, and there are in general no guarantees for finding the optimum solution. It is therefore essential to consider our priorities in order to find a suitable optimization routine, and to take measures to alleviate some of the shortcomings of the chosen method.

For this particular application, one may take advantage of physical understanding of the problem to increase the optimization efficiency. Some specific choices to consider are:

- Use a simplified method to calculate the trajectory derivatives with respect to the control input. In other words how the trajectory of the trawl system is affected by each control input. In this way the objective gradient may be estimated with less computational effort.
- Do initial iterations with a simplified model and increase model complexity as the optimization progresses. Implementation of constraints would be a challenge, but may not be important in the initial phase, as it may be solved by the more complex models.
- Decrease the number of unknowns during optimization:
  - Input blocking is an existing method which reduces the number of unknowns by allowing the control signals to change only at some fixed times (Maciejowski, 2002). The control signal can, using this method, be found by

$$\mathbf{u}(t) = \begin{bmatrix} q^a_{1+iN} \\ q^a_{2+iN} \\ \vdots \\ q^a_{N+iN} \end{bmatrix} \ , \ t_i < t \leq t_{i+1} \ , \ i = 0, 1, ..., N_k \tag{4.1}$$

    where $\mathbf{u}(t)$ is the control signal containing the setpoints for the plant and low level controllers, $\mathbf{q}^a$ is one option for the condensed control vector used in the optimization, and t_i is the time when the control signal value changes for the i'th time. N is the number of elements in the control signal, and N_k is the number of time intervals. The size of $\mathbf{q}^a$ is defined by (4.1).
  - Motivated by the Fourier transform and modal superposition, the setpoint of a plant or low level controller may be formulated as

$$\mathbf{u}(t) = \sum_{j=0}^{N_j} \mathbf{f}_j \left(\mathbf{q}^b, \ t \right) \tag{4.2}$$

    where $\mathbf{f}_j$ acts as a form function, N_j is the number of such functions and $\mathbf{q}^a$ is one option for the condensed control vector used in the optimization. Note that the formulation allows for arbitrary nonlinear formulations with regard to $\mathbf{q}^b$, as opposed to both the Fourier transform and modal superposition. The size of $\mathbf{q}^b$ would vary with the formulation of $\mathbf{f}_j$.

It is in this work proposed to decrease the number of unknowns in the optimization by letting the control vector represent the amount of total control forces acting on the net at predefined points in time and in predefined directions. The control signal is found as

$$\mathbf{u}(t) = \mathbf{f}\left(\mathbf{f}_c\left(\mathbf{q}\right)\right), \tag{4.3}$$

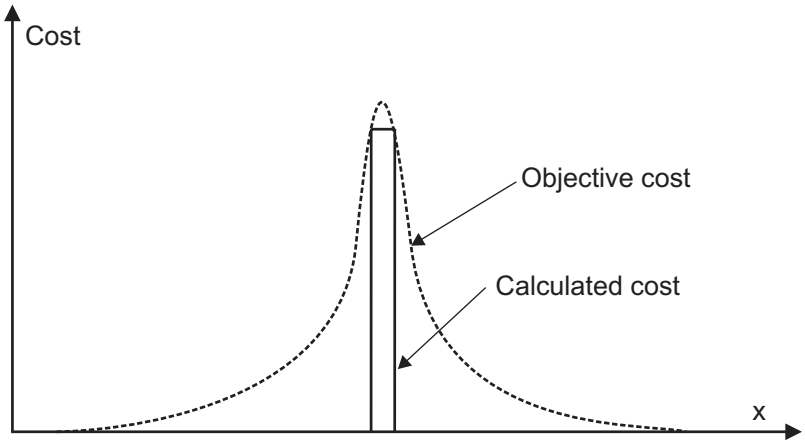

Figure 4.9: Increasing the cost if almost hitting an obstacle.

where $\mathbf{f}_c$ maps the discrete, condensed control vector to a continuous demand for control forces, and $\mathbf{f}$ finds the control signal to produce these forces. This representation causes loss of the ability to optimize how the forces should be created, but it saves computational effort. It is further proposed to enhance convexity in the proximity of a solution by adding benefit if almost catching fish and adding cost if almost hitting an obstacle. This is illustrated in Figure 4.9 for an imaginary, 2D case. The horizontal axis may for example be a choice of heading in a given period of time, and the vertical axis represents the disadvantage of a given heading. Objective cost is the cost that the objective function returns, while the calculated cost is an estimation of the real cost associated with for example hitting an obstacle. The real cost may include for example the cost associated with the lost fishing time and the damage to the net.

4.4 The trajectory controller

The trajectory controller and its sub-controllers are illustrated in Figure 4.10. The darker boxes represent components installed on most trawlers. The trajectory controller takes as its input the reference trajectories of various parts of the trawl system and the control signal trajectories (thrust, trawl doors hydrodynamic forces, warp lengths and heading) predicted to make the trawl system follow the reference. It uses the predicted trajectories of the plant controllers as an initial output, but adds corrections according to the difference between the reference and the estimated trawl system trajectories.

The distinction between tracking and maneuvering control is clarified in Fossen (2002) and references therein. In the trajectory controller, tracking control is employed. This is motivated by the fact that the initial trajectory errors are bounded by the accuracy of the FCPM, which is continuously improved by the model corrector, and the succeeding errors are bounded by the trajectory controllers ability to follow the reference. The trajectory error is therefore assumed to be small, and, more specifically, the effect of the error in

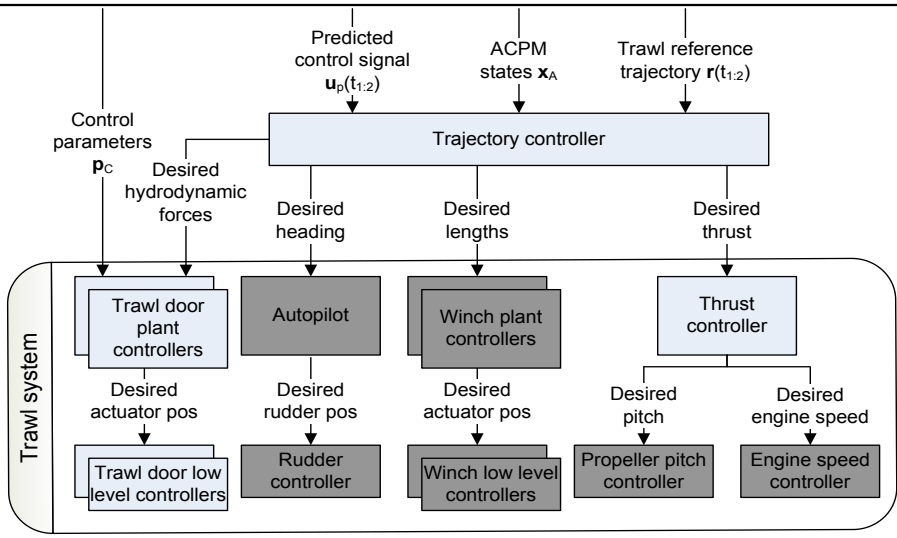

Figure 4.10: The trajectory controller and its subcontrollers.

x^t-position (forward in the trawl system frame) of the various parts of the trawl system are assumed to be negligible, because of the small curvature of the desired trajectory. This implies that it is sufficient to control the trawl system with respect to a reference as an explicit function of time (tracking control) as opposed to a parameterized path reference (maneuvering control).

The trajectory controller transfers the estimated trajectory errors into the appropriate frames, such as the ship frame and the trawl system frame, before the control actions are calculated. The trawl system frame is defined in Section 3.2.1 and illustrated in Figure 3.6. S, Q and R designate the positions of the ship, the port trawl door and the starboard trawl door, respectively. N designates the average position of the trawl net wings.

The relation between position differences in the trawl system frame and the global frame, is defined by the heading of the trawl system, ψ_t, only. This is found as

$$\psi_t = \mathsf{atan2}\left(y^n_{SN}, x^n_{SN}\right), \tag{4.4}$$

where $\mathsf{atan2}$ is the four-quadrant inverse tangent, as it is implemented in the Matlab$^{\text{TM}}$ package. The relation between a position difference in the trawl system frame and in the global frame is found as

$$\mathbf{p}^t_{BA} = \mathbf{R}^t_n \mathbf{p}^n_{BA}, \tag{4.5}$$

$$\mathbf{R}^t_n = \begin{bmatrix} \cos\psi_t & \sin\psi_t & 0 \\ -\sin\psi_t & \cos\psi_t & 0 \\ 0 & 0 & 1 \end{bmatrix}. \tag{4.6}$$

In a similar fashion the relation between a position difference in the ship frame and in

the global frame is found as

$$\mathbf{p}_{BA}^{s} = \mathbf{R}_{n}^{s}\mathbf{p}_{BA}^{n}, \tag{4.7}$$

$$\mathbf{R}_{n}^{s} = \begin{bmatrix} \cos\psi_s & \sin\psi_s & 0 \\ -\sin\psi_s & \cos\psi_s & 0 \\ 0 & 0 & 1 \end{bmatrix}. \tag{4.8}$$

For control purposes, the deviation vector in the global frame at a given time is calculated as

$$\boldsymbol{\varepsilon}^{n}(t) = \begin{bmatrix} \mathbf{p}_{N}^{n}(t) \\ \boldsymbol{\eta}_{S}^{n}(t) \\ \mathbf{p}_{Q}^{n}(t) \\ \mathbf{p}_{R}^{n}(t) \end{bmatrix} - \begin{bmatrix} \mathbf{r}_{N}^{n}(t) \\ \mathbf{r}_{S}^{n}(t) \\ \mathbf{r}_{Q}^{n}(t) \\ \mathbf{r}_{R}^{n}(t) \end{bmatrix}, \tag{4.9}$$

where $\mathbf{p}$ and $\mathbf{r}$ designates estimated and reference positions, respectively. The capital subscripts refer to the objects and positions in Figure 3.6 and the superscript n refers to the global frame. $\boldsymbol{\eta}_{S}^{n}(t) = \begin{bmatrix} x_S^n & y_S^n & \psi_s \end{bmatrix}$ is the 3dof position trajectory of the ship, and $\mathbf{r}_{S}^{n}(t)$ is the corresponding reference. The control deviation vector, $\boldsymbol{\varepsilon}^{c}$, is found in the individual frames by

$$\boldsymbol{\varepsilon}^{c} = \mathbf{R}_{n}^{c}\boldsymbol{\varepsilon}^{n}. \tag{4.10}$$

$$\mathbf{R}_{n}^{c} = \begin{bmatrix} \mathbf{R}_{n}^{t} & \mathbf{0}_{3\times3} & \mathbf{0}_{3\times3} & \mathbf{0}_{3\times3} \\ \mathbf{0}_{3\times3} & \mathbf{R}_{n}^{s} & \mathbf{0}_{3\times3} & \mathbf{0}_{3\times3} \\ \mathbf{0}_{3\times3} & \mathbf{0}_{3\times3} & \mathbf{R}_{n}^{t} & \mathbf{0}_{3\times3} \\ \mathbf{0}_{3\times3} & \mathbf{0}_{3\times3} & \mathbf{0}_{3\times3} & \mathbf{R}_{n}^{t} \end{bmatrix}. \tag{4.11}$$

The control vector $\mathbf{u}$ is calculated as the sum of the predicted control signal and a correction based on the estimated deviation:

$$\mathbf{u} = \mathbf{u}_p + \mathbf{f}_c(\boldsymbol{\varepsilon}^{c}), \tag{4.12}$$

where $\mathbf{u}_p$ is the predicted control vector, and $\mathbf{f}_c$ is the control feedback function. The control vector $\mathbf{u}$ is assembled as

$$\mathbf{u} = \begin{bmatrix} \alpha_{Q,d}^{d} & \gamma_{Q,d}^{g} & \alpha_{R,d}^{d} & \gamma_{R,d}^{g} & \psi_{s,d} & T_d & l_{w,d} & \Delta l_{w,d} \end{bmatrix}^{T}, \tag{4.13}$$

where $\alpha_{Q,d}^{d}$, $\gamma_{Q,d}^{g}$, $\alpha_{R,d}^{d}$ and $\gamma_{R,d}^{g}$ are the orientation angles of the two trawl doors. Q and R designate port and starboard trawl door, respectively. $\psi_{s,d}$ is the desired ship heading, T_d is the desired ship thrust, $l_{w,d}$ is the desired average warp length, and $\Delta l_{w,d}$ is the desired warp length difference.

4.5 The trawl door controllers

The control of the trawl doors should be as energy efficient as possible, since the available energy is expected to be limited. Every control action should therefore be well planned to minimize the energy consumption. To accomplish this, step-wise feedforward control

is used, as opposed to continuous feedback control. In feedforward control, the output of the controller is decided without regard to any measurements on the controlled system. By using feedforward control based on the reference, and ensure that the reference is mostly constant, excessive actuator actions are avoided.

The main drawback of feedforward control is that inaccuracies in the model may lead to severe performance degradation, making an accurate system model necessary. Since a sufficiently accurate model of a specific trawl door is in general hard to obtain in advance, online parameter estimation is employed by the model corrector to improve the model. This introduces feedback into the system, but only at certain time instants and at a low update rate. It will therefore not lead to high energy consumption on the trawl door.

The choice of trawl door control reference and setpoints is critical for the performance of the control system. The reference and setpoints may be for example:

- Hydrodynamic forces.
- Orientation angles of the trawl doors (if the hydrodynamic properties of the trawl doors are not altered by the control actions).
- Local actuators positions.

These strategies differ in how the computational burden is divided between the local real-time controller and the model-based control algorithm. The implications are that if more computations are done locally:

- The computational burden on the optimization algorithm is decreased, making it possible to do more objective function evaluations within the available time.
- The control system becomes more modular, making it possible to use completely different kinds of devices to obtain the hydrodynamic forces necessary to spread the trawl system, as long as their properties are known. The main control system doesn't have to be adapted to the choice of spreading device.
- It may get more difficult to take some of the nonlinearities of the system into account. Especially how the hydrodynamic forces are affected by other parameters than the local actuators positions, such as turning of the ship, changes in the warp lengths, changes in the trawl net and speed changes. This makes the calculations less accurate, and it makes the constraints of the system difficult to handle correctly.
- A model must be made to map the relation between the control input of the trawl doors and the output, or more specifically: The necessary local actuators positions must be calculated as a function of the desired output, such as the hydrodynamic forces or orientation angles. For such a highly nonlinear system this is not straightforward, and iterations or approximations are necessary.

It is chosen to use the desired orientation angles as input for the local trawl door controller. Compared to using the local actuators positions, this choice reduces computation time in the optimization process, as the mapping between the local actuators positions and the orientation angles can be left out of the FCPM. As computer capacity improves, it may in the future be advantageous to use the local actuators positions as input, and

maybe also include the dynamics of the trawl doors, but for the near future this does not seem possible.

Compared to using the hydrodynamic forces, this choice separates the estimation of the hydrodynamic forces and the orientation angles between the control plant models and the control influence model, respectively. Since the hydrodynamic (lift) forces are more likely to be sufficiently accurate modeled, while the orientation angles are easier to measure, this division seems beneficial.

4.6 The observers

The measurements on the trawl system are expected to be inaccurate, scarce, scattered in time and unreliable. At the same time, the trawl system is assumed to be kept stable by the plant controllers. Independent models are therefore used for state estimation, one for each control plant model.

The observers take the control signal from the trajectory controller and the parameters of its mathematical model as input, and return the states of the dynamic model. The feedback from measurements are thus obtained purely through the correction of the model parameters by the model corrector.

The ACPM independent model estimates the trawl system states. The reason for using an observer based on the FCPM in addition to the one based on the ACPM, is that the initial states of the "Predictor 1" FCPM in the predictive controller (Figure 4.7) have to be set each time the predictive controller returns a reference. These initial states could be calculated from the states of the ACPM, eliminating the need for the FCPM observer, but due to the difference in formulations this would be more complicated and result in transients in the start of the predictions.

4.7 The control plant models

4.7.1 The accurate control plant model (ACPM)

The accurate control plant model (ACPM) is run for the purpose of state estimation, so it should be able to run real-time while being fairly accurate. The ACPM is formulated as the process plant model presented in Section 3.4, but includes some parameters representing the uncertainties of the mathematical modeling. These parameters are supplied by the model corrector, and they decrease the errors in the mathematical models of the trawl system.

The vector of ACPM correction parameters, $\mathbf{p}_A$, is collected as

$$\mathbf{p}_A = \begin{bmatrix} p_{A,1} & p_{A,2} & p_{A,3} & p_{A,4} & p_{A,5} & p_{A,6} & p_{A,7} \end{bmatrix}^T, \tag{4.14}$$

where the relation between the individual elements of $\mathbf{p}_A$ and the correction terms are explained in the following.

The hydrodynamic forces on the trawl door

The coefficients of the steady state hydrodynamic forces on the trawl door in the trawl door frame $\mathbf{C}^{\infty}_{d\Upsilon}\left(\alpha^d, \beta^d\right)$ are only corrected by a common factor. The resulting hydrodynamic coefficients are calculated as

$$\mathbf{C}^{\infty}_{d\Upsilon}\left(\alpha^d, \beta^d\right) = p_{A,1}\bar{\mathbf{C}}^{\infty}_{d\Upsilon}\left(\alpha^d, \beta^d\right), \tag{4.15}$$

where $\bar{\mathbf{C}}^{\infty}_{d\Upsilon}\left(\alpha^d, \beta^d\right)$ are the originally calculated hydrodynamic constants. The use of higher order correction terms are avoided.

The weight force on the trawl doors

The weight of the trawl doors are used for calibration purposes, by multiplying its net weight in water by a factor:

$$\vec{f}_{d\rho} = p_{A,2}\vec{f}^{0}_{d\rho}, \tag{4.16}$$

where $\vec{f}^{0}_{d\rho}$ is the trawl door weight force originally estimated, and $\vec{f}_{d\rho}$ is the resulting trawl door weight force.

The drag of the trawl net

The drag of the trawl net is corrected by multiplying the hydrodynamic forces on each member of the trawl net by a common factor, $p_{A,3}$, according to

$$\vec{f}^{j}_{v_n} = p_{A,3}\ \vec{f}^{0,j}_{v_n}, \tag{4.17}$$

$$\vec{f}^{j}_{v_t} = p_{A,3}\ \vec{f}^{0,j}_{v_t}, \tag{4.18}$$

where $\vec{f}^{j}_{v_n}$ and $\vec{f}^{0,j}_{v_n}$ are the corrected and original hydrodynamic normal force on the net element number j, and $\vec{f}^{j}_{v_t}$ and $\vec{f}^{0,j}_{v_t}$ are the corrected and original hydrodynamic tangential force on the same element.

The weight forces on the lower wings

The weight forces on the lower wings are adjusted by multiplying their net weight in water by a common factor. This force is found as

$$\vec{f}_{lpw} = p_{A,4}\vec{f}^{0}_{lpw}, \tag{4.19}$$

$$\vec{f}_{lsw} = p_{A,4}\vec{f}^{0}_{lsw}, \tag{4.20}$$

where the subscripts l, p, s, and w designate lower, port, starboard and wing, respectively, and the superscript 0 designates the original values.

The length of the warps

The length of the warps are corrected by a common factor for both warps:

$$l_{pw} = p_{A,5}\, l^0_{pw}, \tag{4.21}$$
$$l_{sw} = p_{A,5}\, l^0_{sw}, \tag{4.22}$$

where l_{pw} and l_{sw} are the port and starboard warp length, respectively, and the superscript 0 designates the original values.

The heading of the ship

The ship heading is corrected by adding a value:

$$\psi_{s,d} = \psi^0_{s,d} + k_\psi \left(p_{A,6} - 1\right), \tag{4.23}$$

where k_ψ is a constant.

The ship thrust

The ship thrust is corrected by adding a value:

$$T_d = T^0_d + k_T \left(p_{A,7} - 1\right), \tag{4.24}$$

where k_T is a constant.

4.7.2 The fast control plant model (FCPM)

Since the fast control plant model in the predictor must run many times for every MPC output, it is important to minimize the associated computational effort. This rises the question of simplicity vs. accuracy. Less accuracy not only renders the results less accurate, but introduces problems with the implementation of restrictions/constraints. This means that the trajectory that is found to be optimal may be infeasible. It may also be the other way around: The optimum trajectory may not be found because it is found to be infeasible. If the accuracy of (and the computational effort associated with) the objective function on the other hand is increased, the optimization may have to be aborted long before the optimum solution is found.

If the accuracy of the FCPM is improved, the rate of the output may on the other hand be much smaller. This would leave more time for each optimization. The minimum rate is determined by both theoretical and practical aspects. The theoretical aspects are for example the inaccuracies in the model and how these propagate with time. Practical aspects are for example sonar range and accuracy.

Since the demands on accuracy and efficiency oppose each other, the FCPM formulation is a compromise. To implement as much as possible of the benefits of both ways of doing the modeling, the references of the plant and low level controllers are assumed to be followed perfectly and can thus be eliminated from the model. This speeds up the model evaluations considerably. The following plant and low level controllers are assumed to work perfectly:

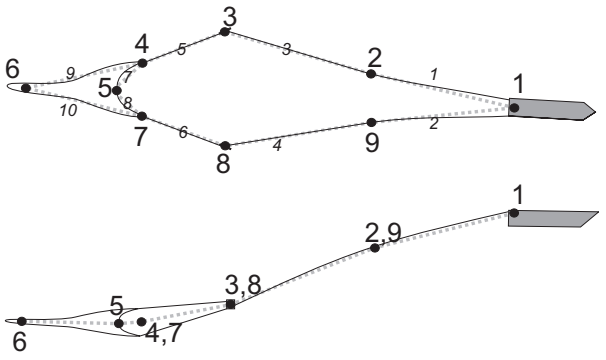

Figure 4.11: The nodes of the fast control plant model.

- The autopilot.
- The thrust controller.
- The winch controllers.
- The trawl door controllers.

To avoid large transients in the simulation and to approximate the real system better, the dynamics of these controllers are replaced by rate limitations. The rate limits are found through trial and error. In addition, the dynamics of the autopilot is replaced by a changing thrust direction, and is implemented as

$$\psi_{thrust} = \psi_s - k\left(\psi_s - \psi_t\right), \tag{4.25}$$

where ψ_s is the heading of the ship, ψ_t is the heading of the trawl system, as defined in (4.4), and k is a constant chosen between 0 and 1. For the simulations, $k = 0.9$ is used. The difference in heading angles are computed such that no problems occur because of the 360 degrees heading cycle.

The input of the FCPM is:

- Desired hydrodynamic orientation angles on each trawl door.
- Desired warp lengths.
- Desired vessel heading.
- Desired thrust.

In addition, the estimated model parameters must be supplied, and the initial states of the model must be given when it is initialized.

The geometry of the fast control plant model is shown in Figure 4.11. The trawl system is modeled as nine nodes with interconnections. All mass and all forces are distributed amongst the nodes. The elements are modeled by the cable element developed

in Section 3.4.2. The warps and the bridles are modeled by their physical properties, but their stiffness is reduced to accommodate faster simulations.

All the nodes are attacked by the forces on the connected elements, such as hydrodynamic, hydrostatic, gravity and contracting forces. Some of the nodes are affected by additional forces:

- Node 1 is attacked by the net thrust vector from the vessel.
- Node 3 and 8 are attacked by the hydrodynamic forces on and the net weight of the trawl doors.
- Node 4 and 7 are attacked by the net weight of the weights attached to the trawl net wings.

Only the steady state hydrodynamic forces on the trawl doors are calculated, and the angle of slip is assumed to be zero. The trawl door is assumed to maintain the desired angles of roll and attack in the trawl system frame, and a constant trawl door speed is used for the hydrodynamic force calculations. Linear damping is used both to model the effect of angle of slip, and to increase the simulation speed.

The properties of the rest of the trawl system are set to approximate the performance of the ACPM.

Model adjustments through parameter estimation are essential to obtain an adequate accuracy. The vector of correction parameters, $\mathbf{p}_F$, is collected as

$$\mathbf{p}_F = \begin{bmatrix} p_{F,1} & p_{F,2} & p_{F,3} & p_{F,4} & p_{F,5} & p_{F,6} & p_{F,7} \end{bmatrix}^T . \tag{4.26}$$

The individual elements of $\mathbf{p}_F$ are various correction terms:

1. The calculated hydrodynamic forces on the trawl doors (nodes 3 and 8) are multiplied by $p_{F,1}$.
2. The weight of the trawl doors (nodes 3 and 8) are multiplied by $p_{F,2}$.
3. The hydrodynamic forces on the trawl net (elements 7 to 10) are multiplied by $p_{F,3}$.
4. The weight of the wings (nodes 4 and 7) are multiplied by $p_{F,4}$.
5. The warp lengths (elements 1 to 4) are multiplied by $p_{F,5}$.
6. The ship heading is added a value $k_\psi \left(p_{F,6} - 1\right)$, where k_ψ is the same as in (4.23).
7. The ship thrust is added a value $k_T \left(p_{F,7} - 1\right)$, where k_T is the same as in (4.24).

4.7.3 The control influence model

The control influence model calculates the local actuators positions needed to obtain the desired response. If, for example, the trawl door orientation angles are used for controlling the hydrodynamic forces on the trawl doors, the CIM does the mapping from the desired orientation angles to the desired local actuators positions.

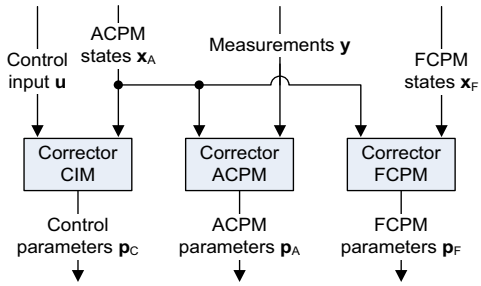

Figure 4.12: The corrector.

The CIM is in this case formulated as

$$\mathbf{u}^d = \mathbf{f}_{CIM}\left(\mathbf{p}_C, \begin{bmatrix} \alpha^d_{Q,d} \\ \gamma^g_{Q,d} \\ \alpha^d_{R,d} \\ \gamma^g_{R,d} \end{bmatrix}\right), \tag{4.27}$$

where $\mathbf{u}^d$ is the local actuators positions predicted to result in the desired trawl door orientation angles. $\mathbf{f}_{CIM}$ is the control influence model, and $\mathbf{p}_C$ is a set of parameters determining this model.

The formulation of $\mathbf{f}_{CIM}$ must provide enough flexibility to ensure that adjusting the parameters $\mathbf{p}_C$ may render it sufficiently accurate. At the same time, the number of parameters must be kept low enough to make the parameter estimation practical, and care should be taken if using higher order terms.

4.8 The model corrector

The model corrector estimates the parameters of the mathematical models of the trawl system, as shown in Figure 4.12. This improves the accuracy of the mathematical models, which improves the performance of the control system.

The model corrector calculates the model parameters of:

- The ACPM, based on the trawl system measurements and the ACPM independent model states.
- The FCPM, based on the ACPM and FCPM independent model states.
- The CIM, based on the trawl system control input and the ACPM states.

The parameter estimation is performed both on-line and off-line. Off-line parameter estimation is performed on a set of measurements, for example using simulations before the system is implemented into a real plant, and may use conventional parameter estimation to estimate $\mathbf{p}_A$, $\mathbf{p}_F$ and $\mathbf{p}_C$.

On-line estimation is performed while the system is running. This means that new measurements are continuously used to update $\mathbf{p}_A$, $\mathbf{p}_F$ and $\mathbf{p}_C$. A method for estimating the necessary parameters of the trawl system may consist of three different phases:

1. Initial parameters are estimated before first haul with a new trawl system.
2. On-line parameter estimation during each haul.
3. Off-line parameter estimation between hauls, based on selected measurements from previous history with the particular trawl system.

The method for on-line estimation of the parameters of the control plant models is motivated by the Fourier transform and neural networks. A recursive algorithm is desirable, as it saves computation time and avoids excessive memory requirements.

Since the procedure of correcting the model is similar for both the ACPM and the FCPM, except for the fact that all states are available for correction of the FCPM, the procedure is only explained for the correction of the ACPM.

The positions from available measurements and the corresponding states of the ACPM, are for the ship found relative to the ship position of the last parameter update, and for the trawl net and the trawl doors found relative to the ship:

$$\hat{\mathbf{p}}_S = \mathbf{p}_S - \mathbf{p}_S^0, \tag{4.28}$$

$$\hat{\mathbf{p}}_N = \mathbf{p}_N - \mathbf{p}_S, \tag{4.29}$$

$$\hat{\mathbf{p}}_Q = \mathbf{p}_Q - \mathbf{p}_S, \tag{4.30}$$

$$\hat{\mathbf{p}}_R = \mathbf{p}_R - \mathbf{p}_S, \tag{4.31}$$

where $\mathbf{p}_S$, $\mathbf{p}_Q$, $\mathbf{p}_R$ and $\mathbf{p}_N$ are the positions of the ship, the port and starboard trawl door and the trawl net, respectively. The accent $\hat{}$ denotes relative positions. $\mathbf{p}_S^0$ denotes the position of the ship for the last parameter update. These positions are all given in the global frame. The deviations between the measurements on the real system and those calculated by the ACPM are found as

$$\Delta\hat{\mathbf{p}}^n = \hat{\mathbf{p}}^A - \hat{\mathbf{p}}^m, \tag{4.32}$$

where $\hat{\mathbf{p}}^A$ denotes a position calculated by the ACPM and $\hat{\mathbf{p}}^m$ denotes a measurement on the trawl system. These position differences are transferred from the global frame to the trawl system frame by

$$\Delta\hat{\mathbf{p}}^t = \mathbf{R}_n^t \Delta\hat{\mathbf{p}}^n, \tag{4.33}$$

where $\mathbf{R}_n^t$ is the rotation matrix defined in (4.6). This is found using the average heading of the trawl system, ψ_t, calculated from the predictions of the ACPM. As an example, $\Delta\hat{\mathbf{p}}_Q^t$ denotes the difference between the relative positions of the port trawl doors, in the trawl system frame of the ACPM. The deviations between these relative positions are used for the parameter updates. The parameters of the ACPM are updated by

$$\mathbf{p}_{A,k+1} = \mathbf{p}_{A,k} + \mathbf{J}_k^A \mathbf{K}_k^A \left(\boldsymbol{\varepsilon}_k^A\right)^T, \tag{4.34}$$

where $\mathbf{K}_k^A$ and $\mathbf{J}_k^A$ are the weight matrix and the influence matrix, respectively. The deviation vector is collected as

$$\boldsymbol{\varepsilon}_k^A = \begin{bmatrix} \Delta\mathbf{p}_S^t \\ \Delta\hat{\mathbf{p}}_S^t \\ \Delta\hat{\mathbf{p}}_N^t \\ \Delta\hat{\mathbf{p}}_Q^t \\ \Delta\hat{\mathbf{p}}_R^t \end{bmatrix}. \tag{4.35}$$

If more than one measurement is available for the parameter estimation, the average values are used for the deviation of the trawl doors and the trawl net, while the current estimation is always used for the ship position and the ship deviation. The influence matrix $\mathbf{J}_k^A$ reflects the influence on the various parameters from the deviations in different directions and for different parts of the trawl system. $\mathbf{J}_k^A$ is initially found by considering how the various model parameters should be adjusted:

$p_{A,1}$: This parameter controls the hydrodynamic forces on the trawl doors. It should be adjusted to give equal distance between the trawl doors for the two models.

$p_{A,2}$: This parameter controls the weight force attacking the trawl doors. It should be adjusted to give equal depth of the trawl doors and the trawl net for the two models.

$p_{A,3}$: This parameter controls the drag of the trawl net. It may be adjusted to give equal trawl net and trawl door depths for the two models, and also to equal the thrust and the ship travel in the x^t-direction (forward) for the two models. This parameter is redundant, and allows for the parameter estimation to avoid some of the other parameters to deviate too much from the original value (1), such that the model remains as close to the original as possible. It is here adjusted only to control how far the ship travels.

$p_{A,4}$: This parameter controls the weight on the wings of the trawl net. It should be adjusted to give equal difference in depth between the trawl net and the trawl doors for the two models.

$p_{A,5}$: This parameter controls the warp lengths. It should be adjusted to give equal horizontal distance between the ship and the other parts of the trawl system for the two models. It is also used for correcting the depth of the trawl net.

$p_{A,6}$: This parameter controls the heading of the ship. It should be adjusted to give equal travel in the y^t-direction (sideways) for the two models, and to eliminate the accumulated position difference in this direction.

$p_{A,7}$: This parameter controls the thrust of the ship. It should be adjusted to give equal travel in the x^t-direction (forward) for the two models, to eliminate the accumulated position difference in this direction, and to adjust the depth of the trawl doors and the trawl net.

From these considerations, the influence matrix $\mathbf{J}_k^A$ is proposed to have the structure

$$\mathbf{J}_k^A = \begin{bmatrix} 0 & 0 & 0 & 0 & 0 & 0 & 0 & 0 & 0 & 0 & 1 & 0 & 0 & -1 & 0 \\ 0 & 0 & 0 & 0 & 0 & 0 & 0 & 0 & -1 & 0 & 0 & -1 & 0 & 0 & -1 \\ 1 & 0 & 0 & 1 & 0 & 0 & 0 & 0 & 0 & 0 & 0 & 0 & 0 & 0 & 0 \\ 0 & 0 & 0 & 0 & 0 & 0 & 0 & 0 & -2 & 0 & 0 & 1 & 0 & 0 & 1 \\ 0 & 0 & 0 & 0 & 0 & 0 & 1 & 0 & -1 & 1 & 0 & 0 & 1 & 0 & 0 \\ 0 & -1 & 0 & 0 & -1 & 0 & 0 & 0 & 0 & 0 & 0 & 0 & 0 & 0 & 0 \\ -1 & 0 & 0 & -1 & 0 & 0 & 0 & 0 & 1 & 0 & 0 & 1 & 0 & 0 & 1 \end{bmatrix}. \tag{4.36}$$

The influence matrix $\mathbf{J}_k^A$ should include properties to avoid the change in one parameter to affect other parts of the trawl system than intended. If for example the thrust is increased to adjust the position of the ship, it might be beneficial to increase the trawl door weights or decrease the trawl net drag to keep the depth of the trawl net. The gain matrix $\mathbf{K}_k^A$ should take into account the expected accuracy of the measurements and the time since the last parameter update.

The FCPM is corrected in the same manner, only using the ACPM states instead of the trawl system measurements when calculating the corrections.

Chapter 5

Case studies

In this chapter, some case studies are presented. Simulations are performed to verify the various parts of the control system, and the results form a basis for assessing the supervisory control structure. The following parts of the control structure are evaluated:

The control plant models: The ability of the FCPM to estimate the states of the ACPM is studied, and the relation between the PPM, the ACPM and the FCPM is documented.

The corrector: The ability of the corrector to adjust the model parameters of the FCPM and the ACPM to match the performance of the PPM is verified.

The trawl door controllers: The effect of the trawl door control on the trawl system is compared to the effect of thrust and winch control.

The trajectory controller: The ability of the trajectory controller to make the trawl system follow the reference trajectory obtained from the predictive controller is verified.

The predictive controller: The ability of the predictive controller to find a close-to-optimum control and trajectory reference is evaluated.

When nothing else is stated, the simulations are based on the base case trawl system defined in Appendix B.

5.1 The control plant models

The ACPM can not be expected to possess exactly the same characteristics as the real trawl system. Three mathematical models of the trawl system is therefore needed for control system robustness evaluation: The PPM, the ACPM and the FCPM. The PPM and the ACPM is essentially the same model, but a difference is created by changing the

t [s]	0	500	900	1300
$\alpha^d_{Q,d}$	25 °	22 °	28 °	25 °
$\gamma^g_{Q,d}$	0 °	10 °	15 °	−10 °
$\alpha^d_{R,d}$	25 °	22 °	28 °	25 °
$\gamma^g_{R,d}$	0 °	10 °	15 °	−10 °
$\psi_{s,d}$	270 °	180 °	150 °	180 °
T^s_d	400 kN	450 kN	350 kN	400 kN
$l_{w,d}$	500 m	450 m	550 m	500 m
$\Delta l_{w,d}$	0 m	0 m	0 m	0 m

Table 5.1: Control trajectory used in the simulations of Sections 5.1, 5.2 and 5.4.

model parameters of the PPM. The following parameters are used:

$$\begin{aligned} \mathbf{p}_P &= \begin{bmatrix} 0.9 & 0.9 & 0.9 & 0.9 & 0.9 \end{bmatrix}, \\ \mathbf{p}_A &= \begin{bmatrix} 1.0 & 1.0 & 1.0 & 1.0 & 1.0 \end{bmatrix}, \\ \mathbf{p}_F &= \begin{bmatrix} 1.0 & 1.0 & 1.0 & 1.0 & 1.0 \end{bmatrix}, \end{aligned}$$

where the elements of $\mathbf{P}_P$, $\mathbf{P}_A$, and $\mathbf{P}_F$ are described in Section 4.7.

This choice of parameters is believed to render the control plant models at least as different from the PPM as they could be expected to be in relation to the real trawl system. The following two sections document the difference between the three models in steady state and for a predetermined control trajectory.

5.1.1 Constant control signal

Since the PPM is assumed to be unknown, the FCPM is initially calibrated against the ACPM for the steady state conditions defined by the control input shown for $t = 0$ in Table 5.1. Starting at their individual steady states for the chosen constant control input, the three models are simulated for 1500s. The positions of their various parts at the end of the simulations are found in relation to the initial position of the ship. The final positions of the FCPM and the PPM in relation to the ACPM are presented in Table 5.2. The values should be seen in relation to the approximately 3000 m the trawl system has traveled and the roughly 200 m depth of the trawl net. It can be seen that the steady states of the FCPM match those of the ACPM quite closely, as expected, since the FCPM is calibrated against the ACPM.

These changes in the PPM parameters are seen to give the desired deviation from the ACPM states.

5.1.2 Predetermined control trajectory

Having calibrated the FCPM towards the ACPM in the steady state scenario, and having changed the parameters of the PPM to make it less accurate, it is of interest to see how the models perform when receiving an equal, predetermined control trajectory with no feedback. The control trajectory is shown in Table 5.1, where the header row shows the

	Δx^n [m]	Δy^n [m]	Δz^n [m]
FCPM net opening	3.1	−4.8	−0.2
FCPM ship	4.8	−25.5	–
FCPM ptd	8.2	−1.8	2.8
FCPM std	−2.8	−3.4	1.9
PPM net opening	−29.6	396.3	−36.0
PPM ship	27.2	487.7	–
PPM ptd	−13.0	398.8	−36.0
PPM std	−40.0	428.4	−36.4

Table 5.2: Steady state deviations of the FCPM and the PPM in relation to the ACPM after 1500s with no feedback. The deviations of the PPM are intentional, representing modeling uncertainty.

time in seconds since the start of the simulation. Each column shows the control input at that time. The control input is obtained by linear interpolation between the values at given times, and by holding the last value after the last given time.

Figures 5.1 - 5.4 show how the three mathematical models perform for this control input trajectory. Relating the PPM and the FCPM to the ACPM, it is seen that in both the horizontal and vertical plane, the largest deviations occur for the PPM, as expected.

A potential problem with the FCPM is its simplified heading dynamics. Even if it seems like the ability of the FCPM to create a trajectory in the horizontal plane approximately matches that of the ACPM, this is tested for one case only. As the FCPM is used in the optimization to evaluate and find the best control and reference trajectories, this is the most important aspect. It keeps the part of the reference describing the motion in the horizontal plane feasible, while not rejecting feasible trajectories as infeasible because of erroneous capability estimates.

The changes in thrust between 350kN and 450kN and the changes in warp lengths between 450 m and 550 m are done simultaneously and in such a way that they act together. At the same time, the depths of the various parts of the trawl system are affected by the turning of the ship. It is seen in Figures 5.3 - 5.4 that both the ACPM and the PPM predict a notable difference between the depth of the port and the starboard trawl door, while this is not the case for the FCPM. The ACPM predicts the deepest point to be 227 m and 212 m for the port and starboard trawl door, respectively, while the FCPM predicts both trawl doors to reach a maximum depth of approximately 200 m (203 m and 198 m). This trawl door depth difference is probably caused by the heading change, but the reason why the FCPM is not showing this as pronounced as the more accurate models is not obvious. One explanation may be that the hydrodynamic forces on the trawl doors are by the FCPM calculated for a fixed speed and orientation, and that it is these factors that cause the PPM and the ACPM to predict the larger depth difference.

In Figure 5.1 it is seen that the deviation between the depth of the trawl net predicted by the ACPM and the PPM is approximately constant, while the depth dynamics of the FCPM seem to be different. The grey drawing in the upper plot indicates the size of the trawl system.

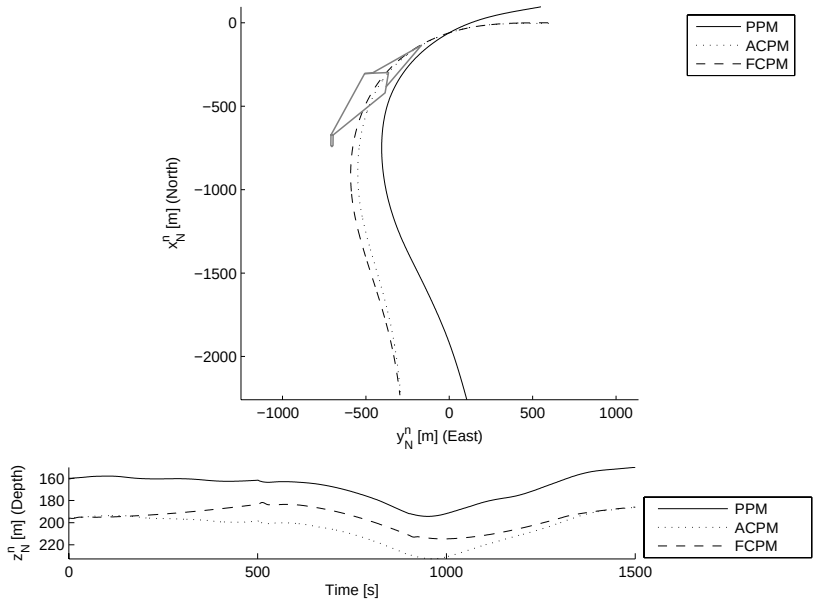

Figure 5.1: Comparison between the trawl net trajectory of the three mathematical models, using predetermined control actions and no feedback.

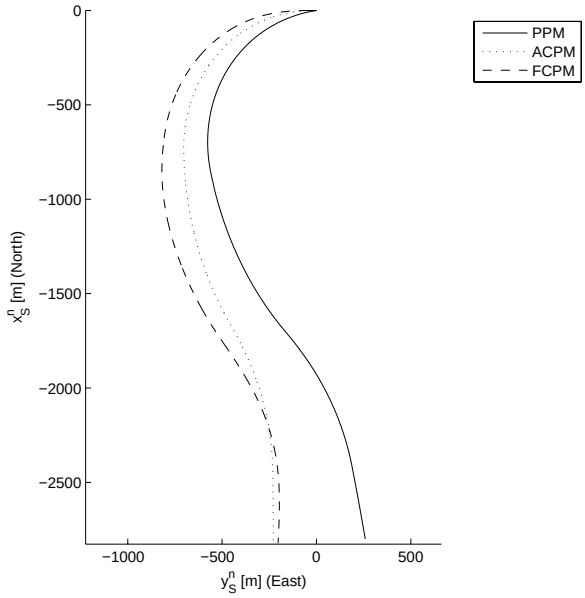

Figure 5.2: Comparison between the ship trajectory of the three mathematical models, using predetermined control actions and no feedback.

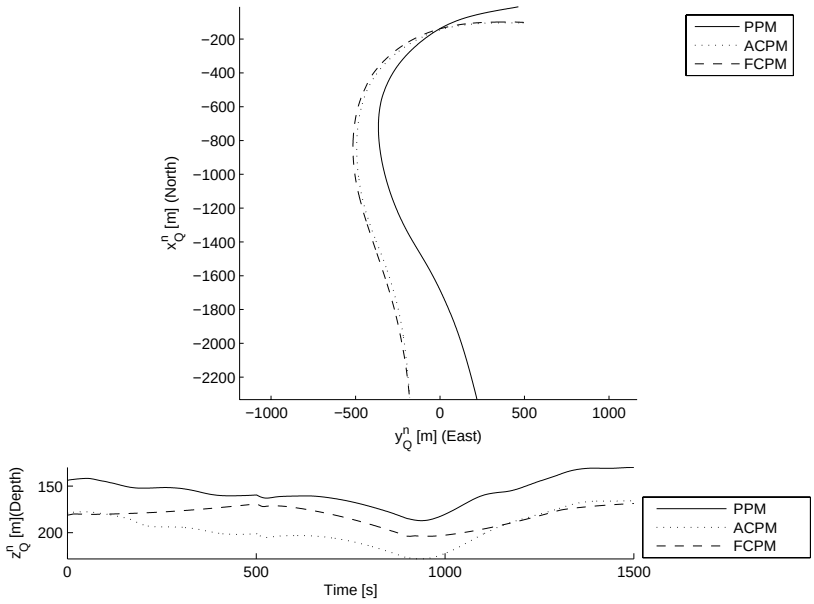

Figure 5.3: Comparison between the port trawl door trajectory of the three mathematical models, using predetermined control actions and no feedback.

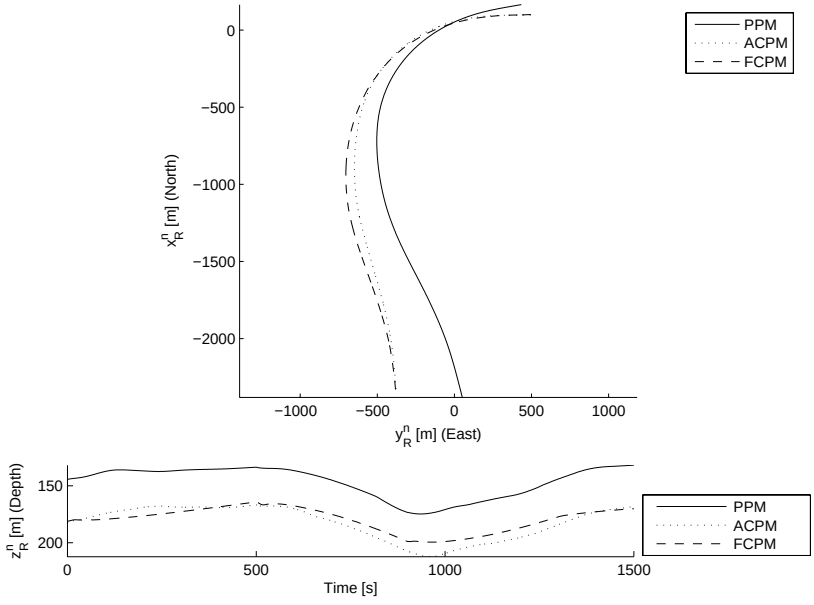

Figure 5.4: Comparison between the starboard trawl door trajectory of the three mathematical models, using predetermined control actions and no feedback.

5.1.3 Conclusion

For the cases tested in this section, the steady states of the FCPM and the ACPM matched each other closely, while the dynamic properties were less accurate. The FCPM seemed to predict slower depth changes than the other models, and it did not reflect the trawl doors depth dynamics well while turning. This may origin in the simplified modeling of the trawl net and the trawl doors in the FCPM, and it indicates that the FCPM should be calibrated also for unsteady conditions. It is also seen that the proposed changes in the process plant parameters lead to a significant deviation between the PPM and the control plant models, as was the intention. The size of this deviation seems sufficient for testing the robustness of the control system.

5.2 The corrector

The main task of the corrector is to update the model parameters of the control plant models to make their response closer to that of the real system. The real trawl system is for the simulations replaced by the PPM. The performance of the corrector is shown through repeated simulations of the three models, using the control trajectory defined in Table 5.1 and no feedback control action. The corrections on the control plant parameters are calculated and the parameters updated after each simulation.

5.2.1 Measurement error dynamics

For this case study, the following measurements are assumed to be available:

- Ship position from GPS or DGPS.
- Trawl door positions from hydro acoustic and water pressure measurements.
- Trawl net position from hydro acoustic and water pressure measurements.

The various available measurements have different error characteristics. For the simulations, these characteristics are modeled as

$$y_i = y_i^P + N_i\left(\sigma_m\right), \tag{5.1}$$

where y_i is the measured value at sample i, which is taken at time iT_m. y_i^P is the corresponding PPM prediction, and $N_i\left(\sigma_m\right)$ is the i'th sample of the normal distribution with standard deviation σ_m. The measurements are assumed to have a variance σ_m^2, but no bias. In addition to the added error, the measurements are made available only at some specific points in time, with interval T_m.

The horizontal positions of the trawl net and the trawl doors are measured using acoustic transponders. These measurements are relatively inaccurate and have a low update rate. Using an independent mathematical model of the trawl system for state estimation, these measurements are not essential. For generality, they are, however, implemented into the PPM. These measurements are in the simulations modeled with standard deviation $\sigma_m = 40\,\mathrm{m}$ and interval between measurements $T_m = 20\,\mathrm{s}$.

The depths of various parts of the trawl system are usually measured by pressure sensors. These are modeled as in (5.1), using a standard deviation of $\sigma_m = 5\,\text{m}$ and $T_m = 20\,\text{s}$.

The ship position is usually measured by GPS or DGPS. Since the SA code was discontinued, the GPS accuracy has improved, and for the simulations $\sigma_m = 5\,\text{m}$ and $T_m = 1\,\text{s}$ is used.

5.2.2 Implementation of the corrector

Since the simulations are restarted with the same states every 1500s, the implementation of $\Delta\mathbf{p}_S^t$ (the accumulated deviation in ship position) in the deviation vector, as proposed in Section 4.8, would lead to saturation of the parameters. To avoid this, $\Delta\mathbf{p}_S^t$ is for the case studies replaced by $\Delta\hat{\mathbf{p}}_S^t$ (the deviation in ship position since the last corrector update). The deviation vector of the corrector is for the simulations found as:

$$\varepsilon_k^A = \begin{bmatrix} \Delta\hat{\mathbf{p}}_S^t \\ \Delta\hat{\mathbf{p}}_S^t \\ \Delta\hat{\mathbf{p}}_N^t \\ \Delta\hat{\mathbf{p}}_Q^t \\ \Delta\hat{\mathbf{p}}_R^t \end{bmatrix} = \begin{bmatrix} \bar{\mathbf{R}}_n^t \frac{\sum_{i=N_r-N_{r0}}^{N_r}\left(\mathbf{p}_{S,i}^A - \mathbf{p}_{S,i}^m\right) - \sum_{i=1}^{N_{r0}}\left(\mathbf{p}_{S,i}^A - \mathbf{p}_{S,i}^m\right)}{N_{r0}} \\ \bar{\mathbf{R}}_n^t \frac{\sum_{i=N_r-N_{r0}}^{N_r}\left(\mathbf{p}_{S,i}^A - \mathbf{p}_{S,i}^m\right) - \sum_{i=1}^{N_{r0}}\left(\mathbf{p}_{S,i}^A - \mathbf{p}_{S,i}^m\right)}{N_{r0}} \\ \frac{\sum_{i=1}^{N_a}\mathbf{R}_n^t\left(\mathbf{p}_{N,i}^A - \mathbf{p}_{S,i}^A - \mathbf{p}_{N,i}^m + \mathbf{p}_{S,i}^m\right)}{N_a} \\ \frac{\sum_{i=1}^{N_a}\mathbf{R}_n^t\left(\mathbf{p}_{Q,i}^A - \mathbf{p}_{S,i}^A - \mathbf{p}_{Q,i}^m + \mathbf{p}_{S,i}^m\right)}{N_a} \\ \frac{\sum_{i=1}^{N_a}\mathbf{R}_n^t\left(\mathbf{p}_{R,i}^A - \mathbf{p}_{S,i}^A - \mathbf{p}_{R,i}^m + \mathbf{p}_{S,i}^m\right)}{N_a} \end{bmatrix}, \tag{5.2}$$

where N_a is the number of acoustic measurements since the last parameter update (assumed to be the same for all acoustic measurements), N_r is the number of radio navigation measurements since the last parameter update, and N_{r0} is the number of measurements used to estimate the position of the ship at the start and the end of each measurement period. $\bar{\mathbf{R}}_n^t$ is the rotation matrix from the global frame to the trawl system frame, based on the average heading of the trawl system. The sub indices N, Q, R and S denote the trawl net, the port and starboard trawl door, and the ship, respectively. The super indices m and A denote measurements on the real system (here found from the PPM) and estimates from the ACPM, respectively. The subindex i denotes the measurement number, and the estimations at this point in time is given the same index.

The updated parameters are found according to (4.34) as

$$\mathbf{p}_{A,k+1} = \mathbf{p}_{A,k} + \mathbf{J}^A\mathbf{K}^A\left(\boldsymbol{\varepsilon}_k^A\right)^T, \tag{5.3}$$

where the influence matrix $\mathbf{J}^A$ is set constant and equal to that in (4.36), only changing the elements $\mathbf{J}_{6,2}^A$ and $\mathbf{J}_{6,5}^A$ from -1 to -0.3. The weight matrix $\mathbf{K}^A$ is also constant, and set to

$$\mathbf{K}^A = \frac{1}{\sqrt{\Delta X^2 + \Delta Y^2}}\mathbf{I}_{15\times 15}, \tag{5.4}$$

where $\mathbf{I}_{15\times 15}$ is the identity matrix. ΔX and ΔY are the approximated distance travelled since the last corrector update in the North and the East direction, respectively:

$$\Delta X = \frac{1}{N_r}\sum_{i=N_r-N_{r0}}^{N_r} x_{S,i}^{n,A} - \frac{1}{N_r}\sum_{i=1}^{N_{r0}} x_{S,i}^{n,A}, \tag{5.5}$$

$$\Delta Y = \frac{1}{N_r}\sum_{i=N_r-N_{r0}}^{N_r} y_{S,i}^{n,A} - \frac{1}{N_r}\sum_{i=1}^{N_{r0}} y_{S,i}^{n,A}. \tag{5.6}$$

The distance travelled while averaging the radio measurements for estimating the ship position is assumed negligible, compared to the travelled distance since the last parameter update ($N_{r0} \ll N_r$).

The correction of the FCPM is done in a similar fashion, except that the states of the ACPM are used instead of the PPM measurements. This procedure is therefore not described.

5.2.3 Results

Figures 5.1 - 5.4 show the simulation results when the corrector is not active.

Figure 5.5 shows the performance of the different models after two corrector iterations. The response of the ACPM is seen to become more equal to that of the PPM, but the FCPM converges more slowly. This is an effect of the FCPM tracking the ACPM instead of the trawl system (PPM). As a result of this, the FCPM always stays one step behind the ACPM. The reason for doing it this way, is that the ACPM can make unmeasured properties available for the correction of the FCPM, especially if few or poor measurements are available. The initial convergence rate is, as demonstrated on Figure 5.5, quite good.

Figures 5.6 and 5.7 show the improvement on the trawl net trajectory after 5 and 10 iterations by the corrector. Initially, a rapid increase in the depth of the trawl net and the trawl doors are seen. The reason for this is probably that the corrector has increased the warp length of the FCPM and the ACPM. Since the initial states were established for shorter warp lengths, the warps are initially untensioned, causing the trawl system to rapidly sink. This irregularity is thus caused by the simulations always starting in the same initial states. Except for this effect, the performance of the models seem to be comparable after five iterations.

Some fluctuations were detected between iterations during the convergence. These are probably caused by interactions between the various parameters, such as how the changes in thrust affect both the depth of the trawl net, the distance travelled, and the direction travelled. The major part of these fluctuations can probably be cancelled by calibration of the full $\mathbf{J}^A$ and $\mathbf{K}^A$ matrices. For the case study these matrices were implemented in a simple and straightforward way, and the performance of the corrector is bound to improve by a more thorough choice and calibration of these matrices.

5.2.4 Conclusions

The trawl system may be used under a variety of operational conditions. Wind, waves, current, and the heading of the ship in relation to these, may change at irregular intervals,

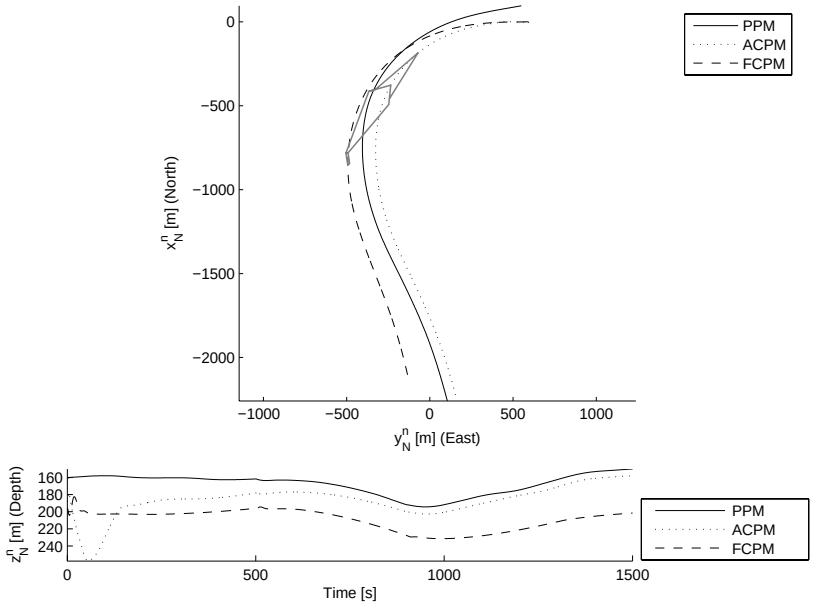

Figure 5.5: The predicted response of the trawl net after 2 corrector iterations.

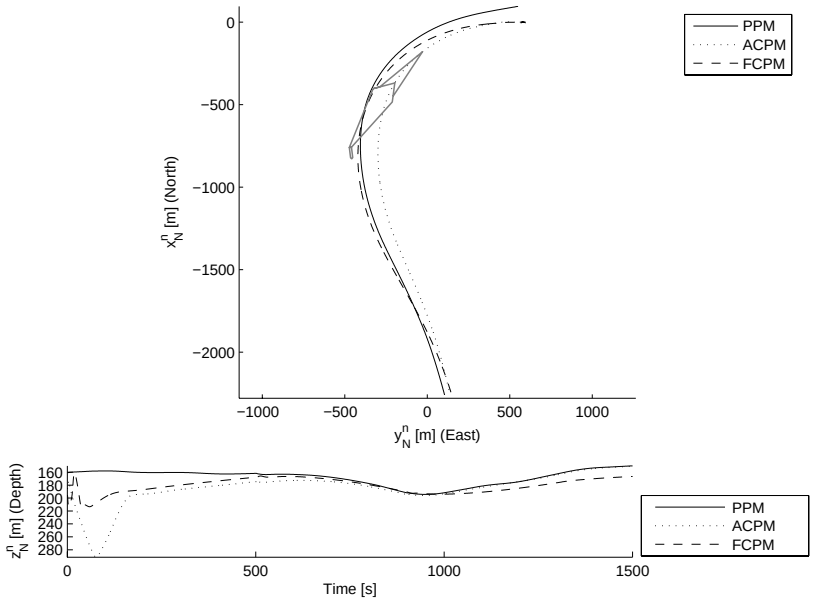

Figure 5.6: The predicted response of the trawl net after 5 corrector iterations.

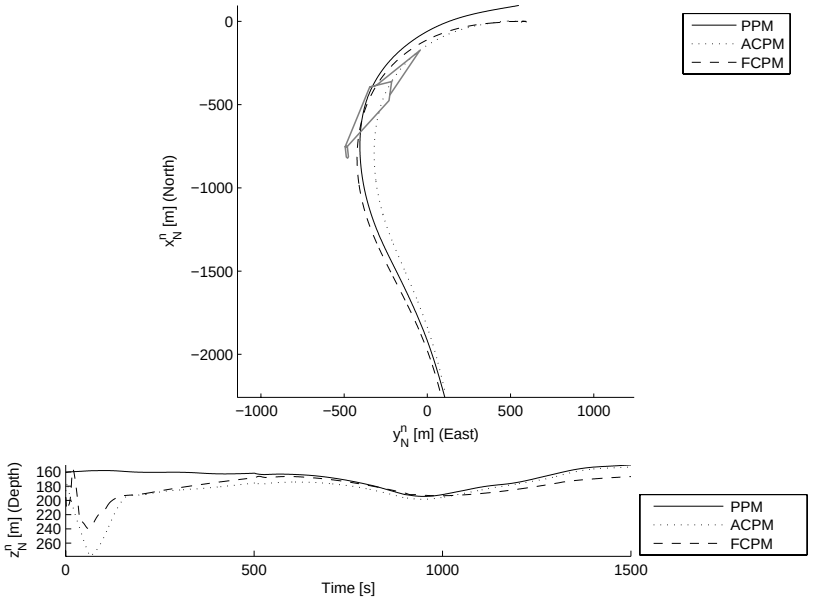

Figure 5.7: The predicted response of the trawl net after 10 corrector iterations.

as well as the desired trawl net depth. Such changes may happen within 20 minutes, or the conditions may be unchanged for several days.

If the corrector works sufficiently fast, it could be able to update the mathematical models as the conditions change. For this to be the case, it would have to be able to correct the models within roughly 10 minutes. If this is possible, depends upon the available measurements. If the measurements are such that a period of a couple of hours is needed to correct the models, one would risk the models to be adapted to obsolete operational conditions. This could be the case if, for example, the trawling is done in alternating directions along an edge with strong winds and currents, and could cause the models to be quite inaccurate each time the conditions change.

If the convergence rate of the corrector is very slow, so that it needs many days to correct the models, the models would be adapted to the average operating conditions. The models would often be less correct than when using the faster correctors, but the largest errors would be avoided. It is therefore not obvious that the convergence rate of the corrector should be made as fast as possible. If it is not possible to make the models converge within $10 - 20$ minutes, it may be better to decrease the convergence rate so that the models are adapted to the average conditions.

From the simulations, it is verified that the proposed corrector is able to correct the ACPM and the FCPM according to the available measurements. It also seems possible, with the correct tuning of the corrector, to make the corrector able to correct the models in a relatively short period of time. If this proves important, correcting also the FCPM directly against the trawl system measurements should be considered. It should be noted that in most cases, fewer measurements than what is assumed here are available. In many

	Case 1	Case 2	Case 3	Case 4	Control ↑	Control ↓
Warp length	500 m	1600 m	500 m	1600 m	$l_{w0} - 100\,\text{m}$	$l_{w0} + 100\,\text{m}$
Thrust	400 kN	500 kN	400 kN	500 kN	$T_0 + 100\,\text{kN}$	$T_0 - 100\,\text{kN}$
Trawl doors aoa	30 °	30 °	30 °	30 °	–	–
Trawl doors aor	0 °	0 °	40 °	40 °	−40 °	+40 °

Table 5.3: The characteristics of the simulation cases. aoa and aor designate the angles of attack and roll, respectively.

cases, no measurements of the horizontal position of the submerged parts of the trawl system are available. In such cases, the convergence rate and the accuracy of the model correction drops, and the models should probably be adapted to the average conditions.

5.3 The trawl door controllers

When the trawl door control is used in coordinated control actions together with the existing actuators, the responsiveness of the trawl system is improved. To illustrate this point, the depth control performance using various control actions are compared through simulations. In these simulations, the trawl doors angles of roll are assumed controlled in order to increase/decrease the depth of the trawl net. The performance of this control is compared to depth control using the winches and the vessel thrust, as well as the control performance using coordinated control actions.

The simulations start from a steady state with a constant heading. It is worth noting that the performance of the winch and thrust control actions to a large extent depends on the winch capabilities and the available thrust, respectively. These specifications are given in Appendix B.

The specifics of the control actions are given in Table 5.3, where the two rightmost columns define the control actions for decreasing and increasing the depth of the trawl. To illustrate the performance gain using trawl door control, simulations are performed for four cases. In Case 1 and 3, the initial warp length is 500m, while in Case 2 and 4, the initial warp length is 1600m. In Case 1 and 2, the trawl doors initial angle of roll is zero, while in Case 3 and 4, the trawl doors are initially rolled 40 °outwards. The control actions are carried out after 5 s, approximately 10 m on the figures.

5.3.1 Results

Case 1: Figure 5.8 shows the simulation results for Case 1. The upper plot shows the response to an ordered decrease in depth, while the lower plot shows the response to an ordered increase in depth. The trawl door control is seen to perform relatively better upwards than it does downwards. Under these conditions, the winch control give the best short-term individual response.

Case 2: Figure 5.9 shows the simulation results for Case 2. The trawl door control performs relatively better for longer warp lengths, as may be expected. The thick line in the lower plot on Figure 5.9 shows the effect of using all actuators together.

The collective response is seen to perform significantly better than the individual results.

Case 3: Figure 5.10 shows the simulation results for Case 3. Use of the winches gives the fastest initial upwards movement of the trawl net, but this is surpassed by the rolling of the trawl doors after approximately 30m. The trawl doors rolling is from then on superior to the other methods of decreasing the trawl net depth. The lower plot shows, however, that this makes it impossible to use the trawl doors for further increasing the depth of the trawl net.

Case 4: Figure 5.11 shows the simulation results for Case 4. The use of the trawl doors roll angles seems to be the far most efficient way of decreasing the trawl net depth. It seems like the performance of the trawl door control is approximately 5 times that of the winch and the thrust control. But also in this case the trawl doors are incapable of increasing the depth of the trawl net.

5.3.2 Conclusion

One thing to keep in mind, especially when increasing the depth of the net, is that the use of the thrust or the winches to achieve this may deform the net shape, reducing the fishing efficiency. Trawl door control will probably have a far less influence on this, since the tension and the forward speed of the net is maintained.

A potential danger of using the trawl doors to decrease the depth of the trawl net, is that the rolling of the trawl doors leads to a smaller spreading force, and that this may decrease the tension in the footrope, causing the footrope to fall down. This effect would not be desirable if operating a trawl system close to rough bottom. It is, however, eliminated, and the performance of the trawl door control improved, by using the trawl doors with a positive angle of roll (outwards), as done in Cases 3 and 4. When the trawl door is rolled inwards to lift the net from the bottom, not only will the net not go down, the opposite may happen. In addition, a larger increase in upwards force is available, at the expense of the possible increase in downwards force. This is illustrated in the Figures 5.10 and 5.11. It is seen that the trawl doors' ability to lift the trawl net is significantly improved, and outperforms use of winch and thrust. The ability to decrease the depth of the trawl net is, on the other hand, lost. This trade-off is probably acceptable in areas where the trawl net can not afford to touch the bottom. If the trawl system is to be used for pelagic trawling, however, the ability to control the trawl net both upwards and downwards may be equally important, and the trawl doors should initially not be given extreme angles of roll. When used in conjunction with predictive control, these effects could be exploited. By for example increasing the angle of roll as the trawl net approaches an obstacle, while decreasing the warp length to maintain the depth, a more rapid upwards response is possible when the obstacle is reached.

5.4 The trajectory controller

In this case study, the performance of the trajectory controller is evaluated. The corrector is assumed to maintain an accurate ACPM. Since the ACPM models the dynamics of

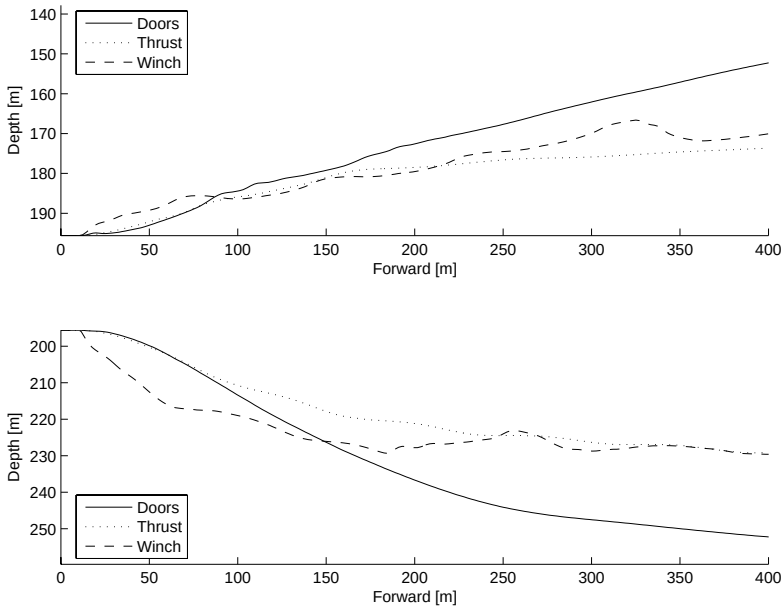

Figure 5.8: Case 1: The response to an order of changed depth, for trawl door control, winch control and thrust control. Initial warp length is 500m.

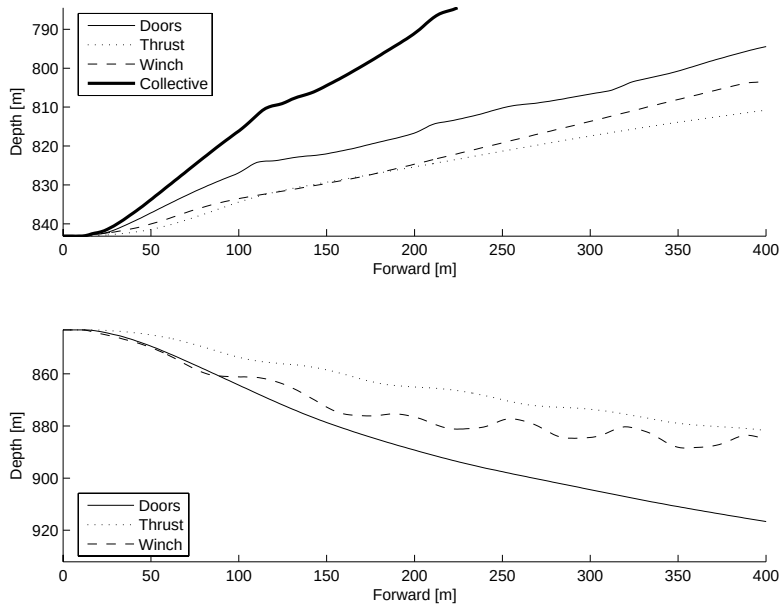

Figure 5.9: Case 2: The response to an order of changed depth, for trawl door control, winch control, thrust control and collective control. Initial warp length is 1600m.

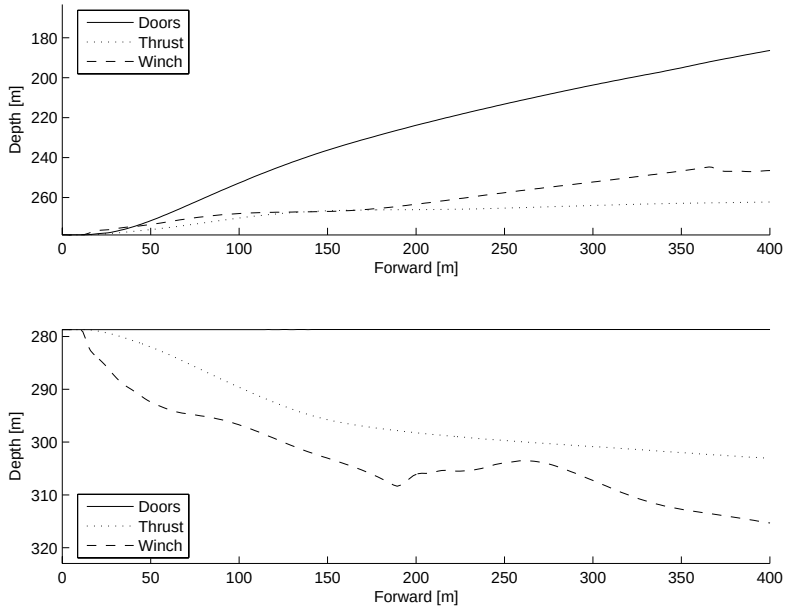

Figure 5.10: Case 3: The response to an order of changed depth, for trawl door control, winch control and thrust control. Initial warp length is 500m, and the trawl door is initially rolled 40° outwards.

the real trawl system, this makes state feedback available for the controller. In order to test the robustness of the trajectory controller, errors are added to reflect possible FCPM errors.

5.4.1 Preliminaries

The reference trajectory

Initially, the PPM is run with a fixed control input, until a steady state is established. This steady state is the starting point of the simulations and is in the following referred to as $\mathbf{x}_0$. The corresponding control input is referred to as $\mathbf{u}_0$. The simulation procedure is illustrated in Figure 5.12. A reference trajectory is created by running the simulator with a predefined control trajectory, starting at $\mathbf{x}_0$. The control trajectory is defined in Table 5.1. The resulting trajectory of the ship, the trawl net opening, and the two trawl doors are in this case study used as references for the trajectory controller to follow.

Adding errors to the predicted control trajectory

The off-line ACPM in Figure 5.12 represents the FCPM in the predictive controller. Since the FCPM will not be correct in real life, the robustness of the trajectory controller with respect to FCPM errors needs to be tested. This is done by adding errors to the predicted control trajectory. The added values are given in Table 5.4. As the gross of these errors

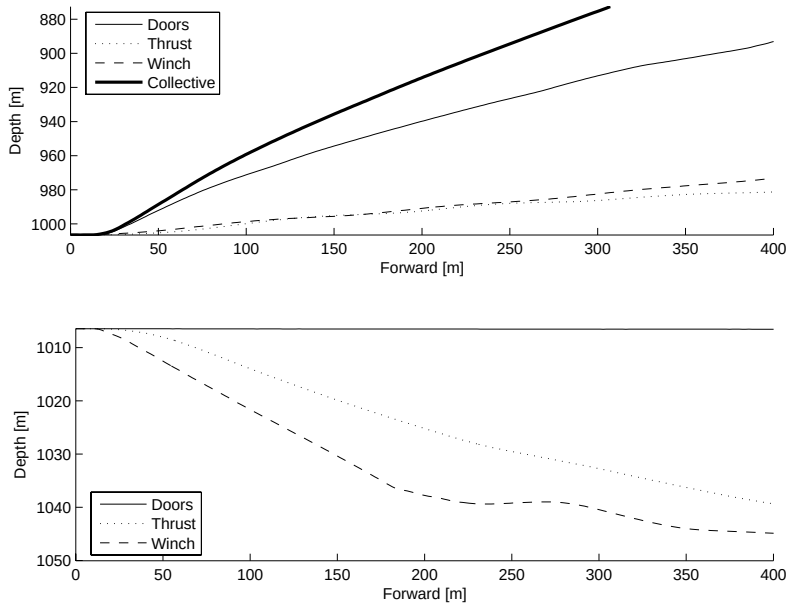

Figure 5.11: Case 4: The response to an order of changed depth, for trawl door control, winch control, thrust control and collective control. Initial warp length is 1600m, and the trawl door is initially rolled 40° outwards.

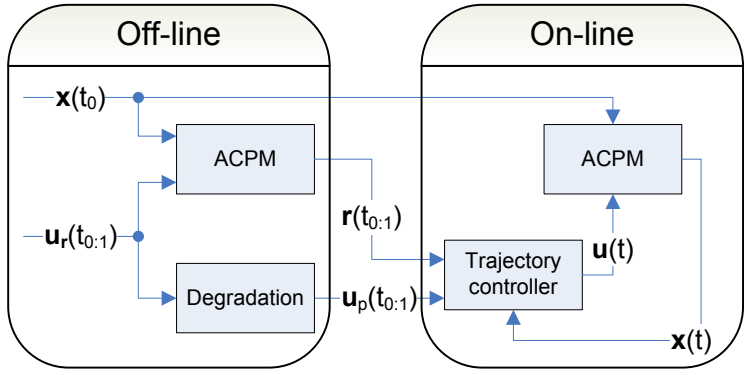

Figure 5.12: The simulation process for the trajectory controller case study.

$\alpha^d_{Q,d}$	$3\,^\circ$
$\gamma^g_{Q,d}$	$5\,^\circ$
$\alpha^d_{R,d}$	$3\,^\circ$
$\gamma^g_{R,d}$	$5\,^\circ$
$\psi_{s,d}$	$-10\,^\circ$
T^s_d	50 kN
$l_{w,d}$	-30 m
$\Delta l_{w,d}$	-2 m

Table 5.4: The values added to the predicted control signal from the FCPM to test the robustness of the trajectory controller towards modeling errors.

would be eliminated by the corrector in the real system, these values represent larger errors than expected to be present in the real system. These errors therefore represent a worst-case scenario, except for the fact that errors in the dynamics of the models are not reflected.

The feedback formulation

For the case studies, the feedback part of the trajectory controller is in principle formulated as

$$f_{c,j}\left(\boldsymbol{\varepsilon}^c\right) = K_p \mathbf{C}_j \left(\boldsymbol{\varepsilon}^c + \frac{1}{T_{i,j}} \int_0^t \boldsymbol{\varepsilon}^c d\tau + T_{d,j} \dot{\boldsymbol{\varepsilon}}^c \right), \tag{5.7}$$

where $f_{c,j}$ is element j of the control feedback function in (4.12), K_p is the common proportional gain, $\mathbf{C}_j$ is row j of the control allocation matrix, $\boldsymbol{\varepsilon}^c$ is the system deviation vector in (4.10), $T_{i,j}$ is the element number j of the integration time constant vector, and $T_{d,j}$ is the element number j of the derivative time constant vector. The derivative time constant vector and the integral time constant vector are collected as

$$\mathbf{T}_d = \left[\begin{array}{cccc} T_{d,1} & T_{d,2} & \cdots & T_{d,N} \end{array} \right], \tag{5.8}$$

$$\mathbf{T}_i = \left[\begin{array}{cccc} T_{i,1} & T_{i,2} & \cdots & T_{i,N} \end{array} \right], \tag{5.9}$$

where N is the number of elements in the reference trajectory. For this case study, $N = 12$. This formulation allows for separate time constants for integral and derivative action for the different elements of the deviation vector. The proportional gain can be separately controlled both for each sub-controller and for the different elements of the deviation vector, through the control allocation matrix. To increase robustness, the following practical improvements are done:

- Constraints are placed on the control signals to each sub-controller and actuator.
- Anti wind-up is implemented for the integral action, by introducing separate saturation limits on each integrator in the controller.
- The input to the derivative part of the controller is filtered through a low-pass filter. This filter eliminates any excessive control signals originating in the derivative action. The introduced delay in the control signals probably degrades control performance only to a minor degree.

Tuning of the trajectory controller

The control allocation matrix is assembled as

$$\mathbf{C} = \begin{bmatrix} \frac{\partial u_1}{\partial \varepsilon_1^c} & \cdots & \frac{\partial u_1}{\partial \varepsilon_{12}^c} \\ \vdots & \ddots & \vdots \\ \frac{\partial u_8}{\partial \varepsilon_1^c} & \cdots & \frac{\partial u_8}{\partial \varepsilon_{12}^c} \end{bmatrix}, \tag{5.10}$$

where the members are initially set using physical insight. $\mathbf{C}$ is improved by sequentially setting all rows but one to zero, thus only considering one control input. All but one elements in this row is sequentially set to zero, and the simulator is run using only proportional controller gain. This way, the value of the elements can be separately adjusted. When all elements in a row have been adjusted, the whole row is applied and the collective performance evaluated. If necessary, the individual elements are changed to improve control performance. This procedure is repeated for every row of $\mathbf{C}$. When the values of all rows of $\mathbf{C}$ are set, further improvements are carried out based on the performance of the full matrix.

After the proportional action is calibrated, integral and derivative action is implemented where it is assumed beneficial. Due to the differences in the dynamics of the various parts of the trawl system, the elements of $\mathbf{T}_i$ and $\mathbf{T}_d$ must be individually tuned. The elements of $\mathbf{T}_i$ are initially adjusted based on the slowest dynamics affecting the corresponding element of the deviation vector, while the elements of $\mathbf{T}_d$ is initially adjusted based on the fastest dynamics affecting the corresponding element of the deviation vector. Trial and error are used for further improvements.

5.4.2 Simulation studies

Control performance using no feedback

The result of the simulations using no feedback in the trajectory controller is shown in Figures 5.13 to 5.15. The grey drawing in the upper plot of Figure 5.14 indicates the size and position of the trawl system at a single point in time. In this case, the trajectory controller only outputs the predicted control signal. This causes the inaccuracies in the predicted control signal to accumulate, and the effects of the modeling errors are seen to increase with time. This is especially true for the error in heading and horizontal position, and it illustrates the integral effect the heading and the thrust control input has on the position.

The difference between the actual and the predicted ship heading is caused by the ships autopilot not being able to follow the commanded heading. The difference between the commanded and predicted control trajectory of the angle of attack on the two trawl doors, as seen in the two upper of the left side plots of Figure 5.15, is due to the constraints placed on the commanded angle of attack for the trawl door controllers. The original input is 28 ° and the added error is 3 °, giving a predicted control input of 31 °. Since the commanded angle of attack of the trawl door controllers is limited to 30 °, a difference between the control prediction and the actual control command arise.

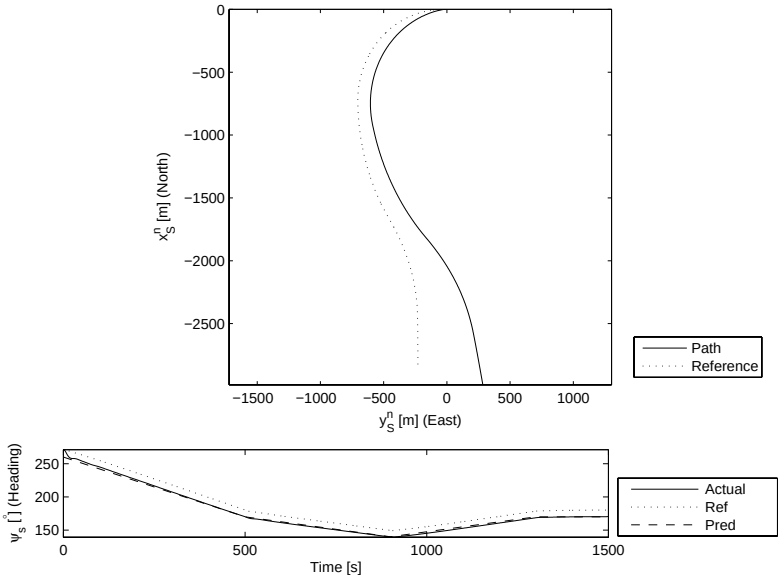

Figure 5.13: Ship trajectory using trajectory controller without feedback.

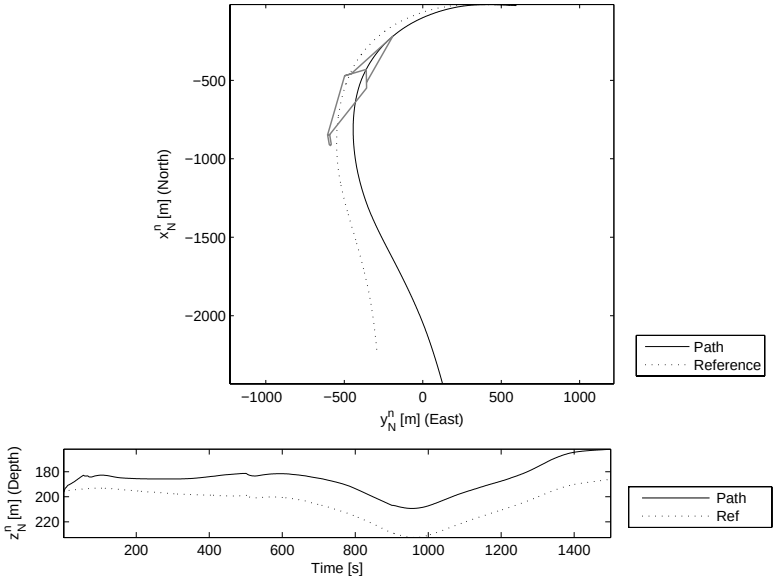

Figure 5.14: Net trajectory using trajectory controller without feedback.

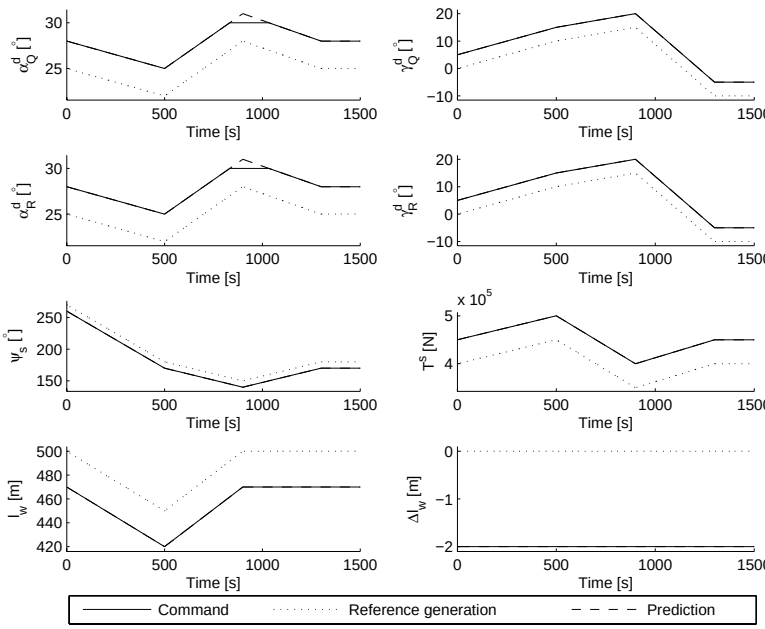

Figure 5.15: Control commands using trajectory controller without feedback.

Control performance using proportional action

Figures 5.16 - 5.18 show the performance of the proportional feedback control. The errors are decreased significantly. Figure 5.18 shows how the control action for some of the more important controllers are approximating the control signal used for making the reference trajectory. The reasons for the relative good performance of the proportional action, is both that state feedback is available, making it possible to use a relative high proportional gain, and that the trawl system is itself well damped. The lack of integral control action does, however, lead to steady state deviations. This is seen in Figure 5.17. For the chosen control trajectory this is seen both for the depth of the trawl net, which is seen to be less than the reference through the whole simulation, and for the trajectory in the horizontal plane. The representative cross track error is roughly 11 m, and the depth error roughly 6 m. The final along-track error of the net is 38 m.

Control performance using PID control

The trawl system is well-damped and responds only slowly to the control actions, especially in the horizontal plane. Only limited integral and derivative control actions are therefore implemented. Some derivative, and a very slow integral action, is applied to the control actions reacting on the error of the trawl net in the y^t-direction (sideways). The damping counteracts the overshoot tendency and the instability risk associated with the heading control of the ship. The reason for adding a minute integral action on the same tracking error, is to eliminate the heading errors between the models, and to eliminate

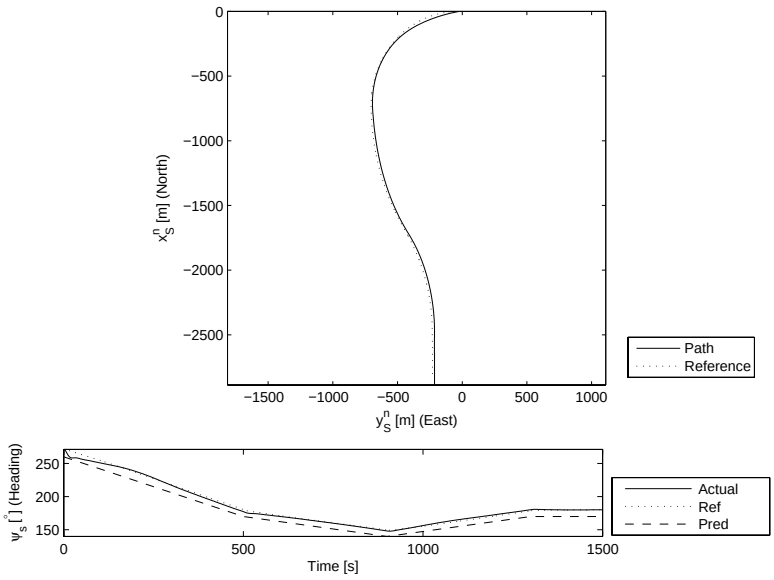

Figure 5.16: Ship trajectory using trajectory controller with proportional feedback.

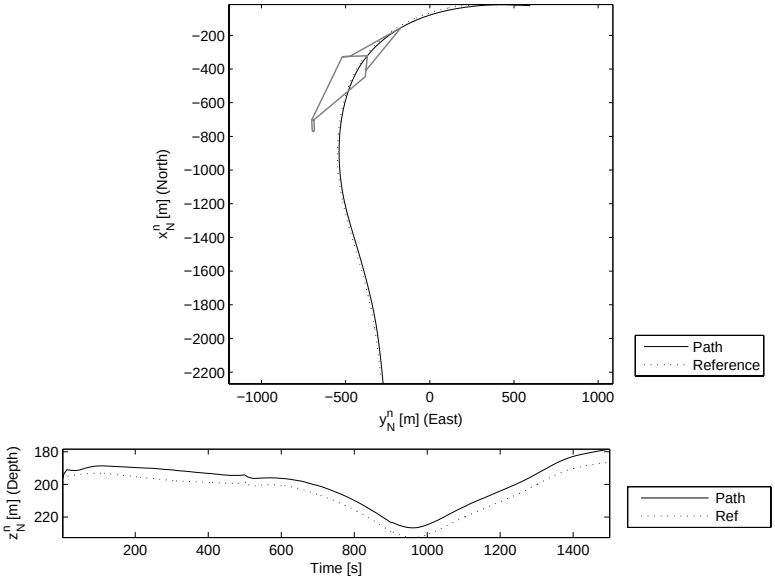

Figure 5.17: Net trajectory using trajectory controller with proportional feedback.

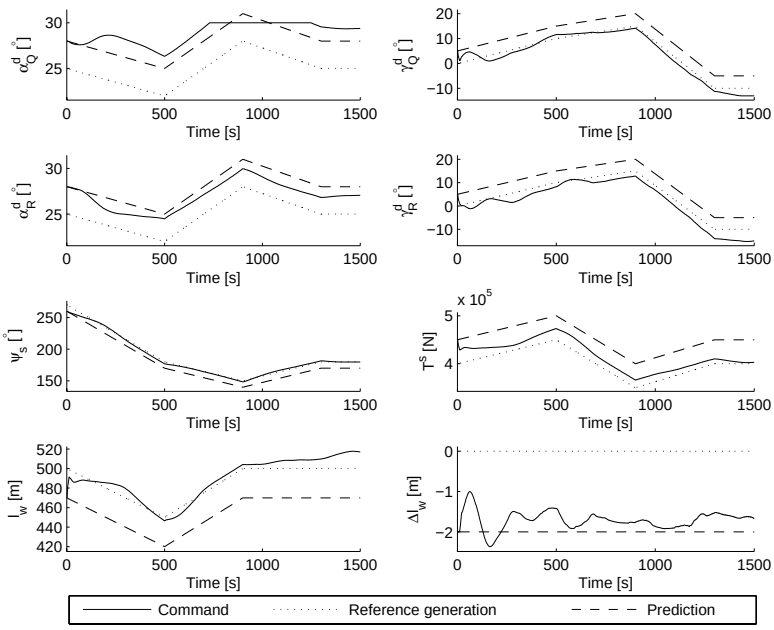

Figure 5.18: Control commands using trajectory controller with proportional feedback.

the effects from unmodeled external forces, like wind, waves and currents. As the depth and the length of the warps increase, the derivative control action will probably grow more important, while the integral control action should be reduced further, to avoid instability.

For the depth control, the trawl system contains no natural integral effects, and errors in the modeling may result in a steady state depth error. Integral action is therefore included for the depth error of the trawl doors and the trawl net. In addition, a minute derivative action is included.

Figures 5.19 - 5.21 show the performance with PID control action implemented and calibrated, and Figures 5.22 - 5.25 show some time series of the same simulations. The performance of the trajectory controller is improved, at least for this simulation case. This is seen not as much for the ship, as for the trawl net. The reason for this is probably that the path following accuracy of the trawl net is given more emphasis in the controller than the ship. The ship is in many respects regarded as an actuator more than a controlled object. The representative cross track error for the trawl net is reduced to roughly less than 2 m, and the depth error to roughly 0.3 m. The final along-track error of the net is 14 m. This error is not controlled.

5.4.3 Conclusion

The reason for the good performance of the proportional controller is probably mostly due to the availability of state feedback. This makes it possible to use a high proportional

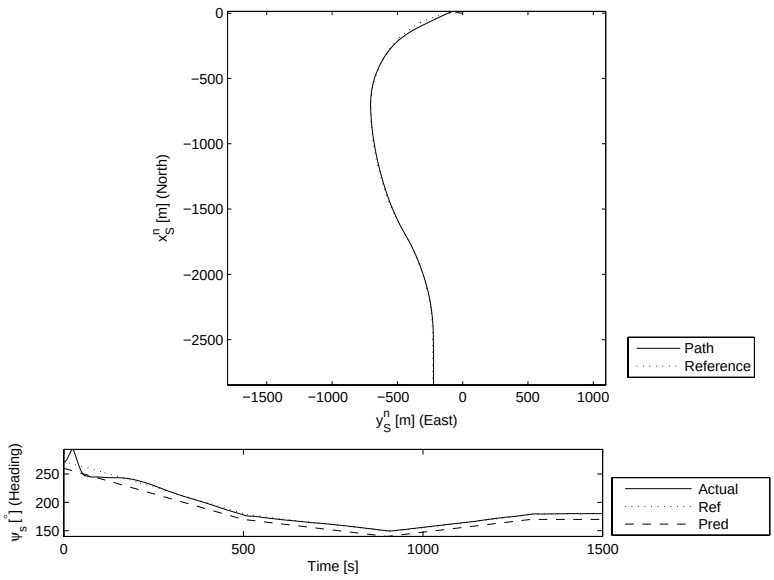

Figure 5.19: Ship trajectory using trajectory controller with PID feedback control.

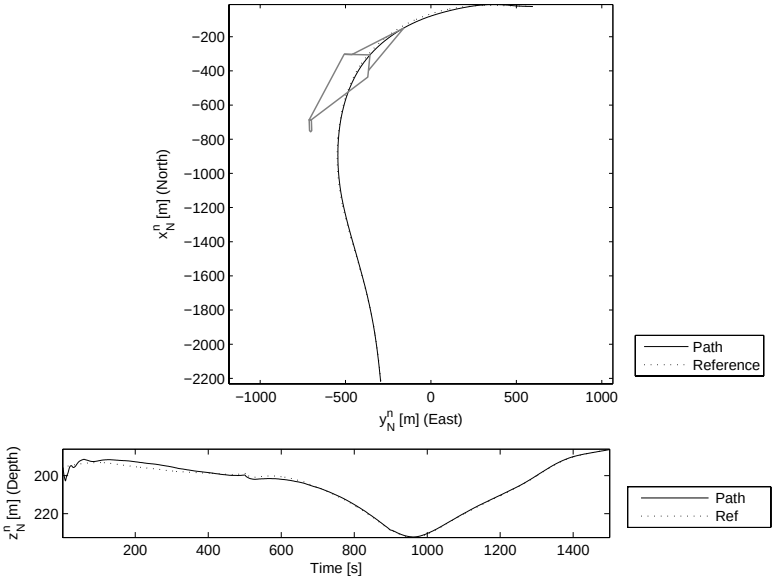

Figure 5.20: Net trajectory using trajectory controller with PID feedback control.

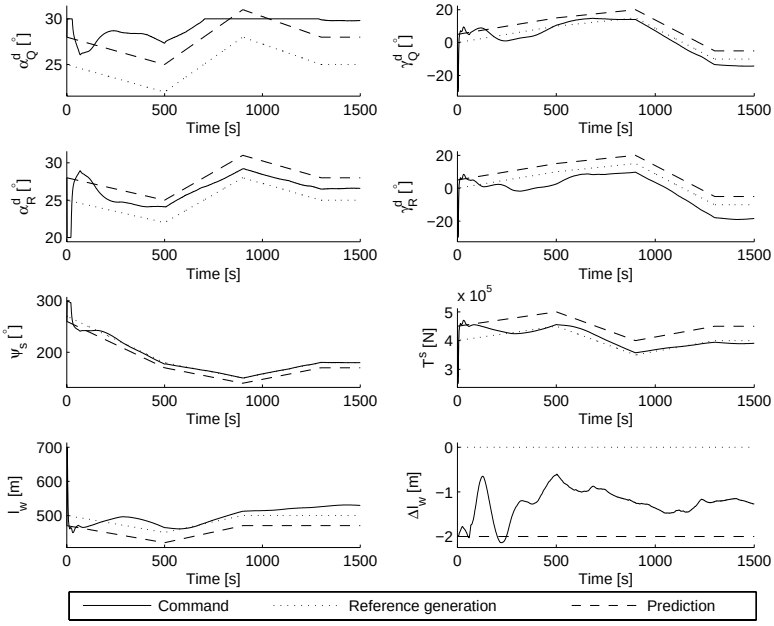

Figure 5.21: Control commands using trajectory controller with PID feedback control.

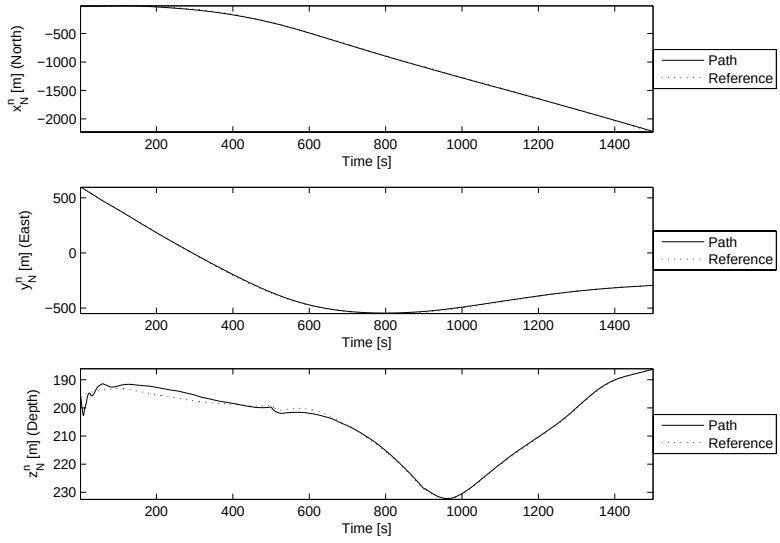

Figure 5.22: Time series of the trawl net trajectory using trajectory controller with PID feedback control.

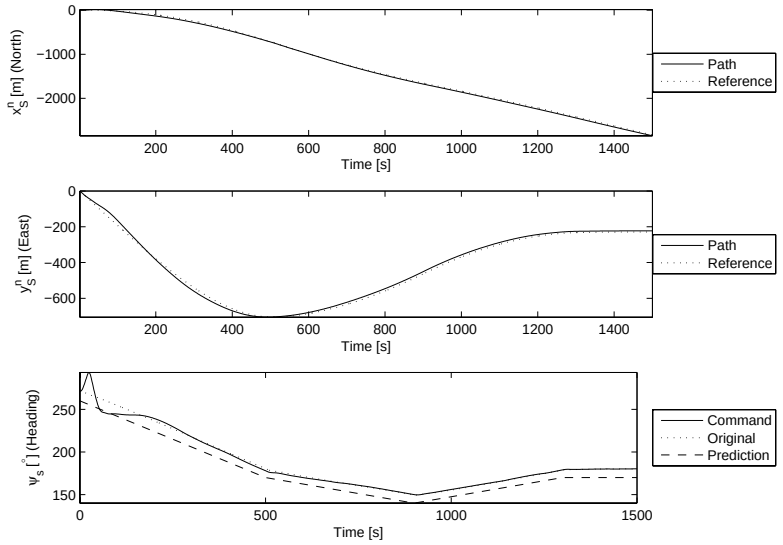

Figure 5.23: Time series of the ship trajectory using trajectory controller with PID feedback control.

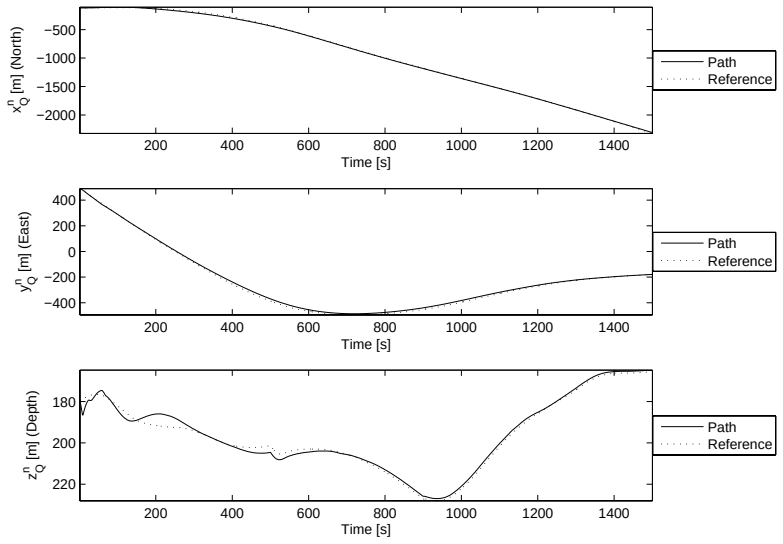

Figure 5.24: Time series of the port trawl door trajectory using trajectory controller with PID feedback control.

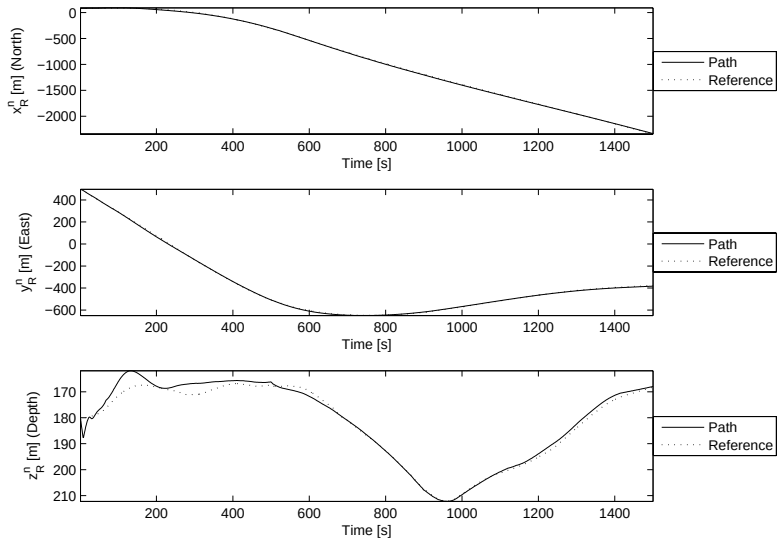

Figure 5.25: Time series of the starboard trawl door trajectory using trajectory controller with PID feedback control.

gain, giving small tracking errors without stability problems. In addition, the natural damping effects in the trawl system and the fact that the ship position is used as reference, makes the system easier to control.

The use of heading control to decrease the cross-track error of the trawl net is an example of natural integral action. If significant integral action is added to the heading control, based on the cross track error of the trawl net, oscillations and instability may occur. If only proportional action is employed, the proportional heading control is enough to limit the steady state error. The main problem associated with the heading control is avoiding overshoot. The reason for this is the time delay between the change of ship heading (control action) and the response on the trawl net position. As the warp lengths increase, the time delay and the problems with overshooting the desired net trajectory will increase. To avoid this (without forcing the ship to follow the ship reference), the control system integration and derivative time constants may be found as a function of the warp lengths. This could for example be done as:

$$T_{i,j} = T^0_{i,j}\left(-k_{ij1}l_w + k_{ij2}\right), \tag{5.11}$$

$$T_{d,j} = T^0_{d,j}\left(k_{dj1}l_w + k_{dj2}\right), \tag{5.12}$$

where k_{ij1}, k_{ij2}, k_{dj1} and k_{dj2} are positive constants, and $T^0_{i,j}$ and $T^0_{d,j}$ are the reference values of the integration and derivative time constants, respectively.

Using the heading of the trawl system, ψ_t, as both reference and virtual control actuators, would probably improve the control performance, especially for long warp lengths.

5.5 The predictive controller

The model predictive controller (MPC) is implemented for waypoint following. The corrector is assumed to maintain the ACPM and the FCPM sufficiently accurate. The goal of the predictive controller is in this case study to make the middle of the trawl net opening pass through a series of waypoints, in a predetermined order.

To avoid excessive control actions, the objective value is dependent not only on the minimum distance between the waypoints and the net opening, but also on the predicted control actions. Other objectives would be straightforward to implement, since the optimization of the objective function must already be performed by nonlinear optimization methods.

To decrease the optimization time, the following measures are taken:

- The initial conditions of the optimization is found by simulating a PID controller maneuvering the trawl system from waypoint to waypoint.
- Only the thrust, the heading of the vessel and the average of the two warp lengths are optimized. The trawl doors and the warp length differences are controlled by the trajectory controller.
- The optimized control signal is specified only at 6 points in time. These are specified in Section 5.5.2.

The waypoints, through which the center of the trawl net opening is to pass, are collected in the matrix $\mathbf{W}$. Each row i of $\mathbf{W}$ contains the position of the i'th waypoint:

$$W_i = \begin{bmatrix} x_{w,i} & y_{w,i} & z_{w,i} \end{bmatrix}, \tag{5.13}$$

where W_i is the i'th row of $\mathbf{W}$, and $x_{w,i}$, $y_{w,i}$ and $z_{w,i}$ are the position of the i'th waypoint in the global frame.

5.5.1 Prediction horizon

If the predictive controller was to optimize the trajectory over a constant prediction horizon, problems would arise. If the trawl system was trying to reach a waypoint, and the prediction horizon did not allow this, it would seem beneficial in terms of the objective to increase the thrust, in an attempt to reach the waypoint. This would not be beneficial for the performance of the system.

In contrast to the fixed prediction horizon otherwise used, the predictive controller in this work changes the length of the prediction horizon for each iteration. The prediction horizon is chosen as the expected time to reach the last considered waypoint, multiplied by a fixed constant. This constant is chosen to ensure that the prediction horizon extends past the last waypoint considered. As a trade-off between the accuracy of and the computational effort associated with the objective function, it is chosen to take into account the next three waypoints for each output of the predictive controller.

5.5.2 The control signal representations

The various representations of the control signals are illustrated in Figure 5.26. The thick, solid-drawn line represents one of the control inputs, for example desired thrust, used creating the reference trajectory. The thin, horizontal lines represent the ranges for which mean values are calculated, as well as the mean value itself. The mean values are collected in a vector $\mathbf{a}$, marked by the asterisks (*). The broken line shows the continuous control signal created from the discretized signal.

The vector to be optimized is constructed as

$$\mathbf{q} = \begin{bmatrix} \mathbf{a}_1 \\ \mathbf{a}_2 \\ \vdots \\ \mathbf{a}_{N_c} \end{bmatrix}, \tag{5.14}$$

where N_c is the number of elements in the control signal, and $\mathbf{a}_i$ is the discretization of the element i of the continuous control signal, collected as

$$\mathbf{a}_i = \begin{bmatrix} c_i(t_0) \\ c_i(t_1) \\ \vdots \\ c_i(t_{N_k-1}) \end{bmatrix}, \tag{5.15}$$

where c_i designates element i, and N_k is the number of times the control signal is set during the control horizon. For the case studies, three control signals are used:

$$c_1(t) = \psi_{s,d}(t), \tag{5.16}$$
$$c_2(t) = T_d(t), \tag{5.17}$$
$$c_3(t) = l_{w,d}(t). \tag{5.18}$$

The points in time are determined according to:

$\hat{t}_0$: The time when the optimized control signal is predicted to be made available for the trajectory controller.

$\hat{t}_1$: An estimated $\frac{1}{3}$ of the time to the first waypoint.

$\hat{t}_2$: An estimated $\frac{2}{3}$ of the time to the first waypoint.

$\hat{t}_3$: The estimated time to reach the first waypoint.

$\hat{t}_4$: The estimated time to reach midway between the first and the second waypoint.

$\hat{t}_5$: The control horizon. This is found as the estimated time to reach the second waypoint.

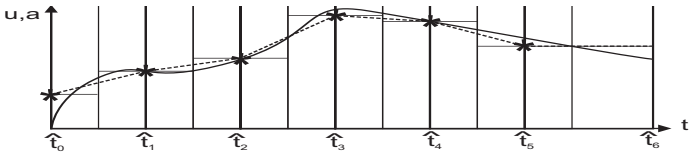

Figure 5.26: The relation between one element of the continuous initial control signal (solid line), the corresponding discrete optimized control signal **a** (asterisks), and the resulting continuous control signal (broken line).

$\hat{t}_6$: The prediction horizon. This is found as the estimated time to reach the third waypoint, multiplied by a factor greater than one. The factor should be large enough to ensure that the objective function evaluates beyond passing the third waypoint. In this case study, the value 1.2 is used.

In addition to discretizing the signal in this way, it is scaled to make the optimization faster. This is done by subtracting an assumed average value from each element and dividing it by an assumed working range. The average value and assumed working range are specific to the type of control action.

When the control vector is sent to either the FCPM, the ACPM or the real trawl system, the opposite scaling procedure is performed, and a continuous signal is obtained by linear interpolation between the discrete signal values (similar to a first order hold element). After the last defined signal value, the signal is held constant until the end of the simulation (like a zero order hold element). This is illustrated by the broken line in Figure 5.26.

5.5.3 The initial conditions of the optimization

As stated earlier, the initial conditions are found as the control actions needed to maneuver the trawl system between the waypoints. These are estimated by controlling the FCPM from waypoint to waypoint in such a way that it always heads for the next waypoint. The desired heading of the ship is found by regarding the trawl system as a rigid body with heading ψ_t. Just like an autopilot controls the heading of a ship in relation to a desired heading, a PID controller is used for controlling the heading of the trawl system in relation to the direction to the next waypoint. The heading of the ship act as an actuator in this control system. This heading control is formulated as

$$\psi_{s,d} = \psi_t + \Delta\psi, \tag{5.19}$$

$$\Delta\psi = -K_{p,\psi}\left(\psi_t - \psi_w\right) - K_{p,\psi}T_{d,\psi}\dot{\psi}_t - \frac{K_{p,\psi}}{T_{i,\psi}}\int_0^t \left(\psi_t - \psi_w\right) d\tau, \tag{5.20}$$

where $\psi_{s,d}$ is the input to the ship's autopilot and ψ_t is the heading of the trawl system. ψ_w is the heading from the trawl net to the next waypoint. $K_{p,\psi}$, $T_{d,\psi}$ and $T_{i,\psi}$ are

the proportional gain, the derivative time and integral time constants for the heading controller, respectively. The heading to the next waypoint is kept out of the derivative action, because of the steps it is subject to when the active waypoint changes. The heading deviation is confined between $-\pi$ and π, and $\Delta\psi$ is limited, avoiding unrealistic performance.

The depth control is performed by the thrust and winch controllers, also formulated as PID controllers:

$$T_d = T_0 + \Delta T, \tag{5.21}$$

$$l_{w,d} = l_{w,0} + \Delta L, \tag{5.22}$$

$$\Delta T = K_{p,T}\left(z_N^n - z_{w,i}\right) + K_{p,T}T_{d,T}\dot{z}_{w,i} + \frac{K_{p,T}}{T_{i,T}}\int_0^t \left(z_N^n - z_{w,i}\right) d\tau, \tag{5.23}$$

$$\Delta L = -K_{p,L}\left(z_N^n - z_{w,i}\right) - K_{p,L}T_{d,L}\dot{z}_{w,i} - \frac{K_{p,L}}{T_{i,L}}\int_0^t \left(z_N^n - z_{w,i}\right) d\tau, \tag{5.24}$$

where T_d and $l_{w,d}$ are the reference warp length and thrust, passed on to the thrust and winch controllers. T_0 and $l_{w,0}$ are the initial thrust and length. $z_{w,i}$ is the depth of the next waypoint, $K_{p,T}$, $T_{d,T}$ and $T_{i,T}$ are the proportional gain, the derivative time and integral time constants for the thrust controller, while $K_{p,L}$, $T_{d,L}$ and $T_{i,L}$ are the proportional gain, the derivative time and integral time constants for the winch controller. As for the heading controller, the references are kept out of the derivative actions. ΔT and ΔL are limited to avoid unrealistic performance. At the start of each optimization (at time $t = t_0$), T_0 and L_0 are set to the values $T_d\left(t_0\right)$ and $l_{w,d}\left(t_0\right)$ predicted by the previous optimization, and the integrators are reset.

As the current waypoint is reached, the next waypoint on the list is used as the reference. Reaching the current waypoint is detected when the following two requirements are simultaneously found to be true:

1. The distance between the trawl net and the waypoint is less than a predefined threshold.

2. The distance between the trawl net and the waypoint changes from decreasing to increasing.

At the end of the simulation, the ordered control actions are used to construct the initial conditions for the optimization, as illustrated in Figure 5.26.

5.5.4 Verification of the initial conditions

To verify that the initial conditions are sufficiently accurate, the predictive controller is run with no optimization. This means that the initial conditions found by simulations of the waypoint controller are used directly as control input by the ACPM and the FCPM.

Figures 5.27 and 5.28 show the trajectory of the FCPM and the ACPM, respectively, when using the initial conditions as input. The trawl system travels from the left to the right. Integral and derivative control actions are removed from the trajectory controller to increase simulation speed. It can be seen from Figure 5.27 how the position of the

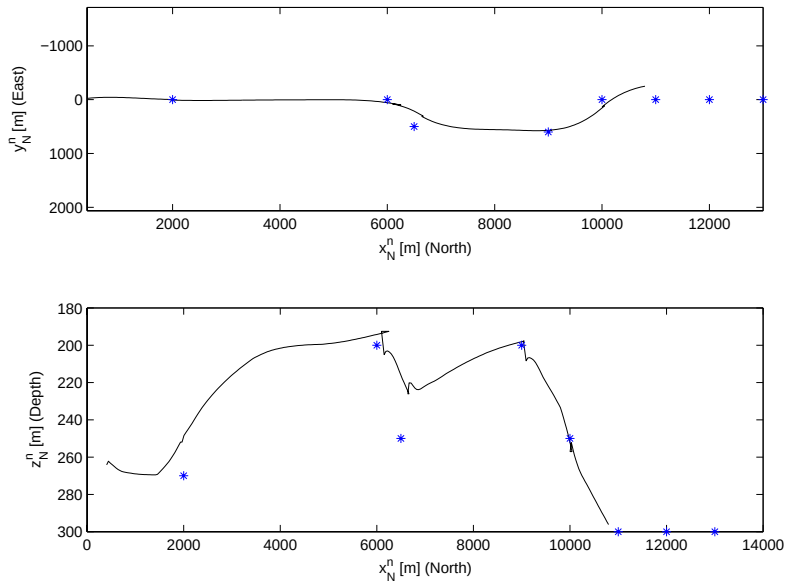

Figure 5.27: The trajectory of the trawl net calculated by the FCPM when using the MPC without optimization. The asterisks (∗) mark the waypoints.

trawl system is reset according to the ACPM observer for each new iteration, especially by the second waypoint. This is due to the ACPM and the FCPM ending up in different places after the estimated time to reach the first waypoint, and may result from the trajectory controller not being able to follow the reference. This is probably due to inaccuracies of the FCPM, maybe because of the warp lengths being different than what it was calibrated for.

It is also seen that the control system is not able to track all waypoints. This happens because it only regards one waypoint at the time, causing it to come into situations where reaching the next waypoint is not feasible. This is seen happening for waypoint number three. The trawl system is not able to turn fast enough after the waypoint number two, gives up halfway to waypoint number three, and heads for the fourth waypoint.

The initial conditions seem to be sufficiently accurate, but the control actions should maybe have been calculated more often, as it seems like there sometimes is a deviation between the predicted distance the net should go before the trajectory changes for the next waypoint, and the actual travelled distance. This is seen from the raising of the net before the first waypoint. It is also seen that the FCPM reaches the second waypoint in neither the horizontal nor the vertical plane.

5.5.5 Model predictive control

The objective is formulated as:

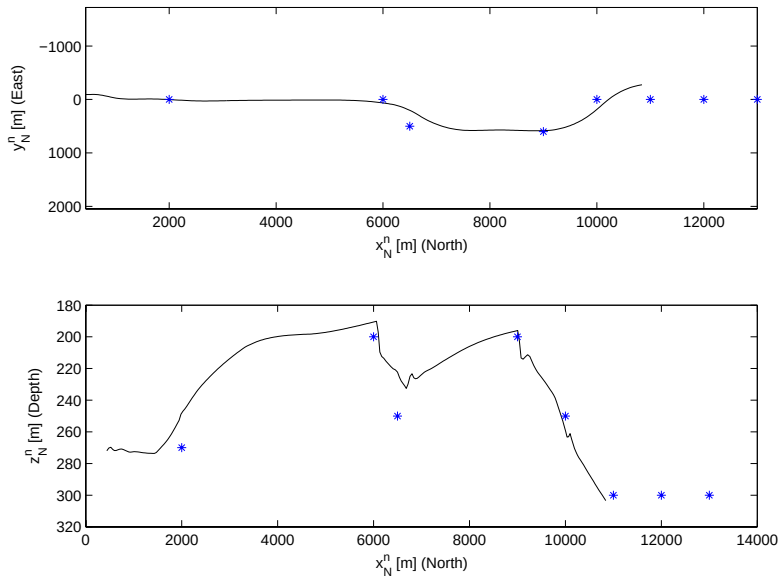

Figure 5.28: The trajectory of the trawl net calculated by the ACPM when using the MPC without optimization. The asterisks (∗) mark the waypoints.

$$O = \sum_{i=j}^{j+2} \min \left(\frac{\left\| W_i^T - \mathbf{p}_N^n \right\|}{2^{2(i-1)}} \right) + k_1 \sqrt{\frac{\mathbf{q}_T^T \mathbf{q}_T}{N_k}} + k_2 \frac{\sqrt{\mathsf{diff}\left(\mathbf{q}_w\right)^T \mathsf{diff}\left(\mathbf{q}_w\right)}}{N_k - 1}, \tag{5.25}$$

where j is the number of the next waypoint to reach, $\mathbf{q}_T$ and $\mathbf{q}_w$ denote the elements in $\mathbf{q}$ containing the thrust and winch control signals, respectively, and $k_1$and k_2 are constants, both set to 10. min(∗) is a function returning the least element of its input vector, and $\mathsf{diff}\,(*)$ is a function returning a vector of the differences between the elements of its input vector. N_k is the number of times the control signal is set in the optimization. In this case study, $N_k = 6$.

The first part of the objective function penalizes according to how close to each waypoint the center of the trawl net passes, emphasizing the first waypoint. The second part penalizes the use of thrust far from the normal value, which would mean loss of fishing efficiency or increased energy consumption, and the third part penalizes winch usage, which means increased wear and tear.

Figures 5.29 and 5.30 show the resulting trajectories of the FCPM and the ACPM, respectively, when the optimization part of the MPC is activated. The improvement in control performance is obvious, and all waypoints are reached. Reaching the waypoints is due to the ability of the predictive controller to plan not just to reach the next waypoint, but to reach it in such a way that it can also reach the second and the third one. These simulations do, however, also expose a not unexpected crucial detail; the time spent in the optimization process is too long for practical use. For the case shown in these

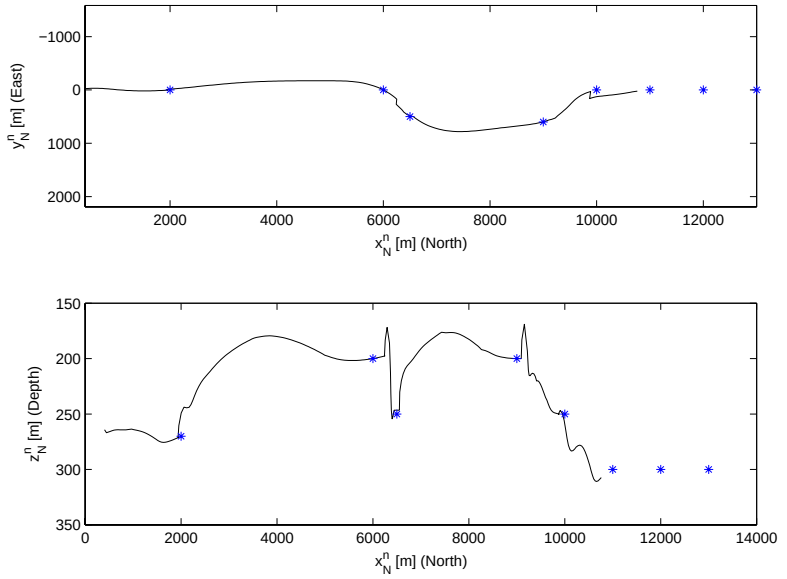

Figure 5.29: The trajectory of the trawl net calculated by the FCPM when optimizing for 3000 iterations for each waypoint passing. The asterisks (∗) mark the waypoints.

figures, 3000 iterations were performed for each waypoint passing. The whole simulation took approximately six hours to complete, which is maybe three times longer than what would be available for this specific case. In addition, 3000 iterations does not seem to be enough, as especially the depth trajectory appears less smooth than what would be desired.

5.5.6 Discussion

It is obvious that if this MPC control system was to be implemented today, some aspects of the implementation would have to change to reduce its computational effort. Most such measures would, however, also include some additional disadvantages. Some measures are presented in Section 4.3.4. Other, specific measures to improve the overall performance of the MPC control system are:

Simplify or improve the efficiency of the FCPM: If the FCPM was simplified, the optimum predicted control actions would be further from the real optimum, increasing the demands on the trajectory controller. Since the trajectory controller seems to be able to handle inaccurate predicted control actions, however, this may not be a problem. If the control action is specified less often (while maintaining the length of the prediction and control horizons), the reference control trajectory and the reference trawl system trajectory would be both less smooth and further from optimum. It is, however, probable that the existing formulation may be improved by additional calibration for unsteady cases.

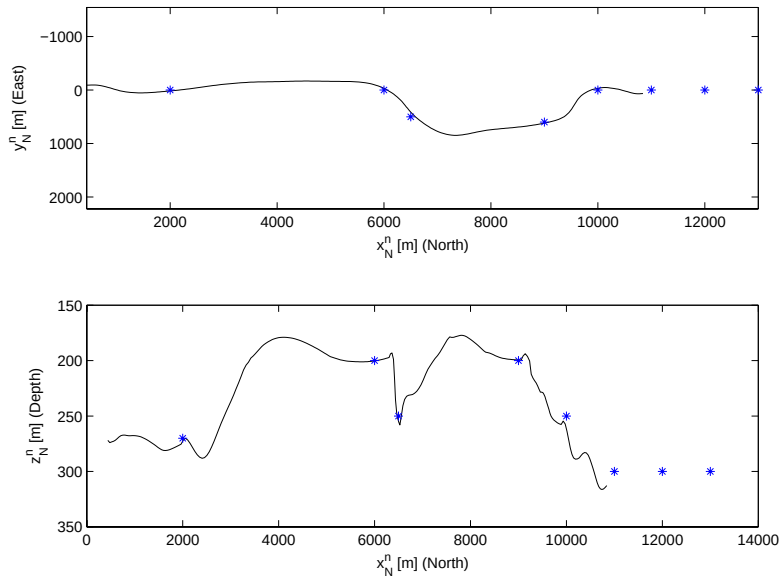

Figure 5.30: The trajectory of the trawl net calculated by the ACPM when optimizing for 3000 iterations for each waypoint passing. The asterisks (∗) mark the waypoints.

Reduce the number of control actions specified in q: If the control signal is allowed to change only at a lower rate, the number of unknowns in the optimization would be reduced, decreasing the necessary number of iterations. This would make the optimization faster, but, at the same time, the optimum control signal would be further from the real optimum, since it would be discretized by fewer points.

Reduce the prediction and control horizons: If the number of waypoints to consider when searching for the optimum trajectory is decreased, the reduced number of unknowns would cause the optimization to converge faster. Unfortunately, the performance of the control system would in some cases deteriorate, as illustrated in Figure 5.31. The line **A** represents the optimum trajectory when assessing only the next two waypoints, while the line **B** represents the optimum trajectory when the next three waypoints are taken into account. It is self-explanatory that planning for also the third waypoint in some cases improves the control performance.

Reduce the number of individual control actions: If the number of individual control actions to optimize is reduced to two, by merging the desired thrust and the desired warp length to one depth actuation force, the number of unknowns in the optimization could be reduced by one third. This would, however, make it harder to take advantage of the different properties of these two control actions, with respect to both costs and dynamics.

Improve the initial conditions of the optimization: The initial conditions could be improved by for example calculating a reference trajectory through the way-

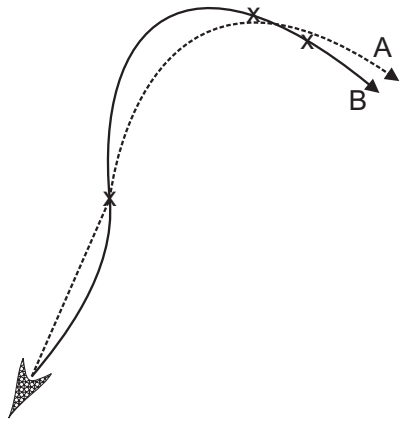

Figure 5.31: The influence of prediction horizon on the waypoint following ability of the trawl system.

points from restrictions with regard to maximum curvature in the horizontal plane, and for example maximum velocity and acceleration in the vertical plane. If such a reference is used in generating the initial conditions (using the FCPM), instead of using only the waypoints themselves, the initial conditions would improve considerably, reducing the number of iterations necessary for the optimization to converge. Another option would be to use preliminary optimizations with a simpler mathematical model of the trawl system.

Use a more efficient optimization method: No effort has been spent finding the optimization routine best suited for the problem at hand. Instead, a standard simplex method is used. This method is briefly explained in Appendix A.1.1. Other optimization methods are not unlikely to prove more efficient.

In the author's opinion, the most promising practical way of increasing the possible control performance using MPC *for waypoint following* consist of a mix of some of these measures:

1. Improve the initial conditions by calculating a smoother initial reference trajectory.

2. Simplify the FCPM. It may be sufficient to regard the trawl system only as two mass points connected by a non-flexible bar.

3. Merge the thrust and warp length control signals into one combined signal.

4. Find a more efficient optimization method.

Some of these measures would, however, restrict the use of more complex objectives, which is the reason for applying model predictive control in the first place.

5.6 Conclusions

The various parts of the control system were shown to perform mostly as expected.

It was demonstrated that the corrector is able to adjust the control plant models to model the trawl system, using only available measurements. It was however seen that differences in the dynamics of the FCPM and the PPM may lead to deviations, especially during control actions or under circumstances different from those the FCPM was calibrated for. As the model corrector adjusts the ACPM to equal the PPM, state feedback is made available to the rest of the control system, facilitating improved control performance. For the state feedback to be accurate, the PPM and the ACPM must be able to represent the dynamics of the real system. This is not verified against full scale measurements. It is possible that other tuning parameters are needed, for example to adjust the heading dynamics. For the tested cases, however, the corrector was working satisfactorily, even if its possibilities for tuning and calibration were not exploited.

The trajectory controller was shown to make the trawl system follow a reference trajectory, even when there was large errors were added to the model creating the reference. It should still be noted, that even if large errors were added, the dynamic properties of the model was not altered. It is evident that the performance would not be equally good if the reference was made by a model possessing dynamic properties very different from the ACPM.

The use of trawl door control was seen to be more advantageous for longer warp lengths, as might be expected. An initial outwards angle of roll was demonstrated to make the trawl doors more powerful in terms of lifting the trawl net. If the predictive controller is able to predict when lifting the net is desired, it would be possible to exploit this by rolling the trawl doors outwards in advance, and at the same time decrease the warp lengths. A larger upwards force would then be available when rolling the trawl doors inwards.

The model predictive controller was shown to be able to find a reference trajectory and reference control trajectory between waypoints, better than that attainable by simply controlling the trawl system against the next waypoint. The ability of this control structure to control the trawl system along a route of planned waypoints seems to be confirmed. Computational efficiency seems, not unexpectedly, to be the major issue. It seems like the optimization will not be able to use objectives making it necessary to include more than a few control signals in the optimization. This means that it is difficult to optimize the distribution of the control actions between all the actuators. If only the three main actuators, winches, thrust and heading, are considered, such an optimization may be possible. This requires, however, improvements with regard to the computational efficiency of the optimization.

Chapter 6

The trawl door control concept

6.1 Introduction

To increase the bandwidth of the trawl system control, it is desirable to generate control forces not only from the ship, but more directly on the trawl net. To accomplish this, it is decided to utilize the hydrodynamic forces on the trawl doors. To control these forces, a trawl door control concept is needed. This chapter aims at developing such a trawl door control concept.

6.1.1 Previous work

The forces developed by the trawl doors can be controlled by changing their orientation, size and/or shape. Various concepts have been proposed. Some of these have been patented, but, as far as we know, none are used in commercial fishing:

- The South-African company Active Fishing Systems proposes to control the lift and the angle of roll of the trawl doors using two rotating cylinders (Shenker, 2005). The concept is illustrated in Figure 6.1. This concept is based on the Magnus effect (Figure 6.2), utilizing that the hydrodynamic forces acting on rotating cylinders in a transversal fluid flow are near proportional to the rotational velocity.

- The Norwegian company Scanmar has done full scale sea trials, focusing on how a trawl door can be controlled by either shifting the fastening point of the warp or by controlling hatches in the trawl door (Scanmar, 2000). The system is illustrated in Figure 6.3.

- A method of controlling the warp fastening point have been patented for use in both trawling and seismic surveys (Seismograph Service, 1984). This concept is illustrated in Figure 6.4.

- A system based on opening and closing of hatches in the trawl door, but without remote control, has been patented (Rasmussens Skibs Baadebygg, 1986).

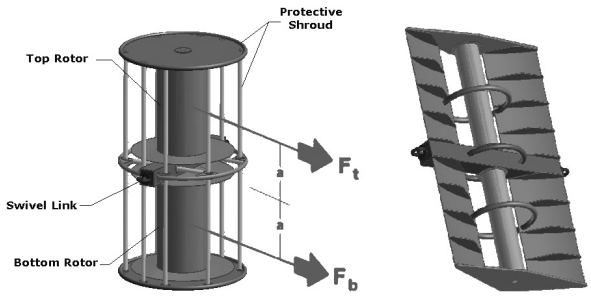

Figure 6.1: Principle and implementation of rotors in the trawl door. Figure from Shenker (2005).

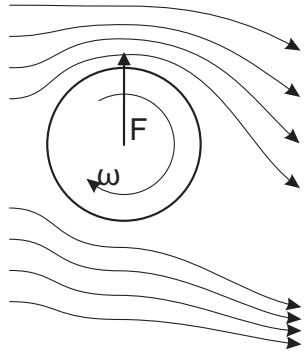

Figure 6.2: The Magnus effect on a rotating cylinder in a fluid flow. See also 6.2.6.

Marine seismic survey systems are quite similar to trawl systems, but the trawl net is replaced by an array of parallel cables. These cables are horizontally separated by deflectors, whose purpose are similar to that of the trawl doors. Some concepts are suggested to control these systems:

- A multifoil deflector with a rotating cylinder in the front of the foremost foil (Figure 6.5) is proposed by Petroleum Geo-Services (2001). By varying the rotational velocity of this cylinder, the lifting force of the deflector may be controlled.
- The concept proposed by Henriksen (2000), shown in Figure 6.6, is based solely on rotating cylinders to create the hydrodynamic forces.
- The concept proposed by Geco (1993), shown in Figure 6.7, is based on shifting the position of the "bridle". This alters the moment balance of the deflector, and makes it possible to control the angle of attack and thereby the lift force.
- The concept in Schlumberger (2002), shown in Figure 6.8, utilizes two different

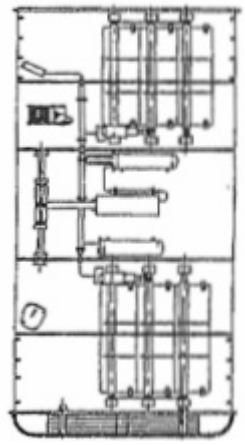

Figure 6.3: Concepts developed by Scanmar based on control of the warp fastening point and hatches in the trawl door.

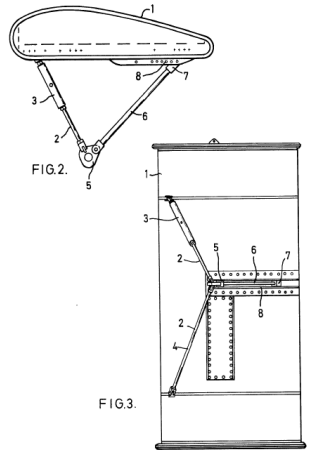

Figure 6.4: Control by shifting the position of the warp fastening point.

principles. To control the angle of attack, the angle of attack of the aft foil in relation to the main foil is varied. To control the angle of roll, the length of one of the lines in the "warp" crow foot is adjusted.

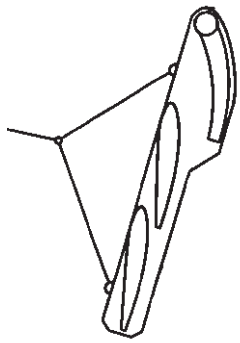

Figure 6.5: Control by combined use of rotor and foils.

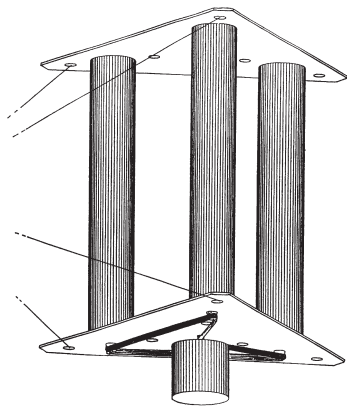

Figure 6.6: Control by an array of rotors.

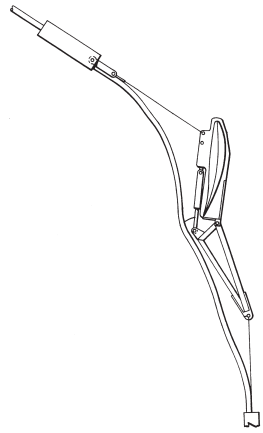

Figure 6.7: Control by shifting the position of the "bridle".

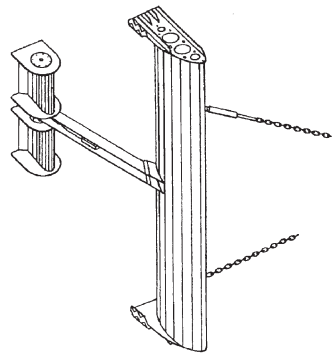

Figure 6.8: Control by the combined use of an extra foil and the fastening point.

6.1.2 Present work

In Section 6.2, the background for the conceptual choice in this work is presented. This includes a presentation as well as an evaluation of some possible control principles. Based on this evaluation, towing tank experiments are performed on the most promising concepts, and a choice for the remainder of this thesis is made. The chosen concept is further improved, using numerical optimization.

6.2 Presentation and evaluation of possible control principles

The hydrodynamic forces on the trawl doors may be controlled by altering a combination of their orientation, area and shape. The following concepts are based on primarily one of these variables, but most changes in developed hydrodynamic forces are followed by a change in orientation. This orientation change changes the hydrodynamic forces, making it possible to amplify the control forces. This could be beneficial in terms of energy efficiency, but must be weighed against the destabilizing effect on the trawl door.

The aim of orientation control is to control the three orientation angles of the trawl door by means of local actuators. Since there are no obvious advantages of changing the pitch angle, it is probably sufficient to control yaw and roll, while keeping the pitch angle within a reasonable range. Such methods are relatively easy to adapt to the various kinds of trawl doors, making it beneficial in terms of commercialization and implementation. Such control methods do also not alter the hydrodynamic properties of the trawl doors. These properties may therefore be found independent of the control concept and the actuator positions, making it easier to develop an accurate process plant model. Such a model would be beneficial during the development and assessment of a control concept.

Control of the hydrodynamic properties of the trawl door, on the other hand, makes mathematical modeling more difficult, but it may give lower energy consumption and thereby better performance. It is therefore possible that such concepts will be preferred in the long run.

Some possible trawl door control principles are presented in the following.

6.2.1 Control of the warp fastening point

The moment balance of the trawl door is controlled by changing the fastening point of the warp. This changes the trawl door orientation and, consequently, the hydrodynamic forces on the trawl door. This could be done for example with a pivot line and two control lines. Such a setup is shown in Figure 6.9. The characteristics of a warp control concept would probably be:

- It can be used for any trawl door, with only minor modifications to the trawl door.
- If the actuators are malfunctioning, the trawl door could be used as normal.
- Vulnerable parts of the actuators can be protected.
- It may be difficult to significantly reduce the hydrodynamic lift force, since a decrease in angle of attack only slowly decreases this force while increasing the risk of instability.
- The energy consumption of the actuators will be rather high, unless the trawl door is made less stable. This stability will have to be investigated, especially how it will develop during deployment and recovery.
- The hydrodynamic properties of the trawl door will be unaltered. This means that these properties can be found once, facilitating good predictions with respect to both design and use of such a concept.

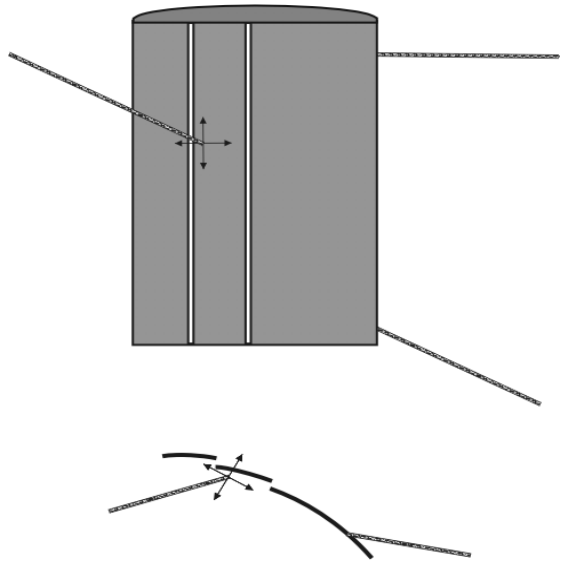

Figure 6.9: Control of the warp fastening point.

6.2.2 Control of the bridle fastening points

By moving one or more of the bridle fastening points, the moment balance of the trawl door is affected, as illustrated in Figure 6.10. This will cause the trawl door orientation to change, changing the hydrodynamic forces on the trawl door. Bridle control will resemble warp control in many respects. The forces are similar, and it is not easy to predict how the energy consumption compares to that of warp control. What would set it apart from control of the warp fastening point, is that

- Vulnerable parts of the actuators may be better protected, since the actuation itself will be done on the suction side, and this side will not be in contact with the ship during normal operations.
- Maintenance may be more difficult, since the suction side of the trawl doors are difficult to reach during normal use.

6.2.3 Hatches in the trawl door

The area and the distribution of area in the trawl door are controlled by the opening and closing of hatches, as shown in Figure 6.11. By adding area, the lift forces in a section is increased. Since this may change the moment balance in addition to giving the local increase in lift force, the total effect of such an additional area will depend on where this area is situated. If an additional area is added in the frontmost parts of the trawl door while the angle of attack is less than what gives maximum lift, the lift will increase from both the lift of the added area itself and from the increased angle of attack. This would

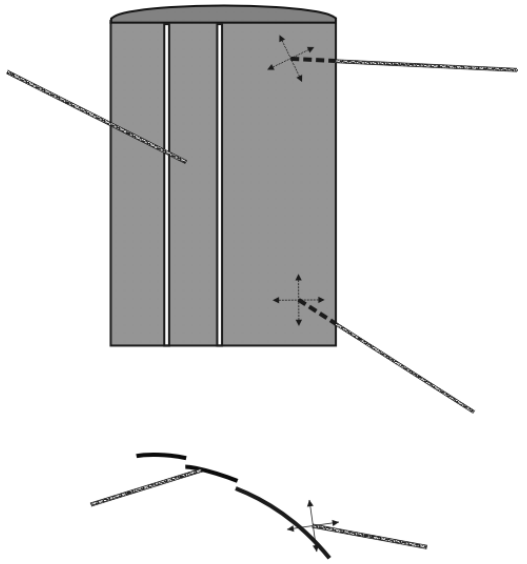

Figure 6.10: Control of the bridles fastening point.

increase the energy efficiency of the control. The hatches could be implemented either as sliding or hinged hatches. Such solutions would probably be characterized by:

- Low actuator energy consumption, especially for the hinged hatches.
- Degraded hydrodynamic efficiency of the trawl doors when retrofitting existing trawl doors,
- For modern trawl doors with small front foils, the only suitable placements for the hatches may be in the aft foil. For such a placement, the change in angle of attack may contradict the change in local lift forces, reducing the energy efficiency.
- It requires openings to be made in the trawl door.
- It may be possible to reduce the lift force substantially without loss of stability.
- If the hatches are placed in the aft parts of the trawl door, a stable rigging of the trawl door would be beneficial.
- The hydrodynamic properties of the trawl door are changed by the hatches, making mathematical modeling more difficult.

6.2.4 Adjustable foils

One of the frontmost foils of the trawl door is split into an upper and a lower section. The angle of attack of these two sections are made separately controllable, either by

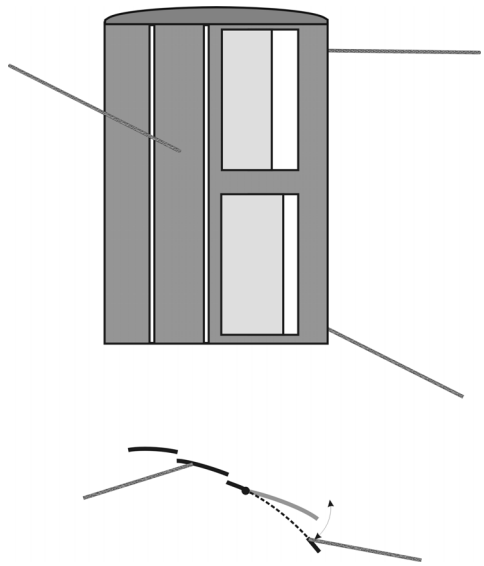

Figure 6.11: Control of hatches in the trawl door.

adjusting the whole sections or by adjusting parts of these sections. It will then be possible to control both the lift force and the vertical force. This setup is shown in Figure 6.12. The implications of such a concept would probably be:

- Good hydrodynamic performance, at least within a certain working range.
- There would be a trade-off between high vulnerability during recovery of the trawl doors (if the frontmost foil is chosen for control), and poorer performance (if the second foil is used).
- Low actuator energy consumption, especially if the controlled foil is hydrodynamically balanced.
- Modifications to existing trawl doors may be difficult and expensive, making it necessary to design and build the trawl door from scratch.
- The hydrodynamic properties of the trawl door are changed by the actuator, making mathematical modeling more difficult.
- 3D effects may make it necessary to use trawl doors of a large aspect ratio or with large end plates.

6.2.5 External foils

It is possible to connect one or more external foils to the trawl door. By changing the hydrodynamic forces on these foils, the trawl door orientation can be changed. The total

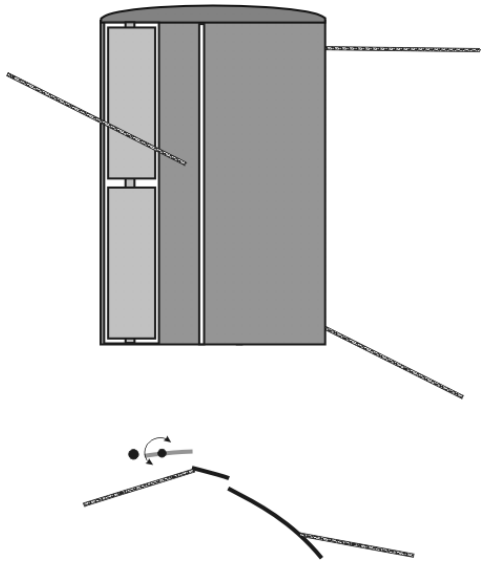

Figure 6.12: Control by adjusting the angle of the frontmost foil.

change in the hydrodynamic forces will be the sum of the differences in the hydrodynamic forces on the trawl door caused by the change in orientation and the change in the hydrodynamic forces on the external foils. Such a setup is shown in Figure 6.13. The characteristics of a system based on external foils may be:

- It is vulnerable to damage caused by entanglement in bridles and contact with the ship or the seabed.
- The large size of the external foils needed to provide sufficient roll control may be difficult to handle during deployment and recovery.
- The angle of attack will be stabilized, since the external foil will counteract any change in the main foil angle of attack.
- If large external foils are used, the hydrodynamic properties of the trawl door are changed, making mathematical modeling more difficult. If smaller external foils are used, a long lever is needed.

6.2.6 Rotating cylinders

When a cylinder is rotated while a fluid is passing it with a transversal velocity component, lift forces will be developed. This is called the Magnus effect. The developed forces can be controlled by adjusting the rotational speed. If one or more cylinders are placed in the trawl door, as shown in Figure 6.14, the hydrodynamic forces on the cylinders may

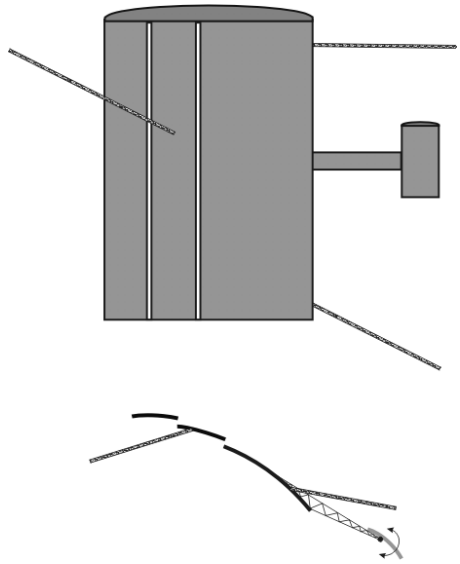

Figure 6.13: Control using an adjustable, additional foil.

change the trawl door orientation. The control forces origin in the changes in hydrodynamic forces on the trawl door from changes in orientation, and from the changes in hydrodynamic forces on the cylinders. The main disadvantage of such a concept is that it is quite energy consuming, making it difficult to avoid power supply through electric cables from the ship.

6.2.7 Flaps

Flaps may alter the hydrodynamic forces on the trawl door. The flaps could be placed on the aft part of the aft foil to increase the lifting forces in a particular area, as shown in Figure 6.15. Such a concept would probably be able to provide good variations in the lift force. Flaps could also be placed on the suction side on the frontmost part of the trawl door to decrease the lifting forces. Experiments do however indicate that the 3D nature of the flow degrades the ability of these concepts to control the roll angle and the vertical forces. Flaps on the suction side may still be an efficient way (in terms of local energy consumption) to decrease the lifting forces, and small control surfaces would probably be sufficient.

6.3 Concept comparison

A comparison between the various control principles is shown in Table 6.1. The concepts are evaluated and given a grade of 1, 2 or 3 with respect to different criteria, where 1 is the best. These evaluations are based solely upon the authors own opinion, and will be dependent on the implementation. It is possible to combine different principles to

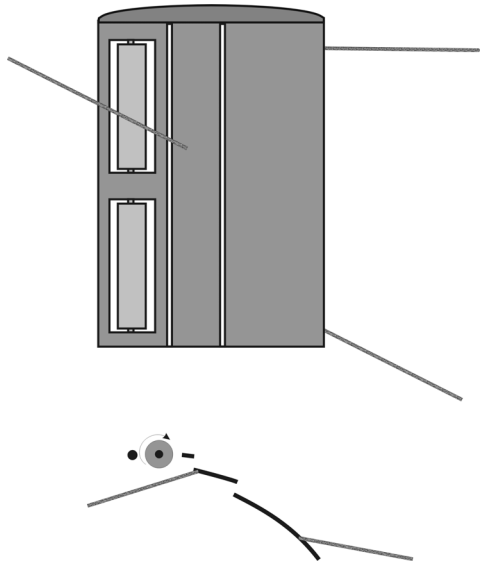

Figure 6.14: Control using rotating cylinders.

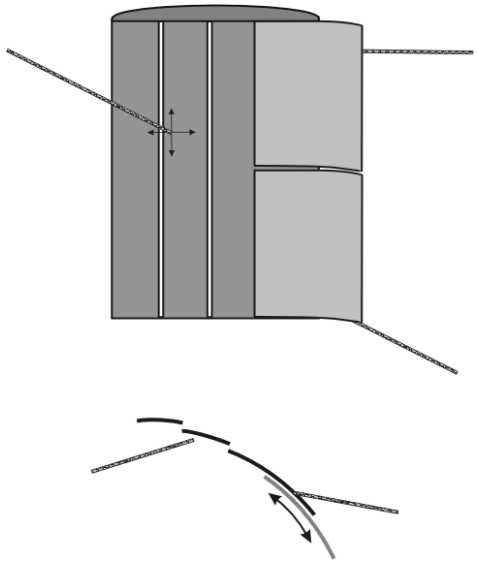

Figure 6.15: Control using flaps.

Control principle	Robust-ness	Energy eff.	Imple-mentation	Hor. contr.	Vert. contr.
Warp control	1	2	1	2	1
Bridle control	1	2	1	2	1
Hatches	1	2	2	1	2
Adjustable foils	2	1	3	1	2
Extra foil	3	1	2	2	3
Rotating cylinders	2	3	3	1	2
Flaps (front/aft)	1/2	1/2	1/2	1/1	3/3

Table 6.1: Comparison of different control concepts.

complement each other, such as for example warp control and flaps on the suction side. Such combinations are not pursued any further.

From the table it seems like control of the warp or bridles fastening points or adjustable foils would be promising control principles, depending on the specific requirements in each case. Since only minor changes have to be done to the trawl door, and the hydrodynamic properties of the trawl door are not altered, these control principles simplifies model experiments and industrialization. Warp and bridle control also seem to be the most suitable for theoretical design and analysis, because of the possibility to establish the hydrodynamic properties of the trawl door independent of the actuator use. This facilitates accurate mathematical modeling and simulation of the concept. Based on these considerations, warp control is chosen for the remainder of this thesis.

6.4 Destabilization of the trawl door

It is crucial for the trawl door control to minimize the demand on local energy, since this energy is expected to be scarce. This has two implications:

1. The frequency of actuator use must be kept to a minimum. It is then not possible to actively use the control system to keep the trawl door stable, and the trawl door must by itself be open loop stable.

2. The amount of energy needed to do the actuating must be minimized. Since this energy is approximately proportional to how stable the trawl door is, the trawl door should not be more stable than needed.

It is therefore beneficial to be able to change the stability of the trawl door in the different dof. The forces that stabilizes the trawl door may be divided into three different categories:

The weight and buoyancy forces on the trawl door: As trawl doors are usually made of one material, iron, and are without air pockets, also the buoyancy forces attack in the center of gravity. Since the net force is downwards and the center of gravity is usually below the attack point of their counteracting forces (mainly the warp forces), these forces usually add stability in both pitch and roll.

The hydrodynamic forces and moments on the trawl door: Changes in the hydrodynamic forces and moments from changes in orientation and velocity components affect the stability of the trawl door. This may in some circumstances add stability and in other circumstances make the trawl door less stable. A short discussion about the moment about the z^d-axis is given in Section 3.3.2.

The forces from the warp and the bridles: The stability of the trawl door is affected by these forces, according to the position of the fastening points. The fastening points are traditionally chosen to make the trawl door as stable as possible, while giving the desired hydrodynamic forces. The stabilizing effect origins in the large forces in the warp and the bridles, and the distance between the fastening points.

Destabilization of the trawl door may be achieved by altering the moments from each of these categories, but it is in the following assumed that the shape and weight distribution of the trawl door is fixed, and that its shape is not altered. The destabilization is thus done by changing the fastening points of the warp and bridles.

The moment $\vec{m}$ about the origin from a force $\vec{f}$ attacking in the position $\vec{p}$ may be written as

$$\vec{m} = \vec{p} \times \vec{f}.$$

To analyze the stability implications of the different forces attacking the trawl door, the change in moments about the trawl door frame origin from a small change in orientation angles are considered. Motivated by Fossen (2002), the change in orientation angles are expressed by the change in Euler angles

$$d\boldsymbol{\Theta} = \boldsymbol{\Theta} - \boldsymbol{\Theta}_0, \tag{6.1}$$

where $\boldsymbol{\Theta}_0$ and $\boldsymbol{\Theta}$ are the Euler angles before and after the rotations, respectively. The attack position of the forces in the trawl door frame after an incremental rotation may be approximated as

$$\mathbf{p}^d \approx \mathbf{p}_0^d + d\mathbf{R}\mathbf{p}_0^d, \tag{6.2}$$

$$d\mathbf{R} = \begin{bmatrix} 0 & -d\psi & d\theta \\ d\psi & 0 & -d\varphi \\ -d\theta & d\varphi & 0 \end{bmatrix}, \tag{6.3}$$

where $\mathbf{p}_0^d$ is the attack position of the forces before the rotations. If the forces are assumed to be independent of the orientation angles, which will be practically the case if the angular velocity of the trawl door and the change in hydrodynamic forces and moments are disregarded, the change in moments will originate in the position change of the attack point of the forces. The change in moment of this force from the incremental

rotation can then be found as

$$\begin{aligned} d\mathbf{m}^d &= \left(d\mathbf{R}\mathbf{p}_0^d\right) \times \mathbf{f}^d, \\ &= \left(\begin{bmatrix} 0 & -d\psi & d\theta \\ d\psi & 0 & -d\varphi \\ -d\theta & d\varphi & 0 \end{bmatrix} \begin{bmatrix} p_1^d \\ p_2^d \\ p_3^d \end{bmatrix} \right) \times \mathbf{f}^d, \\ &= \begin{bmatrix} -f_2^d\left(-d\theta p_1^d + d\varphi p_2^d\right) + f_3^d\left(d\psi p_1^d - d\varphi p_3^d\right) \\ f_1^d\left(-d\theta p_1^d + d\varphi p_2^d\right) - f_3^d\left(d\theta p_3^d - d\psi p_2^d\right) \\ f_2^d\left(d\theta p_3^d - d\psi p_2^d\right) - f_1^d\left(d\psi p_1^d - d\varphi p_3^d\right) \end{bmatrix}. \end{aligned} \tag{6.4}$$

If the trawl door is initially in equilibrium, the following relation must hold if the trawl door should be stable:

$$\frac{\partial \sum_{i=1}^{N} d\mathbf{m}_i^d}{\partial \mathbf{\Theta}^T} < 0, \tag{6.5}$$

where $d\mathbf{m}_i^d$ is the change in the moment vector from force number i, and N is the number of forces acting on the trawl door. These are the forces from the warp, the bridles, the buoyancy, the gravity and the hydrodynamic forces.

More specifically, the following relations are to be expected for a typical midwater trawl door:

- Moving the trawl door's center of gravity up decreases the stability in the angles of roll and slip.
- Moving either bridle fastening point forward decreases the stability in the angle of attack.
- Moving the upper bridle fastening point downwards decreases the stability in the angles of roll and slip.
- Moving the lower bridle fastening point upwards decreases the stability in the angles of roll and slip.
- Moving the warp fastening point downwards reduces the stability in the angle of roll.
- Moving the warp fastening point backwards reduces the stability in the angles of attack and slip.

These qualitative results form the basis for deciding the rigging of the trawl door to give the desired stability. This is needed for both the towing tank experiments and the numerical optimization, elaborated in the following sections.

6.5 Concept choice - the towing tank experiments

Experiments in a towing tank were performed to compare the control concepts identified as the most promising. The experiments involved estimating their performance and energy consumption, as well as their feasibility.

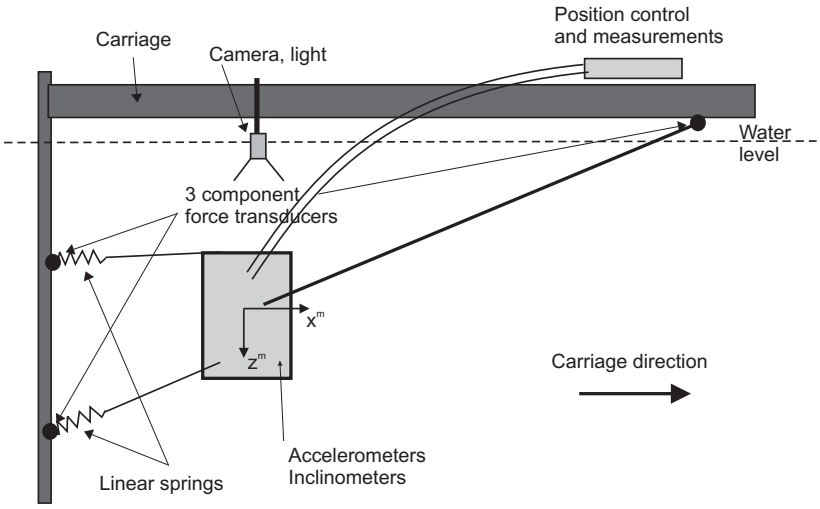

Figure 6.16: The setup of the towing tank experiment as seen from the side.

6.5.1 Experiment setup

The experiment setup is shown in the Figures 6.16 and 6.17, using the trawl door described in Section 3.3.2. The trawl door was hanging freely, only attached by three lines, simulating the warp and the two bridles of a real system. Springs were used as substitutes for the flexibility in the real trawl system. Inclinometers and accelerometers were used for estimating the roll and pitch angle of the trawl door. An optical system based on a video camera were employed to estimate the angle of attack. A reflective line were attached to the upper endplate to increase the accuracy of this system. Three-axis force transducers were attached to each of the warp and bridle lines to measure the external forces. Two wires in separate hoses were used for controlling the trawl door actuators during the experiments, similar to what is commonly used for bike breaks and gear shifters. Actuator positions were measured in the control device on the carriage, while the force measurements were done on the trawl door to eliminate the friction in the hoses.

6.5.2 Simulations

The experiments were preceded by simplified simulations, to reduce the time in the towing tank. Even though these simulations were performed before the accurate hydrodynamic properties of the trawl door were known, they gave some answers with respect to finding the initial rigging and how to adjust this according to the progress of the experiments. An example of the results of these simulations is given in Figure 6.18. In this figure, the angle of attack is presented as a function of the x^m-coordinate of the bridles and the warp, assuming everything else to be constant. The horizontal black lines marks the

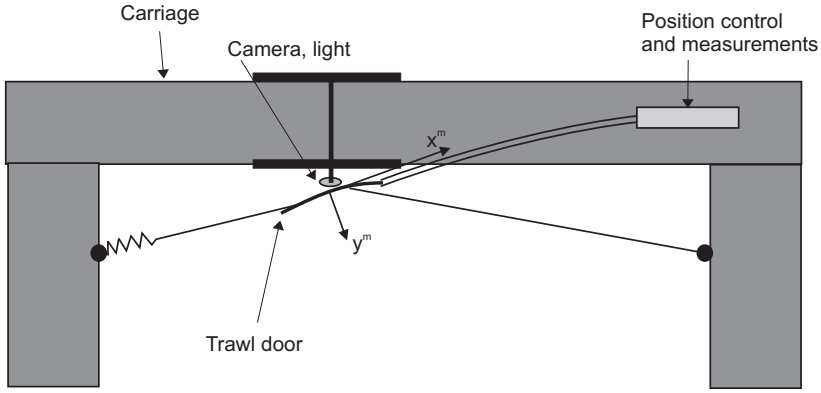

Figure 6.17: The setup of the towing tank experiment as seen from above.

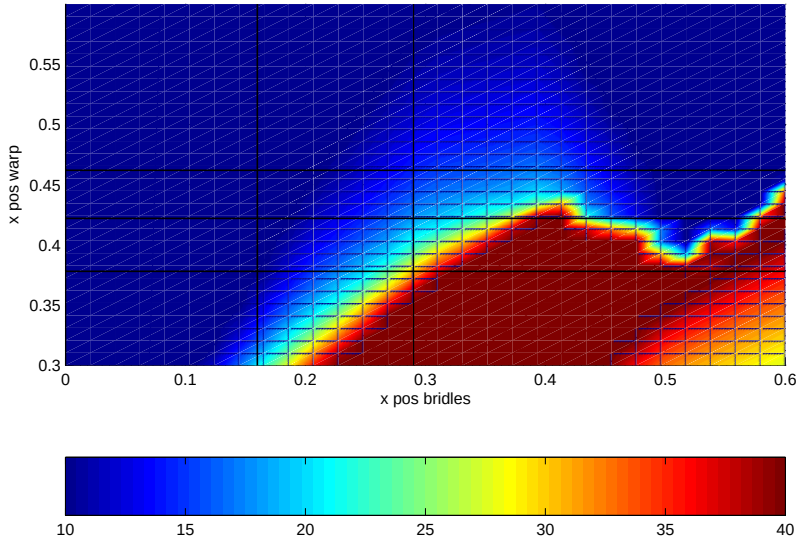

Figure 6.18: Angle of attack as a function of x^m_{lb}, x^m_{ub} and x^m_{warp}. $x^m_{lb} = x^m_{ub}$ and $y^m_{warp} = -0.01m$.

three original possibilities for fastening the warp, while the two vertical black lines mark the range of original fastening points for the bridles. Similar figures were made for angle of roll and angle of pitch, and also for variations of other variables. These figures are shown in Appendix F. The superscript m denotes the model frame, as defined in Section 3.3.2.

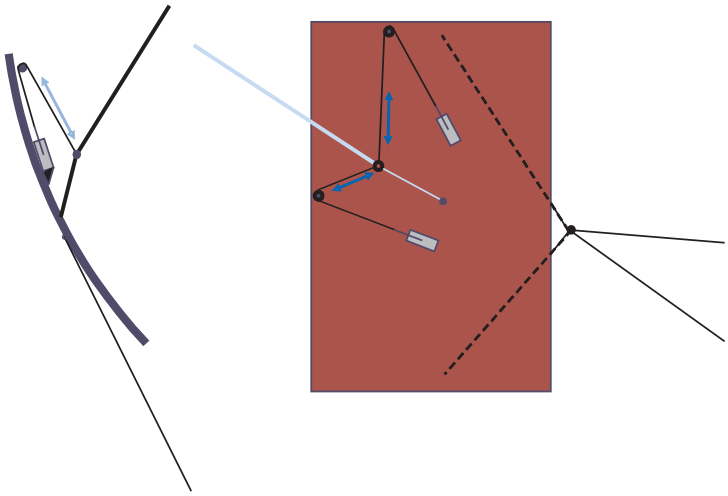

Figure 6.19: The warp control concept tested in the towing tank experiments.

6.5.3 The experiments

The experiments were divided into five distinct phases:

1. **Setup verification.** The setup was adjusted until the original rigging gave the orientation angles expected for the full scale system.

2. **Destabilization of the trawl door.** This was done to make the trawl door more susceptible to changes in the orientation, reducing the energy consumption of the control system.

3. **Control of the fastening point of both bridles in the y^m-direction.** This gave good control with the angle of attack, but much force were needed to control the angle of roll. This concept was therefore rejected.

4. **Control of the fastening point of the lower bridle in both the y^m- and z^m- direction.** This gave better control with the angle of roll, but there were strong dependencies between the angle of roll and the angle of attack. This made it difficult to obtain small angles of roll for large angles of attack.

5. **Control of the warp fastening point.** The trawl door was further destabilized by attaching the bridles in a crowfoot, as shown in Figure 6.19. This reduced the stability in roll while maintaining the stability in pitch. The angles of roll and attack could be controlled more independent of each other, and the energy consumption decreased.

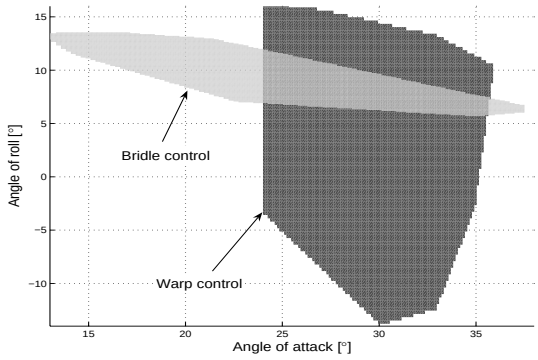

Figure 6.20: Warp and bridle control performance comparison.

6.5.4 Experimental results

Figure 6.20 shows the control range of the two best candidate concepts during the experiments, warp and lower bridle control. It seems clear that for this setup the warp control had a wider working range, except for the fact that the lower bridle control made it possible to obtain smaller angles of attack.

If the tension in the control lines are linearly dependent on their length, the change in potential energy in the lines between the two actuator positions A and B may be found by

$$E = \sum_{i=1}^{2} \frac{\left(T_i^B + T_i^A\right)\left(l_i^B - l_i^A\right)}{2}, \tag{6.6}$$

where T_i^A and l_i^A are the tension and length of the control line i in position A, respectively. T_i^B and l_i^B are the initial tension and length of the control line i in position B, respectively. Figures 6.21 to 6.24 show the potential energy in the control lines for the two potential concepts. Note the different axis scaling for the two concepts.

The ideal energy consumption for a given cycle, assuming no friction, other energy losses or energy recuperation, is further estimated by

$$W_m = \left(|\Delta E_1| + |\Delta E_2|\right), \tag{6.7}$$

where W_m is the energy consumption for the model and ΔE_i is the difference in potential energy in control line i between the two end points of the cycle. To scale these results to

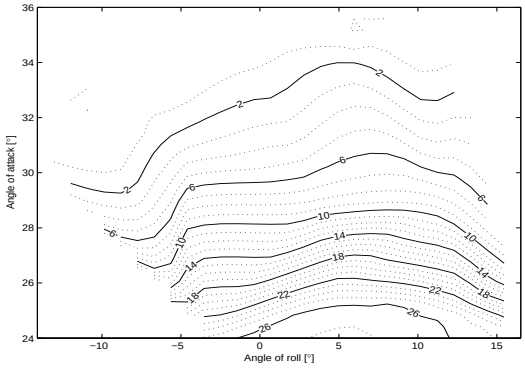

Figure 6.21: Potential energy in the lower control line during the warp control experiments.

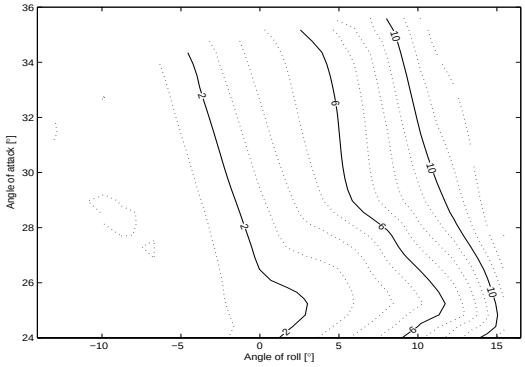

Figure 6.22: Potential energy in the upper control line during the warp control experiments.

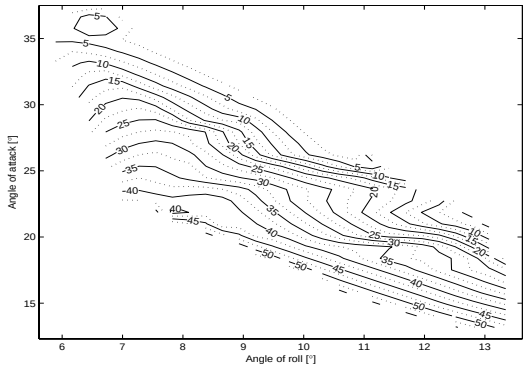

Figure 6.23: Potential energy in the lower control line during the bridle control experiments.

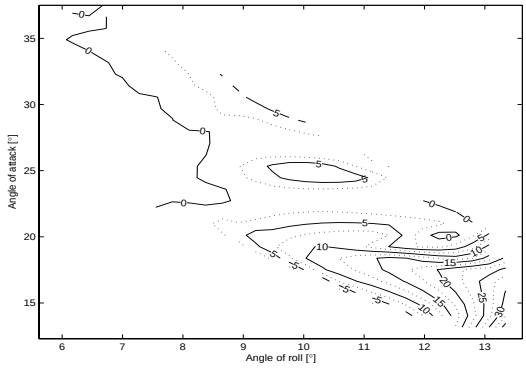

Figure 6.24: Potential energy in the upper control line during the bridle control experiments.

Warp control	W_m [kJ]	W_d [kJ]
$24\,^\circ < \alpha_d < 34\,^\circ$	0.029	15
$-10\,^\circ < \gamma_d < 15\,^\circ$	0.015	8

Table 6.2: The estimated energy consumption for the warp control concept.

Bridle control	W_m [kJ]	W_d [kJ]
$20\,^\circ < \alpha_d < 30\,^\circ$	0.040	20
$6\,^\circ < \gamma_d < 10\,^\circ$	0.018	9

Table 6.3: The estimated energy consumption for the bridle control concept.

a full-scale trawl door, the following reasoning is employed:

$$\begin{aligned} W_m &\propto Fs \\ &\propto \frac{1}{2}\rho U_m^2 A_m s_m \qquad (6.8) \\ \frac{W_d}{W_m} &= \frac{U_d^2 A_d s_d}{U_m^2 A_m s_m} \\ &= \frac{U_d^2}{U_m^2}\lambda^3, \qquad (6.9) \end{aligned}$$

where W_d is the energy consumption of the full scale trawl door, and F and s are measures of the forces acting on the trawl door and the change of control line length, respectively. It is assumed that the tension in the control lines are proportional to the hydrodynamic forces acting on the trawl door. λ is the ratio between the length scale of the trawl door and the model. For a full-scale trawl door area of $15\,\mathrm{m}^2$, this ratio is found to be $\lambda = 5$. The model trawl door speed was approximately $1.0\,\mathrm{m/s}$ during the experiments. Assuming a forward velocity of $2\,\mathrm{m/s}$ for the full-scale trawl door, the ratio between the energy consumption on the full-scale trawl door and the model is estimated to $\frac{W_d}{W_m} = 500$. The estimated energy consumption for the two control concepts, using these approximations, are shown in Tables 6.2 and 6.3.

Based on these results, warp control seems to give the better performance with regard to both force control and energy consumption. These differences may, however, be a result of how successfully the concepts were implemented during the experiments, and especially how the trawl door was destabilized. It is therefore not unlikely that similar results could be achieved for the bridle control concepts by further destabilizing the trawl door. Better results could probably be achieved also for warp control by further improving the rigging of the trawl door.

6.5.5 Conclusion

In these experiments, warp control seemed to perform better than bridle control. This can, however, not be proven based on these limited experiments. Still, it is rendered probable that a concept based on warp control may be suitable for practical use. Such technology will probably be simple to introduce, since the trawl doors themselves will not

have to be significantly modified, and it would be easy to revert to the original trawl door after a trial period. For our purpose it was also important that this concept does not alter the hydrodynamic properties of the trawl door, making it possible to develop a process plant model of sufficient accuracy. Its main drawbacks are the energy consumption and that it may be difficult to reduce the lift force considerably without loosing stability. As a result of the experiments, warp control is chosen for this thesis.

6.6 Modeling the fastening points of the warp and the bridles

Mathematical models of the pivot line, the control lines and the bridle crowfoot are needed to simulate the control performance. This is needed both for optimizing the trawl door control concept and for evaluating the performance of the trawl control system. It is important to avoid a computational demanding model. How this is achieved is elaborated in this section.

6.6.1 The control lines and the pivot line

The control of the warp fastening point is achieved using two control lines and a fixed pivot line. This reduces friction and makes it more robust compared to a rigid solution. The concept is illustrated in Figures 6.25 and 6.27, where line 1 and 2 are the control lines, and line 3 is the pivot line.

Actuator modeling

The actuators are modeled as:

$$\begin{aligned} \dot{l}_{i,d} &= \begin{cases} -k_u & , \quad \varepsilon_{l,i} > \varepsilon_{l,\max} \wedge T_i < T_{\max} \\ k_u & , \quad \varepsilon_{l,i} < -\varepsilon_{l,\max} \wedge T_i > 0 \\ 0 & , \quad \textit{otherwise} \end{cases} , \; i = 1, 2 \\ \varepsilon_{l,i} &= l_i - l_{i,d} \; , \end{aligned} \tag{6.10}$$

where k_u is the speed of the control lines actuators, l_i and $l_{i,d}$ are the actual and desired length of the control line i, and $\varepsilon_{l,\max}$ is the allowed control line length error. T_i is the tension in the control line i, and $T_{\max}$ is the maximum tension while shortening the control lines.

The dynamics of the control actions

The dynamics of the control actions could be modeled by including the approximate nonlinear stiffness, damping and mass of each line. This would be easy to implement, and it would give straightforward computation of the energy consumption in the actuators, if only the transients were filtered out. The bandwidth of this system would however be very high, giving very small integration step sizes for the trawl system simulation. This would add significantly to the total computational effort. Using a quasi-static approach

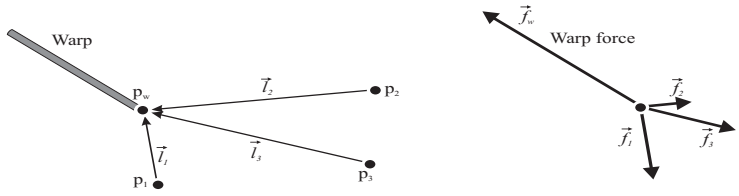

Figure 6.25: The modeled warp control concept.

like the one in (Coope, 2000) is feasible, but since it requires all lines to be tight, expensive methods must be used to take care of the cases where one or more of the lines are not tightened. An iterative procedure to solve the problem was initially implemented, but it was also rejected because of the computational effort. To keep the computational effort at a minimum, it is instead chosen to model the warp fastening point as a virtual dynamic system. The method is described in the following.

Solution method

The warp fastening point is modeled as a mass point under the influence of linear and nonlinear damping, the forces from the two control lines, the pivot line and the warp. The calculations are done as if the trawl door system is inertial. By choosing the mass, the linear and nonlinear damping of the fastening point and the relation between strain and tension in the lines, the response and computational effort of the system can be tuned. This method provides easy implementation and straightforward computation of the energy consumption in the actuators. Decomposing all positions and forces in the trawl door frame, and omitting this index for notational simplicity, the model is formulated as

$$m_w \ddot{\mathbf{p}}_w = \mathbf{f}_d \left(\dot{\mathbf{p}}_w \right) + \mathbf{f}_w + \mathbf{f}_l \left(\mathbf{p}_w \right), \tag{6.11}$$

where $\mathbf{p}_w$ is the position of the warp fastening point, m_w is the virtual mass of the warp fastening point, $\mathbf{f}_d$ are the sum of the damping forces, $\mathbf{f}_w$ is the force from the warp, and $\mathbf{f}_l$ is the sum of the forces from the control lines and the pivot line acting on the warp fastening point.

The sum of the forces on the warp point from the control lines and the pivot line are calculated as

$$\vec{f_l} \left(\mathbf{p}_w \right) = \sum_{i=1}^{3} k_k \frac{\vec{l_i}}{l_i} \frac{l_{0i} - l_i}{l_{0i}} u_H \left(l_i - l_{0i} \right), \tag{6.12}$$

where k_k is a constant representing the stiffness of the lines and l_{0i} is the untensioned length of line i. u_H is the discontinuous Heaviside step function, also known as the unit step function. This is defined by

$$u_H \left(x \right) = \begin{cases} 0 & , \ x < 0 \\ \frac{1}{2} & , \ x = 0 \\ 1 & , \ x > 0 \end{cases}. \tag{6.13}$$

The damping forces are computed as

$$\mathbf{f}_d\left(\dot{\mathbf{p}}_w\right) = -k_{dl}\dot{\mathbf{p}}_w - k_{dq}\ \mathsf{diag}\left(|\dot{\mathbf{p}}_w|\,\dot{\mathbf{p}}_w^T\right), \tag{6.14}$$

where k_{dl} and k_{dq} are the linear and quadratic damping coefficients.

Tuning algorithm

The parameters of this method can be found by:

1. Choose the constant k_k from steady state accuracy demands. This can be estimated as

$$k_k \approx \frac{\|\mathbf{f}_w^\infty\|}{\|\Delta\mathbf{p}_{\max}\|}, \tag{6.15}$$

   where $\|\Delta\mathbf{p}_{\max}\|$ is the allowed error in the warp position during steady state conditions, and $\mathbf{f}_w^\infty$ is the expected forces from the warp under steady state conditions.

2. Choose the apparent mass of the warp point from response demands. This can be estimated as

$$m_w \approx \frac{k_k}{\omega_0^2}, \tag{6.16}$$

   where ω_0 is the desired eigenfrequency of this system.

3. Choose the linear damping coefficient k_{dl} to get a specified relative damping ratio, disregarding quadratic damping:

$$k_{dl} = \frac{r_d}{2\sqrt{k_k k_i}}, \tag{6.17}$$

   where r_d is the wanted relative damping ratio, typically set to 1.

4. Choose the quadratic damping coefficient k_{dq} to give quadratic damping equal to linear damping at a desired velocity

$$k_{dq} = \frac{k_{dl}}{u_{eq}}, \tag{6.18}$$

   where u_{eq} is the velocity where the quadratic and linear damping should be equal.

This method adds little to the computational effort, even if good accuracies are demanded, and the energy consumption of the control system is easily estimated. To ensure sufficient accuracy of the energy consumption computations, transients in this system are limited by limiting the speed of the change in control line lengths, k_u.

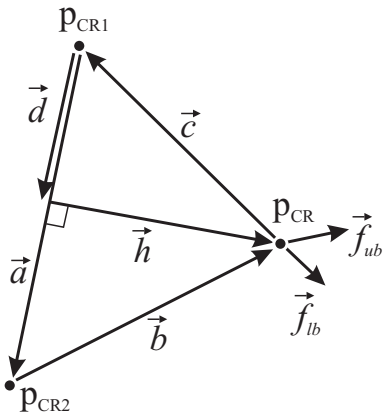

Figure 6.26: Notation for calculating the position of the crowfoot attachment point.

6.6.2 The bridle crowfoot

The same procedure could be used for the bridle crowfoot as for the warp fastening lines. It is, however, in the following assumed that the two lines of the crowfoot are always tensioned. Since the dynamics of the crowfoot are very fast in relation to those of the trawl door, a quasi-static approach is employed to find an equilibrium for each integration step. Figure 6.26 illustrates the method and how it relates to the concept in Figure 6.27.

$\vec{a}$ is the vector from $\mathbf{p}_{CR1}$ to $\mathbf{p}_{CR2}$, and $\vec{f}_{lb}$ and $\vec{f}_{ub}$ are the forces on the trawl door from the lower and upper bridles, respectively. The sum of the forces from the two bridles are designated $\vec{f} = \vec{f}_{lb} + \vec{f}_{ub}$. Requiring that $a + b > c$ yields that $\vec{f} \times \vec{a} \neq 0$, and the area of the spanned triangle can be found as

$$A = \frac{1}{2}ha = \frac{1}{4}\sqrt{4a^2b^2 - \left(a^2 + b^2 - c^2\right)^2}. \tag{6.19}$$

The length of $\vec{h}$ is then found as

$$h = \sqrt{b^2 - \frac{\left(a^2 + b^2 - c^2\right)^2}{4a^2}}. \tag{6.20}$$

It is further found from Pythagoras

$$d = \sqrt{c^2 - h^2}, \tag{6.21}$$

and the vector $\vec{d}$ is found in the trawl door frame as

$$\vec{d} = d\frac{\vec{a}}{a}. \tag{6.22}$$

The direction of $\vec{h}$ is found from

$$\vec{h} \cdot \vec{a} = 0 \tag{6.23}$$

$$\left(\vec{f} \times \vec{a}\right) \cdot \vec{h} = 0 \tag{6.24}$$

In matrix form this is formulated as

$$\begin{bmatrix} \mathbf{a}^T \\ -\mathbf{f} \times \mathbf{a}^T \\ \mathbf{h}_1^T \end{bmatrix} \mathbf{h}_0 = \begin{bmatrix} 0 \\ 0 \\ h_2 \end{bmatrix}, \tag{6.25}$$

where $\mathbf{h}_1 \in \mathbb{R}^3$ is chosen so that the matrix has full rank. A natural choice would be to use $\mathbf{h}_1 = \mathbf{f}$, since $\vec{f}$ is known to be perpendicular to the second row of the matrix and will not be parallel to $\vec{a}$ for any practical case. h_2 is a random number larger than zero. $\vec{h}$ is then found from

$$\vec{h} = h\frac{\vec{h}_0}{h_0}, \tag{6.26}$$

and the position of the fastening point is found from

$$\mathbf{p}_{CR} = \mathbf{d} + \mathbf{h}. \tag{6.27}$$

6.7 Numerical optimization of the control concept

The towing tank experiments gave some answers with respect to designing the control concept. The details of this design will, however, affect both the energy consumption and control performance, and should therefore be further improved. This would traditionally be done by trial and error, requiring many experiments and accurate measurements. In this work, however, numerical optimization is used. This has some advantages:

- The time and cost to evaluate possible configurations are reduced.
- The optimization process is automated.
- The other parts of the trawl system may be more accurately accounted for.

The drawbacks of numerical optimization is that:

- Developing a sufficiently accurate mathematical model is time consuming.
- Modeling errors may degrade the results.
- It may be more difficult to benefit from intuition and physical understanding.

Even if numerical optimization seems to be the better choice, it is acknowledged that experiments should be performed to verify and adjust the results. The reasons for this are the difficulties associated with developing a sufficiently accurate mathematical model of the trawl system in general, and the trawl doors and the trawl net in particular.

6.7.1 The trawl door controllers for the optimization

Separate PID controllers are implemented to calculate the control line length references according to the desired orientations. This length reference could have been part of the optimized variable, but using controllers instead reduces the size of the optimization drastically, and is therefore chosen. The controllers are single input single output (SISO) controllers, controlling the angles of attack and roll independently. This introduces additional objectives, causing the fastening points of the two control lines to be positioned so that control line 1 reduces the angle of attack, while control line 2 rolls the trawl door inwards. These additional objectives act as soft constraints on the solution.

Using one multiple input multiple output (MIMO) controller for both control lines may increase performance, since it would in practice remove these additional objectives. MIMO controllers would, however, complicate the optimization, since their control laws would, at least in principle, have to be changed according to the design to be evaluated. In contrast, the control law of the SISO controllers may remain unchanged from case to case.

Integrator effect is not implemented in the controllers, since this would increase the overshoot in the system, making the energy consumption calculations less accurate. The speed of the references is limited to avoid significant overshoot and to make it possible for the actuators to follow. The controllers are formulated as:

$$\dot{l}_{i,d} = \begin{cases} \max\left(-k_{pi}\varepsilon_i, -\dot{l}_{d,\max}\right) & , \quad \varepsilon_i > \varepsilon_{o,\max} \wedge T_i < T_{d,\max} \\ \min\left(-k_{pi}\varepsilon_i, \dot{l}_{d,\max}\right) & , \quad \varepsilon_i < -\varepsilon_{o,\max} \wedge T_i > 0 \\ 0 & , \quad otherwise \end{cases} , \; i = 1,2 \tag{6.28}$$

where k_{pi} is the proportional gain, $\varepsilon_{o,\max}$ is the accepted orientation deviation and $\dot{l}_{d,\max}$ is the maximum speed of the control line reference. $l_{i,d}$ is the reference length of control line i, which is the input of the actuators described in (6.10). $T_{d,\max}$ is the maximum tension in the control lines before this controller avoids shortening the lines any more. To get reliable estimates of the energy consumption, excessive actuator use must be avoided. This is achieved by choosing k_{pi} and $\dot{l}_{d,\max}$ sufficiently small and $\varepsilon_{o,\max}$ sufficiently large. $T_{d,\max}$ must be chosen smaller than the value for the corresponding actuators ($T_{\max}$).

The deviation from the orientation reference is defined as

$$\boldsymbol{\varepsilon} = \begin{bmatrix} \alpha^d - \alpha^d_d \\ \gamma^g - \gamma^g_d \\ u_H\left(\beta^g - \beta^g_{\max}\right)\left(\beta^g - \beta^g_{\max}\right) + u_H\left(\beta^g_{\min} - \beta^g\right)\left(\beta^g - \beta^g_{\min}\right) \end{bmatrix}, \tag{6.29}$$

where the subscript d designates the desired values. β^g and γ^g are the pitch and roll of the trawl door defined in relation to the gravity vector. $\beta^g_{\max}$ and $\beta^g_{\min}$ are the desired maximum and minimum of these angles. β^g and γ^g are defined as

$$\beta^g = -\arcsin\left(\frac{\vec{g}\cdot\vec{e}_{x^d}}{\|\vec{g}\|}\right)\operatorname{sgn}\left(\vec{g}\cdot\vec{e}_{x^d}\right), \tag{6.30}$$

$$\gamma^g = \arcsin\left(\frac{\vec{g}\cdot\vec{e}_{y^d}}{\|\vec{g}\|}\right)\operatorname{sgn}\left(\vec{g}\cdot\vec{e}_{y^d}\right), \tag{6.31}$$

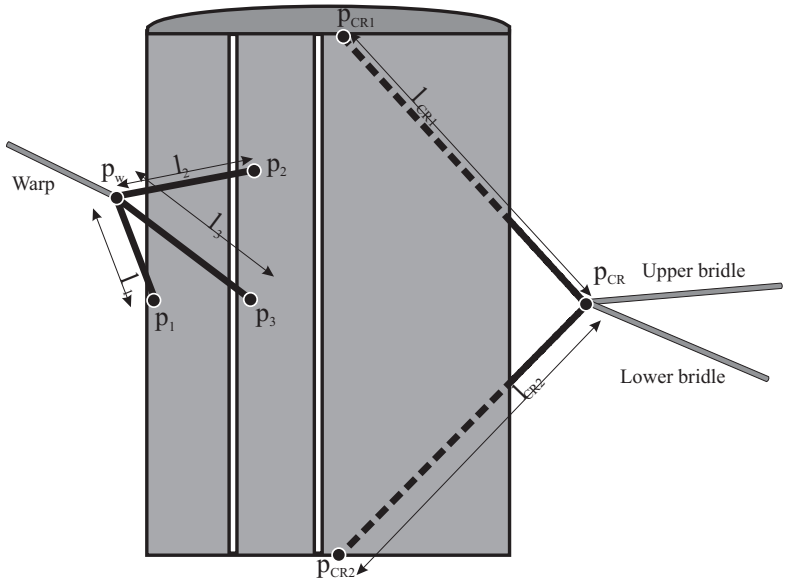

Figure 6.27: The variables to be optimized.

where $\vec{e}_{x^d}$ and $\vec{e}_{y^d}$ are the unity direction vector of the x^d- and y^d-axis, respectively. The reason for choosing this representation is that this is what is most easily measured on the trawl door during real operations, and also that it may give a more intuitive meaning than for example the Euler angles.

6.7.2 Properties to be optimized

The search for an optimal concept is limited to finding the main characteristics of the concept determined from the towing tank experiments. This reduces the size of the problem considerably and allows intuition and physical understanding to enter the design process. The variables to optimize are illustrated in Figure 6.27:

- Position of the control lines fastening points $\left(x_1^d, y_1^d, z_1^d, x_2^d, y_2^d, z_2^d\right)$.
- Position of the pivot line fastening point $\left(x_3^d, y_3^d, z_3^d\right)$.
- Position of the crow lines fastening points $\left(x_{CR1}^d = x_{CR2}^d, y_{CR1}^d = y_{CR2}^d\right)$.
- Length of the pivot line (l_3).
- Ratio between the length of the upper crowfoot line and the sum of the length of the two crowfoot lines $\left(\frac{l_{CR1}}{l_{CR1}+l_{CR2}}\right)$.

The sum of the length of the crowfoot lines are predefined, using a combination of physical insight and trial-and-error. The crow lines are restricted to be fastened at

$z^d_{CR1} = -\frac{s_d}{2}$, $z^d_{CR2} = \frac{s_d}{2}$ and with common x^d- and z^d-coordinates. The variables to be optimized are collected in the variable $\mathbf{x}^{opt}$:

$$\mathbf{x}^{opt} = \left[\begin{bmatrix} x^d_3 & y^d_3 & z^d_3 & \frac{l_{CR1}}{l_{CR1}+l_{CR2}} & x^d_{CR} & y^d_{CR} & \cdots \\ & x^d_1 & y^d_1 & z^d_1 & x^d_2 & y^d_2 & z^d_2 & l_3 \end{bmatrix} \right]^T. \tag{6.32}$$

6.7.3 Constraints

The optimization includes constraints on the solution. These constraints are based on practical considerations, such as:

- The lines are not allowed to go through the trawl door.
- The fastening points should not protrude more than what is practical.
- The trawl door should be stable also when no hydrodynamic forces act on it.
- The pivot line should be short enough to not complicate handling.

The following constraints are posed on the solution:

$$\begin{aligned} \mathbf{x}^{lb} &< \mathbf{x}^{opt} < \mathbf{x}^{ub}, \\ \mathbf{x}^{lb} &= \begin{bmatrix} -0.4 & -0.5 & -1.0 & 0.5 & -1.7 & 0.2 & \cdots \\ 1 & -0.4 & -2 & -1.6 & -0.4 & -2.5 & 0.5 \end{bmatrix}^T, \\ \mathbf{x}^{ub} &= \left[\begin{bmatrix} 0.8 & 0.3 & 0.4 & 0.65 & 0.0 & 0.8 & \cdots \\ 1.6 & 0.1 & 2.0 & 1.6 & 0.2 & -1.0 & 1.0 \end{bmatrix} \right]^T, \end{aligned}$$

where $<$ and $>$ impose restrictions on the individual elements:

$$\mathbf{x}^{lb} < \mathbf{x}^{opt} < \mathbf{x}^{ub} \tag{6.33}$$

$$\Updownarrow \tag{6.34}$$

$$x^{lb}_i < x^{opt}_i < x^{ub}_i \ , i = 1, 2 \ldots 13. \tag{6.35}$$

Element number 4 is a ratio, the values of the other elements are given in meters.

6.7.4 Objectives

The main objective is to minimize the energy consumption on the trawl door, while giving adequate control performance and hydrodynamic efficiency. The trawl system simulator is used as part of the objective evaluations. It is initially run with a manual setup chosen to give steady and high angles of attack and outwards roll with untensioned control lines. This steady state is used as the initial states for every iteration during the optimization. A transient will be present in the initial motion of the trawl door for different configurations. To avoid this being reflected in the objective, the objective evaluation begins a specified amount of time after the simulation is started.

To quantify the performance of a possible configuration, the ability of the trawl door to follow a specific reference is considered. The reference used in the optimization is

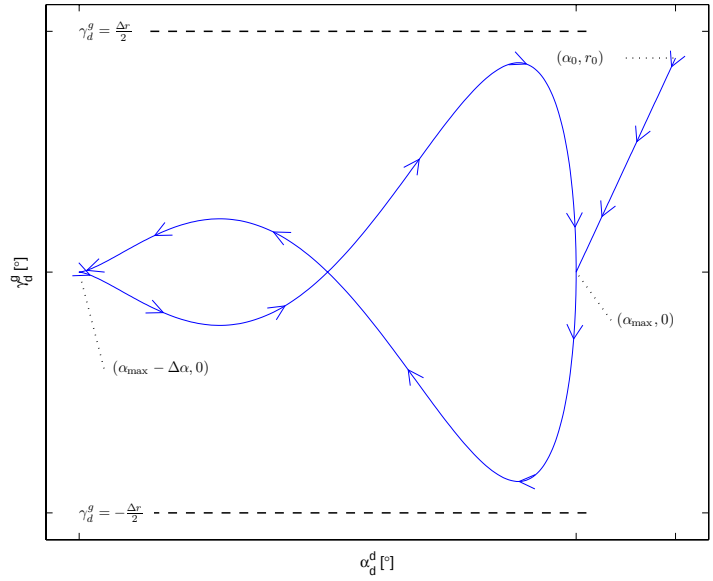

Figure 6.28: The desired trajectory of the trawl door orientation angles.

shown in Figure 6.28. The desired pitch angle (β_d^g) is zero, since small pitch angles are found to give the highest hydrodynamic efficiency of the trawl door. The simulation starts with no tension in the control lines, and the reference is kept fixed to allow the controller to adjust. The reference is first driven towards zero roll angle and angle of attack $\alpha_{\max} = 30\,^\circ$. The performance is only evaluated from the time when the reference reaches this point ($t = t_1$). The trawl door is then controlled to give variations in angle of attack and angle of roll as shown in Figure 6.28. The arrows indicate the direction of the trajectory, and the distance between them indicates the speed of the change. The desired orientation angles are calculated as

$$\alpha_d^d(t) = \begin{cases} \alpha_0 + (\alpha_{\max} - \alpha_0)\frac{t}{t_1} & , t < t_1 \\ \alpha_{\max} - \frac{\Delta\alpha}{2}\left(1 - \cos\left(2\pi\frac{t-t_1}{t_2-t_1}\right)\right) & , t_1 \le t \le t_2 \end{cases}, \tag{6.36}$$

$$\gamma_d^g(t) = \begin{cases} r_0\left(1 - \frac{t}{t_1}\right) & , t < t_1 \\ \frac{\Delta r(\alpha - \alpha_{\max} + \Delta\alpha)}{2\Delta\alpha}\sin\left(2\pi n_L \frac{t}{t_2-t_1}\right) & , t_1 \le t \le t_2 \end{cases}, \tag{6.37}$$

$$\beta_d^g = 0, \tag{6.38}$$

where n_L is the number of loops on the reference ($n_L = 2$ is used for the optimization) and t_1 is the time when the reference first reaches $\alpha_d^d = \alpha_{\max}$, $\gamma_d^g = 0$. At time t_2 the reference reaches the same state as in t_1. t_2 is chosen to give a sufficiently slow progress of the simulations. The remaining symbols are presented in Figure 6.28.

The objective value for completed simulations

Provided the simulation completes, the objective value is based on the energy consumption of the actuators and the control performance. It is assumed that no energy can be recovered from the actuators, and the system is (for the optimization) treated as if it were 100% efficient (without friction and other losses). The performance of the trawl door control is evaluated based on the deviation between the reference and the actual orientation trajectory. The objective function is formulated as

$$O = \int_{t_0}^{t_1} \begin{pmatrix} \boldsymbol{\varepsilon}^T \mathbf{K}_{\boldsymbol{\varepsilon}} \boldsymbol{\varepsilon} + k_\omega u_H \left(\omega_{amp} - \omega_{\max}\right) \omega_{amp}^2 \\ -T_1 \dot{l}_{1,d} u_H \left(\dot{l}_{1,d}\right) - T_2 \dot{l}_{2,d} u_H \left(\dot{l}_{2,d}\right) \end{pmatrix} d\tau + \mathbf{k}_\varepsilon^T \boldsymbol{\varepsilon}_{ex}, \tag{6.39}$$

$$\omega_{amp} = \left\| \vec{\omega}_{dn} \right\|, \tag{6.40}$$

$$\varepsilon_{ex,i} = \max\left(\left|\varepsilon_i\left(t\right)\right|\right), \tag{6.41}$$

where $\mathbf{K}_{\boldsymbol{\varepsilon}} \in \mathbb{R}^{3\times 3}$ is the diagonal orientation deviation weight matrix, T_i is the tension in the control line i, and k_ω is the instability weight factor. $\boldsymbol{\varepsilon}_{ex}$ is the absolute value of the largest error in orientation for each orientation angle, and $\mathbf{k}_\varepsilon^T$ is the maximum error weight factor. The first part of the integrand evaluates the control performance, the second part evaluates the stability and the next two parts evaluate the energy consumption of each actuator. The last part of the objective function increases the penalty for solutions leading to large orientation deviations in a narrow region.

The objective value for aborted simulations

The objective evaluation is aborted if the evaluated solution is regarded to be computational costly and far from the optimum. This situation is detected if one of the following criteria are true:

$$\begin{aligned} \int_0^t \left\| \vec{\omega}_{dn} \right\| d\tau &> \omega_{\lim} \\ &or \\ t^{RT} &> t_{\lim}, \end{aligned} \tag{6.42}$$

where t^{RT} is the real amount of time spent for the simulation in question. The constants $t_{\lim}$ and $\omega_{\lim}$ are chosen by trial and error. The first criterion detects instability, while the second detects long simulation times. Aborting the simulation in such cases improves the optimization performance, as it prevents excessive computational effort to be spent far from the optimum. The penalty for aborted simulations is found as

$$O_{abort} = k_1 + k_2 \left(t_{end} - t_{stop}\right)^2, \tag{6.43}$$

where k_1 and k_2 are positive constants, and t_{end} and t_{stop} are the chosen simulation time and the simulation time when the simulations were aborted, respectively. $k_1$must be chosen sufficiently large to avoid creating local optima where the simulations are only just aborted.

Case	$\alpha_{\max}$	$\Delta\alpha$	Δr
1	30 °	10 °	40 °
2	30 °	10 °	70 °
3	30 °	10 °	100 °
4	30 °	20 °	40 °
5	30 °	20 °	70 °
6	30 °	20 °	100 °

Table 6.4: The reference trajectories for which the control concept was optimized.

6.7.5 Optimization routines

Various optimization routines have been tried out. Even for long computation times ($\sim$ 100 h), most of these would not converge towards a credible global optimum. The reason for this is probably that the objective function contains multiple local optima. The genetic algorithm described in Houck et al. (1995) does, however, converge. This is probably due to the fact that genetic algorithms do not follow a search path determined by the objective function derivatives, but "jump" all over as they search for the optimum solution. This renders them usable for global optimization, but it also leads to poor performance close to an optimum, compared to gradient methods. The basics of genetic algorithms are presented in Appendix A.

To improve the convergence rate when closing in on a solution, additional constraints are posed on the solution after a number of generations. The new constraints are updated every few generations, and they are calculated as

$$x^{lb}_{temp,i} = \max\left(x^{lb}_i, x^{opt}_{temp,i} - k\left(x^{ub}_i - x^{lb}_i\right)\right), \tag{6.44}$$

$$x^{ub}_{temp,i} = \min\left(x^{ub}_i, x^{opt}_{temp,i} + k\left(x^{ub}_i - x^{lb}_i\right)\right), \tag{6.45}$$

where $x^{lb}_{temp,i}$ and $x^{ub}_{temp,i}$ are the temporary lower and upper bounds on variable i, respectively. x^{lb}_i and x^{ub}_i are the lower and upper bounds on variable i, respectively. k is a factor deciding how narrow the feasible region should be, and $x^{opt}_{temp,i}$ is the best solution for variable i found so far.

Genetic optimization routines are not as efficient as optimization routines based on objective function gradients when the objective function is convex. Assuming the objective function to be convex close to the solution, the simplex search method of Lagarias et al. (1998), incorporated in the `fminsearch` function of the Matlab™ software is used when the genetic algorithm is believed to converge towards a global optimum.

6.7.6 Results

The optimization is performed for six different cases, as defined in Table 6.4. The results in terms of control performance are shown in Figure 6.29, with the predicted energy consumption and the objective value printed above each plot. The thin line shows the trajectory of the trawl door angles of attack and roll, while the thick line shows the reference trajectory of the same. Neither the pitch angle reference nor the pitch angle trajectory are shown in the plot.

It is important to notice that the performance of the control concept design is defined in the objective function to include not only the angles of attack and roll, but also the energy consumption, the angle of pitch, stability measures, and the maximum deviation from the reference (including the pitch angle). This is part of the reason why the control performance in terms of angles of attack and roll may not seem as good as desired. The other reason is that the optimizations, even after more than 1000 h, are still improving. Further improvements may therefore be expected.

The most distinctive feature on the plots, is probably the loop that is sometimes formed for small angles of attack and large angles of roll. This is particularly pronounced for Case 6. It is not precisely known what causes it, but one possible explanation is that the warp fastening point is placed so that the angle of attack is smaller than 30 ° when the control lines are not tensioned. To obtain the maximum angle of attack, the control line controlling the angle of roll is placed far aft. When tightened, it will then increase the angle of attack. This means that at large angles of roll (when this control line pays out), the angle of attack can not be maintained. The reason for this design being chosen, even if it is not able to follow the reference in one part of the working area, is probably that it reduces the energy consumption. If the reference were to be followed exactly, the warp fastening point had to be placed such as to give a larger angle of attack. The tension in the control line controlling the angle of attack would increase, increasing the energy consumption. Another cause may be that the optimization still has not converged, and that this phenomena will disappear as the design improves.

To compare the performance of the various design solutions, simulations are performed for all solutions, using identical reference trajectories. The reference trajectory of Case 1 is chosen, since all the other design cases should be able to follow this. The reference trajectory is then given by $\alpha_{\max} = 30\,^\circ$, $\Delta\alpha = 10\,^\circ$ and $\Delta r = 30\,^\circ$. The performance of the various solutions are shown in Figure 6.30. The energy consumption of Case 1 would be expected to be the lowest, since this concept is optimized for this particular reference trajectory. The energy consumption of Case 2 is, however, equally low. But its objective value is still higher than for Case 1. This indicates that there are some drawbacks of Case 2 not visible on the figure. The pitch angle may for example be further from the desired range.

The objective values of these design solutions show that there is a strong connection between which trajectory the design is optimized for, and how it performs, as is expected. This means that optimizing the trawl door design for a too wide control range will lead to an increased energy consumption, and the control concept should be optimized according to the actual needs.

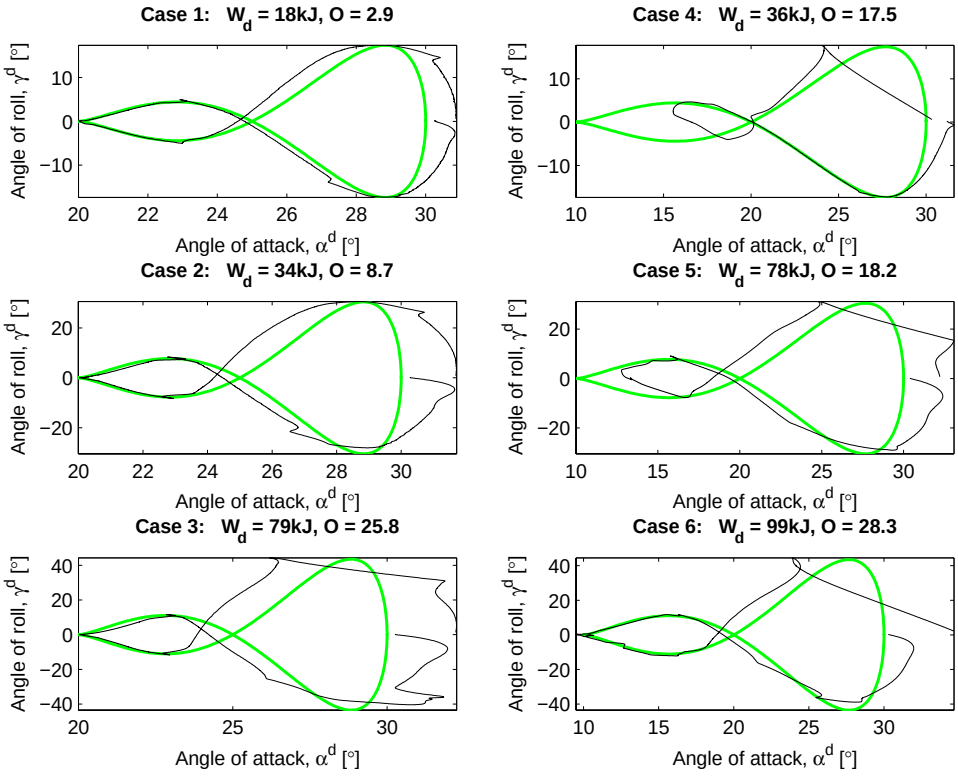

Figure 6.29: The performance of the optimized design for the reference trajectories.

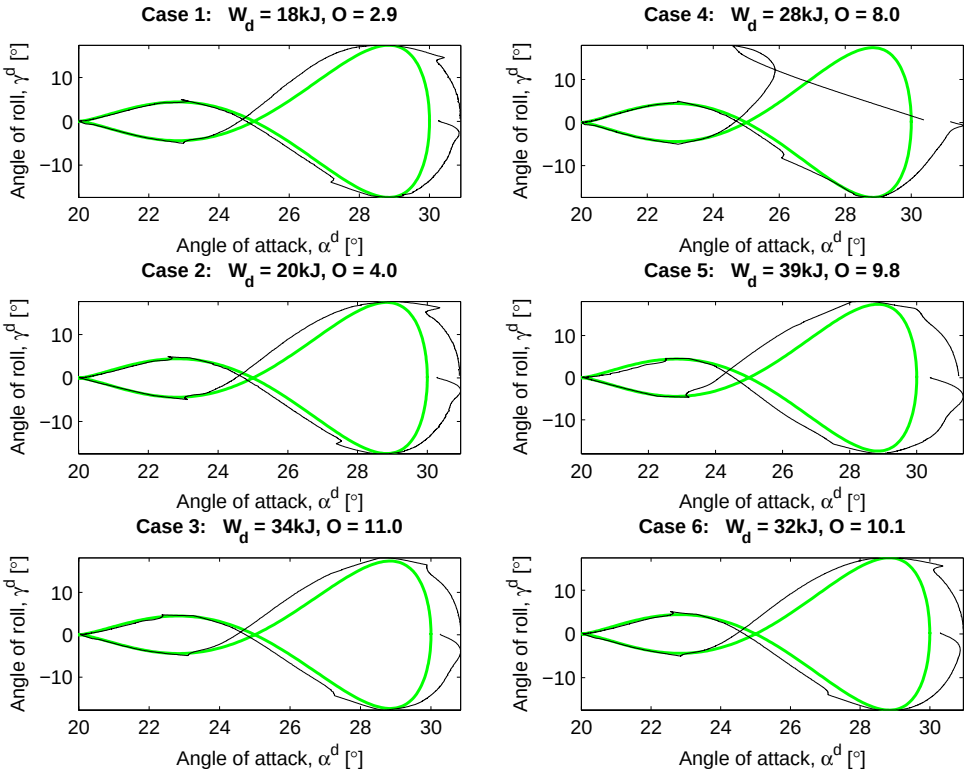

Figure 6.30: The performance of the optimized design for an equal reference trajectory.

Chapter 7

Conclusions and proposals for further work

7.1 Conclusion

The aim of this work has been to develop a framework making improved trawl control possible. This has been done by modeling the hydrodynamic forces on the trawl doors, describing a supervisory control architecture, and developing a control concept.

A model of the hydrodynamic forces on a trawl door was developed, based on wind tunnel experiments and a developed computational fluid dynamics software based on potential theory. The resulting model calculates the 6dof steady state and transient hydrodynamic forces on a 3D trawl door moving in 6dof. The measurements of the hydrodynamic forces showed that these forces tend to destabilize the trawl door about the vertical axis for some ranges of angle of attack, while they for other ranges tend to stabilize it. This should be taken into consideration when developing both trawl doors and trawl door control concepts.

The change in angle of attack due to a rotation about the vertical axis of the trawl door lead to different transient hydrodynamic forces than if the same change in angle of attack originated from a change in the transversal velocity component. This means that if the transient hydrodynamic forces on foils are to be accurately calculated, the velocity of the foil relative to the water should not be defined only by the angles of attack and slip. It was shown that the proposed model of the hydrodynamic forces rendered the trawl doors stable during simulations, with no artificial damping.

Having evaluated several possible trawl door control principles, it was clear that the various principles possess different characteristics, and that the choice of concept must be done according to the requirements of the individual user. The need for energy efficiency and performance may, for example, oppose the desire for using existing equipment. It was shown how the control concept design could be improved using mathematical modeling and numerical optimization. Genetic algorithms were proposed for such optimization, as these are robust with regard to nonlinearities and the existence of local optima in the objective function. Since their convergence rate is low, a local optimization method was

proposed for the final convergence towards an optimum solution. The performance of the chosen control concept was shown to be dependent on the requirements for which it was optimized, calling for accurate identification of the demands on control performance and energy consumption before optimization.

A supervisory control architecture was proposed, and its performance was verified through case studies. It was seen that the various parts of the control system performed well, but the available computer capacity limited the use of model predictive control. It is clear that for such a system to be practical, measures must be taken to decrease the gap between available computing capacity and the needs of the control system. If the computing power is not to be significantly increased, such measures could be for example to simplify the fast control plant model and to find improved initial conditions.

Regardless of the use of automatic control, it is rendered probable that using independent models for state estimation may replace and/or improve the expensive and inaccurate trawl system measurements of today. Even using only measurements readily available on most ships (the ship position, the depth of the trawl net and the warp lengths), an adequate representation of the positions of the various parts of the trawl system should be attainable.

7.2 Proposals for further work

The developed mathematical model is focused towards control of trawl systems. Although the modeling of the trawl net is probably sufficiently accurate for this purpose, the specifics on how the trawl net is built is not fully accounted for. As a next step, it would be beneficial to develop a model of the trawl net based on its specific construction. The mathematical model of the trawl system should also be verified by full scale experiments.

The model of the hydrodynamic forces on trawl doors should be verified through model experiments, especially the modeling of transient forces and the extension to other types of trawl doors. If the accuracy of the transient hydrodynamic forces are important, an improved model of these forces should be developed, and computational fluid dynamics taking the viscosity into account should be considered. If an improved parameterized model of the transient hydrodynamic forces is to be developed, using the relative velocity components of the trawl door instead of its hydrodynamic orientation angles would increase its accuracy.

When evaluating the various principles the trawl door control concept could be based upon, it seemed clear that if initial costs and practical problems were disregarded, other control principles may be more advantageous than the chosen one. Control concepts based on controlling the hydrodynamic properties of the trawl door may be the most promising. Such concepts could be designed for low energy consumption, and still give good control performance. Since the hydrodynamic forces on the trawl door would be dependent on the specifics of the control concept, and therefore more time consuming to find, such concepts would probably be developed more easily based on more extensive experiments.

Using an independent model to estimate the states of the system seemed to work fine. A robust method to adapt the model parameters fast without risking instabilities to occur should, however, be developed and implemented in the model corrector. Such a

system would probably be of interest for the trawling industry, as it could both replace and make better use of existing measurements.

Not unexpected, the model predictive control optimization proved to be too time consuming to be practical useful. To solve these problems, methods to improve the initial conditions of the optimization should be developed. This could be achieved by constructing an initial reference trajectory using no trawl system model at all, only requiring the trajectory to satisfy some constraints with regard to smoothness. Simulating a trawl system following this trajectory, using only feedback control, would then provide the initial conditions for the optimization. If only waypoint following is to be considered, and no other objectives are present, the winch and the thrust control action may be merged to decrease the computational demands.

To take use of the possibilities that MPC provides, more complex objectives should be taken into account. This poses even harder requirements on the computational efficiency of the optimization. Much research is needed in this field, but the implementation of objectives with regard to amount of bottom contact, avoidance of obstacles and reduced costs seem possible.

Bibliography

I. H. Abbott and A. E. V. Doenhoff. *Theory of wing sections: Including a summary of airfoil data*. McGraw-Hill Book Company, New York, 1959.

J. A. D. Ackroyd. On the analysis of turbulent boundary layers on slender cylinders. *Journal of Fluids Engineering*, 104:185–190, 1982.

J. V. Årsnes, G. Løland, and H. Rudi. Current forces on cage, net deflection. In *Engineering for offshore fish farming*, Glasgow, UK, 1990.

J. Bessonneau and D. Marichal. Study of the dynamics of submerged supple nets (applications to trawls). *Journal of Ocean Engineering*, 25(7):563–583, 1998.

M. Blanke and A. Christensen. Rudder roll damping autopilot robustness to sway-yaw-roll couplings. In *Procedings of 10th SCSS*, pages 93–119, Ottawa, Canada, 1993.

J. R. Botta and G. Bonnell. Causes of reduced quality of fresh Atlantic cod (Gadus Morhua) caught by otter trawl. In *World Symposium on Fishing Gear and Fishing Vessel Design*, St. John's, New Foundland, Canada, 1988. Marine Institute.

M. J. Casarella and M. Parsons. Cable systems under hydrodynamic loading. *Marine Technology Society Journal*, 4(4):27–44, 1970.

S. Chakrabarti. *Hydrodynamics of offshore structures*. Computational Mechanics Publications. Springer Verlag, 1987.

M. Clark and R. O'Driscoll. Deepwater fisheries and aspects of their impact on seamount habitat in New Zealand. *Journal of Northwest Atlantic Fishery Science*, 31:151–163, 2003.

I. Coope. Reliable computation of the points of intersection of n spheres in R^n. *The ANZIAM journal*, 42:461–477, 2000.

T. Digernes and C. M. Yi. Regression analyses of model resistance : Norwegian and Danish vessels. Technical report, Fiskeriteknologisk Forskningsinstitutt (FTFI), 1983.

H. Digre and U. J. Hansen. Forholdet mellom redskap og kvalitet på fisk, råstoffbehandling ombord i fartøy, del II. Dokumentasjon av egenskaper ved T90 trålsekk. Technical Report 342102, The Norwegian Fishery and Aquaculture Industry Research Fund, SINTEF Fisheries and Aquaculture, 2005.

O. Egeland and J. T. Gravdahl. *Modeling and simulation for automatic control*. Marine Cybernetics, Trondheim, 2002.

H. Ellingsen and S. A. Aanondsen. Energy use in the norwegian fishing industry. Environmental consequences of alternative energy carriers. In *LCM2005*, Barcelona, Spain, 2005. The Catalan and Spanish LCA Networks.

H. Ellingsen and S. A. Aanondsen. Environmental impacts of wild caught cod and farmed salmon - a comparison with chicken. *International Journal of LCA*, 1:60–65, 2006.

A. Engås, B. Isaksen, and J. W. Valdemarsen. Artsselektivt fiske. Sluttrapport til Norges Forskningsråd. Technical report, Institute of Marine Research, Norway, 1996.

S. Ersdal. *An experimental study of hydrodynamic forces on cylinders and cables in near axial flow*. PhD thesis; 2004:125. Department of Marine Technology, Faculty of Engineering Science and Technology, Norwegian University of Science and Technology, Trondheim, 2004.

D. Fahti. ShipX vessel responses (VERES). Technical report, MARINTEK AS, Trondheim, 2004.

O. M. Faltinsen. *Sea loads on ships and offshore structures*. Cambridge University Press, Cambridge, 1990. Cambridge ocean technology series.

FAO. *The state of world fisheries and aquaculture (SOFIA) 2002*. Food and Agriculture Organization of the United States, Fisheries Department, Rome, 2002.

R. Ferro and E. Hou. Selected review of hydrodynamic force coefficient data on stranded wires used in fishing gear. Technical Report 31, Department of Agriculture and Fisheries for Scotland, 1984.

J. Fosså, P. Mortensen, and D. Furevik. The deep-water coral Lophelia Pertusa in Norwegian waters: Distribution and fishery impacts. *Hydrobiologia*, 471(1 - 3):1–12, 2002.

J. H. Fosså. Sluttrapport - Effekter av fiske på korallrev på den norske kontinentalsokkelen (in Norwegian). Technical Report 121 122/122, Norwegian Research Council, 2000.

J. H. Fosså. Annual coral mapping. `http://www.imr.no/coral/`, July 2003. Last accessed 30.03.2006.

T. I. Fossen. *Marine control systems : Guidance, navigation and control of ships, rigs and underwater vehicles*. Marine Cybernetics, Trondheim, 2002.

T. I. Fossen. A nonlinear unified state-space model for ship maneuvering and control in a seaway. *Journal of Bifurcation and Chaos*, 15, 2005.

T. I. Fossen and Ø. N. Smogeli. Nonlinear time-domain strip theory formulation for low-speed manoeuvring and station-keeping. *Modelling, Identification and Control, MIC-25(4)*, 2004.

A. Fredheim. *Current forces on net structures.* PhD thesis; 2005:64. Department of Marine Technology, Faculty of Engineering Science and Technology, Norwegian University of Science and Technology, Trondheim, 2005.

A. Fredheim and O. M. Faltinsen. Hydroelastic analysis of a fishing net in steady inflow conditions. In *International Conference on Hydroelasticity in Marine Technology*, Oxford, 2003. University of Oxford.

C. S. C. Gatti. *Numerical simulations of large deformation cable synamics.* PhD thesis, University of Michigan, 2002.

Geco AS. Deflector. European patent number EP0562780, 1993.

M. Gianni. High seas bottom trawl fisheries and their impacts on the biodiversity of vulnerable deep-sea ecosystems. Technical report, IUCN/the World Conservation Union, Natural Resources Defense Council, WWF International and Conservation International, 2004.

D. Gréboval. Assessing excess fishing capacity at world-wide level. Technical report, FAO Fisheries Department, 1999. FAO Fisheries Technical paper 386, ISBN 92-5-104295-0.

T. Hattula, T. Luoma, R. Kostiainen, J. Poutanen, M. Kallio, and P. Suuronen. Effects of catching method on different quality parameters of Baltic herring (Clupea Harengus l.). *Fisheries Research*, 23(3-4):209–221, 1995.

M. Heino. Blue Whiting: Playing a big game with small fish. *ICES Newsletter*, 11:19–20, September 2004.

O. Henriksen. Deflector. Patent number US6142091, 2000.

S. F. Hoerner. *Fluid-dynamic lift : Practical information on aerodynamic and hydrodynamic lift.* Brick Town, N.J., 1975.

C. Houck, J. Joines, and M. Kay. A genetic algorithm for function optimization: A Matlab implementation. *North Carolina State University*, 1995.

I. Huse (ed), S. A. Aanondsen, H. Ellingsen, A. Engås, D. Furevik, N. Graham, B. Isaksen, T. Jørgensen, S. Løkkeborg, L. Nøttestad, and A. V. Soldal. A desk-study of diverse methods of fishing when considered in perspective of responsible fishing, and the effect on the ecosystem caused by fishing activity. In I. Huse, editor, *TemaNord 2003.501*, Copenhagen, 2002. Nordic Council of Ministers.

ICES. The status of fisheries and related environment of northern seas. In *Nord*, Copenhagen, 2000. Nordic Council of Ministers.

H. M. Irvine. *Cable structures.* The MIT Press series in structural mechanics 1. The MIT Press, Cambridge, Mass., 1981.

V. Johansen, O. Egeland, and A. J. Sørensen. Modelling and control of a trawl system in the transversal direction. *IFAC*, pages 292–297, 2002.

V. Johansen, S. Ersdal, A. J. Srensen, and B. Leira. Modelling of inextensible cable dynamics with experiments. *International Journal of Non-Linear Mechanics*, 41(4): 543–555, May 2006.

R. T. Jones. The unsteady lift of a wing of finite aspect ratio. Technical Report 681, NACA, 1940.

J. M. J. Journée and L. J. M. Adegeest. Theoretical manual of strip theory program "SEAWAY for Windows". Technical Report DUT-SHL Report 1370, Delft University of Technology, Amarcon, 2003.

J. M. J. Journée and W. W. Massie. *Offshore Hydromechanics*. Delft University of Technology, 1st edition, 2001. Last accessed 31.07.2006.

L. Karlsen. *Redskapsteknologi i fiske*. Universitetsforlaget, Oslo, 1989.

L. Karlsen. *Redskapslære og fangstteknologi*. Landbruksforlaget, Oslo, 1997.

J. Katz and A. Plotkin. *Low-speed aerodynamics: From wing theory to panel methods*. McGraw-Hill, New York, 1991. McGraw-Hill series in aeronautical and aerospace engineering.

H. G. Küssner. Das zweidimensionale Problem der beliebig bewegten Tragfläche unter berücksichtigung von partialbewegung der flüssigkeit. *Luftfahrtsforsch.*, 371(2):355–361, 1940.

P. F. Lader, B. Enerhaug, A. Fredheim, and J. Krokstad. Modelling of 3d net structures exposed to waves and current. In *3rd International Conference on Hydroelasticity in Marine Technology*, Oxford, UK, 2003.

J. Lagarias, J. A. Reeds, M. H. Wright, and P. E. Wright. Convergence properties of the Nelder-Mead simplex method in low dimensions. *SIAM Journal of Optimization*, 9(1): 112–147, 1998.

C.-W. Lee. Depth control of a midwater trawl gear using fuzzy logic. *Fisheries Research*, 24:311–320, 1995.

C.-W. Lee. Depth control of a midwater trawl net using fuzzy logic. In M. Paschen, W. Köpnick, G. Niedzwiedz, U. Richter, and H.-J. Winkel, editors, *Contributions on the theory of fishing gears and related marine systems*, pages 169–176, Rostock, 1999. Neuer Hochschulscriftenverlag Dr. Ingo Koch Co.

C.-W. Lee, J.-H. Lee, B.-J. Cha, H.-Y. Kim, and S.-J. Won. Calculation model to describe the fishing gear behavior. In M. Paschen, editor, *DEMAT'01*, volume 2, pages 15–20, Rostock, Germany, 2001a. Ingo Koch Verlag & Co. KG.

C.-W. Lee, C.-I. Zhang, and H.-O. Shin. Simplified trawl system modeling and design of a depth control system using fuzzy logic. *Fisheries Research*, 53:83–94, 2001b.

J. G. Leishman. Challenges in modeling the unsteady aerodynamics of wind turbines. In *21st ASME Wind Emergy Symposium and the 40th AIAA Aerospace Sciences Meeting; 2002-0037*, Reno, NV, 2002. AIAA.

G. Løland. *Current forces on and flow through fish farms*. PhD thesis, Division of Marine Hydrodynamics, The Norwegian Institute of Technology, 1991.

A. Lovatt, H. Shercliff, and P. Withers. Ropes case study. http:// www- materials. eng. cam. ac. uk/ mpsite/ short/ OCR/ ropes/ default. html, 2005. Last accessed 31.07.2006.

J. M. Maciejowski. *Predictive control : With constraints*. Prentice Hall, Harlow, 2002.

R. Margason, S. Kjelgaard, W. S. III, C. M. Jr., K.B.Walkey, and E. Shields. Subsonic panel methods - A comparison of several production codes. *AIAA 23rd Aerospace Sciences meeting, Reno, Nevada*, 1971.

J. H. Milgram, M. S. triantafyllou, F. C. Frimm, and G. Anagnostou. Seakeeping and extreme tensions in offshore towing. *SNAME Transactions*, 96:35–70, 1988.

N. Mulvany, J. Y. Tu, L. Chen, and B. Anderson. Assessment of two-equation turbulence modelling for high Reynolds number hydrofoil flows. *International Journal for Numerical Methods in Fluids*, 45(3):275–299, May 2004.

J. D. Neilson, K. Waiwood, and S. J. Smith. Survival of Atlantic halibut (Hippoglossus Hippoglossus) caught by longline and otter trawl gear. *Canadian Journal of Fisheries and Aquatic Sciences*, 46:887–897, 1989.

J. A. Nelder and R. Mead. A simplex method for function minimization. *Computer Journal*, 7:308–313, 1965.

J. N. Newman. *Marine hydrodynamics*. The MIT Press, Cambridge, 1977.

G. Niedzwiedz. Computer-aided simulation of shape and strength of trawls after changes in design and operational conditions. In M. Paschen et al, editor, *DEMAT'99*, pages 119–135, Rostock, Germany, 1999. Neuer Hochschulschriftenverlag Dr. Ingo Koch & Co. KG.

J. Nocedal and S. J. Wright. *Numerical optimization*. Springer series in operations research. Springer, New York, 1999.

NPO Promrybolovstva. Trawl System "Warp". Brochure from Marine Scientific Production Corporation on Fishing Technology (Marinpo).

M. Paschen. A two-dimensional model for the prediction of the behaviour of towed underwater vehicles in marine research. *Proceedings of the Sixth International Conference on Stability of Ships and Ocean Vehicles, Varna, Bulgarien, 22.-27. September*, 1997.

M. Paschen. Strmungsuntersuchungen an Netzstrukturen der Meeresforschung und der Fischerei. *Schiffbauforschung*, 42(2):65–75, 2003.

M. Paschen, G. Niedzwiedz, and H.-J. Winkel. Fluid structure interactions at towed fishing gears. In *23rd International Conference on Offshore Mechanics and Arctic Engineering, Jun 20-25 2004*, volume 3 of *Proceedings of the International Conference on Offshore Mechanics and Arctic Engineering - OMAE*, pages 855–865, Vancouver,

BC, Canada, 2004. American Society of Mechanical Engineers, New York, NY 10016-5990, United States.

M. Paschen, U. Richter, and W. Köpnick. Trawl penetration in the sea bed. Technical Report European Community contract 96-006, UNI-ROS, RVZ, RIVO-DLO, NITG-TNO, 2000.

E. Pedersen. *A nautical study of towed marine seismic streamer cable configurations.* PhD thesis, Department of Marine Hydrodynamics, Faculty of Marine Technology, The Norwegian University of Science and Technology, 1996.

Petroleum Geo-Services AS. Deflector. US patent no. 6 234 102 B1, 2001.

Petroleum Geo-Services AS. System for controlling a marine seismic array. US patent no. 6 681 710 B2, 2004.

D. Priour. Net shape calculation by the finite element method. In *International Workshop Dedicated to the Hydrodynamic Aspects of Fishing Gears*, page 14, 1997.

D. Priour. Calculation of net shapes by the finite element method with triangular elements. *Communications in Numerical Methods in Engineering*, 15(10):755–763, 1999.

D. Priour. Introduction of mesh resistance to opening in a triangular element for calculation of nets by the finite element method. *Communications in Numerical Methods in Engineering*, 17(4):229–237, 2001.

D. Priour. Analysis of nets with hexagonal mesh using triangular elements. *International Journal for Numerical Methods in Engineering*, 56(12):1721–1733, 2003.

D. Priour. FEM modeling of flexible structures made of cables, bars and nets. In G. Soares and G. Fonseca, editors, *Maritime Transportation and Exploration of Ocean and Coastal Resources*, pages 1285–1292. Taylor & Francis Group, London, 2005.

Rasmussens Skibs Baadebygg. A trawl door. World patent number 8602525, 1986.

K.-J. Reite, V. Johansen, and A. J. Sørensen. Control structure for trawl systems. *The 7th Conference on Manoeuvring and Control of Marine Craft*, Accepted, not printed, 2006.

K.-J. Reite and A. J. Sørensen. Hydrodynamic properties important for control of trawl doors. In R. Katebi and S. Longhi, editors, *CAMS*, pages 143–148, Ancona, Italy, 2004. International Federation of Automatic Control.

K.-J. Reite and A. J. Sørensen. Mathematical modeling of the hydrodynamics forces on a trawl door. *IEEE Journal of Oceanic Engineering*, 31(2), 2006.

B. Ren, P. Zhu, and S. Wei. Numerical wind tunnel software system. *Journal of Northwestern Polytechnical University*, 18(1):44–47, Feb 2000.

R. Robinson. *Trawling: The Rise and Fall of the British Trawl Fishery.* University of Exeter press, Exeter, 1996.

J. A. Rossiter. *Model based predictive control : A practical approach.* CRC Press, Boca Raton, 2003.

T. Sarpkaya and M. Isaacson. *Mechanics of wave forces on offshore structures.* Van Nostrand Reinhold Company, New York, 1981.

Scanmar AS. Sea trials with controllable trawl door. Personal communication, 2000.

Scantrol AS. Method and device for operation of a trawl. US patent no. 6 138 397, 2000.

K. Schittkowski. NLQPL: A FORTRAN-subroutine solving constrained nonlinear programming problems. *Annals of Operations Research*, 5:485–500, 1985.

Schlumberger Ltd. Deflector devices. Canadian patent number 2433286, 2002.

Seismograph Service. Improved pelagic trawl door or paravane. Great Britain patent number 2122562, 1984.

H. Sendlak. Model research as a base of pelagic trawl development. *The International Symposium on Responsible Fisheries and Fishing Techniques*, 1999.

M. Shenker. The active trawl system. `http:// users. iafrica. com/ m/ ms/ mshenker/`, jan 2005. Last accessed 31.07.2006.

A. J. Sørensen. Structural issues in the design and operation of marine control systems. *Annual Reviews in Control*, 29:125–149, 2005.

D. Standal. Fishing the last frontier–controversies in the regulations of shrimp trawling in the high Arctic. *Marine Policy*, 27(5):375–388, 2003.

D. Standal. Nuts and bolts in fisheries management–a technological approach to sustainable fisheries? *Marine Policy*, 29(3):255–263, 2005.

P. A. M. Stewart and R. S. T. Ferro. Four experiments investigating codend drag. *Fisheries Research*, 5(4):349–358, 1987.

K. Suzuki, T. Takagi, T. Shimizu, T. Hiraishi, K. Yamamoto, and K. Nashimoto. Validity and visualization of a numerical model used to determine dynamic configurations of fishing nets. *Fisheries Science*, 69(4):695–705, 2003.

A. Takinaci. A practical surface panel method to predict velocity distribution around a three-dimensional hydrofoil including boundary layer effects. *Journal of Ocean Engineering*, 30:163–183, 2003.

The Mathworks Inc. *Optimization Toolbox Users Guide.* The Mathworks Inc, 2006.

F. Theret. A mathematical model for the determination of the shape and tension of a trawl placed in a uniform current. In *ICES Fish capture committee*, volume B:24. ICES, St. John's, ND, Canada, 1994.

R. Tønnessen. *A finite element method applied to unsteady viscous flow around 2D blunt bodies with sharp corners.* PhD thesis, Department of Marine Hydrodynamics, Faculty of Marine Technology, The Norwegian University of Science and Technology, 1999.

M. S. Triantafyllou. Dynamics of cables and chains. *The Shock and Vibration Digest*, 19 (12):3–5, 1987.

M. S. Triantafyllou. Dynamics of cables, towing cables and mooring systems. *The Shock and Vibration Digest*, 23:3–8, 1991.

H. Tronstad. *Nonlinear hydroelastic analysis and design of cable net structures like fishing gear based on the finite element method.* PhD thesis, Deparetment of Marine Structures, Faculty of Marine Technology, Norwegian University of Science and Technology, 2000.

I. Tsukrov, O. Eroshkin, D. Fredriksson, M. R. Swift, and B. Celikkol. Finite element modeling of net panels using a consistent net element. *Journal of Ocean Engineering*, 30(2):251–270, 2003.

UK Centre for Materials Education. Polymeric ropes for sport activities. `http://www. materials. ac. uk/ resources/ casestudies/ ropes.asp`, 2004. Last accessed 31.07.2006.

N. Umeda. An optimal regulator for a midwater trawl system. *Bulletin of National Research Institute of Fisheries Engineering (Japan)*, 12:31–41, 1991. Eng. transl.

S. Vannuccini. Overview of fish production, utilization, consumption and trade. Based on 2004 data. Technical report, FAO, Fishery Information, Data and Statistics Unit, November 2004.

B. Vincent. A new generation of tools for trawls. Dynamic numerical simulation. In M.Paschen et al., editor, *DEMAT'99*, pages 99–107, Rostock, Germany, 1999. Neuer Hochschulschriftenverlag Dr. Ingo Koch & Co. KG.

W. W. Warner. *Distant water: The fate of the North Atlantic fisherman.* Penguin Books Ltd., Middlesex, England, 1998.

L. Watling and E. A. Norse. Disturbance of the seabed by mobile fishing gear: A comparison to forest clearcutting. *Conservation Biology*, 12(6):1189–1197, 1998.

R. Watson, E. Hosino, J. Beblow, C. Revenga, Y. Kura, and A. Kitchingman. Fishing gear associated with global marine catches. Technical Report 12-6, The Fisheries Centre, University of British Columbia, 2004. ISSN 1198-6727.

F. M. White. *Fluid mechanics.* McGraw-Hill, New York, 1994.

M. Wigan. *The last of the hunter gatherers.* Swan Hill Press, 1998. ISBN 1-85310-771-9.

L. C. Woods. *The theory of subsonic plane flow.* Cambridge University Press, Bentley House, 200 Euston Road, London, N.W.1, 1961.

Appendix A

Numerical optimization and model predictive control

A.1 Numerical optimization

Numerical optimization provides a variety of methods for finding the arguments that return the optimum of a mathematical function, the optimum defined as either the maximum or the minimum. To solve a specific problem using numerical optimization, the problem must therefore first be expressed in terms of such a function. The function must contain the relation between the arguments and the objective, as well as the necessary constraints on its input. The degree of fulfilment of the objective must be returned as a single number, so that maximizing/minimizing the function optimizes the objective.

There is no universal optimization algorithm, and the choice of algorithm is crucial for its success. The wrong choice may lead to inferior performance, and in some cases the solution will not be found at all. The optimization algorithm should be chosen according to the objective function at hand, such as

- How many arguments does it take? Are the arguments discrete, continuous or a mix?
- Are there constraints on its arguments? How are these formulated?
- Is it linear or nonlinear? How nonlinear? Does it have local optima?
- Is it smooth or nonsmooth, continuous or discontinuous?
- Is it stochastic or deterministic?
- What is the computational effort associated with its evaluation?
- Can its gradient be calculated directly?

Some optimization routines particular relevant to this thesis are presented in the following. For further reading on numerical optimization, see Nocedal and Wright (1999).

A.1.1 The nonlinear simplex method

The nonlinear simplex method is resistant to noise in the objective function, and it requires the user to supply only function values, not derivatives. It may therefore be appropriate when the gradient of the objective function can not be calculated directly, or when the function value contains noise.

For a n-dimensional problem, this method maintains a simplex of $n + 1$ points (a triangle in two dimensions, a pyramid in three dimensions etc.). The simplex moves, expands, contracts, and distorts its shape as it attempts to find a minimizer. This method is slow and can be applied only to problems in which n is small. The software packages IMSL, Matlab, NAG(Fortran), NAG(C), PORT 3 and PROC NLP all contain implementations of this method. The method is described in Nelder and Mead (1965), and its convergence properties are studied in Lagarias et al. (1998).

A.1.2 Sequential quadratic programming

Sequential quadratic programming (SQP) methods represent the state of the art in nonlinear programming methods, and a number of packages, including NPSOL, NLPQL, OPSYC, OPTIMA, Matlab, and SQP, are founded on this approach. As an example, Schittkowski (1985) has implemented and tested a version that outperforms every other tested method in terms of efficiency, accuracy and percentage of successful solutions, and over a large number of test problems (Mathworks 2006).

The SQP algorithm is a generalization of Newton's method for unconstrained optimization in that it finds a step away from the current point by minimizing a quadratic model of the problem. In its purest form, the SQP algorithm replaces the objective function with the quadratic approximation and replaces the constraint functions by linear approximations. At each major iteration, an approximation is made of the Hessian of the Lagrangian function, using a quasi-Newton updating method. This is then used to generate a quadratic programming subproblem, whose solution is used to form a search direction for a line search procedure.

To summarize, the three main stages of the SQP implementation are:

- Updating the Hessian matrix of the Lagrangian function.
- Finding the solution of the quadratic programming problem.
- Using line search and merit function calculations to find a new starting point.

A.1.3 Genetic algorithms

In nature, the genes contain the information that define how plants and creatures are constructed. These genes are passed over from one generation to the next through reproduction. For heterogeneous reproduction, the genes from the male and female parent are mixed to form the genes of the child. This mixture determines the future success of the child. In addition, effects such as mutation and dominant/recessive genes play an important role for the success of the population as a whole. Success does in this case mean fitness to survive in the given environment. Normally, only the children who are best adapted to their environment (who are "the fittest") will survive long enough

to be able to reproduce themselves. So the genes leading to a successful creature have the largest possibility for getting passed on to future generations.

Genetic algorithms mimic nature's way of finding the best fit creature to a (changing) environment. Genetic algorithms start with a small group of potential answers, called a population. Each member of the population is called a chromosome, representing one particular group of settings. Each setting in a chromosome is called a gene. The optimization begins by testing each chromosome in the population, assigning it a value indicating how "fit" it is. This is done by the objective function. After the entire population is tested, a new population, called a new generation, is created. In short, parents are chosen among the best fitted chromosomes. These are allowed to breed, such that the chromosomes of the children will be a mix of the parents. In addition, some mutation is allowed. The best fitted parents may also be kept for the next generation. When the optimization is finished, the chromosome with the best fitness is returned as the solution.

Genetic algorithms are not following a search path determined by the object function gradients, but they will jump all over as they search for the optimum solution. This makes them usable for global optimization. They are however not as efficient as optimization routines based on objective function gradients when the objective function is convex.

The genetic algorithm used in this thesis is described in Houck et al. (1995).

A.2 Model predictive control

In contrast to most other advanced control methods, model predictive control (MPC) was developed by the industry to suit its needs. It's use began in the late 1970s in the refining and petrochemical industries, and it is now an industry proven solution to deal with large multivariable constrained control problems.

The main idea of MPC is to choose the control action by repeatedly optimizing the plant behaviour. A mathematical model of the process is used to predict future process behaviour based on future control actions. Using numerical optimization, the controller is able to calculate an optimum set of control actions, which minimise the error between actual and desired process behaviour, subject to actuator and process constraints.

In the optimization, two different receding time spans, or horizons, are used. The *control horizon* is the time span for which the control inputs are optimized, and the *prediction horizon* is the time span for which the states of the dynamic model are evaluated by the objective function. The notion of receding control and prediction horizons is illustrated in Figure A.1. The numerical optimization routine is then employed to find the optimal control trajectory, from the current time step to the end of the control horizon. To reduce the computational effort of the numerical optimization, it is common to require the control input to be constant in certain intervals. As this directly reduces the number of unknowns, the impact on optimization speed can be significant.

The first value of the optimal time history of the control input is applied to the real system. For the next time step, the whole optimization process is repeated. This means that for each time step the optimum time history of the control input is calculated, but only the values for the first time step are actually used. This approach can be summarized in the following steps:

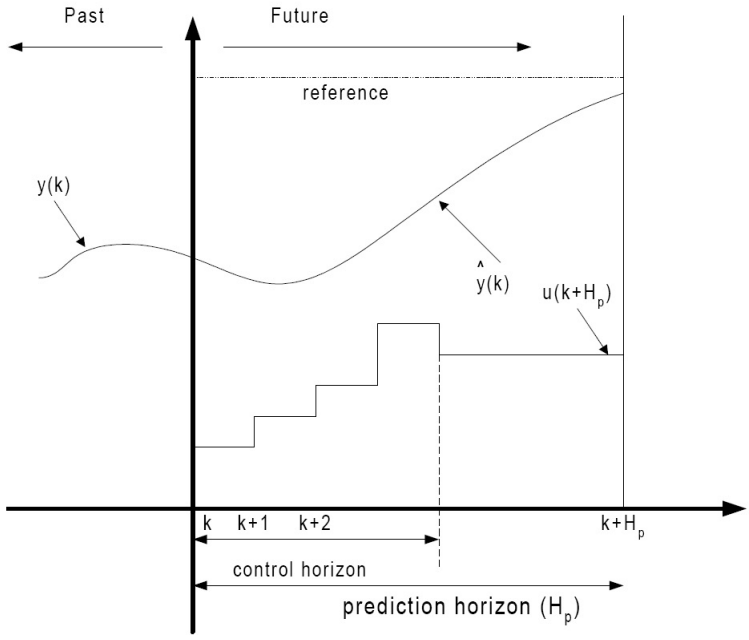

Figure A.1: The concept of receding control and prediction horizon.

- At time k and for the current state $\mathbf{x}(k)$, an open-loop optimal control problem is solved on-line, over some future interval taking account of the current and future constraints.
- The first step in the optimal control sequence is applied to the real system.
- The procedure is repeated at time $k+1$, using the current state $\mathbf{x}(k+1)$.

MPC has many advantages that sets it apart from other control methods. In particular, numerical optimization allows for the use of nonlinear objective functions. This makes it easy to implement constraints and restrictions, multivariable problems, nonlinear models and complex objectives. The main disadvantages of MPC are also closely related to the numerical optimization. The computational demands of the numerical optimization may prohibit using MPC for a given problem, especially if the system to be controlled includes fast dynamics and/or a complex process model. In addition, convergence may not be guaranteed, and it may be necessary to take precautions in such cases.

Predictive control has been successful in the process industries, where the dynamics of the systems are typically slow, and the multivariable nature of the problems dominates. For further reading, see for example Rossiter (2003) or Maciejowski (2002).

Appendix B

Specifications for the base case trawl system

The details of the base case trawl system are given in Tables B.1 to B.4. These tables define the basis for most simulation studies, but do not claim to define a "standard" trawl system. It is based on a normal pelagic trawl system, but the warp lengths and the bridle lengths are decreased from approximately 1500m and 300m, respectively. The net size is slightly decreased and the trawl door size slightly increased, to facilitate improved trawl door control.

Length	75 m
Breadth	14 m
Displacement	3000 m^3
Bollard pull	760 kN

Table B.1: Main particulars of the ship.

Max winch torque	400 kNm
Max winch speed	1 rad/s
Max hauling power	150 kW
Average winch drum diameter	1.0 m

Table B.2: Important properties of the trawl winches.

Warp diameter	30 mm
Warp material	steel
Upper bridle length	100 m
Upper bridle diameter	20 mm
Upper bridle material	steel
Lower bridle length	100 m
Lower bridle diameter	20 mm
Lower bridle material	steel
Net size (stretched circumference of opening)	1600 m
Weights at each lower wing	2000 kg
Trawl door size	15 m^2

Table B.3: Important properties of the trawl doors , the trawl net and the associated lines.

Average warp length	500 m
Average warp tension	150 kN
Average speed	2.0 m/s
Average trawl net drag	200 kN

Table B.4: Operational data of the trawl system.

Appendix C

Parameterization of the trawl door forces

This appendix contains some specifics of the parameterization of the steady state hydrodynamic forces acting on a trawl door. The optimum coefficient matrix is found to be

$$\mathbf{K}_{m\Upsilon}^{opt} = \tag{C.1}$$

$$\begin{bmatrix} -95.01 & -0.2471 & -0.25 & 0.0411 & 0.004599 & 6.3 \\ 0.118 & -0.8926 & 0.4809 & -3.563 & 0.03989 & -10.06 \\ 6.01 & -3.328 & 2.128 & -13.79 & 0.02766 & 2.651 \\ -2.417 & 0.1449 & -0.05048 & 3.572 & -0.03257 & 1.193 \\ 95.13 & -1.508 & 3.203 & -0.1114 & -0.003684 & -0.00126 \\ -0.1009 & 7.122 & 6.55 & 2.573 & 1.315 & -0.1432 \\ 1.632 & -2.16 & -0.3066 & -0.0567 & -9.066 & -0.3649 \end{bmatrix}^T .$$

The objective weight function of (3.69) is shown in Figure C.1. The found parameter functions are:

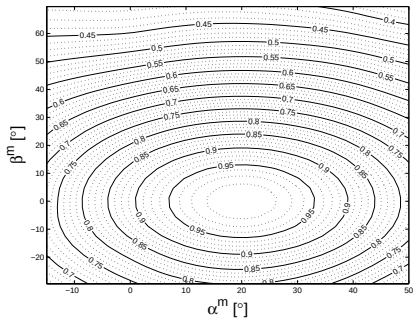

Figure C.1: Objective weight function for $k = 1$.

$$\bar{\mathbf{C}}^{\infty}_{m\Upsilon}\left(\alpha^m, \beta^m\right) = \hat{\mathbf{C}}^{\infty}_{m\Upsilon}\left(\alpha^m, \beta^m, \mathbf{K}^{opt}_{m\Upsilon}\right) = \tag{C.2}$$

$$\begin{bmatrix}
K^{opt}_{m\Upsilon,11} + K^{opt}_{m\Upsilon,12} s\left(K^{opt}_{m\Upsilon,13}\alpha^m + K^{opt}_{m\Upsilon,14}\right) c\left(\beta^m\right) \\
+K^{opt}_{m\Upsilon,15} s\left(K^{opt}_{m\Upsilon,16}\alpha^m + K^{opt}_{m\Upsilon,17}\right) \\
\\
K^{opt}_{m\Upsilon,21} + K^{opt}_{m\Upsilon,22} s\left(K^{opt}_{m\Upsilon,23}\alpha^m + K^{opt}_{m\Upsilon,24}\right) c\left(K^{opt}_{m\Upsilon,25}\left(\beta^m\right)^2\right) \\
+K^{opt}_{m\Upsilon,26} exp\left(\alpha^m + K^{opt}_{m\Upsilon,27}\right) \\
\\
K^{opt}_{m\Upsilon,31} s\left(\beta^m\right) s\left(K^{opt}_{m\Upsilon,32}\alpha^m + K^{opt}_{m\Upsilon,33}\right) \\
+K^{opt}_{m\Upsilon,34} s\left(K^{opt}_{m\Upsilon,35}\beta^m\right) s\left(K^{opt}_{m\Upsilon,36}\alpha^m + K^{opt}_{m\Upsilon,37}\right) \\
\\
K^{opt}_{m\Upsilon,41} s\left(K^{opt}_{m\Upsilon,42}\beta^m\right) s\left(K^{opt}_{m\Upsilon,43}\left(\alpha^m\right)^2 + K^{opt}_{m\Upsilon,44}\right) \\
+K^{opt}_{m\Upsilon,45} s\left(K^{opt}_{m\Upsilon,46}\alpha^m\beta^m + K^{opt}_{m\Upsilon,47}\right) \\
\\
K^{opt}_{m\Upsilon,51} + K^{opt}_{m\Upsilon,52}\left(\alpha^m\right)^2\beta^m + K^{opt}_{m\Upsilon,53}\left(\alpha^m\right)^2\left(\beta^m\right)^2 \\
+K^{opt}_{m\Upsilon,54}\left(\alpha^m\right)^2\left(\beta^m\right)^3 + K^{opt}_{m\Upsilon,55} c\left(K^{opt}_{m\Upsilon,56}\left(\beta^m\right)^2 + K^{opt}_{m\Upsilon,57}\left(\alpha^m\right)^2\right) \\
\\
\left(\begin{array}{c}
K^{opt}_{m\Upsilon,61}\left(\alpha^m\right)^5 + K^{opt}_{m\Upsilon,62}\left(\alpha^m\right)^4 + K^{opt}_{m\Upsilon,63}\left(\alpha^m\right)^3 \\
+K^{opt}_{m\Upsilon,64}\left(\alpha^m\right)^2 + K^{opt}_{m\Upsilon,65}\alpha^m + K^{opt}_{m\Upsilon,66}
\end{array}\right) \\
\cdot c\left(\beta^m\right) c\left(\alpha^m + \beta^m + K^{opt}_{m\Upsilon,67}\right)
\end{bmatrix},$$

where $c(\cdot) = \cos(\cdot)$, $s(\cdot) = \sin(\cdot)$, and $K^{opt}_{m\Upsilon,ij}$ is the element in row i and column j of $\mathbf{K}^{opt}_{m\Upsilon}$.The RMS values of the difference between the calculated and measured values

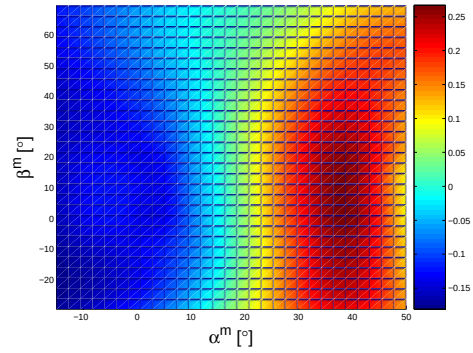

Figure C.2: Measured coefficient of hydrodynamic force along trawl door x^m-axis.

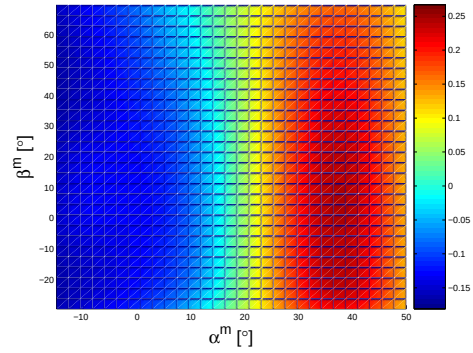

Figure C.3: Calculated coefficient of hydrodynamic force along trawl door x^m-axis.

of the hydrodynamic coefficients in all degrees of freedom for all the combinations of measured orientation angles are

$$\boldsymbol{\sigma}_{\bar{\mathbf{C}}^{\infty}_{m\Upsilon}} = \begin{bmatrix} 3.51 & 76.8 & 1.98 & 6.66 & 0.069 & 1.73 \end{bmatrix}^T \times 10^{-4}. \tag{C.3}$$

The deviation for measurement n in dof i is found as

$$p_{in} = \frac{\bar{C}^{\infty}_{m\Upsilon,in}\left(\alpha^m, \beta^m\right) - C^{\infty}_{m\Upsilon,in}}{\max\left(C^{\infty}_{m\Upsilon,i}\right) - \min\left(C^{\infty}_{m\Upsilon,i}\right)} \ . \tag{C.4}$$

Figures C.2 to C.19 show the results from the measurements and the parameterizations, as well as the deviation between these.

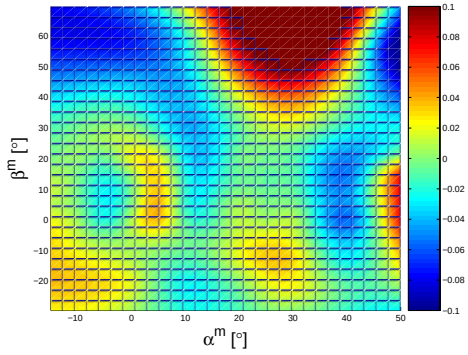

Figure C.4: Error in calculated coefficient of hydrodynamic force along trawl door x^m-axis.

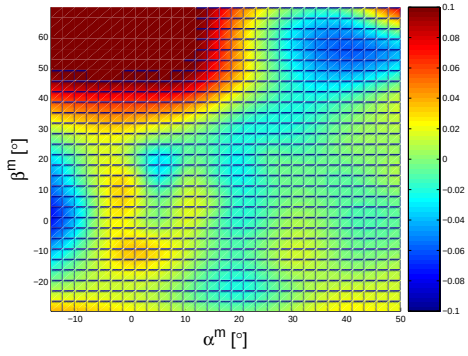

Figure C.5: Measured coefficient of hydrodynamic force along trawl door y^m-axis.

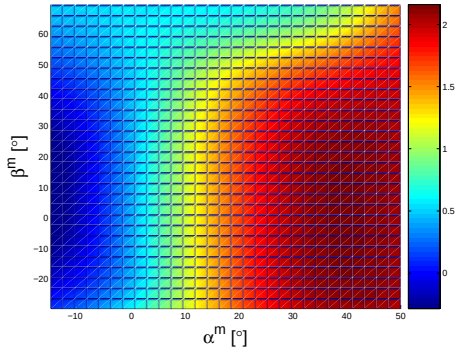

Figure C.6: Calculated coefficient of hydrodynamic force along trawl door y^m-axis.

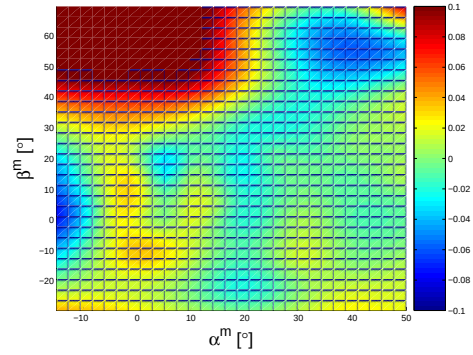

Figure C.7: Error in calculated coefficient of hydrodynamic force along trawl door y^m-axis.

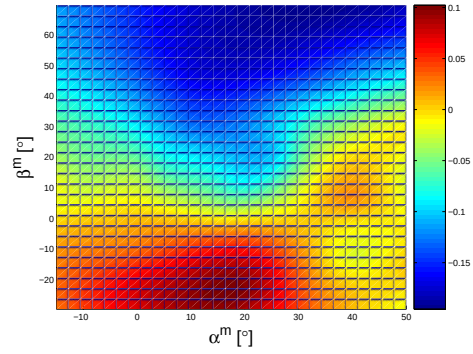

Figure C.8: Measured coefficient of hydrodynamic force along trawl door z^m-axis.

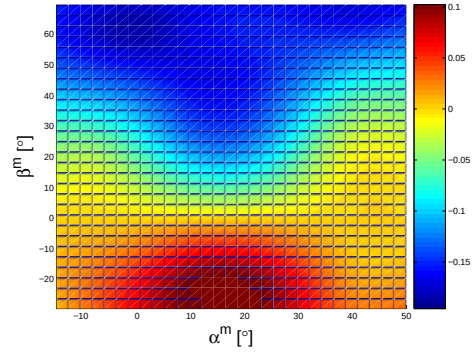

Figure C.9: Calculated coefficient of hydrodynamic force along trawl door z^m-axis.

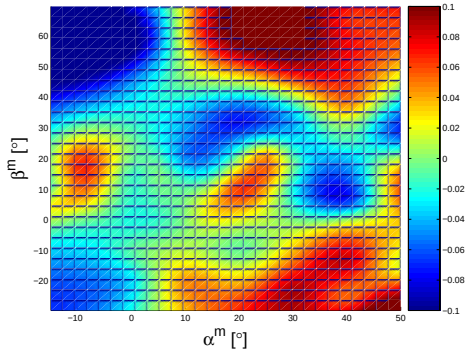

Figure C.10: Error in calculated coefficient of hydrodynamic force along trawl door z^m-axis.

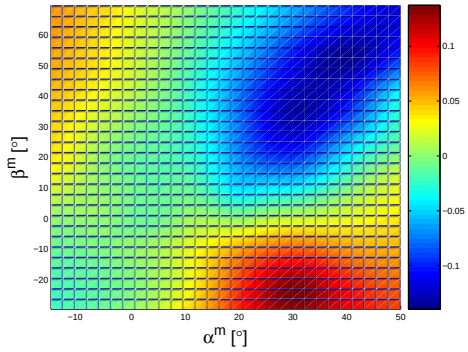

Figure C.11: Measured coefficient of moment about trawl door x^m-axis.

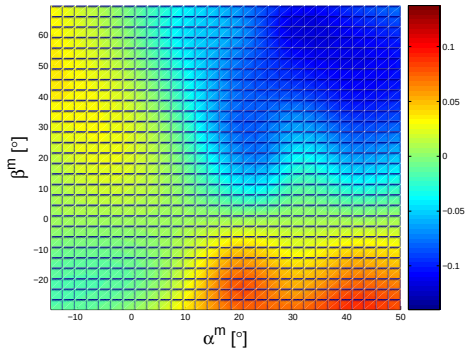

Figure C.12: Calculated coefficient of moment about trawl door x^m-axis.

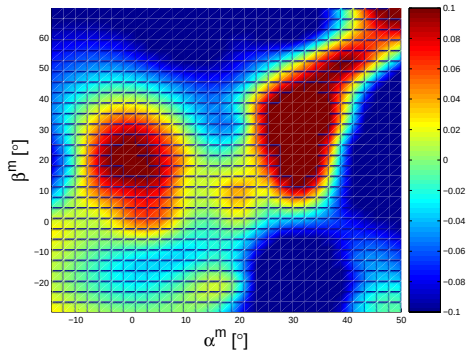

Figure C.13: Error in calculated coefficient of moment about trawl door x^m-axis.

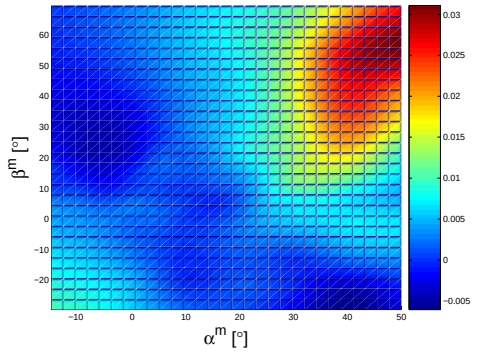

Figure C.14: Measured coefficient of moment about trawl door y^m-axis.

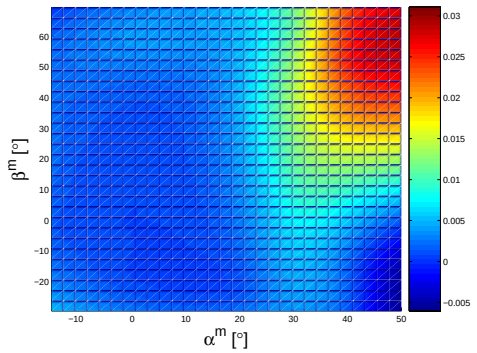

Figure C.15: Calculated coefficient of moment about trawl door y^m-axis.

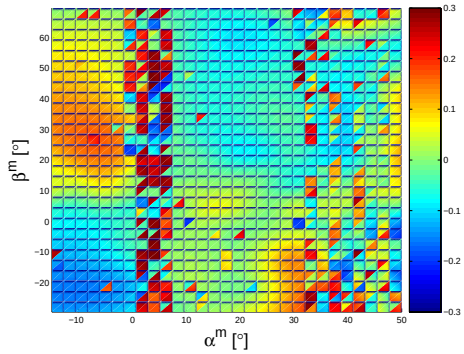

Figure C.16: Error in calculated coefficient of moment about trawl door y^m-axis.

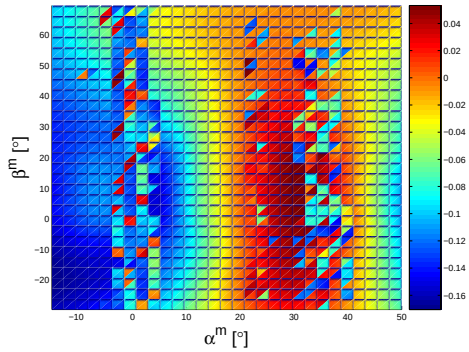

Figure C.17: Measured coefficient of moment about trawl door z^m-axis.

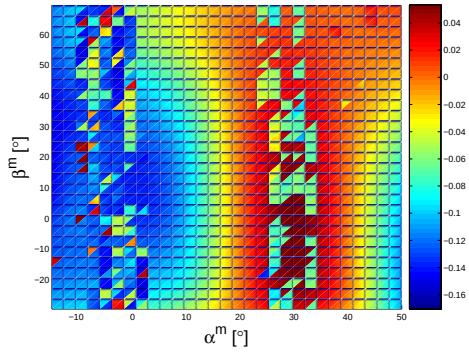

Figure C.18: Calculated coefficient of moment about trawl door z^m-axis.

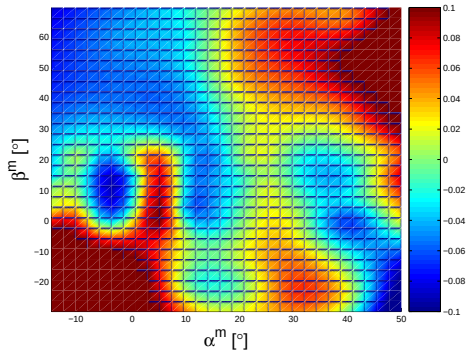

Figure C.19: Error in calculated coefficient of moment about trawl door z^m-axis.

Appendix D

The VLM software

D.1 Notation

The foil frame used in the VLM software is similar to the trawl door and the trawl door model frame, and it is denoted by the index f. The following notation is used in the following:

c_f The chord length of the foil.

h_f The span (height) of the foil.

N_i The number of elements along the span of the foil.

N_j The number of elements along the chord of the foil.

K_c A coefficient describing the curvature of the foil.

D.2 Preparation for simulation

Before simulation can start, some properties are defined:

The trajectory definition (6 DOF) is defined as:

$$\boldsymbol{\eta}^f_{fn}(t) = \begin{bmatrix} \mathbf{p}^n_{fn}(t) \\ \boldsymbol{\Theta}_{fn}(t) \end{bmatrix}. \tag{D.1}$$

The positions of the nodes on the foil grid are defined as:

$$\mathbf{p}^f_{g_f f,ij} = \begin{bmatrix} c_f \frac{N_j - 2j + 1}{2N_j - 2} \\ K_c \cos\left(\frac{N_j - 2j + 1}{2N_j - 2}\pi\right) \\ -h_f \frac{N_i - 2i + 1}{2N_i - 2} \end{bmatrix}, \tag{D.2}$$

where i and j are indices counting the panel from the top of the trawl door ($z^f = -h^f$) and the leading edge of the trawl door, respectively.

The positions of the collocation points are defined as:

$$\mathbf{p}^f_{cf,ij} = \begin{bmatrix} \frac{c_f(2N_j-4j-1)}{4(N_j-1)} \\ K_c \cos\frac{\pi(2N_j-4j-1)}{4(N_j-1)} \\ -\frac{h_f(N_i-2i)}{2(N_i-1)} \end{bmatrix}, \quad \begin{matrix} 1 < i < N_i - 1 \\ 1 < j < N_j - 1 \end{matrix}. \tag{D.3}$$

The positions of the corner points of the ring vortices on the foil are defined as:

$$\mathbf{p}^f_{vf}(i,j,1) = \begin{bmatrix} \frac{c_f(2N_j-4j+1)}{4(N_j-1)} \\ K_c \cos\frac{\pi(2N_j-4j+1)}{4(N_j-1)} \\ -h_f\frac{N_i-2i+1}{2N_i-2} \end{bmatrix}, \quad \begin{matrix} 1 < i < N_i - 1 \\ 1 < j < N_j - 1 \end{matrix}, \tag{D.4}$$

$$\mathbf{p}^f_{vf}(i,j,2) = \begin{bmatrix} \frac{c_f(2N_j-4j+1)}{4(N_j-1)} \\ K_c \cos\frac{\pi(2N_j-4j+1)}{4(N_j-1)} \\ -h_f\frac{N_i-2i-1}{2N_i-2} \end{bmatrix}, \quad \begin{matrix} 1 < i < N_i - 1 \\ 1 < j < N_j - 1 \end{matrix}, \tag{D.5}$$

$$\mathbf{p}^f_{vf}(i,j,3) = \begin{cases} \begin{bmatrix} \frac{c_f(2N_j-4j-3)}{4(N_j-1)} \\ K_c \cos\frac{\pi(2N_j-4j-3)}{4(N_j-1)} \\ -h_f\frac{N_i-2i-1}{2N_i-2} \end{bmatrix}, & \begin{matrix} 1 < i < N_i - 1 \\ 1 < j < N_j - 2 \end{matrix} \\ \begin{bmatrix} -\frac{c_f}{2} - k\,\Delta t\,U_f \\ K_c \cos\frac{\pi(2N_j-4j-3)}{4(N_j-1)} \\ -h_f\frac{N_i-2i-1}{2N_i-2} \end{bmatrix}, & \begin{matrix} 1 < i < N_i - 1 \\ j = N_j - 1 \end{matrix} \end{cases}, \tag{D.6}$$

$$\mathbf{p}^f_{vf}(i,j,4) = \begin{cases} \begin{bmatrix} \frac{c(2N_j-4j-3)}{4(N_j-1)} \\ K_c \cos\frac{\pi(2N_j-4j-3)}{4(N_j-1)} \\ -s\frac{N_i-2i+1}{2N_i-2} \end{bmatrix}, & \begin{matrix} 1 < i < N_i - 1 \\ 1 < j < N_j - 2 \end{matrix} \\ \begin{bmatrix} -\frac{c_f}{2} - k\,\Delta t\,U_f \\ K_c \cos\frac{\pi(2N_j-4j-3)}{4(N_j-1)} \\ -h_f\frac{N_i-2i+1}{2N_i-2} \end{bmatrix}, & \begin{matrix} 1 < i < N_i - 1 \\ j = N_j - 1 \end{matrix} \end{cases}, \tag{D.7}$$

where k is typically chosen between 0.2 and 0.3, according to Katz and Plotkin (1991). $k = 0.3$ is used in the present software. U_f is forward speed of the foil and Δt is the time increment for each iteration.

The foil is assumed to have no curvature along the span, and the surface is modeled as

$$\eta\left(x^f\right) = K_c \cos\left(\frac{\pi x^f}{c_f}\right), \tag{D.8}$$

where η is the y^f-coordinate of the surface. Using this, the normal to the foil surface is in each collocation point found as

$$\mathbf{n}_j = \frac{\begin{bmatrix} K_c \sin\frac{\pi(2N_j-4j-1)}{4(N_j-1)} & 1 & 0 \end{bmatrix}^T}{\sqrt{\left(K_c \sin\frac{\pi(2N_j-4j-1)}{4(N_j-1)}\right)^2 + 1}}. \tag{D.9}$$

The matrix of influence coefficients from vortices on the foil ($\mathbf{C}_I$) is of size $N_\Gamma \times N_\Gamma$, where $N_\Gamma = N_i N_j$, and it is defined as

$$\mathbf{C}_I = \left[\frac{\partial v_k}{\partial \Gamma_l} \right], \tag{D.10}$$

where k and l is the row and column index, respectively. The elements of this matrix gives the induced velocities normal to the foil surface in collocation point k from ring vortex l. These velocities are calculated according to the law of Biot Savart. The indices k and l are related to the indices i and j by $k = i_c + (N_i - 1)\, j_c$ and $l = i_\Gamma + (N_i - 1)\, j_\Gamma$. The influence matrices for induced normal velocities from the free vortices on the foil and the first trailing vortex are calculated in a similar way. These matrices are inverted for later use.

D.3 Calculations in each time step

The global position and orientation of the foil is prescribed by

$$\left[\begin{array}{c} \mathbf{p}^n_{fn}(t) \\ \mathbf{\Theta}_{fn}(t) \end{array} \right] = \boldsymbol{\eta}^f_{fn}(t). \tag{D.11}$$

The rotation matrix between the global frame and the foil frame is calculated as

$$\mathbf{R}^n_f = \mathbf{R}\left(\mathbf{\Theta}_{fn}(t)\right)^T = \left[\begin{array}{ccc} c_\theta c_\psi & c_\varphi s_\psi + c_\psi s_\theta s_\varphi & s_\psi s_\varphi - c_\psi c_\varphi s_\theta \\ -c_\theta s_\psi & c_\psi c_\varphi - s_\theta s_\psi s_\varphi & c_\psi s_\varphi + c_\varphi s_\theta s_\psi \\ s_\theta & -c_\theta s_\varphi & c_\theta c_\varphi \end{array} \right], \tag{D.12}$$

where c_x and s_x is $\cos(x(t))$ and $\sin(x(t))$, respectively. The global positions of the collocation points are found as

$$\mathbf{p}^n_{cn,ij}(t) = \mathbf{p}^n_{fn}(t) + \mathbf{R}^n_f \mathbf{p}^f_{cf,ij}. \tag{D.13}$$

The velocity of each collocation point is found in the foil frame as

$$\mathbf{v}^f_{cf,ij}(t) = \mathbf{R}\left(\mathbf{\Theta}_{fn}\left(t - \tfrac{1}{2}\Delta t\right)\right) \frac{\mathbf{p}^n_{cn,ij}(t) - \mathbf{p}^n_{cn,ij}(t - \Delta t)}{\Delta t}.$$

The positions of the new wake grid points behind the trailing edge is found as

$$\mathbf{p}^n_{g_w n}(i,1,t) = (1-k)\left(\mathbf{p}^n_{fn}(t) + \mathbf{R}\left(\mathbf{\Theta}_{nf}(t)\right)\mathbf{p}^f_{g_f f}(i, N_j)\right) \tag{D.14}$$

$$+k\left(\mathbf{p}^n_{fn}(t - \Delta t) + \mathbf{R}\left(\mathbf{\Theta}_{nf}(t - \Delta t)\right)\mathbf{p}^f_{g_f f}(i, N_j)\right). \tag{D.15}$$

The strength of all new ring vortices in the wake is set equal to the strength of the corresponding vortices on the trailing edge in the previous time step. The induced velocities in each collocation point from all the vortices, except the bound vortices, are calculated according to the law of Biot Savart.

The strength of the bound vortices, $\mathbf{\Gamma}$, is found by demanding no flow through the collocation points. The velocity through each collocation point induced by the bound

vortices must thus eliminate the sum of the free stream velocity and the velocity induced by all other vortices normal to the foil. The strength of the bound vortices are found as:

$$\mathbf{\Gamma} = \mathbf{C_I^{-1}} \mathbf{V}_B \ , \tag{D.16}$$

where $\mathbf{\Gamma}$ is a vector of the strength of every ring vortex and $\mathbf{V}_B$ is a vector of the velocity the ring vortices must induce normal to the foil surface, in each collocation point.

D.4 Force and moment calculations

The hydrodynamic forces are found as the sum of the forces from the fluid accelerations and the circulation about the foil.

D.4.1 The forces from fluid accelerations

The forces from the fluid accelerations are found from Bernoulli's equation. The pressure difference between the suction and the pressure side of the foil from these accelerations is found as

$$\Delta p^a = \ \rho_w \frac{\partial \left(\Phi^+ - \Phi^-\right)}{\partial t}, \tag{D.17}$$

where the velocity potential on the upper (Φ^+) and lower (Φ^-) side can be found by integrating the local vorticity from the leading edge to the local longitudinal position

$$\Phi^{\pm} = \pm \int_{-\frac{1}{2}c_f}^{x^f} \frac{\gamma}{2} dl, \tag{D.18}$$

where γ is the local vorticity (Katz and Plotkin, 1991). In the discretized model this is calculated as

$$\Delta\Phi_{ij} \ = \ \Phi_{ij}^+ - \Phi_{ij}^- = \Gamma_{ij} \tag{D.19}$$

$$\frac{\partial \left(\Phi_{ij}^+ - \Phi_{ij}^-\right)}{\partial t} \ = \ \frac{\partial \Gamma_{ij}}{\partial t} \ , \tag{D.20}$$

where Γ_{ij} is the strength of the vortex ring about the collocation point in panel (i, j). The net force from this pressure difference is found from

$$\Delta \mathbf{F}^a \left(i,j\right) = -\rho \frac{\partial \Gamma_{ij}}{\partial t} \Delta S_{ij} \mathbf{n}_i, \tag{D.21}$$

where ΔS_{ij} is the area of the panel and $\mathbf{n}_i$ is the normal vector of the panel.

D.4.2 The forces from circulation about the foil

The forces from circulation are found by applying the law of Kutta-Joukowski to each member of each vortex ring. These forces are found as

$$\mathbf{F}^c \left(i,j,n\right) = \rho l \left(i,j,n\right) \mathbf{U} \left(i,j\right) \times \mathbf{\Gamma} \left(i,j,n\right), \tag{D.22}$$

where $\mathbf{F}^c(i,j,n)$ is the forces from circulation on member number n of panel i, j, $\mathbf{U}(i,j)$ is the velocity of the collocation point of this panel, relative to the ambient water, $l(i,j,n)$ is the length of the member number n of this panel, and $\mathbf{\Gamma}(i,j,n)$ is the strength and direction of the vorticity of this member.

D.5 Verification of the software

Figure D.1 shows the time dependency of the hydrodynamic lift and drag for a flat plate of very large aspect ratio, at 5 ° angle of attack. The asterices marks the analytic, linearized solution of the lift on a 2D foil, while the solid line marks the lift as calcultated by the VLM software. The dotted line marks the development of the drag force, as calculated by the VLM software. A large discrepancy is seen in the start of the motion, but the solutions are seen to rapidly converge with time.

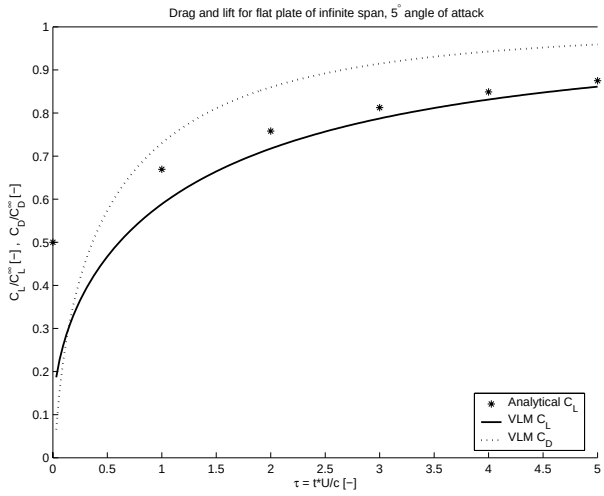

Figure D.1: Comparison between VLM software and analytical solution of the hydrodynamic forces on a flat plate of infinite aspect ratio.

Figures D.2 and D.3 compares the computed lift and drag coefficients for flat plates of various aspect ratios, at 5 ° angles of attack. It is clearly seen how the 3D effects reduces both lift and drag. If the longitudinal center of pressure was plotted, it would be apparent how it shifted towards the leading edge for decreasing aspect ratios, as predicted by theory.

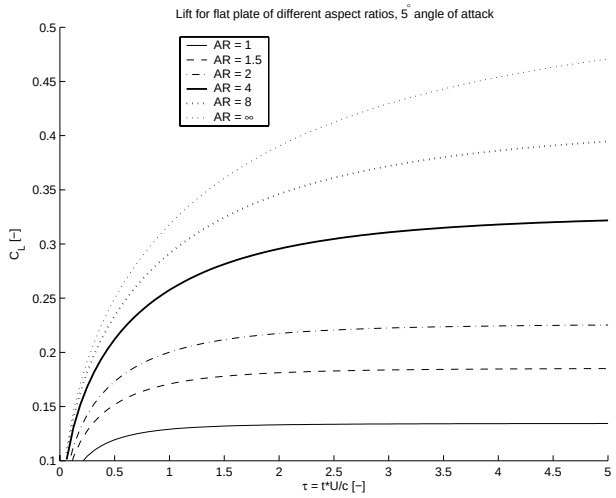

Figure D.2: The calculated hydrodynamic lift on flat plates of various aspect ratios at 5° angle of attack.

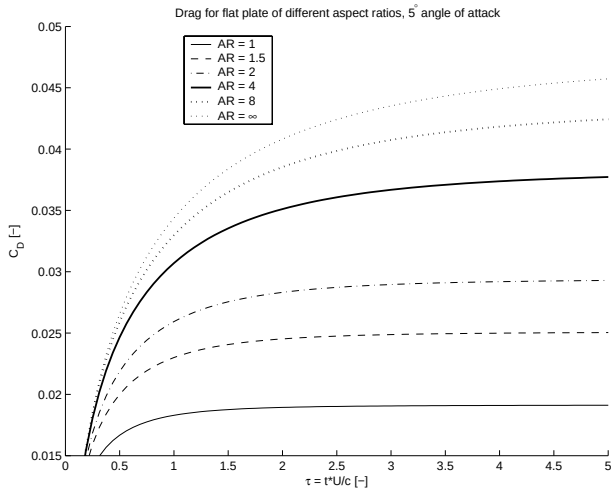

Figure D.3: The calculated hydrodynamic drag on flat plates of various aspect ratios at 5° angle of attack.

D.6 Simulation results

Figures D.4 to D.12 show the effect of some simple movements of a foil approximating the trawl door used for the wind tunnel experiments. The endplates are not modeled, but the aspect ratio is increased from 1.45 to 1.54 to include their influence. The three

separate foils are not modeled, and the surface of the foil is approximated as $\eta\left(x^f\right) = K_c \cos\left(\frac{\pi x^f}{c_f}\right)$, where $K_c = 0.1\,\mathrm{m}$ and $c_f = 0.65\,\mathrm{m}$.

Figures D.4 to D.6 show how the hydrodynamic lift, drag and moment about z^f-axis develop with time when the trawl door is given a sudden forward speed from a state of rest. The various curves are for different angles of attack. The values are given in relation to the steady state values. It is seen that for reasonable angles of attack the development with time is quite similar.

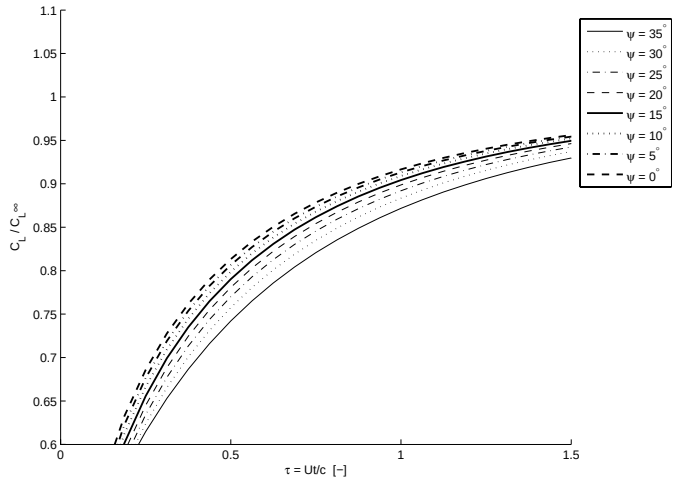

Figure D.4: The calculated hydrodynamic lift on a trawl door given a sudden forward speed from initial rest.

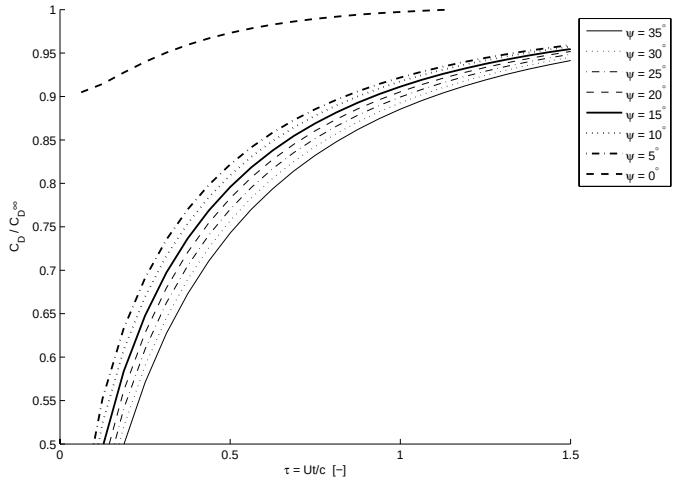

Figure D.5: The calculated hydrodynamic drag on a trawl door given a sudden forward speed from initial rest.

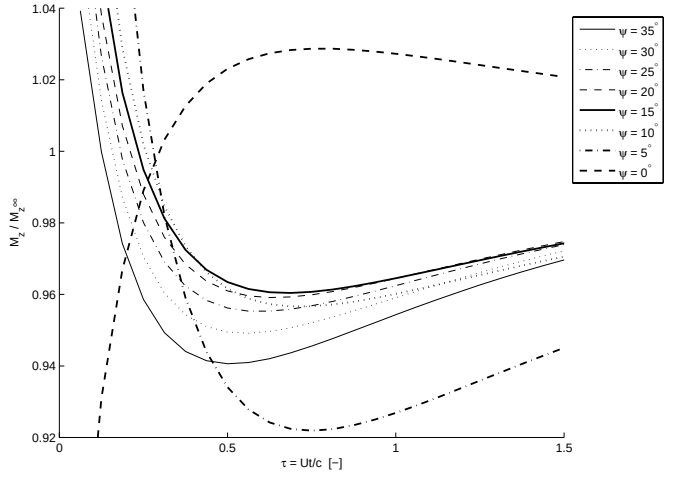

Figure D.6: The calculated hydrodynamic moment about local z^f-axis on a trawl door given a sudden forward speed from initial rest.

Figures D.7 to D.12 show the calculated forces and moments for various trajectories. These simulations form the basis of the model developed in Section 3.3.4. It is worth noting that the change in angle of attack is the same in Figures D.7 and D.8 as in Figures D.9 and D.10. The development in forces are still quite different. This indicates that an accurate model would have to calculate the hydrodynamic forces not only from the angles of attack and slip, but also from the actual relative velocity components. To keep

the model simple, it is, however, in this work chosen to base the model on only the angles of attack and slip.

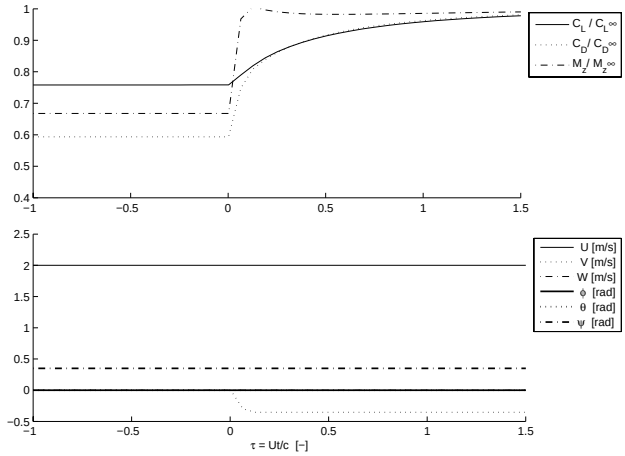

Figure D.7: The calculated hydrodynamic forces on a trawl door at steady state, given a sudden negative heave motion.

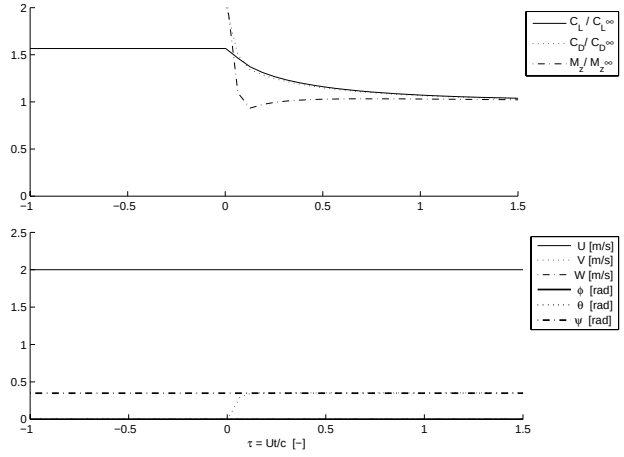

Figure D.8: The calculated hydrodynamic forces on a trawl door at steady state, given a sudden positive heave motion.

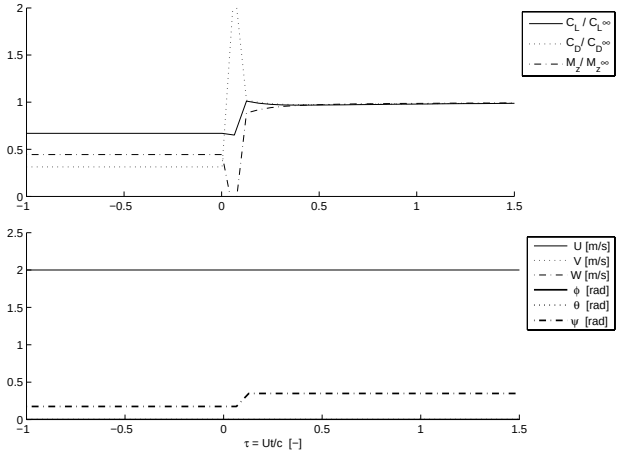

Figure D.9: The calculated hydrodynamic forces on a trawl door at steady state, given a sudden increase in angle of attack.

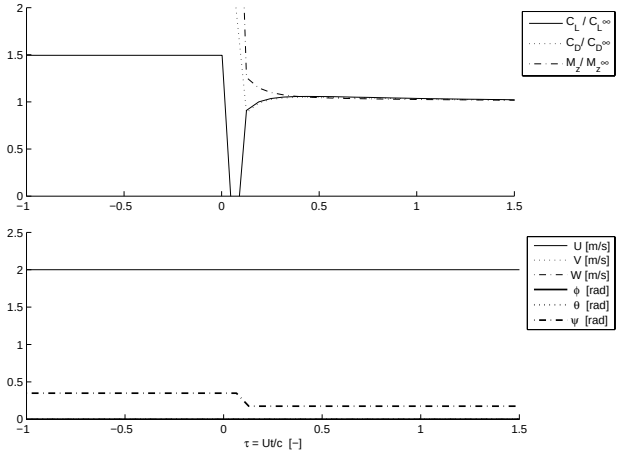

Figure D.10: The calculated hydrodynamic forces on a trawl door at steady state, given a sudden decrease in angle of attack.

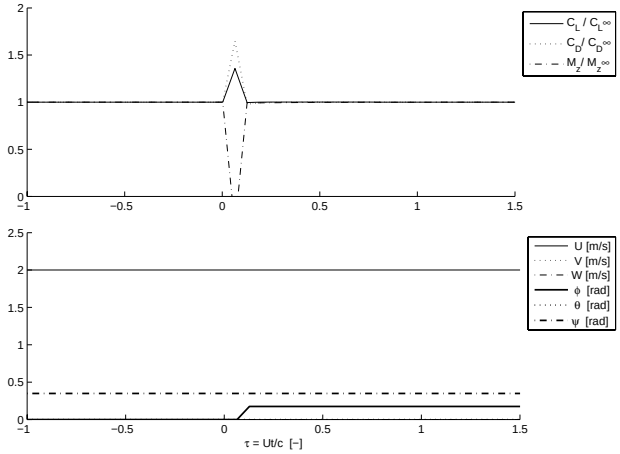

Figure D.11: The calculated hydrodynamic forces on a trawl door at steady state, given a sudden rotation about local x^f-axis.

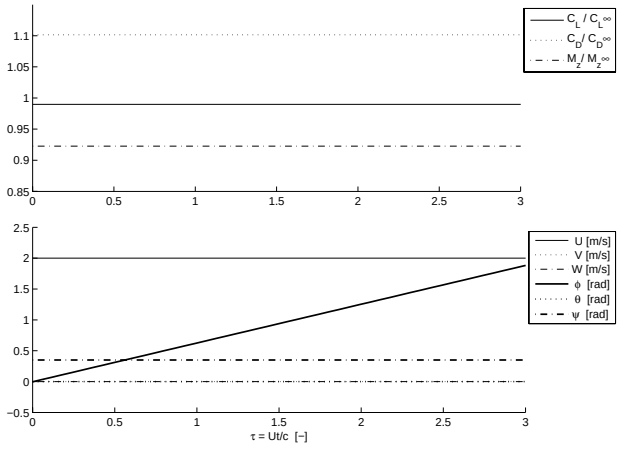

Figure D.12: The calculated hydrodynamic forces on a trawl door with steady rotation about local x^f-axis.

Appendix E

Simulation of the trawl doors

If the acceleration dependent hydrodynamic forces on the trawl door were formulated as in section 3.3.4, algebraic loops would arise during system simulations. These would have to be solved using multiple iterations each timestep, considerably slowing down the simulations. It is therefore chosen to simplify the calculation of these forces.

The dynamics of the trawl door is formulated as

$$\sum \boldsymbol{\tau}_d^d = \mathbf{M}_d^{RB} \dot{\boldsymbol{\nu}}_{dn}^d, \tag{E.1}$$

where $\mathbf{M}_d^{RB} \in \mathbb{R}^{6\times6}$ is the rigid body mass matrix of the trawl door, $\sum \boldsymbol{\tau}_d^d \in \mathbb{R}^6$ is the sum of the forces acting on the trawl door, decomposed in the trawl door frame, and $\dot{\boldsymbol{\nu}}_{dn}^d \in \mathbb{R}^6$ is the acceleration vector of the trawl door decomposed in the trawl door frame. The sum of the forces acting on the trawl door can be divided into:

$$\sum \boldsymbol{\tau}_d^d = \boldsymbol{\tau}_{d\Upsilon}^d + \sum_{k=1}^{N_{dl}} \boldsymbol{\tau}_{dl_k}^d + \boldsymbol{\tau}_{dg}^d + \boldsymbol{\tau}_{db}^d, \tag{E.2}$$

where $\boldsymbol{\tau}_{d\Upsilon}^d$ is the hydrodynamic forces on the trawl door, $\boldsymbol{\tau}_{dl_k}^d$ is the generalized force from external line (such as bridles and warp) number k, N_{dl} is the number of external lines connected to the trawl door, $\boldsymbol{\tau}_{dg}^d$ and $\boldsymbol{\tau}_{db}^d$ are the generalized gravity and buoyancy forces, respectively. It is assumed that the density of the trawl door material is constant, and that there are no cavities filled with air. The gravity and buoyancy forces will then attack along the same line, but in opposite direction. These forces can then be combined into one resulting force:

$$\boldsymbol{\tau}_{d\varrho}^d = \boldsymbol{\tau}_{dg}^d + \boldsymbol{\tau}_{db}^d. \tag{E.3}$$

It is assumed that the water frame is not accelerated in relation to the global frame, and that the coefficients of (3.116) to (3.118) can be approximated as the values for $\alpha^d = 20°$. This yields

$$\dot{\boldsymbol{\nu}}^d_{dw} = \dot{\boldsymbol{\nu}}^d_{dn}, \tag{E.4}$$
$$C^a_{22} = -1.7, \tag{E.5}$$
$$C^a_{44} = -0.067, \tag{E.6}$$
$$C^a_{66} = -0.041. \tag{E.7}$$

This makes it possible to implement the acceleration dependent hydrodynamic forces by an additional mass term:

$$\boldsymbol{\tau}^{dA}_{da} = -\mathbf{M}^A_d \, \dot{\boldsymbol{\nu}}^d_{dw}, \tag{E.8}$$

where $\mathbf{M}^A_d$ is the constant hydrodynamic added mass matrix of the trawl door, taken to be

$$\mathbf{M}^A_d = \begin{bmatrix} 0 & 0 & 0 & 0 & 0 & 0 \\ 0 & M^A_{d,22} & 0 & 0 & 0 & 0 \\ 0 & 0 & 0 & 0 & 0 & 0 \\ 0 & 0 & 0 & M^A_{d,44} & 0 & 0 \\ 0 & 0 & 0 & 0 & 0 & 0 \\ 0 & 0 & 0 & 0 & 0 & M^A_{d,66} \end{bmatrix}, \tag{E.9}$$

where the non zero mass terms are found from

$$M^A_{d,22} = -\frac{1}{2}\rho_w A_d^{\frac{3}{2}} C^a_{22}, \tag{E.10}$$
$$M^A_{d,44} = -\frac{1}{2}\rho_w A_d^{\frac{3}{2}} h_d^2 C^a_{44}, \tag{E.11}$$
$$M^A_{d,66} = -\frac{1}{2}\rho_w A_d^{\frac{3}{2}} c_d^2 C^a_{66}. \tag{E.12}$$

Implementing these approximations into the equations of motion, yields:

$$\boldsymbol{\tau}^c_d + \boldsymbol{\tau}^a_d + \boldsymbol{\tau}^v_d + \sum_{k=1}^{N_{dl}} \boldsymbol{\tau}^d_{dl_k} + \boldsymbol{\tau}^d_{dg} + \boldsymbol{\tau}^d_{db} = \mathbf{M}^{RB}_d \dot{\boldsymbol{\nu}}^d_{dn} \tag{E.13}$$
$$\boldsymbol{\tau}^c_d + \boldsymbol{\tau}^v_d + \sum_{k=1}^{N_{dl}} \boldsymbol{\tau}^d_{dl_k} + \boldsymbol{\tau}^d_{d\varrho} = \mathbf{M}^{RB}_d \dot{\boldsymbol{\nu}}^d_{dn} + \mathbf{M}^A_d \dot{\boldsymbol{\nu}}^d_{dw} \tag{E.14}$$
$$\boldsymbol{\tau}^c_d + \boldsymbol{\tau}^v_d + \sum_{k=1}^{N_{dl}} \boldsymbol{\tau}^d_{dl_k} + \boldsymbol{\tau}^d_{d\varrho} = (\mathbf{M}_d)\, \dot{\boldsymbol{\nu}}^d_{dn}, \tag{E.15}$$

where

$$\mathbf{M}_d = \mathbf{M}^{RB}_d + \mathbf{M}^A_d. \tag{E.16}$$

Appendix F

Simulations preceding the towing tank experiments

Preliminary simulations were performed to minimize the time consumption of the towing tank experiments. These simulations estimated how the rigging of the trawl door would affect the performance of the control actions, and also to better be able to do qualified adjustments of the rigging during the experiments. Since these experiments were done before the wind-tunnel experiments, only rough estimates of the hydrodynamic forces for a few degrees of freedom and for a few orientation angles could be obtained. The simulations were performed until steady states were achieved, for various riggings. The results are plotted in the Figures F.1 - F.18.

The Figures F.1 - F.3 show how the angles of attack, pitch and roll are expected to change as the rigging changes. In these figures, the vertical axis shows how the position of the warp fastening point is moved along the x^m-axis. The horizontal axis shows how the bridle fastening points are moved along the x^m-axis, with identical x^m-coordinates. The y^m-coordinate of the warp fastening point is $y_w^m = -0.01\,\mathrm{m}$. The other coordinates are kept as close to original as possible. The black, vertical lines indicate the range of the original bridle fastening points. The horizontal, black lines indicate the three original fastening points of the warp.

The Figures F.4 - F.6 show the same, only changing the y^m-coordinate of the warp fastening point to $y_w^m = -0.005\,\mathrm{m}$.

The Figures F.7 - F.9 show how the angles of attack, pitch and roll are expected to change as the fastening point of the lower bridle moves. The Figures F.10 - F.12 show the same, but with a changed rigging, and this is the case also for the Figures F.13 - F.15.

The Figures F.16 - F.18 show how the angles of attack, pitch and roll are expected to change as the fastening point of the warp moves.

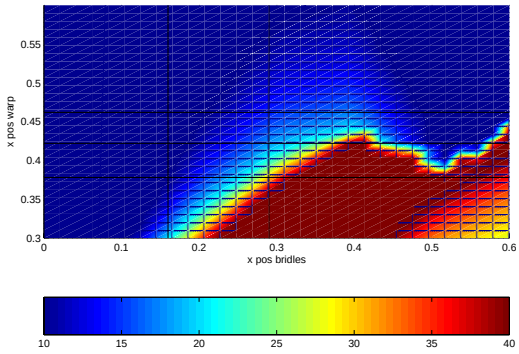

Figure F.1: Angle of attack as a function of x^m_{lb}, x^m_{ub} and x^m_{warp}. $x^m_{lb} = x^m_{ub}$ and $y^m_{warp} = -0.01\,\mathrm{m}$.

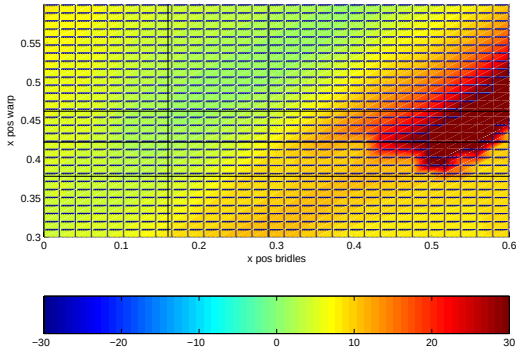

Figure F.2: Angle of roll as a function of x^m_{lb}, x^m_{ub} and x^m_{warp}. $x^m_{lb} = x^m_{ub}$ and $y^m_{warp} = -0.01\,\mathrm{m}$.

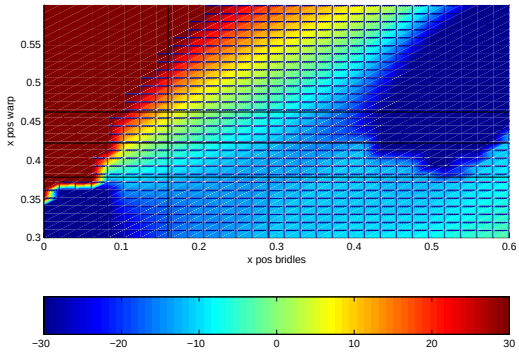

Figure F.3: Angle of pitch as a function of x^m_{lb}, x^m_{ub} and x^m_{warp}. $x^m_{lb} = x^m_{ub}$ and $y^m_{warp} = -0.01\,\mathrm{m}$.

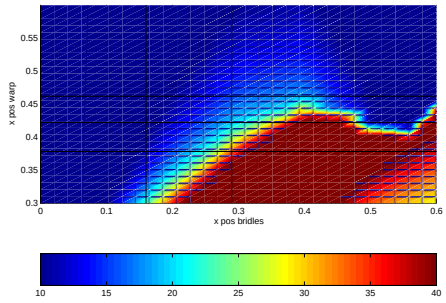

Figure F.4: Angle of attack as a function of x^m_{lb}, x^m_{ub} and x^m_{warp}. $x^m_{lb} = x^m_{ub}$ and $y^m_{warp} = -0.005\,\mathrm{m}$.

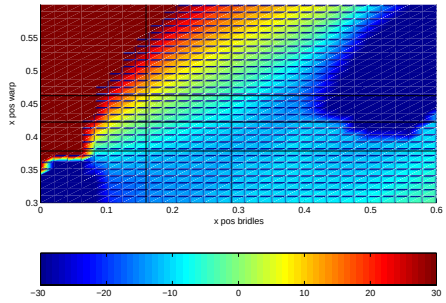

Figure F.5: Angle of roll as a function of x^m_{lb}, x^m_{ub} and x^m_{warp}. $x^m_{lb} = x^m_{ub}$ and $y^m_{warp} = -0.005\,\mathrm{m}$.

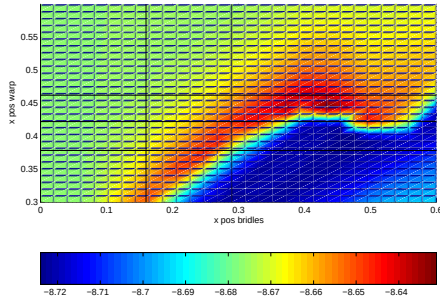

Figure F.6: Angle of pitch as a function of x^m_{lb}, x^m_{ub} and x^m_{warp}. $x^m_{lb} = x^m_{ub}$ and $y^m_{warp} = -0.005\,\mathrm{m}$.

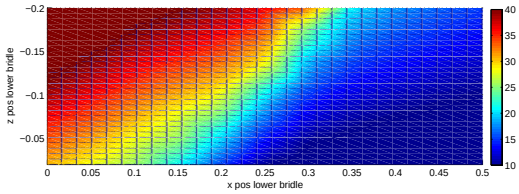

Figure F.7: Angle of attack as a function of y_{lb}^m and z_{lb}^m. $\mathbf{p}_{warp}^m = \begin{bmatrix} 0.422\,\mathrm{m} & -0.01\,\mathrm{m} & -0.07\,\mathrm{m} \end{bmatrix}^T$ and $\mathbf{p}_{ub}^m = \begin{bmatrix} 0.384\,\mathrm{m} & -0.0942\,\mathrm{m} & -0.2\,\mathrm{m} \end{bmatrix}^T$.

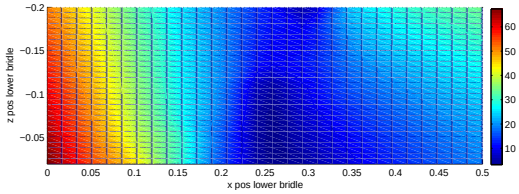

Figure F.8: Angle of roll as a function of y_{lb}^m and z_{lb}^m. $\mathbf{p}_{warp}^m = \begin{bmatrix} 0.422\,\mathrm{m} & -0.01\,\mathrm{m} & -0.07\,\mathrm{m} \end{bmatrix}^T$ and $\mathbf{p}_{ub}^m = \begin{bmatrix} 0.384\,\mathrm{m} & -0.0942\,\mathrm{m} & -0.2\,\mathrm{m} \end{bmatrix}^T$.

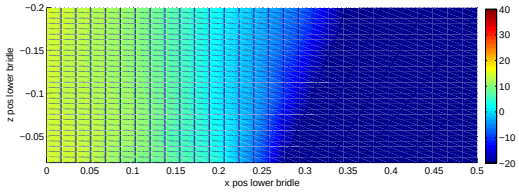

Figure F.9: Angle of pitch as a function of y_{lb}^m and z_{lb}^m. $\mathbf{p}_{warp}^m = \begin{bmatrix} 0.422\,\mathrm{m} & -0.01\,\mathrm{m} & -0.07\,\mathrm{m} \end{bmatrix}^T$ and $\mathbf{p}_{ub}^m = \begin{bmatrix} 0.384\,\mathrm{m} & -0.0942\,\mathrm{m} & -0.2\,\mathrm{m} \end{bmatrix}^T$.

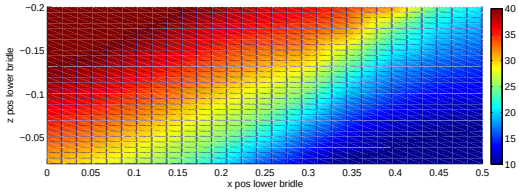

Figure F.10: Angle of attack as a function of y_{lb}^m and z_{lb}^m. $\mathbf{p}_{warp}^m = \begin{bmatrix} 0.422\,\mathrm{m} & -0.01\,\mathrm{m} & -0.07\,\mathrm{m} \end{bmatrix}^T$ and $\mathbf{p}_{ub}^m = \begin{bmatrix} 0.384\,\mathrm{m} & -0.0942\,\mathrm{m} & -0.3\,\mathrm{m} \end{bmatrix}^T$.

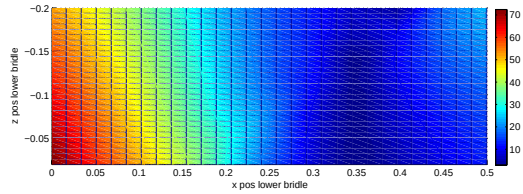

Figure F.11: Angle of roll as a function of y_{lb}^m and z_{lb}^m. $\mathbf{p}_{warp}^m = \begin{bmatrix}0.422\,\text{m} & -0.01\,\text{m} & -0.07\,\text{m}\end{bmatrix}^T$ and $\mathbf{p}_{ub}^m = \begin{bmatrix}0.384\,\text{m} & -0.0942\,\text{m} & -0.3\,\text{m}\end{bmatrix}^T$.

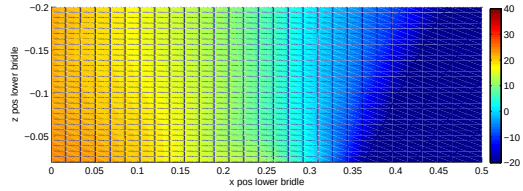

Figure F.12: Angle of pitch as a function of y_{lb}^m and z_{lb}^m. $\mathbf{p}_{warp}^m = \begin{bmatrix}0.422\,\text{m} & -0.01\,\text{m} & -0.07\,\text{m}\end{bmatrix}^T$ and $\mathbf{p}_{ub}^m = \begin{bmatrix}0.384\,\text{m} & -0.0942\,\text{m} & -0.3\,\text{m}\end{bmatrix}^T$.

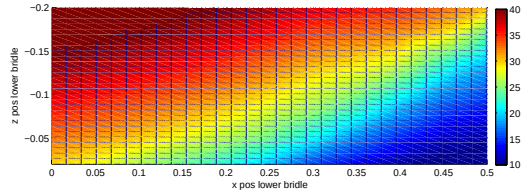

Figure F.13: Angle of attack as a function of y_{lb}^m and z_{lb}^m. $\mathbf{p}_{warp}^m = \begin{bmatrix}0.422\,\text{m} & -0.01\,\text{m} & -0.07\,\text{m}\end{bmatrix}^T$ and $\mathbf{p}_{ub}^m = \begin{bmatrix}0.384\,\text{m} & -0.0942\,\text{m} & -0.4\,\text{m}\end{bmatrix}^T$.

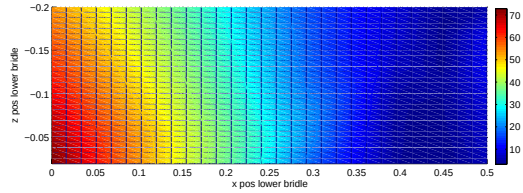

Figure F.14: Angle of roll as a function of y_{lb}^m and z_{lb}^m. $\mathbf{p}_{warp}^m = \begin{bmatrix}0.422\,\text{m} & -0.01\,\text{m} & -0.07\,\text{m}\end{bmatrix}^T$ and $\mathbf{p}_{ub}^m = \begin{bmatrix}0.384\,\text{m} & -0.0942\,\text{m} & -0.4\,\text{m}\end{bmatrix}^T$.

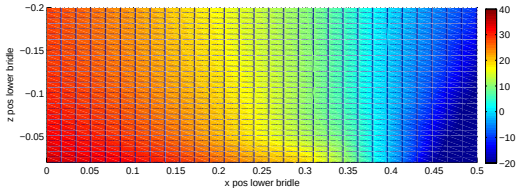

Figure F.15: Angle of pitch as a function of y^m_{lb} and z^m_{lb}. $\mathbf{p}^m_{warp} = \begin{bmatrix}0.422\,\text{m} & -0.01\,\text{m} & -0.07\,\text{m}\end{bmatrix}^T$ and $\mathbf{p}^m_{ub} = \begin{bmatrix}0.384\,\text{m} & -0.0942\,\text{m} & -0.4\,\text{m}\end{bmatrix}^T$.

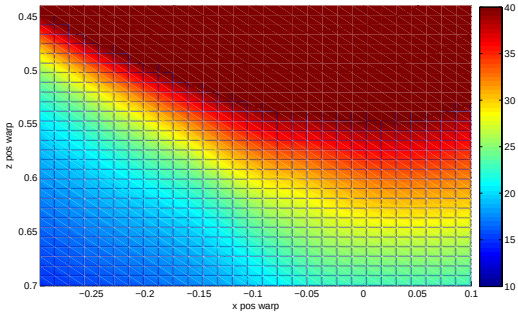

Figure F.16: Angle of attack as a function of x^m_{warp} and z^m_{warp}. $y^m_{warp} = 0.1\,\text{m}$. $\mathbf{p}^m_{ub} = \begin{bmatrix}0.384\,\text{m} & -0.0942\,\text{m} & -0.464\,\text{m}\end{bmatrix}^T$ and $\mathbf{p}^m_{lb} = \begin{bmatrix}0.384\,\text{m} & -0.0942\,\text{m} & 0.367\,\text{m}\end{bmatrix}^T$.

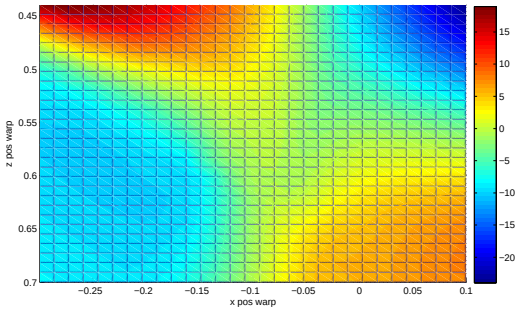

Figure F.17: Angle of roll as a function of x^m_{warp} and z^m_{warp}. $y^m_{warp} = 0.1\,\text{m}$. $\mathbf{p}^m_{ub} = \begin{bmatrix}0.384\,\text{m} & -0.0942\,\text{m} & -0.464\,\text{m}\end{bmatrix}^T$ and $\mathbf{p}^m_{lb} = \begin{bmatrix}0.384\,\text{m} & -0.0942\,\text{m} & 0.367\,\text{m}\end{bmatrix}^T$.

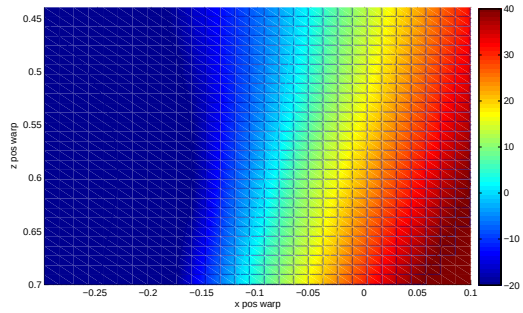

Figure F.18: Angle of pitch as a function of x^m_{warp} and z^m_{warp}. $y^m_{warp} = 0.1\,\text{m}$. $\mathbf{p}^m_{ub} = \begin{bmatrix}0.384\,\text{m} & -0.0942\,\text{m} & -0.464\,\text{m}\end{bmatrix}^T$ and $\mathbf{p}^m_{lb} = \begin{bmatrix}0.384\,\text{m} & -0.0942\,\text{m} & 0.367\,\text{m}\end{bmatrix}^T$.

Previous PhD theses from the Institute of Marine Technology

UR-79-01	Brigt Hatlestad	The finite element method used in a fatigue evaluation of fixed offshore platforms.
UR-79-02	Erik Pettersen	Analysis and design of celluar structures.
UR-79-03	Sverre Valsgård	Finite difference and finite element methods applied to nonlinear analysis of plated structures.
UR-79-04	Nils T. Nordsve	Finite element collapse analysis of structural members considering imperfections and stresses due to fabrication.
UR-79-05	Ivar J.Fylling	Analysis of towline forces in ocean towing systems.
UR-80-06	Nils Sandsmark	Analysis of Stationary and Transient Heat Conduction by the Use of the Finite Element Method.
UR-80-09	Sverre Haver	Analysis of uncertainties related to the stochastic modelling of Three-Dimensional Flow Past Lifting Surfaces and Blunt Bodies.
UR-85-46	Alf G. Engseth	Finite element collapse analysis of turbular steel offshore structures.
UR-86-47	Dengody Sheshappa	A Computer Design Model for Optimizing Fishing Vessel Designs Based on Techno-Economic Analysis.
UR-86-48	Vidar Aanesland	A Theoretical and Numerical Study of Ship Wave Resistance.
UR-86-49	Heinz-Joachim Wessel	Fracture Mechanics Analysis of Crack Growth in Plate Girders.
UR-86-50	Jon Taby	Ultimate and Post-ultimate Strength of Dented Tubular Members.
UR-86-51	Walter Lian	A Numerical Study of Two-Dimensional Separated Flow Past Bluff Bodies at Moderate KC-Numbers.
UR-86-52	Bjørn Sortland	Force Measurements in Oscillating Flow on Ship Sections and Circular Cylinders in a U-Tube Water Tank.
UR-86-53	Kurt Strand	A System Dynamic Approach to One-dimensional Fluid Flow.
UR-86-54	Arne Edvin Løken	Three Dimensional Second Order Hydrodynamic Effects on Ocean Structures in Waves.
UR-86-55	Sigurd Falch	A Numerical Study of Slamming of Two-Dimensional Bodies.
UR-87-56	Arne Braathen	Application of a Vortex Tracking Method to the Prediction of Roll Damping of a Two-Dimension Floating Body.
UR-87-57	Bernt Leira	Caussian Vector Processes for Reliability Analysis involving Wave-Induced Load Effects.
UR-87-58	Magnus Småvik	Thermal Load and Process Characteristics in a Two-Stroke Diesel Engine with Thermal Barriers (in Norwegian)

MTA-88-59	Bernt Arild Bremdal	An Investigation of Marine Installation Processes - A Knowledge- Based Planning Approach.
MTA-88-60	Xu Jun	Non-linear Dynamic Analysis of Space-framed Offshore Structures.
MTA-89-61	Gang Miao	Hydrodynamic Forces and Dynamic Responses of Circular Cylinders in Wave Zones.
MTA-89-62	Martin Greenhow	Linear and Non-Linear Studies of Waves and Floating Bodies. Part I and Part 11.
MTA-89-63	Chang Li	Force Coefficients of Spheres and Cubes in Oscillatory Flow with and without Current.
MTA-89-64	Hu Ying	A Study of Marketing and Design in Development of Marine Transport Systems.
MTA-89-65	Arild Jæger	Seakeeping, Dynamic Stability and Performance of a Wedge Shaped Planing Hull.
MTA-89-66	Chan Siu Hung	The dynamic characteristics of tilting-pad bearings.
MTA-89-67	Kim Wikstrøm	Analysis av projekteringen for ett offshore projekt.
MTA-89-68	Jiao Guoyang	Reliability Analysis of Crack Growth under Random Loading, considering Model Updating.
MTA-89-69	Arnt Olufsen	Uncertainty and Reliability Analysis of Fixed Offshore Structures.
MTA-89-70	Wu Yu-Lin	System Reliability Analyses of Offshore Structures using improved Truss and Beam Models.
MTA-90-71	Jan Roger Hoff	Three-dimensional Green function of a vessel with forward speed in waves.
MTA-90-72	Rong Zhao	Slow-Drift Motions of a Moored Two-Dimensional Body in Irregular Waves.
MTA-90-73	Atle Minsaas	Economical Risk Analysis.
MTA 90 74	Knut Aril Farnes	Long term Statistics of Response in Non linear Marine Structures.
MTA 90 75	Torbjørn Sotberg	Application of Reliability Methods for Safety Assessment of Submarine Pipelines.
MTA 90 76	Zeuthen, Steffen	SEAMAID. A computional model of the design process in a constraint based logic programming environment. An example from the offshore domain.
MTA-91-77	Haagensen, Sven	Fuel Dependant Cyclic Variability in a Spark Ignition Engine - An Optical Approach.
MTA-91-78	Løland, Geir	Current forces on and flow through fish farms.
MTA-91-79	Hoen, Christopher	System Identification of Structures Excited by Stochastic Load Processes.
MTA-91-80	Haugen, Stein	Probabilistic Evaluation of Frequency of Collision between Ships and Offshore Platforms.
MTA-91-81	Sødahl, Nils	Methods for Design and Analysis of Flexible Risers.
MTA-91-82	Ormberg, Harald	Non-linear Response Analysis of Floating Fish Farm Systems.

MTA-91-83	Marley, Mark J.	Time Variant Reliability Under Fatigue
MTA-91-79	Hoen, Christopher	System Identification of Structures Excited by Stochastic Load Processes.
MTA-91-80	Haugen, Stein	Probabilistic Evaluation of Frequency of Collision between Ships and Offshore Platforms.
MTA-91-81	Sødahl, Nils	Methods for Design and Analysis of Flexible Risers.
MTA-91-82	Ormberg, Harald	Non-linear Response Analysis of Floating Fish Farm Systems.
MTA-91-83	Marley, Mark J.	Time Variant Reliability Under Fatigue Degradation.
MTA-91-84	Krokstad, Jørgen R.	Second-order Loads in Multidirectional Seas.
MTA-91-85	Molteberg, Gunnar A.	The application of system identification techniques to Performance Monitoring of four stroke turbocharged Diesel Engines.
MTA-92-86	Mørch, Hans Jørgen B.	Aspects of Hydrofoil Design; with Emphasis on Hydrofoil Interaction in Calm Water.
MTA-92-87	Chan Siu Hung	Nonlinear Analysis of Rotordynamic Instabilities in High-speed Turbomachinery.
MTA-92-88	Bessason, Bjarni	Assessment of Earthquake Loading and Response of Seismically Isolated Bridges.
MTA-92-89	Langli, Geir	Improving Operational Safety through Exploitation of Design Knowledge - an investigation of offfshore platform safety.
MTA-92-90	Sævik, Svein	On Stresses and Fatigue in Flexible Pipes.
MTA-92-91	Ask, Tor Ø.	Ignition and Flame Growth in Lean Gas-Air Mixtures. An Experimental Study with a Schlieren System.
MTA-86-92	Hessen, Gunnar	Fracture Mechanics Analysis of Stiffened Tubular Members.
MTA-93-93	Steinebach, Christian	Knowledge Based Systems for Diagnosis of Rotating Machinery.
MTA-93-94	Dalane, Jan Inge	System Reliability in Design and Maintenance of Fixed Offshore Structures.
MTA-93-95	Steen, Sverre	Cobblestone Effect on SES.
MTA-93-96	Karunakaran, Daniel	Nonlinear Dynamic Response and Reliability Analysis of Drag-dominated Offshore Platforms.
MTA-93-97	Hagen, Arnulf	The Framework of a Design Process Language.
MTA-93-98	Nordrik, Rune	Investigation of Spark Ignition and Autoignition in Methane and Air Using Computational Fluid Dynamics and Chemical Reaction Kinetics. A Numerical Study of Ignition Processes in Internal Combustion Engines.
MTA-94-99	Passano, Elizabeth	Efficient Analysis of Nonlinear Slender Marine Structures.
MTA-94-100	Kvålsvold, Jan	Hydroelastic Modelling of Wetdeck Slamming on Multihull Vessels.
MTA-94-101	NN	Not approved.

MTA-94-102	Bech, Sidsel M.	Experimental and Numerical Determination of Stiffness and Strength of GRP/PVC Sandwich Structures.
MTA-95-103	Paulsen, Hallvard	A Study of Transient Jet and Spray using a Schlieren Method and Digital Image Processing.
MTA-95-104	Hovde, Geir Olav	Fatigue and Overload Reliability of Offshore Structural Systems, Considering the Effect of Inspection and Repair.
MTA-95-105	Wang, Xiaozhi	Reliability Analysis of Production Ships with Emphasis on Load Combination and Ultimate Strength.
MTA-95-106	Ulstein, Tore	Nonlinear Effects of a Flexible Stern Seal Bag on Cobblestone Oscillations of an SES.
MTA-95-107	Solaas, Frøydis	Analytical and Numerical Studies of Sloshing in Tanks.
MTA-95-108	Hellan, øyvind	Nonlinear Pushover and Cyclic Analyses in Ultimate Limit State Design and Reassessment of Tubular Steel Offshore Structures.
MTA-95-109	Hermundstad, Ole A.	Theoretical and Experimental Hydroelastic Analysis of High Speed Vessels.
MTA-96-110	Bratland, Anne K.	Wave-Current Interaction Effects on Large-Volume Bodies in Water of Finite Depth.
MTA-96-111	Herfjord, Kjell	A Study of Two-dimensional Separated Flow by a Combination of the Finite Element Method and Navier-Stokes Equations.
MTA-96-112	Æsøy, Vilmar	Hot Surface Assisted Compression Ignition in a Direct Injection Natural Gas Engine.
MTA-96-113	Eknes, Monika L.	Escalation Scenarios Initiated by Gas Explosions on Offshore Installations.
MTA-96-114	Erikstad, Stein O.	A Decision Support Model for Preliminary Ship Design.
MTA-96-115	Pedersen, Egil	A Nautical Study of Towed Marine Seismic Streamer Cable Configurations.
MTA-97-116	Moksnes, Paul O.	Modeling Two-Phase Thermo-Fluid Systems Using Bond Graphs.
MTA-97-117	Halse, Karl H.	On Vortex Shedding and Prediction of Vortex-Induced Vibrations of Circular Cylinders.
MTA-97-118	Igland, Ragnar T.	A Thesis Submitted in Partial Fulfilment of the Requirements for the Degree of "Doktor Ingeniør".
MTA-97-119	Pedersen, Hans-P.	Levendefiskteknologi for fiskefartøy.
MTA-98-120	Vikestad, Kyrre	Multi-Frequency Response of a Cylinder Subjected to Vortex Shedding and Support Motions.
MTA-98-121	Azadi, Mohammad R.E.	Analysis of Static and Dynamic Pile-Soil-Jacket Behaviour.
MTA-98-122	Ulltang, Terje	A Communication Model for Product Information.
MTA-98-123	Torbergsen, Erik	Impeller/Diffuser Interaction Forces in Centrifugal Pumps.

MTA-98-124	Hansen, Edmond	A Descrete Element Model to Study Marginal Ice Zone Dynamics and the Behaviour of Vessels Moored in Broken Ice.
MTA-98-125	Videiro, Paulo M.	Reliability Based Design of Marine Structures.
MTA-99-126	Mainçon, Philippe	Fatigue Reliability of Long Welds Application to Titanium Risers.
MTA-99-127	Haugen, Elin M.	Hydroelastic Analysis of Slamming on Stiffened Plates with Application to Catamaran Wetdecks.
MTA-99-128	Langhelle, Nina K.	Experimental Validation and Calibration of Nonlinear Finite Element Models for Use in Design of Aluminium Structures Exposed to Fire.
MTA-99-129	Berstad, Are J.	Calculation of Fatigue Damage in Ship Structures.
MTA-99-130	Andersen, Trond M.	Short Term Maintenance Planning.
MTA-99-131	Tveiten, Bård Wathne	Fatigue Assessment of Welded Aluminum Ship Details.
MTA-99-132	Søreide, Fredrik	Applications of underwater technology in deep water archaeology. Principles and practice.
MTA-99-133	Tønnessen, Rune	A Finite Element Method Applied to Unsteady Viscous Flow Around 2D Blunt Bodies With Sharp Corners.
MTA-99-134	Elvekrok, Dag R.	Engineering Integration in Field Development Projects in the Norwegian Oil and Gas Industry. The Supplier Management of Norne.
MTA-99-135	Fagerholt, Kjetil	Optimeringsbaserte Metoder for Ruteplanlegging innen skipsfart.
MTA-99-136	Bysveen, Marie	Visualization in Two Directions on a Dynamic Combustion Rig for Studies of Fuel Quality.
MTA-2000-137	Storteig, Eskild	Dynamic characteristics and leakage performance of liquid annular seals in centrifugal pumps.
MTA-2000-138	Sagli, Gro	Model uncertainty and simplified estimates of long term extremes of hull girder loads in ships.
MTA-2000-139	Tronstad, Harald	Nonlinear analysis and design of cable net structures like fishing gear based on the finite element method.
MTA-2000-140	Kroneberg, André	Innovation in shipping by using scenarios.
MTA-2000-141	Haslum, Herbjørn A.	Simplified methods applied to nonlinear motion of spar platforms.
MTA-2001-142	Samdal, Ole Johan	Modelling of Degradation Mechanisms and Stressor Interaction on Static Mechanical Equipment Residual Lifetime.
MTA-2001-143	Baarholm, Rolf Jarle	Theoretical and experimental studies of wave impact underneath decks of offshore platforms.
MTA-2001-144	Wang, Lihua	Probabilistic Analysis of Nonlinear Wave-induced Loads on Ships.
MTA-2001-145	Kristensen, Odd H. Holt	Ultimate Capacity of Aluminium Plates under Multiple Loads, Considering HAZ Properties.

MTA-2001-146	Greco, Marilena	A Two-Dimensional Study of Green-Water Loading.
MTA-2001-147	Heggelund, Svein E.	Calculation of Global Design Loads and Load Effects in Large High Speed Catamarans.
MTA-2001-148	Babalola, Olusegun T.	Fatigue Strength of Titanium Risers - Defect Sensitivity.
MTA-2001-149	Mohammed, Abuu K.	Nonlinear Shell Finite Elements for Ultimate Strength and Collapse Analysis of Ship Structures.
MTA-2002-150	Holmedal, Lars E.	Wave-current interactions in the vicinity of the sea bed.
MTA20-02-151	Rognebakke, Olav F.	Sloshing in rectangular tanks and interaction with ship motions
MTA-2002-152	Lader, Pål Furset	Geometry and Kinematics of Breaking Waves.
MTA-2002-153	Yang, Qinzheng	Wash and wave resistance of ships in finite water depth.
MTA-2002-154	Melhus, Øyvin	Utilization of VOC in Diesel Engines. Ignition and combustion of VOC released by crude oil tankers.
MTA-2002-155	Ronæss, Marit	Wave Induced Motions of Two Ships Advancing on Parallel Course.
MTA-2002-156	Økland, Ole D.	Numerical and experimental investigation of whipping in twin hull vessels exposed to severe wet deck slamming.
MTA-2002-157	Ge, Chunhua	Global Hydroelastic Response of Catamarans due to Wet Deck Slamming.
MTA-2002-158	Byklum, Eirik	Nonlinear Shell Finite Elements for Ultimate Strength and Collapse Analysis of Ship Structures. .
IMT-2003-1	Chen, Haibo	Probabilistic Evaluation of FPSO-Tanker Collision in Tandem Offloading Operation.
IMT-2003-2	Skaugset, Kjetil Bjørn	On the Suppression of Vortex Induced Vibrations of Circular Cylinders by Radial Water Jets.
IMT-2003-3	Chezhian, Muthu	Three-Dimensional Analysis of Slamming
IMT-2003-4	Buhaug, Øyvind	Deposit Formation on cylinder Liner Surfaces in Medium Speed Engines
IMT-2003-5	Tregde, Vidar	Aspects of Ship Design; Optimization of Aft Hull with Inverse Geometry Design
IMT-2003-6	Wist, Hanne Therese	Statistical Properties of Successive Ocean Wave Parameters
IMT-2004-7	Ransau, Samuel	Numerical Methods for Flows with Evolving Interfaces
IMT-2004-8	Soma, Torkel	Blue-Chip or Sub-Standard. A data interrogation approach of identity safety characteristics of shipping organization
IMT-2004-9	Ersdal, Svein	An experimental study of hydrodynamic forces on cylinders and cables in near axial flow
IMT-2005-10	Brodtkorb, Per Andreas	The Probability of Occurrence of Dangerous Wave Situations at Sea

IMT-2005-11	Yttervik, Rune	Ocean current variability in relation to offshore engineering
IMT-2005-12	Fredheim, Arne	Current Forces on Net-Structures
IMT-2005-13	Heggernes, Kjetil	Flow around marine structures
IMT-2005-14	Fouques, Sebastien	Lagrangian Modelling of Ocean Surface Waves and Synthetic Aperture Radar Wave Measurements
IMT-2006-15	Holm, Håvard	Numerical calculation of viscous free surface flow around Marine structures
IMT-2006-16	Bjørheim, Lars G.	Failure Assessment of Long Through Thickness Fatigue Cracks in Ship Hulls
IMT-2006-17	Hansson, Lisbeth	Safety Management for Prevention of Occupational Accidents
IMT-2006-18	Zhu, Xinying	Application of the CIP Method to Strongly Nonlinear